INVESTIGATIONS ON LIGATING PROPERTIES OF SOME MULTIDENTATE LIGANDS TOWARDS TRANSITION METALS: SPECTRAL STUDIES AND CRYSTAL STRUCTURES

Thesis submitted to

Cochin University of Science and Technology

in partial fulfillment of the requirements

for the award of the degree of

Doctor of Philosophy

in

Chemistry

Under the Faculty of Science

by

Sajitha N. R.

Department of Applied Chemistry

Cochin University of Science and Technology

Kochi – 22

August 2017

Investigations on ligating properties of some multidentate ligands towards transition metals: Spectral studies and crystal structures

Ph.D. Thesis under the Faculty of Science

By

Sajitha N. R.
Research Fellow
Department of Applied Chemistry
Cochin University of Science and Technology
Kochi, India 682022
Email: sajithasubyr@gmail.com

Supervising Guide

Dr. M.R. Prathapachandra Kurup
Rtd. Professor
Department of Applied Chemistry
Cochin University of Science and Technology
Kochi, India 682022
Email: mrp@cusat.ac.in

Department of Applied Chemistry
Cochin University of Science and Technology
Kochi, India 682022

August 2017

Front cover: Hydrogen bonding interactions in $[Ni(anpt)_2]\cdot DMF$.
Back cover: Hydrogen bonding interactions in Hbpdmt.

DEPARTMENT OF APPLIED CHEMISTRY
COCHIN UNIVERSITY OF SCIENCE AND TECHNOLOGY
KOCHI - 682022, INDIA

Dr. M. R. Prathapachandra Kurup
Rtd. Professor

Phone Off. 0484-2862423
Res. 0484-2576904
Telex: 885-5019 CUIN
Fax: 0484-2577595
Email: mrp@cusat.ac.in
mrp_k@yahoo.com

Date: ……..

Certificate

This is to certify that the thesis entitled **"Investigations on ligating properties of some multidentate ligands towards transition metals: Spectral studies and crystal structures"** is an authentic record of research work carried out by **Ms. Sajitha N.R.** under my supervision in partial fulfillment of the requirements for the award of the degree of Doctor of Philosophy in Chemistry under the Faculty of Science of Cochin University of Science and Technology, and further that no part thereof has been presented before for the award of any other degree. All the relevant corrections and modifications suggested by the audience and recommended by the doctoral committee of the candidate during the presynopsis seminar have been incorporated in the thesis.

Dr. M.R. Prathapachandra Kurup
(Supervising Guide)

Declaration

I hereby declare that the work presented in this thesis entitled "**Investigations on ligating properties of some multidentate ligands towards transition metals: Spectral studies and crystal structures**" is entirely original and was carried out independently under the supervision of **Dr. M. R. Prathapachandra Kurup**, Rtd. Professor, Department of Applied Chemistry, Cochin University of Science and Technology and has not been included in any other thesis submitted previously for the award of any other degree.

Kochi-22 **Sajitha N.R.**
03/08/2017

"Confidence and hard work is the best medicine to kill the disease called failure .It will make you a successful person"

Dr. A.P.J. Abdul Kalam

To my dearest

Ikka

Acknowledgement

This doctoral thesis has been seen through to completion only because of the support and encouragement of numerous people. It is a pleasure to express my sincere gratitude to all those who helped me in many ways for the success of this study and made it an unforgettable experience for me.

First and foremost, I thank god almighty for guiding and strengthening me throughout my research work. It is like you fulfilled all my dreams in the present life.

Next, I express my heart-felt gratitude to my supervising guide Prof. M.R. Prathapachandra Kurup who is presently HOD, Department of Chemistry, Central University, Kasargod for his valuable guidance, support and encouragement. He is the person who guides me, walked with me and encouraged me to do whatever I want without any hesitation. Without your help and freedom you offered me I could never complete my work in the form presented in this thesis. I will never forget your patience with me whenever I approached you with a lot of silly questions.

I express my sincere thanks to Dr. P.M. Sabura begum who is my doctoral committee member for all the support and help offered to me constantly during my period of work. Without you madam I could never had find a place in the department. I thank Prof. K. Girish Kumar, Head, Department of Applied Chemistry, CUSAT for his encouragement and support. I extend my thanks to former heads Prof. K Sreekumar and Dr. N. Manoj for all the help and cooperation during the period of this work. I thank Dr. S Prathapan for his wonderful classes during the period of course work. I extend my thanks to Prof. K.K. Mohammed Yusuff and Prof. S. Sugunan for their support and help during my period of work. I am thankful for the support received from all the teaching and non-teaching staff of the Department of Applied Chemistry, CUSAT.

I thank Dr. A. Mathiazhagan, Associate Professor, Department of Ship Technology, CUSAT for his guidance and help to do my application studies in his

department. Your kind and helping attitude as well as the freedom you offered me gave strength for me to do my work in your lab. There is no enough words to thank you sir.

I extend my gratitude to Dr. Jerry P. Jesinski, Department of Chemistry, Keene State College, Keene, NH for his help in doing crystal structure analysis. I sincerely thank the Council of Scientific and Industrial Research, New Delhi, India for financial support offered. I deeply acknowledge the heads of the institutions of SAIF Kochi, IIT Madras and IIT Bombay for the services rendered in sample analyses. I express my thanks to Dr. Shibu Eapen, Sophisticated Testing and Instrumentation Centre, SAIF, Kochi for doing single crystal XRD studies of the compounds. I also extend my thanks to Mr. Melbin, Sophisticated Testing and Instrumentation Centre, SAIF, Kochi for his help in taking SEM images.

I remember all my seniors, Dr. Jinsa Mary Jacob, Dr. Roji J. Kunnath, Dr. Nisha K., Dr. Bibitha Joseph, Dr. Aiswarya N. and Dr. Sreejith S. who helped me a lot in the beginning years of my research. I thank our senior Dr. Sithambaresan for his support and effort in publishing papers and doing EPR simulations without any hesitation.

Friends are those people who criticize, help and support us whenever it is necessary. I can't forget two people in the department, without whose help I think I could never complete this work. Thank you Ambili and Mridula for your support, help and affection you showered upon me like a big sister throughout my research career at department and outside. Your constant encouragement and discussions helped me to complete my work in the present level. I thankfully remember Nithya Mohan for her help and support in the beginning of my work in the department. Without you it could have been very difficult for me to adjust with the new environment in the lab. I thank Mr. Binoop for his timely response in formatting and completion of my thesis.

I remember my lab mates Daly, Lincy, Fousia, Asha, Vineetha and Manjari for your constant support and help. I remember and thank Preetha Pareeth and Bindhu miss for your companionship and support. I thank all my friends and relatives for praying for me and supporting me whenever I felt weak.

I extend my thanks to my dear Ms. Maya Shekar (Principal, GHSS Namakuzhy) and Ms. Marykutty for constant support and encouragement offered me whenever I needed it. Without both of you it was impossible to complete my thesis. I remember all my teachers whose blessings helped me to reach my goal.

Behind the success of every person there will be another one who sacrifices everything for their success. My husband and friend Subyr (Ikka) is the person who paved building blocks of each and every success in my life. There are not enough words to thank you for being with me throughout my life for gaining each step and supporting me whenever I needed you. I can't forget my children Mizhab and Minha who sacrificed their five years for me through adjusting to the situations whenever they needed me as a mother.

I thank my parents for being with me through all the good and hard times during these five years. Dear Umma and Vappa, your prayers, care and support meant a lot for me. I am grateful to my mother-in-law, whom I call Umma for her support and prayers. I thank all those people prayed for me.

Sajitha N.R.

Preface

Coordination chemistry emerged as a branch of chemistry due to the uniqueness of its properties as compared to its counterparts from which they are formed. Thiosemicarbazones are condensation products of thiosemicarbazides and carbonyl compounds. They find their importance in the field of coordination chemistry due to their ability to coordinate to most of metals *via* nitrogen and sulfur in the thiosemicarbazone moiety. It was observed that the properties exhibited by free thiosemicarbazones increased when they form complexes. Moreover they can show variety of coordination modes in complexes. More than 2000 publications on different properties and applications of these compounds reveal the importance of them.

In order to study the interesting coordination modes of thiosemicarbazones to transition metals we choose three different classes of thiosemicarbazones (NS, ONS and NNS). Introduction of heterocyclic bases like 2,2′-bipyridine, 4,4′-bipyridine, 1,10-phenanthroline and pyridine could increase the number of coordination sites. The molecular structure of all thiosemicarbazones and some of the complexes were established *via* single crystal X-ray diffraction studies. The metals selected for the preparation of complexes are vanadium, manganese, cobalt, nickel, copper, molybdenum, palladium and cadmium.

The thesis is divided into seven chapters. Chapter 1 is a brief survey on coordination modes and applications of thiosemicarbazones. It also discusses the objectives of the present work as well as various physicochemical methods used for the study. Chapter 2 to chapter 6 discusses synthesis and characterization of five different thiosemicarbazones and its metal complexes. Chapter 7 is a discussion on corrosion inhibition studies of all prepared thiosemicarbazones and a comparison of this property. Chapter 8 includes a brief summary and conclusion of the work.

Contents

Chapter 2

4-BENZYLOXYSALICYLALDEHYDE-N^4-CYCLOHEXYLTHIOSEMICARBAZONE AND ITS TRANSITION METAL COMPLEXES: SYNTHESIS AND STRUCTURAL CHARACTERIZATION .... 29 -88

List of Abbreviations

H_2bsct	4-benzyloxysalicylaldehyde-N^4-cyclohexylthiosemicarbazone
H_2bsmt	4-benzyloxysalicylaldehyde-N^4-methylthiosemicarbazone
Hbpdmt	6-bromopyridine-2-carbaldehyde-N^4,N^4-dimethylthiosemicarbazone
Hbpct	6-bromopyridine-2-carbaldehyde-N^4-cyclohexylthiosemicarbazone
Hanpt	acetone-N^4-(4-nitrophenyl)thiosemicarbazone
phen	1,10-phenanthroline
bipy	2,2'-bipyridine
4,4'-dmbipy	4,4'-dimethyl-2,2'-bipyridine
Py	pyridine
DMF	dimethylformamide
DMSO	dimethylsulfoxide
Complex **1**	$[VO(bsct)H_2O]_2$
Complex **2**	[Ni(bsct)phen]
Complex **3**	$[Cu(bsct)phen(H_2O)]$
Complex **4**	$[Cu(bsct)bipy(H_2O)]$
Complex **5**	$[MoO_2(bsct)DMSO]$
Complex **6**	$[MoO_2(bsmt)DMF]$
Complex **7**	$[Pd(Hbsct)_2]$
Complex **8**	$[(Cd(bsct)_2(4,4'\text{-bipy})]$
Complex **9**	$[VO(bsmt)]_2$
Complex **10**	$[Co(Hbsmt)_2]$
Complex **11**	$[Ni(Hbsmt)_2]$
Complex **12**	[Ni(bsmt)py]
Complex **13**	[Cu(Hbsmt)Cl]

Complex **14** $[MoO_2(bsmt)py]$

Complex **15** $[MoO_2(bsmt)H_2O]\cdot H_2O$

Complex **16** $[Mn(bpdmt)_2]$

Complex **17** $[Ni(bpdmt)_2]\cdot DMF$

Complex **18** $[Ni(bpdmt)(OAc)(H_2O)_2]$

Complex **19** $[Cu(bpdmt)_2]$

Complex **20** $[MoO_2(bpdmt)\ \mu^2S]$

Complex **21** $[Pd(bpdmt)Cl]$

Complex **22** $[Cd(bpdmt)_2]$

Complex **23** $[Ni(Hbpct)_2](NO_3)_2\cdot H_2O$

Complex **24** $[Ni(bpct)_2]\cdot DMF$

Complex **25** $[Cu(bpct)Cl]$

Complex **26** $[Cu(bpct)Br]$

Complex **27** $[Cu(bpct)(OAc)]$

Complex **28** $[Pd(bpct)Cl]$

Complex **29** $[Cd(bpct)_2]\cdot DMF$

Complex **30** $[Co(Hanpt)Br]$

Complex **31** $[Ni(anpt)_2]\cdot DMF$

Complex **32** $[Cu(anpt)_2]\cdot DMF$

Complex **33** $[Pd(Hanpt)Cl_2]$

Complex **34** $[Cd(anpt)_2]$

Chapter 1

A BRIEF SURVEY ON COORDINATION MODES AND APPLICATIONS OF THIOSEMICARBAZONES AND ITS TRANSITION METAL COMPLEXES

Contents

1.1. Introduction

Coordination chemistry is a vibrant and intellectually challenging field in modern chemistry. It was Alfred Werner who discovered and explained these classes of compounds for the first time and won Nobel Prize in 1919 [1]. After this discovery there was a fast development of coordination chemistry as a branch. This branch of chemistry is important not only because of the ability of these compounds to give a large variety of compounds but due to their application in various fields of medicine, biology, industry and everyday life. These compounds also find their place in formulating devices like catalysts for many reaction, sensors *etc.* The human body itself is a collection of coordination compounds, whose main functions are guided by these compounds. Heamoglobin, the constituent of blood is a coordination complex of iron. Vitamin B_{12}, important for our

body for many biological activities is a complex of cobalt. Apart from this chlorophyll, an important pigment in plant system is a complex of magnesium.

Cancer was a non-curable disease, till *cis*-platin (complex of Pt(II)) [2] was discovered and applied as a good medicine for cancer. Complex formation is used as an important method for detection of metals and for quantitative analysis. Pharmaceutical industries nowadays prefer inorganic drugs to organic drugs because of the following reasons i) it was found that the metal based therapy had increased the simulation of biological activity in the human body ii) it is more easier to introduce the medicine in the inorganic form as most of the metals form complexes with organic molecules. In this thesis we have adopted substituted thiosemicarbazones as ligands due to its application in various fields.

1.2. Thiosemicarbazones

Thiosemicarbaones were prepared by condensation of aldehyde or ketone with thiosemicarbazide under suitable condition [Scheme 1.1].

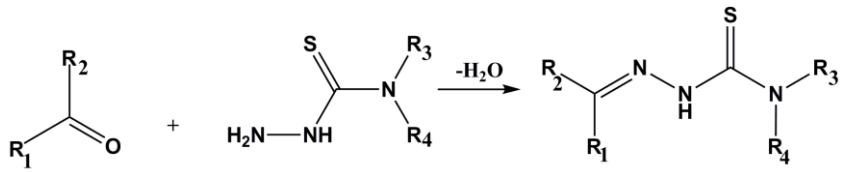

Scheme 1.1

The general numbering pattern of thiosemicarbazone is given in Fig. 1.1. These compounds can show *E* and *Z* isomerism (Fig. 1.1) when the groups R_1 and R_2 are different.

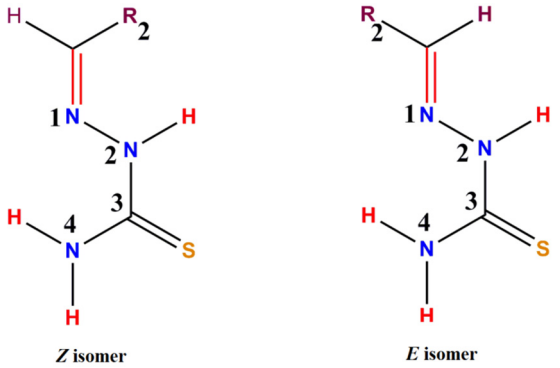

Fig. 1.1. *Z* and *E* isomers of thiosemicarbazone.

Thiosemicarbazones usually exist in neutral thio-amido form in the solid state. In the solution phase, an equilibrium mixture of thio-amido and thio-iminol forms exist, as there is a possibility of tautomerism in the compound by virtue of conjugated double bonds. Thus these compounds can coordinate to a metal centre as an anion or neutral ligand, where the anion is generated by removal of hydrogen from thio-iminol sulfur (Fig. 1.2).

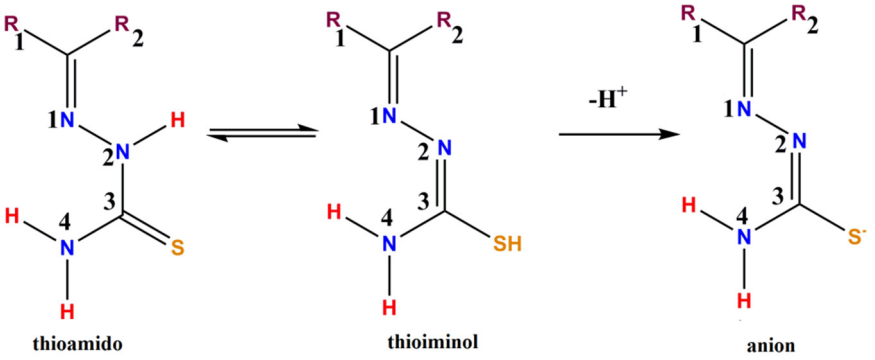

Fig. 1.2. Thioamido-thioiminol tautomerism in thiosemicarbazone.

Depending upon the nature of aldehyde or ketone and thiosemicarbazide used various types of thiosemicabazones have been synthesized. These thiosemicarbazones were capable of showing large variety of coordination modes.

1.3. Coordination modes of thiosemicarbazones in metal complexes

1.3.1. Thiosemicarbazones as NS donor ligands

A thiosemicarbazone can coordinate *via* only azomethine nitrogen and thioamido/thioiminolate sulfur giving an NS type coordination mode in the complex. These thiosemicarbazones were obtained when a simple aldehyde is condensed with a thiosemicarbazide. Castiñeiras *et al.* synthesized a Zn(II) complex (Fig. 1.3) of acetone-3-hexaiminyl thiosemicarbazone ([Zn(Acehexim)$_2$]) in which the thiosemicarbazone acts as NS type ligand [3] and Arce *et al.* [4] synthesized a radioactive Re(I) tricarbonyl complexes (*fac*-[$Re_2(CO)_6(L^2)_2$]) of thisemicarbazone (Fig. 1.4) and was found to adopt an unusual geometry around the metal centre. The complex consist of two Re(I) and is a centrosymmetric dimer with each Re(I) lie in a distorted octahedral environment. The dimer chore found to be an asymmetric rectangular parallelogram with Re(I) and bridged sulfur group occupying the corners (Fig. 1.4).

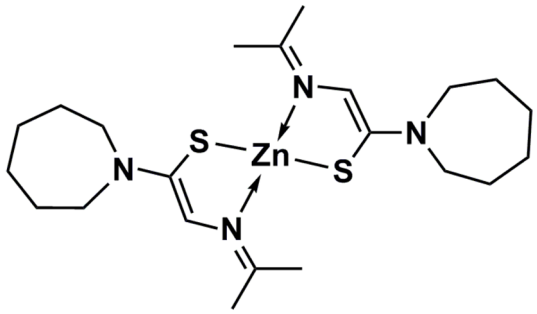

Fig. 1.3. Schematic representation for [Zn(Acehexim)$_2$] (Ref. 3).

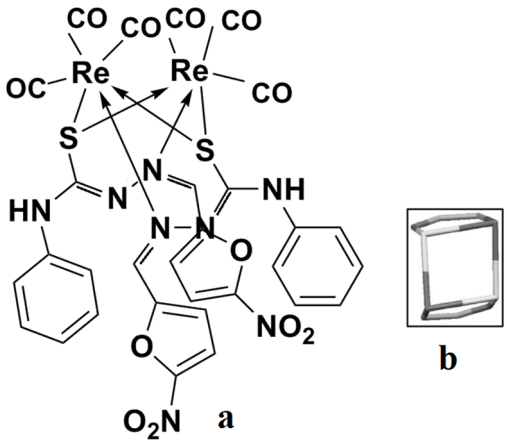

Fig. 1.4. a) Schematic representation for *fac*-$[Re_2(CO)_6(L^2)_2]$ (Ref. 4)
b) The parallelogram inner chore.

1.3.2. Thiosemicarbazones as ONS donor ligands

Thiosemicarbazones have been an area of interest for our group for a long period of time. When a hetero atom was introduced to the aldehyde or ketone in the thiosemicarbazone moiety, the coordination modes of the thiosemicarbazone would be increased and can act as an ONS donor ligand to transition metal. A simple ONS donor thiosemicarbazone can act as a tridentate ligand to transition metals. Kurup and coworkers successfully synthesized many complexes with thiosemicarbazones having ONS type binding mode. Presence of base can evolve different type of coordination eometry. One of the example is the monoligated Cu(II) complex (Fig. 1.5) of 2-hydroxyacetophenone-3-hexamethyleneiminylthiosemicarbazone ([CuLphen]) in which the coordination sphere was completed by the base 1,10-phenanthroline leading to a pentacoordinate geometry around central metal atom [5]. When an anion is incorporated along with a base, an octahedral complex is resulted. Such a complex is synthesized by the same group [6], which was a Co(III) complex of N^4 substituted thiosemicarbazone with azide and 2,2′-bipyridine as coligands ($[CoL^4bipyN_3]$) (Fig 1.6) .

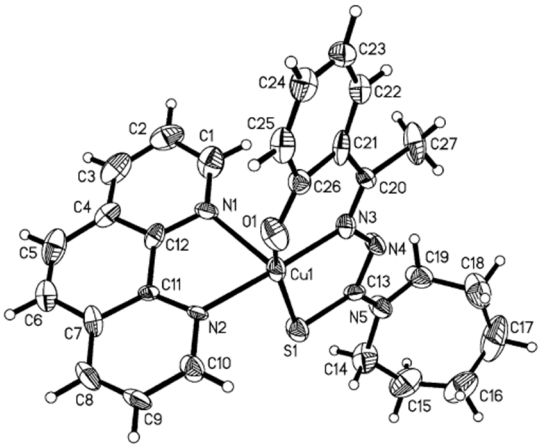

Fig. 1.5. ORTEP diagram for [CuLphen] (Ref. 5).

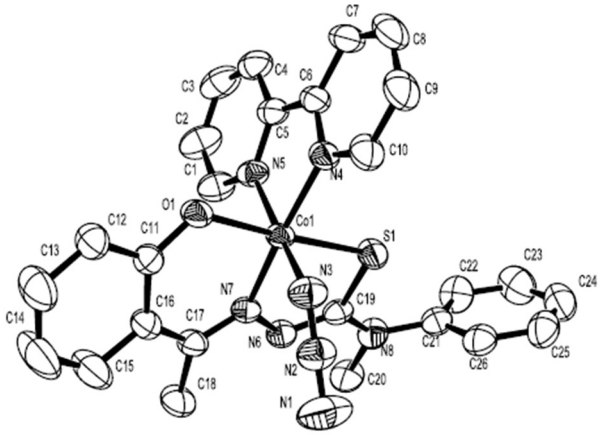

Fig. 1.6. ORTEP diagram for [CoL^4bipyN_3] (Ref. 6).

Presence of heteroatom lead to special coordination modes such as bridging *via* the hetero oxygen atom [7]. Cindrić *et al.* reported a molybdenum complex with salicylaldehyde thiosemicarbazone in which one of the oxygen on *cis*-MoO_2 form a bridge between two Mo(VI) units giving rise to a dimer ($[MoO_2(C_6H_4(O)CH{:}NNC(S)NH_2)]_2$) (Fig. 1.7). When there was a heteroatom on the groups present in the N^4 position, special geometries may be resulted with formation of a dimer. Such a dimer was reported by Zaltariov *et al.* formed from iminodiacetato thiosemicarbazone complexes of

Cu(II) [8]. The first Cu(II) centren adopt a pentacoordiated geometry whose three coordinated sites were occupied by ONS donor thiosemicarbazone and the 4th and 5th positions were employed by chlorine ions one of which form a bridge to the second Cu(II) center. The phenolic oxygen on the thiosemicarbazone as well forms a bridge between the two metal centers. It was observed that the coordination sites of second Cu(II) was occupied by the oxygen atoms on acetate unit on the thiosemicarbazone ([Cu_2HL^4(μ-Cl)Cl_2]) (Fig. 1.8).

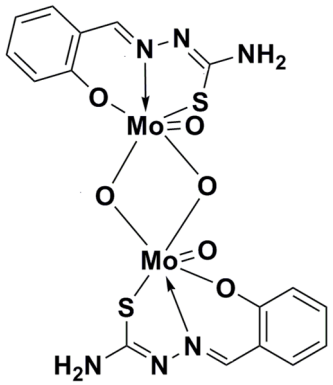

Fig. 1.7. Schematic representation for complex $[MoO_2(C_6H_4(O)CH{:}NNC(S)NH_2)]_2$ (Ref. 7).

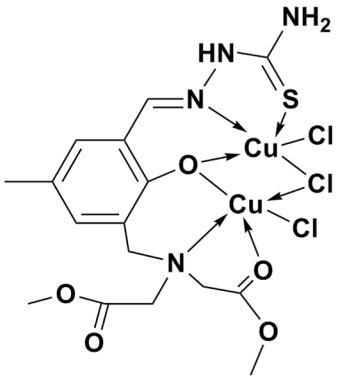

Fig. 1.8. Schematic representation for [Cu_2(HL^4) (μ-Cl)Cl_2] (Ref. 8).

Latheef *et al.* reported two unusual coordination geometry around the metal when ONS donor, salicylaldehyde-3-azacyclothiosemicarbazone was

used as the ligand [9,10]. In the first case the thiosemicarbazone coordinated to Ni(II) in two different way leading to an unusual dimer. The first Ni(II) ion adopt an octahedral geometry around it *via* the deprotonated ligand, 1,10-phenanthroline and bridging phenolic oxygen of the second thiosemicarbazone (Fig. 1.9) ([Ni_2L_2phen]). The second Ni(II) adopt a square planar geometry using the deprotonated thiosemicarbazone and bridging sulfur of the first thiosemicarbazone. In the second case, the Zn(II) adopt a distorted tetrahedral geometry, in which the phenolic oxygen on the ligand remained uncoordinated and hence appeared to be NS donor ligand (Fig. 1.10) ([$Zn(HL)_2$]).

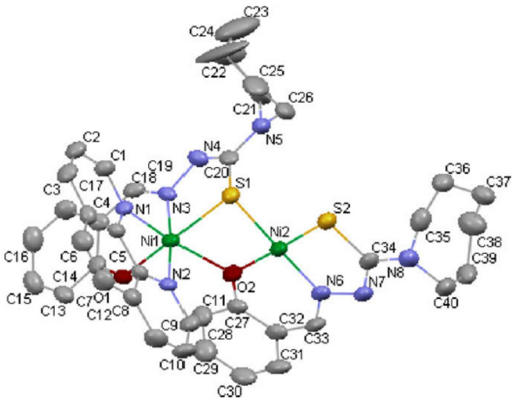

Fig. 1.9 ORTEP diagram for [Ni_2L_2phen] (Ref. 9).

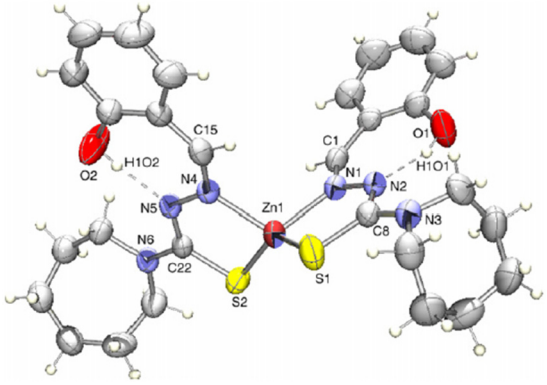

Fig. 1.10. ORTEP diagram for [$Zn(HL)_2$] (Ref. 10).

Saswati *et al.* reported a Ni(II) complex of N^4 substituted salicylaldehyde thiosemicarbazone ([$(NiL^3)_2$(μ-4,4′-byp)]) in which the complex exist as a dimer by the virtue of the base 4,4′-bipyridine [11]. The thiosemicarbazone coordinates to the metal in the dideprotonated form giving rise to a four coordinate geometry around Ni(II) (Fig. 1.11).

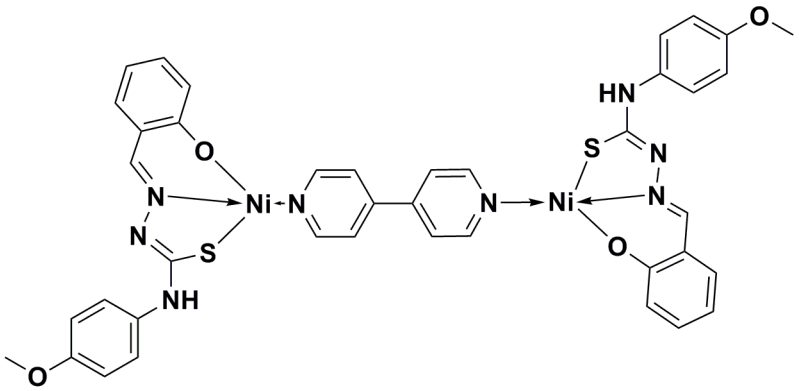

Fig. 1.11. Schematic representation for [$(NiL^3)_2$(μ-4,4′-byp)] (Ref. 11).

1.3.3. Thiosemicarbazones as NNS donor ligands

When the thiosemicarbazone moiety contain groups like pyridine as the substituent the nitrogen on pyridine can also coordinate to the metal centre, leading the thiosemicarbazone to act as an ONS donor ligand. Sreekanth *et al.* successfully synthesized the first Au(III) complex ([Au*Bpyptsc*Cl]$AuCl_2$) of N^4 substituted thiosemicarbazone. The geometry around the Au(III) ion was found to be square planar with a monodeprotonated ligand moiety and a chlorine ion occupying the fourth coordination sites. Electrical neutrality is maintained by linear $AuCl_2^-$ unit present in the crystal lattice (Fig. 1.12) [12]. Usman *et al.* reported an octahedral Mn(II) complex ([$Mn(C_{14}H_{13}N_4S)_2$]) in which the two units of ligands coordinated to metal as NNS donor ligand (Fig. 1.13) [13].

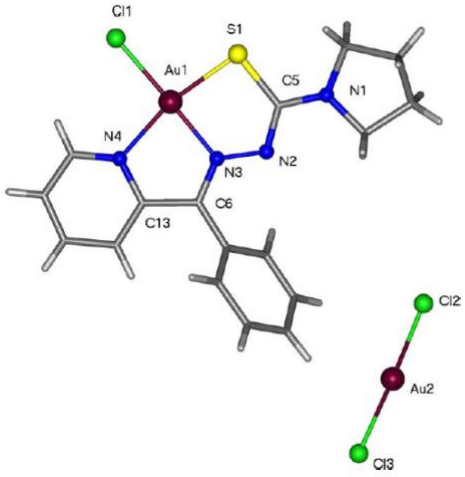

Fig. 1.12 ORTEP diagram for [Au*Bpyptsc*Cl]$AuCl_2$ (Ref. 12).

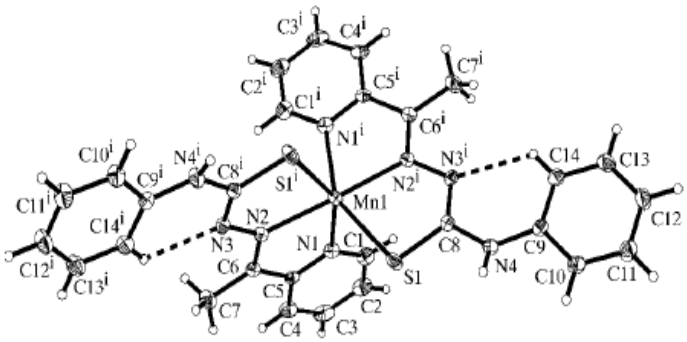

Fig. 1.13. ORTEP diagram for [$Mn(C_{14}H_{13}N_4S)_2$] (Ref. 13).

Dimerization of the complexes may be resulted from the presence of an anion on the metal centre as reported by Sreekanth *et al.* [14] in the Cu(II) complex of N^4 substituted benzoylpyridinethiosemicarbazone. The complex is a centrosymmetric dimer resulted from bridging through Cl^- ion ([Cu*BpypTsc*Cl]) (Fig. 1.14).

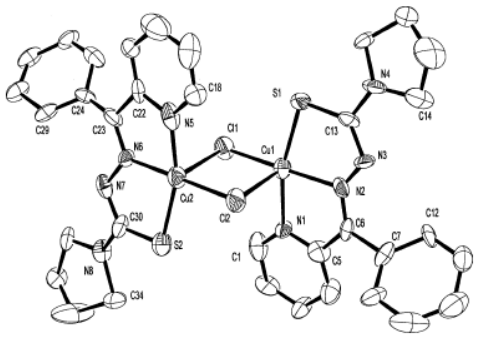

Fig. 1.14. ORTEP diagram for [Cu*BpypTsc*Cl] (Ref. 14).

Kurup and coworkers reported coordination complexes in which dimers were formed with the aid of N on the pyridine (Fig. 1.15) and the sulfur on thiolate group (Fig. 1.16). The first complex was formed with an N^4 substituted di-2-pyridyl ketone as the ligand ($[Cu_2Br_2(C_{12}H_{10}N_5S)_2]\cdot 2CH_3OH$) and the second complex was with an N^4 substituted benzoylpyridine as the ligand ($[Cu_2(C_{17}H_{17}N_4S)Cl_2]$). Both complexes were of Cu(II) ion [15,16]. The same group reported a complex of Cu(II) with two different types of coordination centers. The unit at the centre of $[(Cu_2L_2SO_4)_2]\cdot 3H_2O$) (Fig. 1.17) consist of two Cu(II) atoms and have a geometry similar to ($[Cu_2Br_2(C_{12}H_{10}N_5S)_2]$). The other two identical units are connected to this centre *via* bridging sulfate oxygens and thiolate sulfur giving a distorted square pyramidal geometry [17].

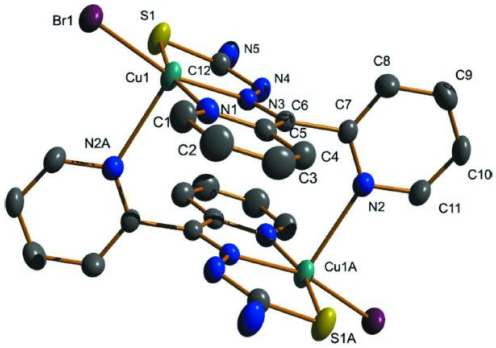

Fig. 1.15. ORTEP diagram for $[Cu_2Br_2(C_{12}H_{10}N_5S)_2]\cdot 2CH_3OH$ (solvent molecules are omitted (Ref. 15).

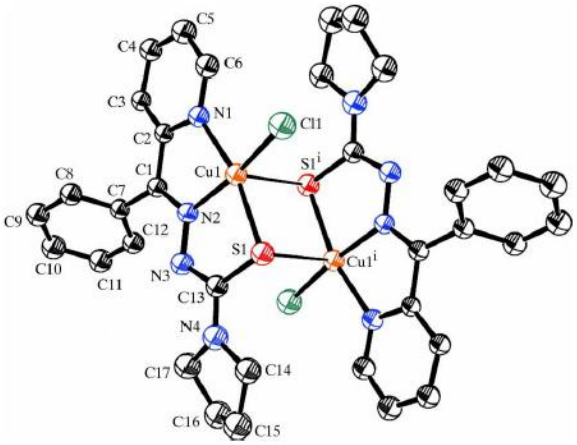

Fig. 1.16. ORTEP diagram for $[Cu_2(C_{17}H_{17}N_4S)Cl_2]$ (Ref. 16**)**.

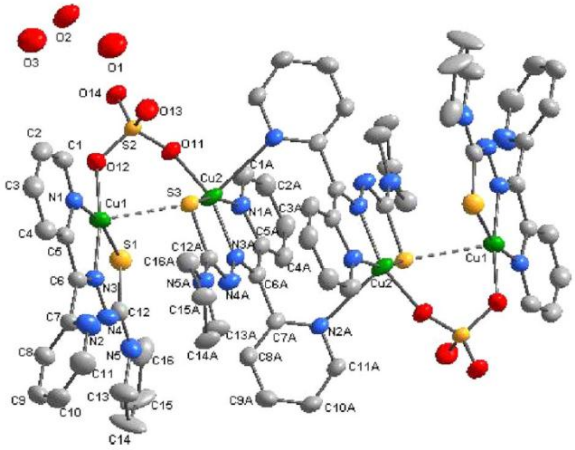

Fig. 1.17. ORTEP diagram for $[(Cu_2L_2SO_4)_2]\cdot 3H_2O$ (Ref. 17).

Thiosemicarbazones coordinate as a neutral ligand in some of the metal complexes. One of such complex was reported by Ibrahim *et al.* [18] in which, the sulfur atom of thiosemicarbazone alone act as a donor and coordinate as a mono dentate ligand to Zn(II) (Fig. 1.18) ($[CdCl_2(LH_2)_2]$). As reported by Lobana *et al.* [19] the coordination is also feasible by hydrazinic nitrogen and sulfur atom (Fig. 1.19) ($[RuL_2(PPh_3)_2]$).

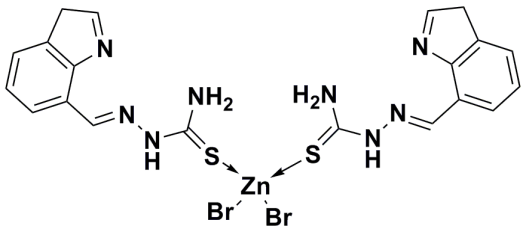

Fig. 1.18. Schematic representation for $[CdCl_2(LH_2)_2]$ (Ref. 18).

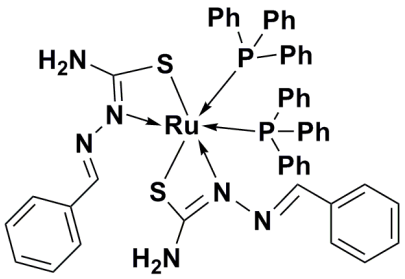

Fig. 1.19. Schematic representation for $[RuL_2(PPh_3)_2]$ (Ref. 19).

1.4. Importance of thiosemicarbazones and its transition metal complexes

Thiosemicarbazones were established as antimalarial agents, when Klayman *et al.* studied the action of a series of 2-acetylpyridine thiosemicarbazones towards *Plasmodium berghei* in 1979 [20]. These compounds found applications in medicine [21,22]. Travallali *et al.* deviced a solid state colorimetric probe for Cu^{2+} determination in water using bis(hydrazine carbothioamide) [23]. Recently, substituted thiosemicarbazones were found to act as sensors for Hg^{2+} and F^- ions [24,25]. A molecular logic-gate device was developed by Basheer *et al.* containing pyrene thiosemicarbazone that could function as a dual mode fluorescent chemosensors [26]

Catalytic activity of thiosemicarbazones and its metal complexes include dehydrogenative amide synthesis using Ru(II) complexes of 2-oxo-1,2-dihydroquinoline-3-carbaldehydethiosemicarbazone [27], C–H activation

using Pd(II) complexes of a series of N^4 substituted thiosemicarbazones [28] and olefin epoxidation of Mo(VI) complex of 1-(2,4-dihydroxybenzylidene)-N-methyl-N-phenylthiosemicarbazone [29].

Biological activity of thiosemicarbazones and its metal complexes had been studied widely. Pape *et al.* synthesized a group of thiosemicarbazones that show anticancer properties with the capability to overcome multidrug resistance [30]. Transition metal complexes of thiosemicarbazones derived from 2-hydroxy-5-methoxy-3-nitrobenzadehyde were found to show anticancer properties, with Ni(II) complex showing more action against human cervical and colon cancer cells [31]. 5-Nitrofuryl derived thiosemicarbazones and its Ru(I) tricarbonyl complexes showed activity against pathogen *Trypanosoma cruzi* which cause American Trypanosomiasis infection [4].

Cytotoxic activity of thiosemicarbazones and their transition metal complexes were investigated by various research groups. Sinniah *et al.* found out that cationic thiosemicarbazones derived from (3-formyl-4-hydroxyphenyl)methyltriphenylphosphonium inhibited the prostate cancer growth (PC-3) [32]. Pd(II) complex of 2-benzoylpyridine-N^4-tolylthiosemicarbazone exhibited cytotoxic activity against leukemia cells [33]. Sîrbu *et al.* found out that Cu(II) complex of 3-formyl-4-hydroxybenzenesulfonic acid thiosemicarbazone act as an agent for ROS accumulation in the cell where by promoting the antioxidant response in highly resistant breast cancer cells [34]. It was observed that Ga(III) complexes of 2-pyridinecarboxaldehyde could show antiproliferate activity [35].

There were reports in which transition metal complexes of thiosemicarbazones could give antimicrobial and cytotoxic properties [36,37]. Umadevi *et al.* reported a Ni(II) complex of salicylaldehyde N^4 substituted

thiosemicarbazone show DNA binding, antibacterial and *in vitro* cytotoxic activities [38].

The Cu(II) complexes of 6-nitropiperonal thiosemicarbzone show antimicrobial activity against ESKAPE pathogens [39]. Mn(II) complexes of thiosemicarbazones were proved to act as antimycobacterium tuberculosis agents [40].

Thiosemicarbazones and their metal complexes could act as good corrosion inhibitor for mild steel and carbon steel in acids. The inhibition action of the thiosemicarbazones was due to their ability to coordinate easily to metal surface *via* sulfur and nitrogen atoms [41,42,43]. Other applications of thiosemicarbazones include metal detection in food stuffs and heavy water remediation [44,45].

1.5 Objectives of the present work

Thiosemicarbazones are intensively studied compounds and have more than 4000 publication are available. Due to its ability to show a large variety of coordination modes, every year many compounds in the class were synthesized and studied for its applications in various fields. As already seen that the area of research include biological, industrial and clinical field. These compounds have got considerable attention throughout. The property of thiosemicarbazone depends upon the type of parent aldehyde or ketone [46]. The presence of heteroatom on the thiosemicarbazone moiety found to give a large number of coordination possibilities to a metal ion. So we have selected thiosemicarbazones with NS, ONS and NNS donor sites in them.

The numerous reviews available on this class of compound show the importance of thiosemicarbazone, which stimulated our interest for the search of new compounds in this series. The NS donor thiosemicarbazone was derived from acetone and N^4 substituted thiosemicarbazide. The NNS and

ONS donor thiosemicarbzones were derived from 4-benzyloxysalicylaldehyde and 6-bromopyridine-2-carbaldehyde respectively and substituted thiosemicarbazide. The presence of bases like 1,10-phenanthroline, 2,2′-bipyridine and 4,4′-bipyridine were also used to get various metal chelates with different geometries.

On the basis of above facts and awareness of importance of this area of research we undertook the present work with the following objectives,

- To synthesize ONS type thiosemicarbazones using N^4-cyclohexylthiosemicarbazide and N^4-methylthiosemicarbzide with 4-benzyloxy-salicylaldehyde.
- To synthesize NNS type thiosemicarbazones using N^4,N^4-dimethylthiosemicarbzide and N^4-cyclohexylthiosemicarbazide with 6-bromopyridine-2-carbaldehyde.
- To synthesize NS type thiosemicarbazone using N^4(4-nitrophenyl) thiosemicarbazide and acetone.
- To synthesize various transition metal complexes of these five thiosemicarbazones as the principal ligand and using some heterocyclic bases as coligands.
- To characterize the thiosemicarbazones and transition metal complexes using various physico-chemical techniques.
- To investigate the coordination geometries of some of the complexes and all the thiosemicarbazones using single crystal X-ray diffraction studies.
- To investigate the corrosion inhibition properties of all the synthesized thiosemicarbazones on mild steel in 1 M HCl solution using weight loss and electrochemical techniques.
- To compare the corrosion inhibition property of thiosemicarbazone and establishing the best corrsion inhibitor among them.

1.6 Various metals used in the present study

1.6.1 Vanadium

Vanadium is a hard and silvery grey transition metal. It was discovered by Spanish scientist Andres Manuel de Rio in 1801. But the name Vandium was given by Nils Gabriel, when he rediscovers the element in 1830. Vanadium can switch between +3, +4 and +5 oxidation states. In complexes, vanadium can exist in VO(II) and VO_2(II) oxidation states. Of these VO(II) is the most stable oxidation state in complexes. Vanadium is a constituent of protein called Vanabins. Vanadium oxide (V_2O_5) is one of the most important compounds in catalysis. Application of vanadium compounds in treating insulin deficiency increased its importance in medicinal field. According to Han *et al.* V(V) complexes possess insulin like activity [47]. Oxidovanadium and dioxidovanadium complexes of thiosemicarbazones show anti-*tuberculosis* and anti-tumor activity [48].

1.6.2 Manganese

Manganese is present in plants and animals in small quantities. It is a part of proteins too. Photosystem II an important component in photosynthesis, contain manganese. John Golltieb Gahn was the first to isolate manganese for the first time in 1774. Manganese function as a cofactor for large variety of enzymes, like oxidoreductase, transferase *etc.* Facile oxidation of Mn(II) complexes help in determining trace of oxygen in solution. Mn(II) complexes can act as good catalysts for disproportionation of hydrogen peroxide and low temperature peroxide bleaching of fabrics [49] Mn(II) complexes of thiosemicarbazone found to act as anti-*tuberculosis* agent [50]

1.6.3 Cobalt

Cobalt has been used as a coloring agent for centuries to impart a rich blue color to glass. Cobalt-60, an artificial isotope, discovered by

John Livingood and Glenn Seaborg, was used as a radiotherapeutic agent. It is the metal present in vitamin B_{12} important for many biological activities. It is a constituent of allows used to make magnets due to its ferromagnetic properties. Cobalt usually shows +2 and +3 oxidation states in its complexes. Co(II/III) complexes of thiosemicarbazones can show anticancer and antibacterial properties [51,52].

1.6.4 Nickel

Nickel is a silvery white metal found in earth crust. Nickel is a corrosion resistant metal due to the formation of protective oxide layer on it. Many alloys were made using this metal as a result of its extra stability. The chemical activity of this metal is pronounced in its powder form. Nickel adopts +2 oxidation states in its complexes. The biological importance of nickel was established in 1970s, when it was found as a cofactor of enzyme urease. From then nickel complexes have attracted attention from scientists all over the world. Nickel complexes of thiosemicarbazones were reported to show anticancer properties [53]. Kaliarasi *et al.* recently identified nickel complexes of thiosemicarbazones can exhibit antioxidant, antimicrobial and *in vitro* cytotoxicity [54].

1.6.5 Copper

Copper is one of the first used metals in human era. It is a constituent of a large number of biologically important compounds. It is present in nature as sulphides and oxides. Copper can exist in Cu(I/II) in its complexes. It can form a large number of alloys like brass, bronze *etc.* Cu(I/II) complexes find application in various fields. Copper complexes of thiosemicarbazones were found to exhibit antimicrobial [55], antiproliferate [56] and cytotoxic [57] properties.

1.6.6 Molybdenum

Molybdenum is a biologically and industrially important metal. It was first discovered by Sweedish chemist Carl Wilhelm Scheele in 1778. It is a constituent of many enzymes important in metabolic activities. The presence of oxo group on oxido and dioxido molybdenum complexes enable it to act as a good intermediate for oxotransference reactions. The discovery of tetrathiomolybdate as an anticopper drug, which can be used for treating Wilson's disease highlights the importance of this metal complex. Molybdenum usually exhibit +5 and +6 oxidation state in its complexes. MoO_2(VI) complexes of thiosemicarbazones were found to act as precursors in oxygen atom transfer process in epoxidation reaction [58].

1.6.7 Palladium

Palladium was discovered and named by William Hyde Wollaston in 1802. Palladium exist in +2 oxidation state in most of it complexes. Palladium also shows +4 oxidation state in some of its complexes. Palladium is an established catalyst in many of the coupling reactions. Palladium has established its importance in medicinal field from anticancer properties of its complexes. Anticancer propertied of Pd(II) complexes of thiosemicarbazones were reported recently [59]. Pd(II) complexes of thiosemicarbazones were also reported to show antibacterial and antiproliferate properties [60,61].

1.6.8 Cadmium

Cadmium was discovered by Friedrich Stromeyer and Karl Samuel Leberecht Herman in 1817. Cadmium is one of the naturally occurring component in the earth's crust and water. Cadmium can show +2 oxidation state in compounds. It can adopt a large number of coordination modes in its complexes. Musavi *et al.* reported binuclear Cd(II) complexes to exhibit antimicrobial activity [62]. Cadmium complexes also act as antifungal and antibacterial agents [63]. Recently it is found that these Cd(II) complexes can show potential activity against *P. insidiosum* growth [64].

1.7 Physical Measurments

1.7.1 Elemental analysis

In elemental analysis, the sample of the chemical compound is analyzed for its chemical composition. It gives a rough idea about the purity of the compound. The elemental analysis of the compounds in the present study was done on a Vario EL III CHNS elemental analyzer at the Sophisticated Analytical Instrumentation Facility, Cochin University of Science and Technology, Kochi, India.

1.7.2 Conductivity measurements

The conductivity is a measure of an electrolytic solution to conduct electricity. This method helps the researcher to identify the ionic content in the test solution. The molar conductivity of all the complexes were measure in 10^{-3} M DMF solution on a Systronic model 303 direct reading conductivity meter at Department of Applied Chemistry, Cochin University of Science and Technology, Kochi, India.

1.7.3 Magnetic susceptibility measurements

Magnetic susceptibility measurements indicate the degree of magnetization of complexes to an applied magnetic field. The magnetic susceptibility measurements of complexes were conducted on a Vibrating Sample Magnetometer using $Hg[Co(SCN)_4]$ as a calibrant at Sophisticated Analytical Instrumentation Facility, Indian Institute of Technology, Madras.

1.7.4 Infrared spectroscopy

The infrared spectrum gives characteristic bands corresponding to different vibrational frequencies of various bonds present in a compound. The formation of a complex can be established from identifying ligand based vibrations, metal-ligand vibrations and new bands corresponding to

new bond formation. Infrared spectra of the complexes were recorded on a JASCO FT-IR-5300 Spectrometer in the range 4000-400 cm^{-1} using KBr pellets at Department of Applied Chemistry, Cochin University of Science and Technology, Kochi, India.

1.7.5 Electronic Spectroscopy

Electronic spectroscopy measures the transitions between energy levels corresponding to wavelengths characteristic of visible and ultraviolet region of the spectrum. The electronic spectrum of a complex may be due to electronic transitions between ligand electronic energy levels leading to $n\rightarrow\pi^*$ and $\pi\rightarrow\pi^*$ type transitions, transitions between orbitals of metal and ligand (LMCT or MLCT) and electronic transitions between partially filled orbitals of metal leading to *d-d* transitions. These transitions throw light to the type of metal present in the complex and give an evidence for complex formation. The electronic spectra of the compounds were recorded in DMF (10^{-3} and 10^{-5} M) on a Thermo Scientific Evolution 220 UV-vis Spectrophotometer in the range 200-900 nm at Department of Applied Chemistry, Cochin University of Science and Technology, Kochi, India.

1.7.6 NMR Spectroscopy

Nuclear magnetic resonance spectroscopy enables the researcher to identify the type of atoms present in a compound. This technique is based on the magnetic properties of an atom's nucleus. In the present study, the chemical environment of the compound was investigated using ^1H NMR and D_2O exchanged ^1H NMR techniques. The NMR spectra of all thiosemicarbazones and some of the complexes were recorded using Bruker AMX 400 FT-NMR spectrometer at the Sophisticated Analytical Instrumentation Facility, Cochin University of Science and Technology, Kochi, India.

1.7.7 EPR spectroscopy

Electron paramagnetic resonance spectroscopy is a technique used to study the absorption of electromagnetic radiation in the microwave region by materials with unpaired electrons. This technique gives an idea about the metal ligand bonding, unpaired electron distribution and spatial disposition of ligands around the central metal ion. The EPR spectra of the complexes in the solid state at 298 K and in DMF solution at 77 K were recorded on a Varian E-112 spectrometer using TCNE as the standard, with 100 kHz modulation frequency, 2 G modulation amplitude and 9.1 GHz microwave frequency at Sophisticated Analytical Instrumentation Facility, Indian Institute of Technology Bombay, India. The spectra were simulated using EasySpin 4.0.0 package [65].

1.7.8 Thermogravimetric analysis

The themogravimetric analysis enable a researcher to determine the moisture content, decomposition points and various physical processes like vaporization, sublimation and desorption in reaction. In this technique, the mass of the sample in a controlled atmosphere is recorded continuously as a function of temperature or time as the temperature of the sample is increased. A plot of mass or mass percentage as a function of time is called a thermogram. TG-DTG analyses of the complexes were carried out in a Perkin Elmer Pyris Diamond TG/DTA analyzer under nitrogen at a heating rate of 10 °C min^{-1} in the 50-700 °C range at the Sophisticated Analytical Instrumentation Facility, Cochin University of Science and Technology, Kochi, India.

1.7.9 Single crystal X-ray diffraction studies

Single crystal X-ray diffraction technique is a non-destructive analytical technique which provides information about the real arrangement of atoms on a compound, including bond lengths bond angles and unit cell

dimensions. An ideal crystal should have size between 150-250 microns. The sample is mounted on the tip of a thin glass fiber using epoxy. This fiber is attached to a brass mounting pin, usually by the use of modeling clay and the pin is then inserted into the goniometer head. The goniometer head and sample are then affixed to the diffractometer. Then data is collected and phase problem is solved to find the unique set of phases that can be combined with the structure factors to determine the electron density and therefore, the crystal structure. The trial structure is then solved and refined.

The single crystal X-ray diffraction studies of some of the compounds were done using a Bruker SMART APEXII CCD diffractometer at Sophisticated Analytical Instrumentation Facility, Cochin University of Science and Technology, Kochi, India. Data acquisition was done using Bruker SMART software and data integration using Bruker SAINT software [66]. Absorption corrections were carried out using SADABS based on Laue symmetry using equivalent reflections [67]. The structure was solved by direct methods and refined by full-matrix least-squares calculations with the SHELXL-2014/7 software package [68]. The graphic tools used were DIAMOND version 3.2g [69] and ORTEP-3 [70]. The single crystal X-ray diffraction studies of some of the compounds were done on Rigaku Oxford Diffraction diffractometer at 173(2) K at Department of Chemistry, Keene State College, 229 Main Street, Keene, NH. The Olex 2 [71] was used to collect data and structure was solved using ShelXT [72] program.

1.7.10 Electrochemical analysis

Corrosion is an electrochemical reaction by the creation of anodic and cathodic sites within the metal surface in the presence of an electrolyte like acid. The electrochemical reactions occurring on the mild steel surface were studied using standard three-electrode cell. The counter electrode was a mesh of platinum of high purity (99.9%) and the reference electrode

consisted of a saturated calomel electrode (SCE). Electrochemical testing was performed using an electrochemical analyzer (CH instrument model 680).

1.7.11 Scanning electron microscopy

The surface topology of a material can be easily understood by scanning electron microscopy. The scanning electron microscope (SEM) uses a focused beam of high-energy electrons to generate a variety of signals at the surface of solid specimens. The signals that derive from electron sample interactions reveal information about the sample including external morphology (texture), chemical composition, and crystalline structure and orientation of materials making up the sample. The data are collected over a selected area of the surface of the sample, and a 2-dimensional image is generated that displays spatial variations in these properties. Areas ranging from approximately 1 cm to 5 microns in width can be imaged in a scanning mode using conventional SEM techniques (magnification ranging from 20X to approximately 30,000X, spatial resolution of 50 to 100 nm). The surface study of the mild steel metal samples was taken on a JEOL JSM–6390LV instrument at Sophisticated Analytical Instrumentation Facility, Cochin University of Science and Technology, Kochi, India.

References

[1] J.E. Huheey, E.A. Keiter, R.L. Keiter, Inorganic Chemistry, Principles of Structure and Reactivity, 4th Edn., Harper Collins College Publishers, New York, 1993.

[2] G. Sava, S. Zorzet, T. Giraldi, G. Mestroni, G. Zassonivich, Eur. J. Cancer Clin. Oncol. 20 (1984) 841.

[3] A. Castiñeiras, D.X. West, J. Mol. Struct. 604 (2002) 113.

[4] E.R. Arce, I. Machado, B. Rodríguez, M. Lapier, M.C. Zúñiga, J.D. Maya, C.O. Azar, L. Otero, D. Gambino, J. Inorg. Biochem. 170 (2017) 125.

[5] R.P. John, A. Sreekanth, M.R.P. Kurup, A. Usman, A.R. Ibrahim, H.-K. Fun, Spectrochim. Acta A59 (2003) 1349.

[6] R.P. John, A. Sreekanth, M.R.P. Kurup, S.M. Mobin, Polyhedron 21 (2002) 2515.

[7] M. Cindrić, V. Vrdoljak, N. Strukan, B. Kamenar, Polyhedron 24 (2005) 369.

[8] M.Z. Zaltriov, M. Hammerstad, H.J. Arabshahi, K. Jovanović, K.W. Richter, M. Cazacu, S. Shova, M. Balan, N.H. Andersen, S. Radulović, J. Reynisson, K.K. Andersson, V.B. Arion, Inorg. Chem 56 (2017) 3532.

[9] L. Latheef, E.B. Seena, M.R.P. Kurup, Inorg. Chim, Acta 362 (2009) 2515.

[10] L. Latheef, E. Manoj, M.R.P. Kurup, Polyhedron 26 (2007) 4107.

[11] Saswati, R. Dinda, C.S. Schmiesing, E. Sinn, Y.P. Patil, M. Nethaji, H. Stoeckli-Evans, R. Acharyya, Polyhedron 50 (2013) 354.

[12] A. Sreekanth, H.-K. Fun, M.R.P. Kurup, Inorg. Chem. Comm. 7 (2004) 1250.

[13] A. Usman, I.A. Razak, S. Chantrapromma, H.-K. Fun, A. Sreekanth, S. Sivakumar, M.R.P. Kurup, Acta Cryst. C58 (2002) m461.

[14] A. Sreekanth, M.R.P. Kurup, Poyhedron 22 (2003) 3321.

[15] R.J. Kunnath, M. Sithambaresan, M.R.P. Kurup, A. Natarajan, A.A. Aravindakshan, Acta Cryst. E68 (2012) m346.

[16] A. Sreekanth, V. Suni, R.P. John, M. Nethaji, M.R.P. Kurup, Acta Cryst. C61 (2005) m284.

[17] V. Philip, V. Suni, M.R.P. Kurup, M. Nethaji, Polyhedron 25 (2006) 1931.

[18] A.A. Ibrahim, H. Khaledi, P. Hassandarvish, H.M. Ali, H. Karimian, Dalton Trans. 43 (2014) 3850.

[19] T.S. Lobana, G. Bawa, R.J. Butcher, B.-J. Liaw, C.W. Liu, Polyhedron 25 (2006) 2897.

[20] D.L. Klayman, J.F. Bartosevich, T.S. Griffin, C.J. Mason, J.P. Scovill, J. Med. Chem. 22 (1979) 855.

[21] B.S. Garg, V.K. Jain, Microchem. J. 38 (1988) 144.

[22] A.R. Cowley, J.R. Dilworth, P.S. Donnelly, J.M. White, Inorg. Chem 45 (2006) 496.

[23] H. Tavallali, G.D. –Red, A. Moaddeli, K. Asghari, Sens. Actuators B244 (2017) 1121.

[24] Y. Li, J. Ma, X. Wang, X. Kong, Y. Zhang, L. Feng, Y. Hui, Z. Xie, J. Photochem. Photobiol. A338 (2017) 1.

[25] N. Gupta, D. Singhal, A.K. Singh, N. Singh, U.P. Singh, Spectrochem. Acta A176 (2017) 38.

[26] S.M. Basheer, A.C. Willis, A. Sreekanth, J. Lumin. 183 (2017) 266.

[27] S. Selvamurugan, R. Ramachandran, G. Prakash, M. Nirmala, P. Viswanathamarthi, S. Fujiwara, A. Endo, Inorg. Chem. Acta 454 (2017) 46.

[28] T.S. Lobana, P. Kumari, R.J. Butcher, T. Akitsu, Y. Aritake, J. Perles, F.J. Fernandez, M.C. Vega, J. Organomet. Chem. 701 (2012) 17.

[29] Z. M. –Shoeili, D.M. Boghaei, M. Amini, M. Bagherzadeh, B. Notash, Inorg. Chem. Comm. 27 (2013) 26.

[30] V.F.S. Pape, S. Tóth, A. Füredi, K. Szebenyi, A. Lovrics, P. Szabó, M. Wiese, G. Szakacs, Eur. J. Med. Chem. 117 (2016) 335.

[31] M.A. Arafath, F. Adam, M.R. Razali, L.E.A. Hassan, M.B.K. Ahamed, A.M. S.A. Majid, J. Mol. Struct. 1130 (2017) 791.

[32] S.K. Sinnah, K.S. Sim, S.W. Ng, K.W. Tan, J. Mol. Struct. 1137 (2017) 253.

[33] K.S.O. Ferraz, L. Lerandes, D. Carrilho, M.C.X. Pinto, M. D. F. Leite, E.M.S. –Fagundes, N.L. Speziali, I.C. Mendes, H. Beraldo, Bioorg. Med. Chem. 17 (2009) 7138.

[34] A. Sîrbu, O. Palamrciuc, M.V. Babak, J.M. Lim, K. Ohul, E.A. Enyedy, S. Shova, D. Darvasiová, P. Rapta, W.H. Ang, V.B. Arion, Dalton Trans. 46 (2017) 3833.

[35] J. Qui, J. Deng, K. Quian, L. Tian, J. Li, K. He, X. Huang, Z. Cheng, Y. Wang, Eur. J. Med. Chem. 134 (2017) 34.

[36] T.T. Taveres, D. Paschoal, E.V.S. Motta, A.G. Carpanez, M.T.P. Lopes, E.S. Fontes, H.F. D. Santos, H. Silva, R.M. Grazul, A.P.S. fonts, J. Coord. Chem. 67 (2014) 956.

[37] A.A. Oliveria, G.M. C. Perdigao, L.e. Rodrigues, J.G. de Selva, E.M.S– Fagundes, J.A. Takahashi, W.R. Rocha, H. Beralo, Dalton Trans. 46 (2017) 918.

[38] C. Umadevi, P. Kaleivani, H. Pushmann, S. Murugan, P.S. Mohan, R. Prabhakaran, J. Photochem. Photobiol. B167 (2017) 45.

[39] F.A. Beckford, K.R. Webb, Spectrochem. Acta A183 (2017) 158.

[40] C.G. Oliveria, P.I.S. Maia, P.C. Souza, F.R. Pavan, C.Q.F. Leite, R.B. Viana, A.A. Batista, O.R. Nascimento, V.M. Deflon, J. Inog. Biochem. 132 (2014) 21.

[41] M.A. Albuquerque, M.C.C. de Oliveria, A. Echevarria, Int. J. Electrochem. Sci. 12 (2017) 852.

[42] M. Muralisankar, R. Sreedharan, S. Sujith, N.S.P. Bhuvanesh, A. Sreekanth, J. Alloys Compd. 695 (2017) 171.

[43] V.P. Singh, P. Singh, A.K. Singh, Inorg. Chem. Acta 379 (2011) 56.

[44] M.R. Moghadam, S.M.P. Jahromi, A. Darehkordi, Food Chem. 192 (2016) 424.

[45] A.L. Werlein, A.J. Crook, E.P. Hoy, A.L. Koch, D.D. Ensor, E.C. Lisic, Sep. Sci. Technol. 50 (2015) 2907.

[46] S. Pandhye, G.B. Kauffman, Coord. Chem. Rev. 63 (1985) 127.

[47] Z.-Q. Han, S. Han, Y. Wang, Inorg. Nano metal Chem. 47 (2017) 127.

[48] W. Rui, X. Tian, P. Zeng, W. Liu, P. Ying, H. Chen, J. Lu, N. Yang, H. Chen, Polyhedron 117 (2016) 803.

[49] M. Devereux, M. McCann, V. Leon, V. McKee, R.J. Ball, Polyhedron 21 (2002) 1063.

[50] P.I.S. Maia, F.R. Pavan, C.Q.F. Leite, S.S. Lemos, G.F. de Sousa, A.A. Batista, O.R. Nascimento, J. Ellena, E.E. Castellano, E. Niquet, Polyhedron 28 (2009) 398.

[51] A.P. King, H.A. Gellineau, J.-E. Ahn, S.N. MacMillan, J.J. Wilson, Inorg. Chem. 56 (2017) 6609.

[52] S. Kumar, A. Hansada, A. Chandra, A. Kumar, M. Kumar, M. Sithambaresan, M.S.H. Faizi, V. Kumar, R.P. John, Polyhedron 134 (2017) 11.

[53] M.A. Arafath, F. Adam, M.R. Razali, L.E.A. Hassan, M.B.K. Ahmed, A.M.S.A. Majid, J. Mol. Struct. 1130 (2017) 791.

[54] G. Kalaiarasi, R. Jain, H. Puschman, S.P. Chandrika, K. Preethi, R. Prabhakaran, New J. Chem. 41 (2017) 2543.

[55] T.S. Lobana, S. Indoria, H. Sood, D.S. Arora, B.S. Randhawa, I.G. -Santos, V.A. Smolinski, J.P. Jesinski, Inorg. Chim. Acta 461 (2017) 248.

[56] D. Rogolino, A. Cavazzoni, A. Gatti, M. Tegoni, G. Pelosi, V. Verdolino, C. Fumarola, D, Cretella, P.G. Petronini, M. Carcelli, Eur. J. Med. Chem. 128 (2017) 140.

[57] S. Kathiresan, S. Mugesh, J. Annaraj, M. Murugan, New J. Chem. 41 (2017) 1267.

[58] J. Pisk, B. Prugovečki, D.M. -Čalogović, R. Poli, D. Agustin, V. Vrdoljak, Polyhedron 33 (2012) 441.

[59] M. Muralisankar, S.M. Basheer, J. Haribabu, N.S.P. Buvanesh, R. Karvembu, A. Sreekanth, Inorg. Chim. Acta 466 (2017) 61.

[60] P. Kalaivani, R. Prabhakaran, E. Ramachandran, F. Dallemer, G. Paramaguru, R. Renganathan, P. Poornima, V.V. Padma, K. Natarajan, Dalton Trans. 41 (2012) 2486.

[61] W. Herńańdez, A.J. Vaisberg, M. Tobar, M. Álvarez, J. Manzur, Y. Echevarria, E. Spodine, New J. Chem. 40 (2016) 1853.

[62] S.A. Musaivi, M. Montazerozohori, A. Masoudiasl, R. Naghiha, S. Joohar, A. Assoud, J. Mol. Struct. 1145 (2017) 65.

[63] L. Panwar, R. Gopal, M. Mohsin, M. Nagar, Biomirror 7 (2016) 11.

[64] T.C. Ribeiro, C. Weiblen, S.D.A. Botton, D.I.B. Pereira, F.P.K. de Jesus, C.M. Verdi, L.T. Gressler, L.A. Sangioni, J.M. Santurio, Med. Mycol. 55 (2017) 669.

[65] S. Stoll, Spectral Simulations in Solid-State Electron Paramagnetic Resonance, Ph. D. Thesis, ETH, Zurich, 2003.

[66] SMART and SAINT, Area Detector Software Package and SAX Area Detector Program, Bruker Analytical X-ray; Madison, WI, USA, 1997.

[67] SADABS, Area Detector Absorption Correction Program; Bruker Analytical X-ray; Madison, WI, 1997.

[68] G.M. Sheldrick, Acta Cryst. C71 (2015) 3.

[69] K. Brandenburg, Diamond Version 3.2g, Crystal Impact GbR, Bonn, Germany, 1997.

[70] L.J. Farrugia, J. Appl. Cryst. 45 (2012) 849.

[71] O.V. Dolomanov, L.J. Bourhis, R.J. Gildea, J.A.K. Howard, H. Puschmann, J. Appl. Cryst. 42 (2009) 339.

[72] G.M. Sheldrick, Acta Cryst. A71 (2015) 3.

.....ꕥ.....

Chapter 2

4-BENZYLOXYSALICYLADEHYDE-N^4-CYCLOHEXYLTHIOSEMICARBAZONE AND ITS TRANSITION METAL COMPLEXES: SYNTHESIS, SPECTRAL AND STRUCTURAL CHARACTERIZATION

Contents

2.1. Introduction

Multidentate thiosemicarbazones were found to show large number of coordination possibilities. The denticity of compounds can be increased by introducing additional heteroatom to the aldehydic part. 4-Benzyloxysalicyladehyde-N^4-cyclohexylthiosemicarbazone was designed by introducing salicylaldehyde at the R_1 site and cyclohexyl group on the R_3 site. The R_2 and R_4 sites are occupied by hydrogen atoms (Scheme 1).

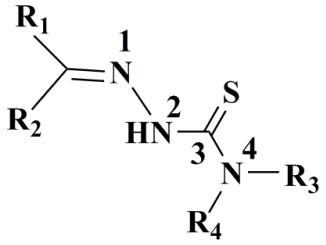

Scheme 2.1

4-Benzyloxysalicyladehyde-N^4-cyclohexylthiosemicarbazone can coordinate to metal *via* hydroxyl oxygen, amide nitrogen and thiol sulfur. Hence it can acts as an ONS type multidentate ligand. The compound can coordinate in the neutral monoanionic or dianionic form. It is reported that salicylaldehyde thiosemicarbazone show greater cytotoxic activity as compared to its metal complexes [1]. Rogolino *et al.* reported that salicylaldehyde thiosemicarbazones can act as inhibitor for influenza virus PA endonuclease [2].

The coordination complexes formed with salicylaldehyde thiosemicarbazone show diverse properties when there is a heterocyclic base present in the coordinating entity. It is found that Cu(II) complexes with heterocyclic ligand show biological activity [3,4,5] and likewise they act as sensors for F^- and CN^- [6]. Due to the virtue of Mo(VI) complex to act as a model system for active sites of molybdoenzymes [7], they have been extensively synthesized and their biological properties have been inspected. It is found that Mo(VI) complexes of salicylaldehyde thiosemicarbazones show *in vitro* DNA binding along with antitumor activities [7]. It is revealed that vanadium complexes of this type of compounds are efficacious against *Mycobacterium tuberculosis* [8,9,10]. Biological activities which include DNA binding, antibacterial and cytotoxic activities of Ni(II) complexes of substituted salicylaldehyde thiosemicarbazone have been explored [11,12]. Kalaiarasi *et al.* reported action of Ni(II) complexes of ONS donor thiosemicarbazones as an antiproliferate towards MCF-7 and HeLa cells [13].

In the current chapter we unleash a new substituted salicylaldehyde thiosemicarbazone and its VO(II), Ni(II), Cu(II), Pd(II), MoO_2(II) and Cd(II) complexes.

2.2. Experimental

2.2.1. Materials

4-Benzyloxysalicylaldehyde (Alfa Aesar), hydrazine monohydrate (98%) (Lancaster), cyclohexylisothiocyanate (Sigma Aldrich), $VOSO_4 \cdot H_2O$ (Alfa Aesar), $Ni(NO_3)_2 \cdot 6H_2O$ (Alfa Aesar), $Cu(OAc)_2 \cdot 2H_2O$ (E-Merck), $MoO_2(acac)_2$ (Sigma Aldrich), $PdCl_2$ (Sigma Aldrich), $Cd(OAc)_2 \cdot 2H_2O$ (Alfa Aesar), pyridine (S.D.Fine), 4,4′-bipyridine (Merck), 1.10-phenanthroline (Merck), 2,2′-bipyridine(Merck), CH_3OH (Spectrochem), CH_3CN (Spectrochem) DMF (Spectrochem) and DMSO (Spectrochem) were of analar grade and used without further purification.

2.2.2. Synthesis of 4-benzyloxysalicylaldehyde-N^4-cyclohexylthiosemi carbazone acetonitrile hemisolvate (H_2bsct·0.5CH_3CN)

Synthesis of H_2bsct·0.5CH_3CN follows a two step process (Scheme 2.1) [14]. In the first step, the cyclohexylisothiocyanate (2.115 g, 15 mmol) in 15 mL methanol was stirred with 15 mL methanolic solution of hydrazine hydrate (4.500 g, 90 mmol). The resulting colourless product, N^4-cyclohexylthiosemicarbazide was filtered, washed with methanol and dried *in vacuo*. In the second step, acetonitrile solution of 4-benzyloxysalicylaldehyde (0.228 g, 1 mmol), was mixed with 20 mL acetonitrile solution of N^4-cyclohexylthiosemicarbazide (0.173 g, 1 mmol) and the mixture was refluxed for 3 h in acidic medium (1 drop glacial acetic acid). The product obtained after one week was separated, washed with acetonitrile and dried *in vacuo*. Single crystals suitable for X-ray diffraction studies were obtained by recrystallization from acetonitrile solution [15].

Yield	:	(0.162 g) 52%; m.p: 172 °C.
Elemental Anal. Found (calcd)%	:	C 65.12 (65.07); H 6.96 (6.65); N 13.14 (13.20); S 7.89 (7.55).

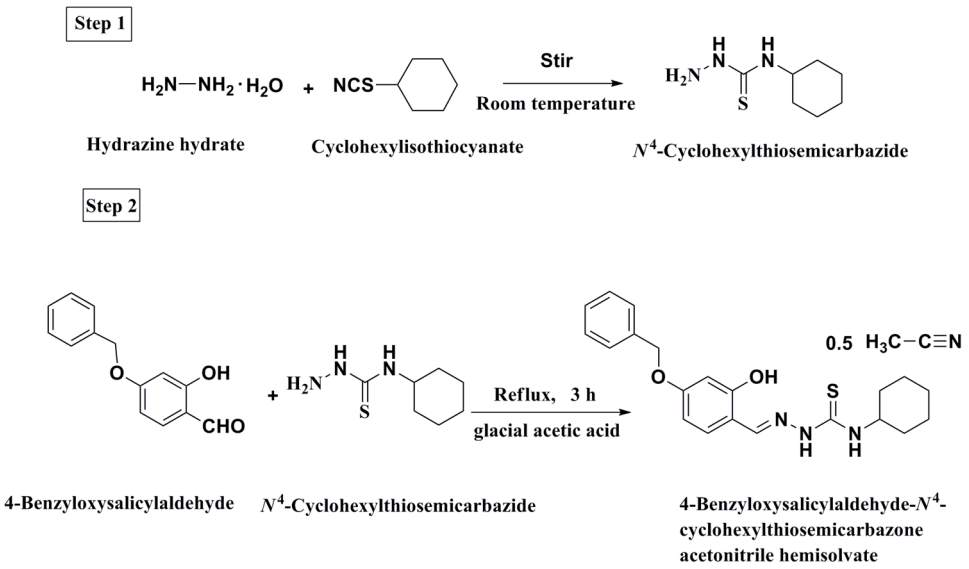

Scheme 2.2

2.2.3. Syntheses of complexes

2.2.3.1. Synthesis of $[VO(bsct)H_2O]_2$ (1)

The complex **1** was synthesized by refluxing an acetonitrile solution of vanadium sulfate monohydrate (0.162 g, 1 mmol) with $H_2bsct{\cdot}0.5CH_3CN$ (0.424 g, 1 mmol) in the same solvent for 6 h. The green colored solution obtained was kept for 2 weeks. A yellow colored compound obtained was filtered, washed with methanol and dried *in vacuo*.

Yield : (0.466 g) 50%.

Elemental Anal. Found (calcd)% : C 53.86 (54.07); H 5.07 (5.40); N 9.00 (9.01); S 6.42 (6.87).

2.2.3.2. Synthesis of [Ni(bsct)phen] (2)

An acetonitrile solution of $H_2bsct{\cdot}0.5CH_3CN$ (0.424 g, 1 mmol) was refluxed with a methanolic solution of $Ni(NO_3)_2{\cdot}6H_2O$ (0.290 g, 1 mmol). After 2 h, 1,10-phenanthroline (0.198 g, 1 mmol) was added and refluxed

further for 3 h. The brown colored product formed was filtered washed with methanol and dried *in vacuo*.

Yield : (0.279 g) 45%.
Elemental Anal. Found (calcd)% : C 63.42 (63.68); H 5.46 (5.34); N 11.7 (11.25); S 4.92 (5.15).

2.2.3.3. Synthesis of [Cu(bsct)phen(H_2O)] (3)

H_2bsct·0.5CH_3CN (0.424 g, 1 mmol) was heated with 10 ml acetonitrile, to ensure complete dissolution. To this hot solution $Cu(OAc)_2·H_2O$ (0.201 g, 1 mmol) in methanol was added and heated for 2 h under reflux. To this mixture, 1,10-phenanthroline (0.198 g, 1 mmol) in methanol was added and refluxed for 3 h. The resulted clear brown colored solution was kept for 1 week and brown colored crystalline product formed was separated by filtration and washed with methanol, dried *in vacuo*.

Yield : (0.374 g) 58%.
Elemental Anal. Found (calcd)% : C 61.52 (61.62); H 4.85 (5.17); N 11.49 (10.89); S 4.90 (4.98).

2.2.3.4. Synthesis of [Cu(bsct)bipy(H_2O)] (4)

A solution of H_2bsct·0.5CH_3CN (0.424 g, 1 mmol) in acetonitrile was heated under reflux with $Cu(OAc)_2·H_2O$ (0.201 g, 1 mmol) in methanol for 2 h. To this hot solution, 2,2′-bipyridine (0.156 g, 1 mmol) was added carefully under stirring and refluxed for further 3 h. The product formed was filtered washed with acetonirile and dried *in vacuo*.

Yield : (0.340 g) 55%.
Elemental Anal. Found (calcd)% : C 60.91 (60.13); H 5.11 (5.37); N 11.58 (11.31); S 4.79 (5.18).

2.2.3.5. Synthesis of [MoO_2(bsct)DMSO] (5)

The complex **5** was synthesized by refluxing a solution of H_2bsct·0.5CH_3CN (0.424 g, 1 mmol) in methanol with $MoO_2(acac)_2$ (0.326 g, 1 mmol) in methanol for 4 h. The resulted orange colored solution was kept for 1 week and the orange colored complex formed was filtered, washed with methanol and dried *in vacuo*. The product was dissolved in DMSO and kept for 1 week and the orange colored crystals obtained were separated.

Yield : (0.382 g) 65%.

Elemental Anal. Found (calcd)% : C 48.58 (48.77); H 5.68 (5.40); N 6.72 (6.83); S 9.97 (10.42).

2.2.3.6. Synthesis of [MoO_2(bsct)DMF] (6)

To a methanolic solution of H_2bsct·0.5CH_3CN (0.424 g, 1 mmol), $MoO_2(acac)_2$ (0.326 g, 1 mmol) in a mixture of methanol and DMF (1:1 v/v) was added and refluxed for 2 h. The orange colored solution obtained was kept for 1 week and brown colored crystalline product formed was separated, washed with methanol and dried *in vacuo*. The product was dissolved in DMF and kept for 1 week and the orange colored crystals obtained were separated.

Yield : (0.348 g) 60%.

Elemental Anal. Found (calcd)% : C 48.23 (48.47); H 3.99 (3.87); N 10.25 (10.77); S 6.48 (6.16).

2.2.3.7. Synthesis of [Pd(Hbsct)$_2$] (7)

To a hot methanolic solution of H_2bsct·0.5CH_3CN (0.424 g, 1 mmol), a solution of $PdCl_2$ (0.088 g, 0.5 mmol) in a mixture of acetonitrile and methanol (1:1 v/v) was added. Two drops of glacial acetic acid was

supplemented to the mixture. The product formed after 2 h was separated, washed with methanol and dried *in vacuo*.

Yield : (0.540 g) 62%.
Elemental Anal. Found (calcd)% : C 57.27 (57.89); H 5.67 (5.55); N 9.45 (9.64); S 7.21 (7.36).

2.2.3.8. Synthesis of $[(Cd(bsct))_2(4,4'\text{-bipy})]$ (8)

A mixture of $H_2bsct \cdot 0.5CH_3CN$ (0.848 g, 2 mmol) in 10 ml acetonitrile and $Cd(OAc)_2 \cdot 2H_2O$ (0.532 g, 2 mmol) in 10 ml methanol was refluxed for 4 h. To this a hot solution of 4,4′-bipyridine (0.156 g, 1 mmol) in 5 ml methanol was added with stirring and refluxed for 2 h. The yellow colored solution obtained was kept for 3 weeks and the product obtained was filtered, washed with methanol and dried *in vacuo*.

Yield : (0.735 g) 64%.
Elemental Anal. Found (Calcd)% : C 55.59 (55.54); H 4.76 (5.02); N 9.79 (9.90); S 5.61 (5.63).

2.2.4. Physico-chemical techniques

2.2.4.1. Elemental analysis

Elemental analyses of the compounds were done on a Vario EL III CHNS elemental analyzer at the Sophisticated Analytical Instrument Facility, Cochin University of Science and Technology, Kochi-22, Kerala, India.

2.2.4.2. Magnetic susceptibility measurements

The magnetic susceptibility measurements of the complexes were taken on a Vibrating sample Magnetometer using $Hg[Co(SCN)_4]$ as a calibrant at the SAIF, Indian Institute of Technology, Madras.

2.2.4.3. Molar conductivity measurements

The conductivity measurements of the complexes were recorded in 10^{-3} M solution in DMF on a Systronic model 303 direct reading conductivity meter at room temperature.

2.2.4.4. Spectroscopic characterization

The infrared spectra of H_2bsct·0.5CH_3CN and complexes **1-8** were recorded on a JASCO FT-IR-5300 Spectrometer in the range 4000-400 cm^{-1} using KBr pellets. The electronic spectra of the prepared compounds were recorded in DMF solution (10^{-3} and 10^{-5} M) on a Thermo Scientific Evolution 220 UV-vis Spectrophotometer in the 200-900 nm range at Department of Applied Chemistry, Cochin University of Science and Technology, Kochi, India. H_2bsct·0.5CH_3CN, complexes **7** and **8** were characterized by ^{1}H NMR techniques and was recorded using Bruker AMX 400 FT-NMR Spectrometer at the Sophisticated Analytical Instrument Facility, Cochin University of Science and Technology, Kochi, India. The Electro Paramagnetic Resonance spectra of complexes **1** and **4** were recorded in the solid state at 298 K and 77 K in DMF on a Varian E-112 spectrometer, with 100 kHz modulation frequency, 2 G modulation amplitude and 9.1 GHz microwave frequency at the Sophisticated Analytical Instrumentation Facility, Indian Institute of Technology, Bombay, India.

2.2.4.5. Thermogravimetric analysis

The TG-DTA analysis of complexes **1, 3, 4** and **8** were carried out using a Perkin Elmer Pyris Diamond TG-DTA analyzer under nitrogen atmosphere at a heating rate of 10 °C min^{-1} in the 50-700 °C range at the Sophisticated Analytical Instrument Facility, Cochin University of Science and Technology, Kochi, India.

2.2.5. Single crystal X-ray diffraction studies

The single crystal X-ray diffraction studies of $H_2bsct \cdot 0.5CH_3CN$ and complex **6** were done at 296(2) K, using a Bruker SMART APEXII CCD diffractometer at the Sophisticated Analytical Instrumentation Facility, Cochin University of Science and Technology, Kochi, India. Data acquisition was done using Bruker SMART software and data integration using Bruker SAINT software [16]. Absorption corrections were carried out using SADABS based on Laue symmetry using equivalent reflections [17]. The structure was solved by direct methods. The single crystal X-ray diffraction study of complex **5** was carried on Rigaku Oxford Diffraction diffractometer at 173(2) K at Department of Chemistry, Keene State College, 229 Main Street, Keene, NH. The CrysAlis Pro software [18a] was used to collect data and structure was solved with Olex 2 program [18b] package using ShelXT [19] program. Both the crystal data were refined with SHELXL-2014/7 software package [20] using least squares minimisation. The graphic tools used were DIAMOND version 3.2g [21] and ORTEP-3 [22].

2.3. Results and discussion

Elemental analyses of the compounds were presented in Sections 2.2.2 and 2.2.3. The structures of the compounds were assigned on the basis of this.

2.3.1. Characterization of 4-benzyloxysalicylaldehyde-N^4-cyclohexylthiosemicarbazone ($H_2bsct \cdot 0.5CH_3CN$)

2.3.1.1. Infrared spectrum

Infrared spectrum of $H_2bsct \cdot 0.5CH_3CN$ was taken in the range 4000-400 cm^{-1}. The band corresponding of ν(OH) vibration is observed at 3400 cm^{-1}. The ν(C=N) vibration gave a band at 1632 cm^{-1} suggesting the formation of azomethine bond as a cause of condenzation between aldehyde and thiosemicarbazide. Absence of bands in the 2800-2500 cm^{-1}

region indicates the absence of –SH stretching vibration [23]. The vibrations as a result of thiocarbonyl stretching (ν(C=S)/ν(C–S)) were observed at 1451 cm^{-1} and 836 cm^{-1}. The C–O–C stretching vibration gives a band at 1171 cm^{-1}. A band observed at 1110 cm^{-1} was assigned to hydrazinic ν(N–N) vibration. The infrared spectrum of the compound $H_2bsct{\cdot}0.5CH_3CN$ is depicted in Fig. 2.1.

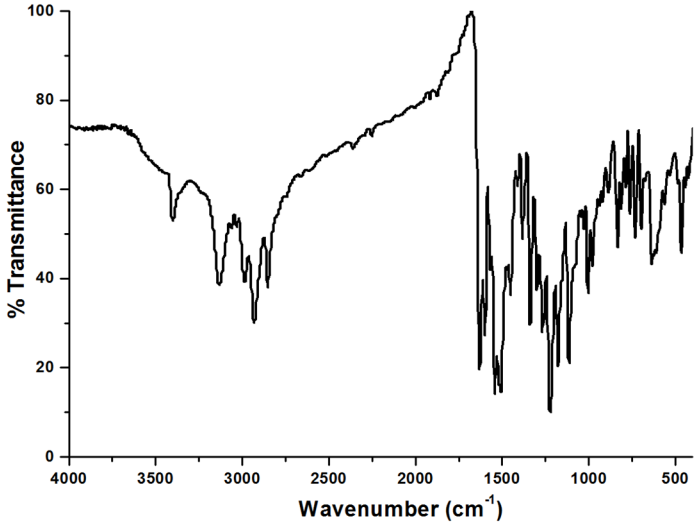

Fig. 2.1. Infrared spectrum of $H_2bsct{\cdot}0.5CH_3CN$.

2.3.1.2. Electronic spectrum

Electronic spectrum of $H_2bsct{\cdot}0.5CH_3CN$ was recorded in 10^{-5} M DMF solution. The electronic spectrum of $H_2bsct{\cdot}0.5CH_3CN$ is given in Fig. 2.2. The compound shows absorptions at 343, 304 and 292 nm with molar absorptivities of 7.31 × 10^4, 3.37 × 10^4 and 2.94 × 10^4 M^{-1} cm^{-1} respectively due to the presence of aromatic groups and non-bonding electrons.

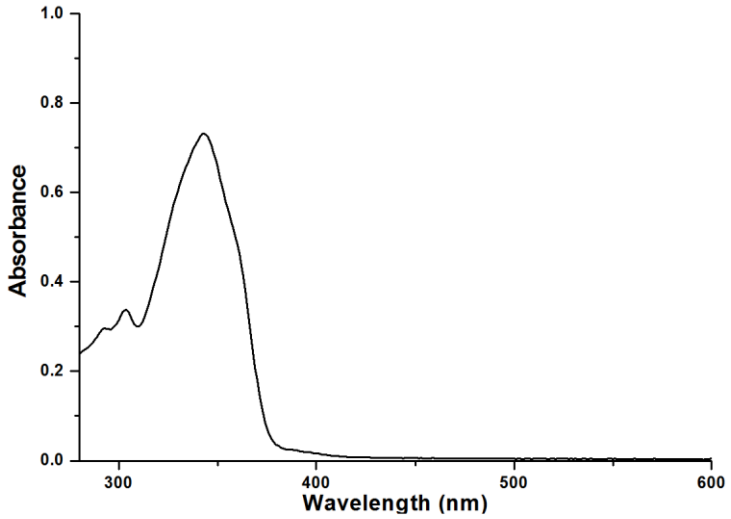

Fig. 2.2. Electronic spectrum of H_2bsct·0.5CH_3CN.

2.3.1.3. ^{1}H NMR spectrum

^{1}H NMR spectrum of H_2bsct·0.5CH_3CN was recorded in $CDCl_3$ accompanied by D_2O exchanged ^{1}H NMR spectrum using TMS as the internal standard. The ^{1}H NMR and deuterium exchanged ^{1}H NMR spectra for H_2bsct·0.5CH_3CN is represented in Fig. 2.3. The singlets at 9.81 ppm (s, 1H) and 9.76 ppm (s, 1H) were designated to –OH and N(2)–H protons respectively. The downfield shift is due to hydrogen bonding interaction exhibited these groups [24]. The peak at 5.5 ppm (s, 1H) corresponds to N(3)–H proton. Absence of these signals in the D_2O exchanged ^{1}H NMR spectrum shows the proton was exchangeable. The aromatic protons appear as multiplets in the region 7.13-7.43 ppm. The O–CH_2 protons appear as a singlet at 5.08 ppm (s, 2H). The down field shift was due to the presence of ether oxygen. The cyclohexyl protons gives a multiplet in the region δ=1.22-2.12 ppm.

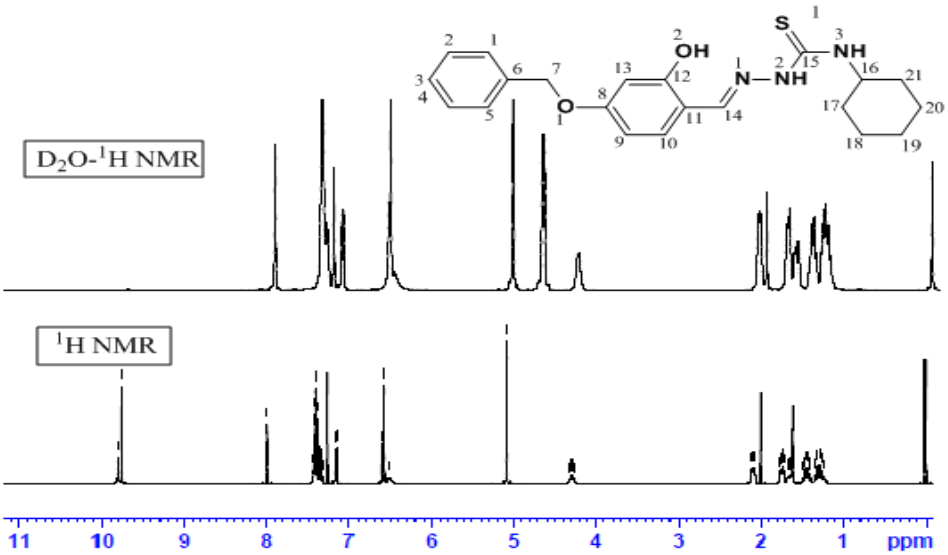

Fig. 2.3. ^{1}H NMR spectrum and deuterium exchanged ^{1}H NMR spectrum of H_2bsct·0.5CH_3CN.

2.3.1.4. Single crystal X-ray diffraction studies

Yellow needle shaped single crystals of H_2bsct·0.5 CH_3CN suitable for X-ray diffraction studies were isolated from acetonitrile solution. The compound crystallized into a triclinic space group $P\bar{1}$. A crystal of size 0.50 × 0.20 × 0.18 mm^3 was mounted on a Bruker SMART APEXII CCD diffractometer to collect data. The instrument is equipped with graphite monochromated Mo Kα (λ = 0.71073 Å) radiation. The non-hydrogen atoms were refined anisotropically and the C–H protons were placed at a distance 0.93–0.97 Å guided by difference map. The hydrogen atoms were assigned as U_{iso}=1.2U_{eq} (1.5 for Me). The N–H bonds are restrained to a bond length of 0.88±0.01 Å using DFIX instruction. The ORTEP diagram for H_2bsct·0.5 CH_3CN is depicted in Fig. 2.4. The asymmetric unit of the compound comprises of two molecules of thiosemicarbazone along with a molecule of acetonitrile. The crystal data and refinement parameters are given in Table 2.1.

Table 2.1. Crystal data and structure refinement parameters of $H_2bsct{\cdot}0.5CH_3CN$

Parameters	**$H_2bsct{\cdot}0.5CH_3CN$**
CCDC	1017712
Empirical formula	$C_{16}H_{17}N_3O_2S$
Formula weight	315.39
Color	Yellow
Temperature/K	296 (2)
Crystal system	monoclinic
Space group	$P2_1/n$
Cell parameters	
a (Å)	17.013(2)
b (Å)	5.9474(10)
c (Å)	17.542(4)
$\alpha = \gamma$ (°)	90
β (°)	117.565(7)
Volume (Å^3)	1573.4(5)
Z	4
Calculated density, ρ (g cm^{-3})	1.331
Absorption coefficient, μ (mm^{-1})	0.216
F(000)	664
Crystal size (mm^3)	0.50 x 0.40 x 0.35
θ range for data collection (°)	2.28 to 28.17
Limiting indices	$-22 \le h \le 22$, $-7 \le k \le 4$, $-22 \le l \le 23$
Reflections collected	10845
Independent reflections	3827 [R_{int} = 0.0232]
Data/restraints/parameters	3827 / 3 / 212
Goodness-of-fit on F^2	1.016
Final R indexes [$I > 2\sigma(I)$]	R_1 = 0.0428, wR_2 = 0.1074
Final R indexes [all data]	R_1 = 0.0719, wR_2 = 0.1280
Largest diff. peak and hole (e Å^{-3})	0.237/-0.240

$R_1 = \Sigma||F_o| - |F_c|| / \Sigma|F_o|$
$wR_2 = [\Sigma w(F_o^2-F_c^2)^2 / \Sigma w(F_o^2)^2]^{1/2}$

The molecule adopt an *E* confirmation with respect to C(14)–N(1) and C(32)–N(4) bond, evident from the C(11)–C(14)–N(1)–N(2) and C(32)–C(35)–N(4)–N(5) torsion angles 177.19(16)° and 178.66(17)° respectively [25]. The N(1)–N(2)–C(15)–S(1) and N(4)–N(5)–C(36)–S(2) torsion angles of 171.78(13)° and 173.54(14)° suggests that the thionyl sufur S(1) and S(2) are *trans* with respect to N(1) and N(4) respectively.

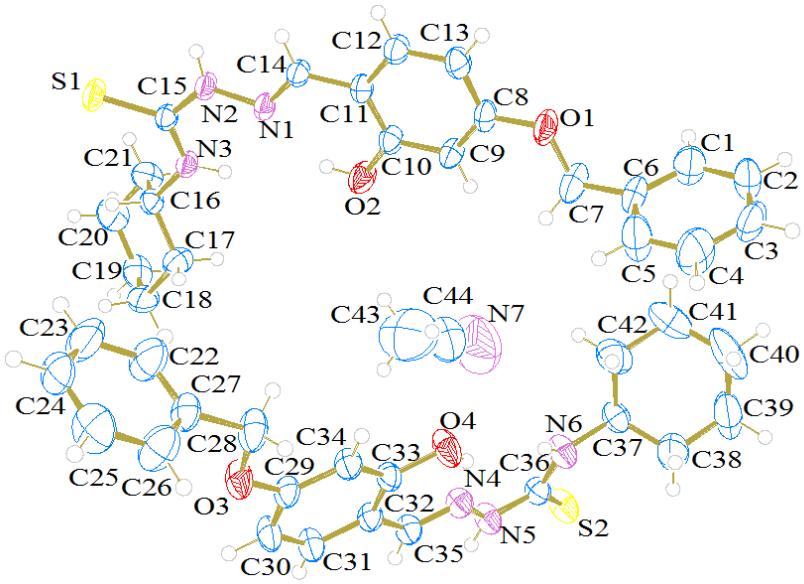

Fig. 2.4. ORTEP diagram of H_2bsct·0.5CH_3CN with displacement ellipsoid of 50% probability.

The C(14)–N(1) and C(35)–N(4) bond lengths 1.281(2) Å and 1.278(2) Å respectively are equivalent to that of standard C=N bond length [26], confirms the condensation of aldehyde and thiosemicarbazide resulted in azomethine bond formation. Further the C(15)–S(1) and C(36)–S(2) bond lengths 1.683(17) Å and 1.682(17) Å close to formal C=S bond length 1.688(2) Å [27], suggesting the existence of both molecules in thio-amido form in the solid state.

The thiosemicarbazone moiety in both the molecules were planar with maximum deviation of 0.013 Å for C15 and 0.007 Å for C36 respectively for each molecule. The least square plane calculations showed that the ring C(1)–C(2)–C(3)–C(4)–C(5)–C(6) in the first molecule was twisted from the ring C(8)–C(9)–C(10)–C(11)–C(12)–C(13) with a dihedral angle 82.93(12)°, similarly the ring C(22)–C(23)–C(24)–C(25)–C(26)–C(27) in the second molecule was twisted away from the ring C(29)–C(30)–C(31)–C(32)–C(33)–C(34) with a dihedral angle 88.59(12)°. From the ring puckering analysis and least square plane calculations, it is evident that the cyclohexyl ring in both molecules adopts a chair conformation with puckering amplitudes Q_T=0.556(2) and 0.568(4) Å respectively. Selected bond parameters were given in Table 2.2.

Table 2.2. Selected bond parameters of H_2bsct·0.5CH_3CN

Bond length (Å)		Bond angle (°)	
C(14)–N(1)	1.285(2)	C(7)–O(1)–C(8)	118.05(16)
C(35)–N(4)	1.278(2)	C(28)–O(3)–C(29)	118.03(15)
N(1)–N(2)	1.379(19)	C(11)–C(14)–N(1)	123.32(16)
N(4)–N(5)	1.378(19)	C(32)–C(35)–N(4)	122.63(16)
C(15)–S(1)	1.683(17)	C(14)–N(1)–N(2)	115.26(14)
C(36)–S(2)	1.682(17)	C(36)–N(5)–N(4)	120.82(15)
C(15)–N(2)	1.346(2)	N(2)–C(15)–S(1)	119.07(13)
C(36)–N(5)	1.343(2)	N(5)–C(36)–S(2)	119.17(14)
C(10)–O(2)	1.355(2)	N(2)–C(15)–N(3)	117.35(15)
C(33)–O(4)	1.350(2)	N(5)–C(36)–N(6)	117.15(15)

The crystal packing of the compound is effective through various interactions present in the molecule. H_2bsct·0.5CH_3CN exhibits an intermolecular and an intramolecular interaction per molecule. The intermolecular interaction N(2)–H(2′)···S(1) and N(5)–H(5′)···S(2) with D···A distance 3.30(16) and 3.35(17) Å connects same type of molecule in the crystal. The intramolecular interaction O(2)–H(2A)···N(1) and O(4)–

H(4′)···N(4) with D···A distance 2.69(2) and 2.68(2) [28] respectively, lead to form a six membered ring comprising of atoms N(1)–C(14)–C(11)–C(10)–O(2)–H(2A) in the first molecule and N(4)–C(35)–C(34)–C(33)–O(4)–H(4′) in the second molecule.

Table 2.3. Interaction parameters in H_2bsct·0.5CH_3CN

Hydrogen bonding interactions

D–H···A	D–H (Å)	H···A (Å)	D···A (Å)	D–H···A (°)
N(2)–H(2′)···S(1)[a]	0.88(9)	2.44(10)	3.30(16)	171(2)
N(5)–H(5′)···S(2)[b]	0.88(9)	2.48(2)	3.35(16)	172(19)
O(2)–H(2A)···N(1)	0.84(10)	1.96(18)	2.69(17)	146(3)
O(4)–H(4′)···N(4)	0.84(10)	1.94(16)	2.68(2)	146(2)

C–H···π interactions

C–H··· Cg	C–H (Å)	C(H···Cg (Å)	C···Cg (Å)	C–H···Cg(°)
C(12)–H(12)···Cg(1)[c]	0.93	2.95	3.81(2)	154
C(20)–H(20B)···Cg(2)[d]	0.93	2.87	3.71(2)	146
C(31)–H(31)···Cg(4)[e]	0.93	2.84	3.71(2)	157

a= -x+1, -y+1, -z+1; b= -x-1, -y+1, z; c=1-x, 2-y, -z; d=-1+x, -1+y, z; e=-x, -2-y, 1-z. Cg(1)= C(1), C(2), C(3), C(4), C(5), C(6); Cg(2)= C(8), C(9), C(10), C(11), C(12), C(13); Cg(4)=C(22), C(23), C(24), C(25), C(26), C(27), D= donor, A= acceptor, Cg= centroid

The crystal packing is further facilitated by C–H···π interactions characterized by C(12)–H(12)···Cg(1), C20–H(20B)···Cg(2) and C(31)–H(31)···Cg(4) with H···Cg distances 2.95, 2.87 and 2.84 Å respectively (Cg(1)→C(1)–C(2)–C(3)–C(4)–C(5)–C(6), Cg(2)→C(8)–C(9)–C(10)–C(11)–C(12)–C(13) and Cg(4)→C(22)–C(23)–C(24)–C(25)–C(26)–C(27)). Various molecular interactions facilitating the effective packing of H_2bsct·0.5CH_3CN are presented in Table 2.3. Figs 2.5 and 2.6 represent the hydrogen bonding interactions and C–H···π interactions in H_2bsct·0.5CH_3CN.

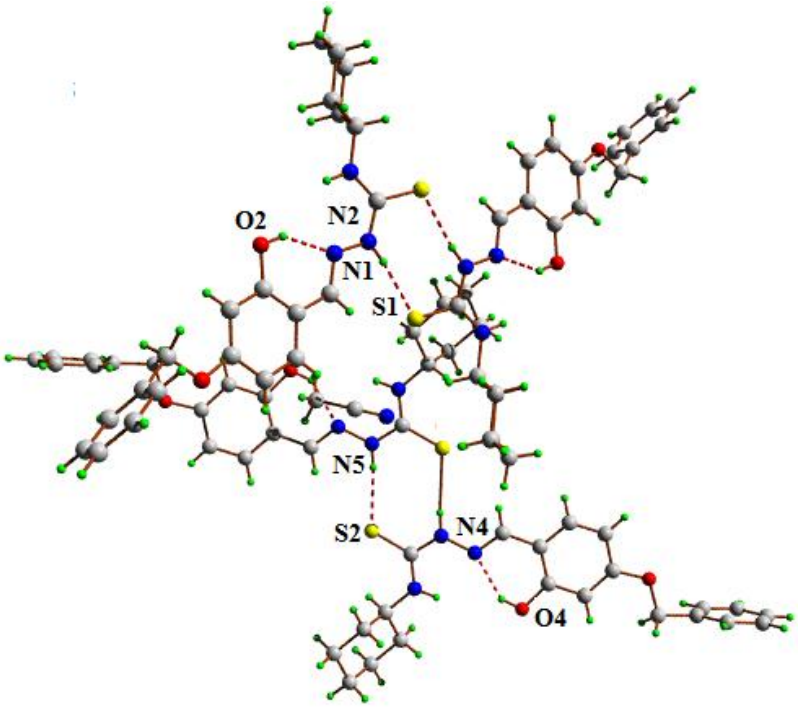

Fig. 2.5. Hydrogen bonding interactions in H_2bsct·0.5CH_3CN.

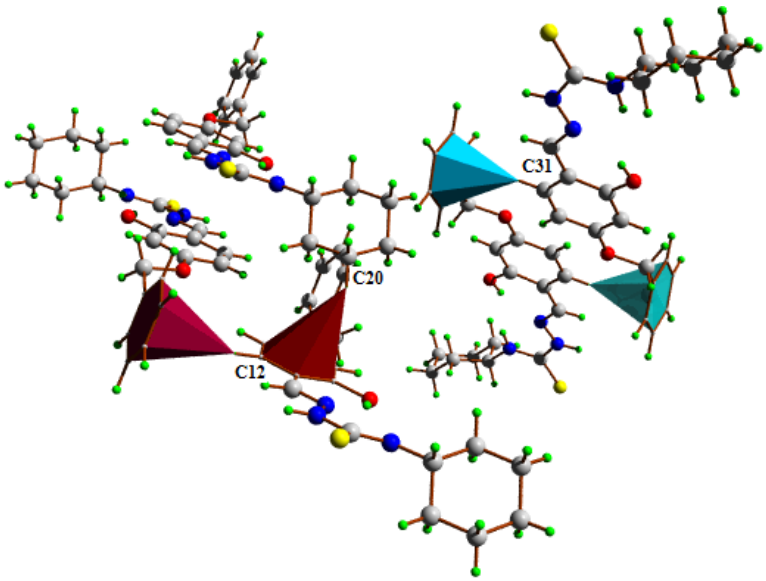

Fig. 2.6. C–H···π interactions in H_2bsct·0.5CH_3CN.

2.3.2. Characterization of complexes of $H_2bsct \cdot 0.5CH_3CN$

$H_2bsct \cdot 0.5CH_3CN$ can show a large number of coordination modes by virtue of the tridentate ONS type linking sites. In the present chapter we have included eight different complexes synthesized using VO(II), Ni(II), Cu(II), MoO_2(II), Pd(II) and Cd(II). Of these, complex **1** was synthesized by refluxing a mixture of solutions of thiosemicarbazone and the metal salt in 1:1 ratio. Complexes **2, 3,** and **4** were synthesized by refluxing a mixture of solutions of thiosemicarbazone, respective metal salt and heterocyclic base (1,10-phenanthroline and 4,4′-bipyridine) in 1:1:1 ratio. The complexes **5** and **6** were synthesized by refluxing solutions of the metal salt with the thiosemicarbazone in 1:1 ratio followed by recrystallisation from the respective solvents (DMSO and DMF). The complex **7** was synthesized by refluxing a mixture of solutions of thiosemicarbazone and metal salt in 1:1 ratio. The complex **8** was synthesized by refluxing a mixture of solutions of metal salt, thiosemicarbazone and 4,4′-bipyridine in 1:1:1 ratio.

2.3.2.1. Molar conductivity and magnetic susceptibility measurements

Molar conductivity as well as magnetic susceptibility measurements give insight into the oxidation state of the metal in the complex, with which we could predict the coordination environment. The molar conductivity measurements were taken in 10^{-3} M solution of DMF. It is observed that the compounds give a molar conductivity between 2.5-18 $ohm^{-1} cm^2 mol^{-1}$, well below the value of uni-univalent electrolyte (60-90 $ohm^{-1} cm^2 mol^{-1}$), justifying the non conducting nature of all the complexes.

Magnetic moment value of complex **1** is 1.26 B.M., very well below the expected value of 1.7 B.M. There are reports for dimeric oxidovanadium(IV) complexes showing abnormal magnetic moments due to antiferromagnetic interactions as a result of the unpaired electron lying in d_{xy} orbital which lead to extended overlapping and spin-spin coupling [29,30]. The magnetic moment value of complex **2**, 2.92 B.M. is near to the expected magnetic

moment value for a pentacoodinated Ni(II) complex. Both complexes **3** and **4** give a magnetic moment of 1.93 and 1.86 B.M. very close to the spin only value for a typical d^9 Cu(II) complex. Complexes **5, 6, 7** and **8** exhibit a diamagnetic nature which is agreement with the Mo(VI), low spin Pd(II) and d^{10} Cd(II) state of the metals in these complexes.

Table 2.4. Molar conductivity and magnetic moment values of complexes of H_2bsct

Compound	λ_m (ohm^{-1}cm^{2}mol^{-1})	μ_{eff} (B.M.)
$[VO(bsct)H_2O]_2$ (**1**)	18	1.26
[Ni(bsct)phen] (**2**)	3.6	2.92
[Cu(bsct)phen(H_2O] (**3**)	4.2	1.93
[Cu(bsct)bipy(H_2O)] (**4**)	4.6	1.86
$[MoO_2$(bsct)DMSO] (**5**)	7.0	0
$[MoO_2$(bsct)DMF] (**6**)	2.5	0
$[Pd(Hbsct)_2]$ (**7**)	14.1	0.02
$[(Cd(bsct))_2$ 4,4′-bipy] (**8**)	3.1	0

2.3.2.2. Infrared spectra

Infrared spectra of the complexes were recorded in the 400-4000 cm^{-1} range using KBr pellets. The H_2bsct·0.5CH_3CN is a salicylaldehyde derivative and hence the presence or absence of –OH band and the shift in the ν(C=S) help us to find whether the compound coordinates in the monodeprotonated or doubly deprotonated form. The important vibrational stretching frequencies accompanied by tentative assignment of groups are given in Table 2.5. It is found that for all the complexes the band at 3400 cm^{-1}, assigned to ν(OH) stretching frequency is absent establishing the coordination of H_2bsct·0.5CH_3CN through deprotonation of phenolic proton. The complexes show a shift in the ν(C–O) stretching vibration by a value of 40-50 cm^{-1}.

Table 2.5. IR spectral assignments (cm^{-1}) of $H_2bsct{\cdot}0.5\ CH_3CN$ and its metal complexes

Compound	ν(O–H)	ν(C=N)	ν(C=N)[a]	ν(C–O)	ν(C=S)/	ν(C–S)	ν(N–N)	ν(M=O) ν(M–O)	ν(M–N)
$H_2bsct{\cdot}0.5CH_3CN$	3400	1632	---	1271	1451, 836		1110	---	---
$[VO(bsct)H_2O]_2$ (**1**)	---	1600	1543	1237	1396, 849		1123	995,532	443
[Ni(bsct)phen] (**2**)	---	1607	1520	1233	1420, 848		1136	569	426
$[Cu(bsct)phen(H_2O)]$ (**3**)	---	1600	1522	1222	1427, 823		1129	407	426
$[Cu(bsct)bipy(H_2O)]$ (**4**)	---	1607	1526	1203	1433,828		1136	413	439
$[MoO_2(bsct)DMSO]$ (**5**)	---	1594	1538	1217	1418, 845		1122	990,927	468
$[MoO_2(bsct)DMF]$ (**6**)	---	1590	1545	1212	1385, 841		1129	995,937	420
$[Pd(Hbsct)_2]$ (**7**)	3412	1619	1523	1252	1445, 836		1116	---	550
$[(Cd(bsct)_2)_2(4,4'\text{-bipy})]$ (**8**)	---	1600	1524	1225	1428, 843		1186	515	443

a- Newly formed C=N

The band at 1632 cm^{-1} for corresponds to azomethine bond, (ν(C=N) streching) showed a shift to 1600 cm^{-1} in the complex $[VO(bsct)H_2O]_2$ **(1)** indicate coordination of azomethine nitrogen to the metal. A shift in the ν(C=S)/ν(C–S) stretching frequency from 1451 cm^{-1} in $H_2bsct{\cdot}0.5CH_3CN$ to 1396 cm^{-1} in the complex **1** suggest that $H_2bsct{\cdot}0.5CH_3CN$ coordinate in the thio-iminolate form. This is further confirmed from the increase in ν(N–N) stretching frequency accompanied by appearance of a new band at 1543 cm^{-1} corresponding to new C=N. The metal to ligand coordination is confirmed form bands at 995, 532 and 443 cm^{-1}, due to ν(V=O), ν(V–O) (phenolic) and ν(V–N) stretching frequencies respectively [32]. As per Maurya *et al.*, the V–O–V bridging gives a stretching band in the region 756-804 cm^{-1}[33]. The band at 760 cm^{-1} is assigned to this ν(V–O–V) vibration for complex **1**. The coordinated water molecule gives a stretching band at 589 cm^{-1} [34]. Fig. 2.7 represents infrared spectrum for complex **1**.

The ν(C=N) band of $H_2bsct{\cdot}0.5CH_3CN$ at 1632 cm^{-1} was found to shift to 1607 cm^{-1} in the [Ni(bsct)phen] (**2**) indicate coordination *via* azomethaine nitrogen. This is further confirmed from the band at 426 cm^{-1}, which was

assigned to ν(Ni–N) band. The coordination of H_2bsct·0.5CH_3CN through phenolic oxygen is confirmed from the ν(Ni–O) stretching band at 569 cm^{-1}. The band corresponding to ν(C=S)/ν(C–S) vibration appearing at 1451 cm^{-1} in H_2bsct·0.5CH_3CN was shifted to 1420 cm^{-1} indicate coordination of thiosemicarbazone in the doubly deprotonated form. This is further confirmed from the increase in ν(N–N) and appearance of a new band corresponding to newly formed C=N. The 1,10-phenanthroline (phen) group give a characteristic vibration corresponding to ν(Ni–N_{phen}) at 465 cm^{-1} [35]. Fig. 2.8 exhibits the infrared spectrum for complex **2**.

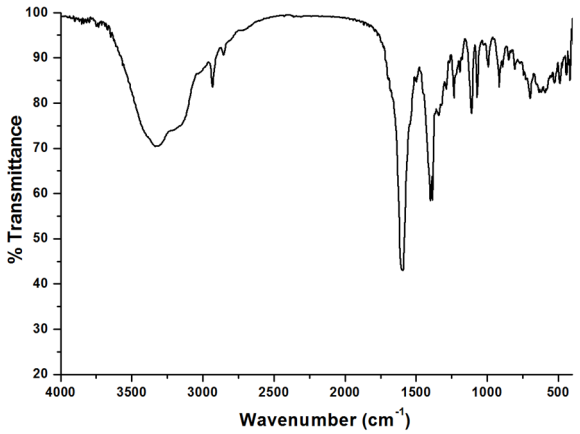

Fig. 2.7. Infrared spectrum of [VO(bsct)H_2O]$_2$ (**1**).

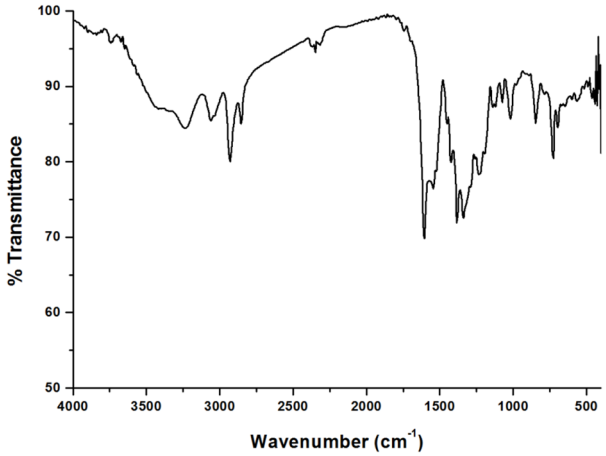

Fig. 2.8. Infrared spectrum of [Ni(bsct)phen] (**2**).

H_2bsct·0.5CH_3CN seems to coordinated *via* azomethine nitrogen in complexes [Cu(bsct)phen(H_2O)] (**3**) and [Cu(bsct)bipy(H_2O)] (**4**). This is evident from the shift for ν(C=N) vibration from 1632 cm^{-1} for H_2bsct·0.5CH_3CN to 1600 cm^{-1} for complex **3** and 1607 cm^{-1} for complex **4** respectively. The shift observed for ν(C=S)/ν(C–S) from 1451 cm^{-1} for H_2bsct·0.5CH_3CN to 1427 cm^{-1} for complexes **3** and 1433 cm^{-1} for compex **4,** suggests that H_2bsct·0.5CH_3CN coordinate in doubly deprotonated form. Appearance of a new ν(C=N) vibration at 1522 cm^{-1} for complex **3** and 1526 cm^{-1} complex **4** were evidence of this observation. This is further confirmed from the bands at 1129 and 1136 cm^{-1} for ν(N–N) respectively for complexes **3** and **4** which shows increase of 20-30 cm^{-1} from that of H_2bsct·0.5CH_3CN. The bands corresponds to the heterocyclic bases are present as bands in the finger print region 1400-600 cm^{-1}. The Cu–L coordination is evident from the ν(Cu–N_{azo}) vibrations at 426, 407 cm^{-1} and ν(Cu–O) vibrations at 413, 439 cm^{-1} for complexes **3** and **4** respectively [36,37]. Similar to complex **1** the coordinated water gave bands at 569 and 567 cm^{-1} respectively for complexes **3** and **4** [35]. The band at 490 cm^{-1} is due to ν(Cu–N_{phen}) stretching vibration. Figs 2.9 and 2.10 represents infrared spectrum for complexes **3** and **4**.

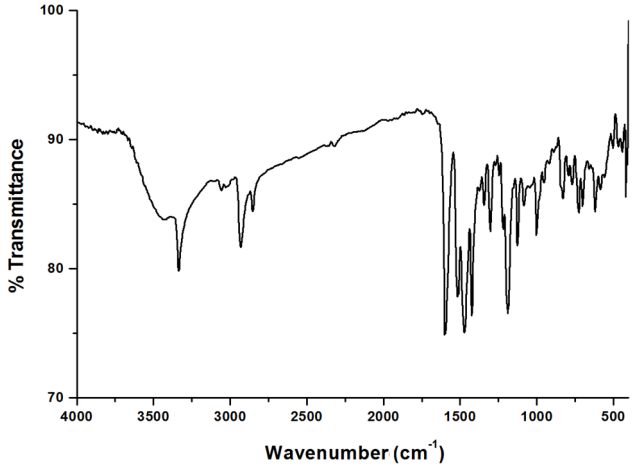

Fig. 2.9. Infrared spectrum of [Cu(bsct)phen(H_2O)] (**3**).

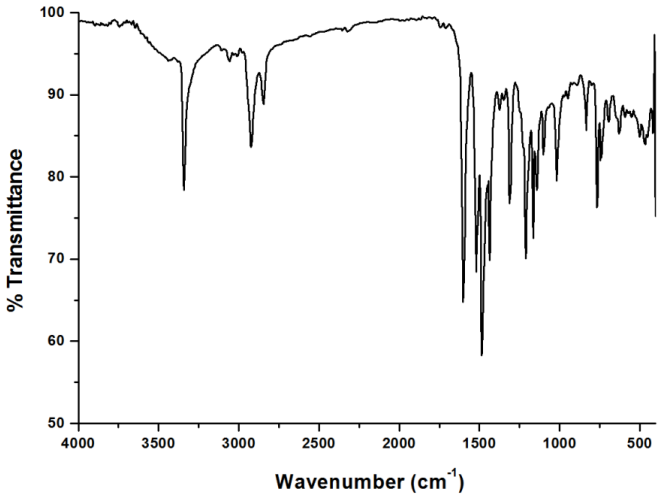

Fig. 2.10. Infrared spectrum of [Cu(bsct)bipy(H_2O)] (**4**).

Both molybdenum complexes [MoO_2(bsct)DMSO] (**5**) and [MoO_2(bsct)DMF] (**6**) show shift in the value for ν(C=N) by 38-40 cm^{-1} indicate the coordination of H_2bsct·0.5CH_3CN through azomethine nitrogen. The ν(C=S) band at 1451 cm^{-1} for H_2bsct·0.5CH_3CN was shifted to 1418 and 1385 cm^{-1} respectively for complexes **5** and **6** indicate the coordination of H_2bsct·0.5CH_3CN in the thio-iminolate form. This is further confirmed from increase in the ν(N–N) stretching and presence of an additional band at 1538 cm^{-1} for complex **5** and 1545 cm^{-1} for complex **6**. The *cis*-MoO_2 vibrations were observed at 990 and 927 for complex **5**. Complex **6** gave this vibration at 995 and 937 cm^{-1}. The complexes gave ν(Mo–O) stretching bands in 560-570 cm^{-1} region and ν(Mo–N) bands in 420-470 cm^{-1} region [38]. Figs. 2.11 and 2.12 depict the infrared spectra for complexes **5** and **6**.

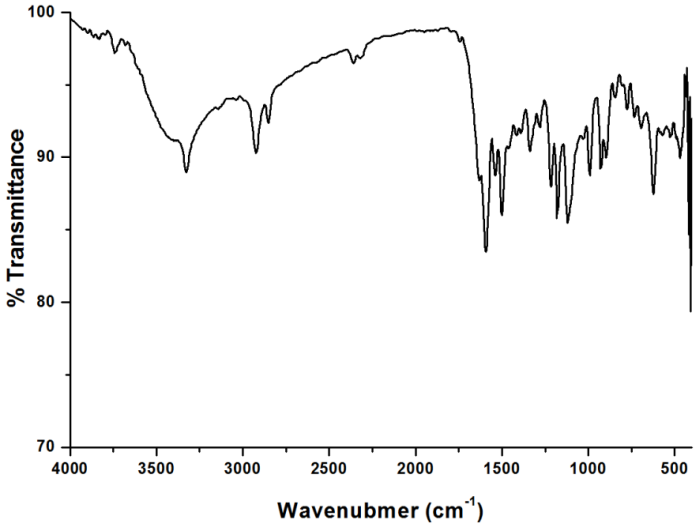

Fig. 2.11. Infrared spectrum of [MoO_2(bsct)DMSO] **(5).**

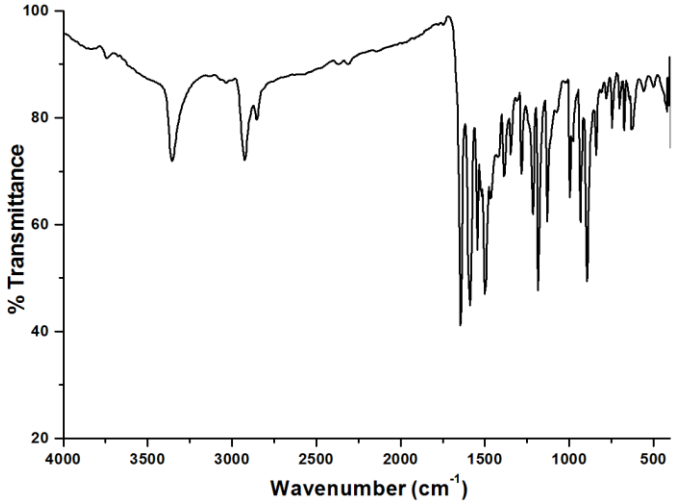

Fig. 2.12. Infrared spectrum of [MoO_2(bsct)DMF] (**6**).

In [Pd(Hbsct)$_2$] (**7**), H_2bsct·0.5CH_3CN was found to coordinate in the monodeprotonated form. The appearance of a band at 3412 cm^{-1} gave information regarding the non involvement of phenolic group in coordination. The deprotonated sulfur coordinates in the thio-iminolate

form, which is confirmed from the shift observed for ν(C=S). The shift in the stretching frequency for ν(C=N) from 1632 cm^{-1} for $H_2bsct{\cdot}0.5CH_3CN$ to 1619 cm^{-1} in complex 7 justifies the coordination of $H_2bsct{\cdot}0.5CH_3CN$ through azomethine nitrogen. The ν(Pd–N) band was observed at 550 cm^{-1} [39,40]. The infrared spectrum for the complex **7** is presented in Fig. 2.13.

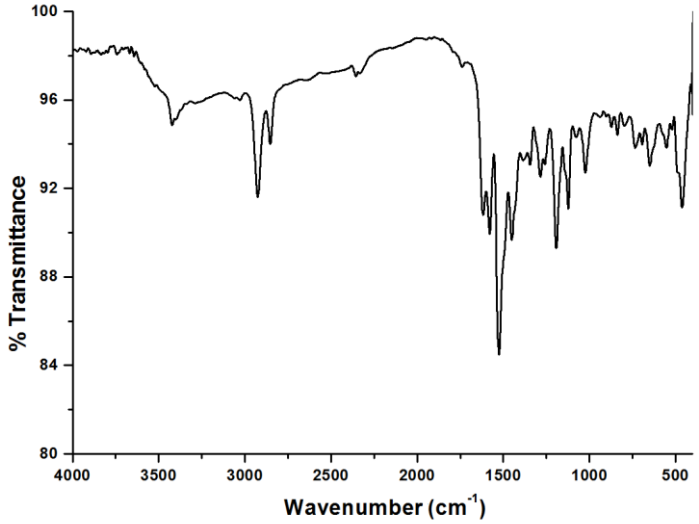

Fig. 2.13. Infrared spectrum of complex $[Pd(Hbsct)_2]$ **(7)**.

In $[(Cd(bsct))_2(4,4'\text{-bipy})]$ (**8**), a single unit of $bsct^{2-}$ is coordinated to one Cd(II) centre. There is a shift in the ν(C=N) vibration from 1632 cm^{-1} for $H_2bsct{\cdot}0.5CH_3CN$ to 1600 cm^{-1} in the complex **8**. A shift ν(C=S) vibration from 1451 cm^{-1} in $H_2bsct{\cdot}0.5CH_3CN$ to 1428 cm^{-1} in the complex **8** and appearance of a new band at 1524 cm^{-1} confirms the coordination of metal to $H_2bsct{\cdot}0.5CH_3CN$ in doubly deprotonated form. These shifts justify the coordination of metal through azomethine nitrogen and thio-iminol sulfur. The coordination of metal to $H_2bsct{\cdot}0.5CH_3CN$ give ν(Cd–O) and ν(Cd–N) at 515 and 443 cm^{-1} respectively [41]. Fig. 2.14 gives infrared spectrum of complex **8**.

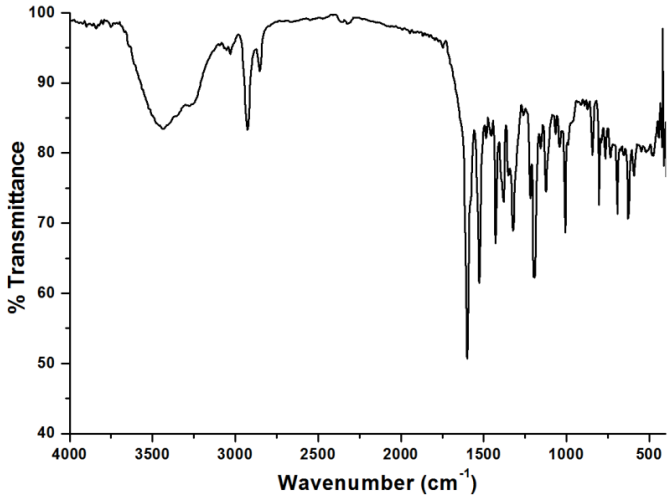

Fig. 2.14. Infrared spectrum of [(Cd(bsct))$_2$(4,4′-bipy)] (**8**).

2.3.2.3. Electronic spectra

The electronic spectra of the complexes were recorded in 10^{-3} and 10^{-5} M solution of DMF. The electronic spectra give characteristic absorption as a clear evidence for aromatic groups as well as non-bonded electrons in the complex. All complexes show absorption in the region 300-405 cm^{-1} correspond to n–π*, π–π* or LMCT transitions. The n–π* and π–π* transitions show red shift in absorption as compared to H_2bsct·0.5CH_3CN. This is due to the weakening of C=S bond and extension of conjugation upon complexation. The electronic transition between ligand and metal orbitals were observed at higher wave lengths, which is an evidence of complex formation. The tentative assignments of various absorptions for H_2bsct·0.5CH_3CN and its metal complexes are given in Table 2.6.

Table 2.6. Electronic spectral assignments (nm) of and complexes

Compound	**n–π*/ π–π* (ε =10^4 M^{-1} cm^{-1})**	**LMCT (nm) (ε=10^4 M^{-1} cm^{-1})**	***d-d* (nm) (ε (M^{-1} cm^{-1}))**
H_2bsct·0.5CH_3CN	292 (2.90), 304 (3.37), 343 (7.31)	---	---
[VO(bsct)$H_2O]_2$ (**1**)	338 (5.84), 355 (5.99)	384 (5.19)	667 (41.8)
[Ni(bsct)phen] (**2**)	345 (7.23), 360 (6.56),	405 (3.06)	---
[Cu(bsct)phen(H_2O)] (**3**)	312 (6.43), 323 (6.78), 379 (7.60)	394 (6.98)	574 (203),735 (104)
[Cu(bsct)bipy(H_2O)] (**4**)	324 (2.54), 380 (2.75)	395 (2.57)	569 (117)
[MoO_2(bsct)DMSO] (**5**)	301 (5.74), 342 (8.77)	---	---
[MoO_2(bsct)DMF] (**6**)	304 (4.48), 341 (8.77)	---	---
[Pd(Hbsct) $_2$] (**7**)	349 (6.38), 381 (7.28)	394 (6.81)	---
[(Cd(bsct)$_2$)$_2$(4,4′-bipy)] (**8**)	307 (2.96), 319 (3.04), 367 (7.41)	384 (6.56)	---

Complex **1** shows absorption with λ_{max} = 338 and 355 nm, with molar absorptivities of 5.84×10^4 and 5.99×10^4 M^{-1} cm^{-1}, were designated to intraligand transitions. A shoulder appear at λ_{max} = 384 nm (ε = 5.19 × 10^4 M^{-1} cm^{-1}), due to LMCT transition from phenolic oxygen to vanadium V←O [42]. The electronic spectra for H_2bsct·0.5CH_3CN and complex **1** are presented in Fig. 2.15.

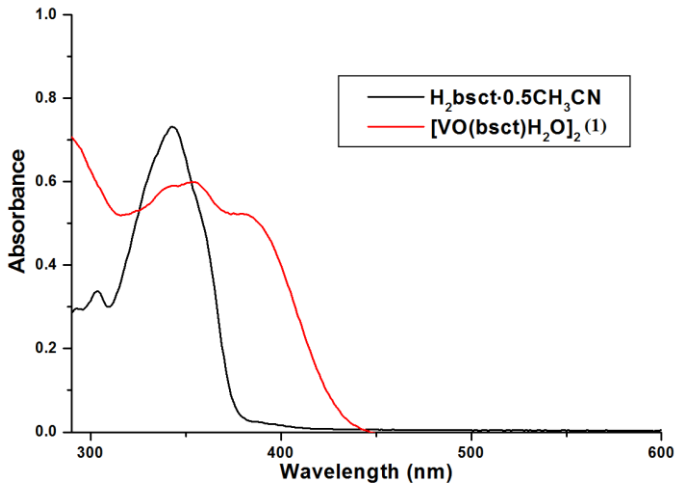

Fig. 2.15. Electronic spectra of H_2bsct·0.5CH_3CN and complex **1**.

The visible spectrum for VO(II) with a d^1 electronic configuration is expected to have an electronic transition $^2E_g \leftarrow {}^2T_{2g}$, but this is possible for a perfect octahedral V(IV) complex [43]. But for a non perfect octahedral complex the expected transitions are $^2E \leftarrow {}^2B_2$ ($d_{xy} \rightarrow d_{xz}, d_{yz}$), $^2B_1 \leftarrow {}^2B_2$ ($d_{xy} \rightarrow d_{x^2-y^2}$) and $^2A_1 \leftarrow {}^2B_2$ ($d_{xy} \rightarrow d_{z^2}$) [44]. Since these splitted levels are close enough to give a band with absorption maximum at 667 nm with molar absorptivity absorptivity of 41.8 M^{-1} cm^{-1}. The visible spectrum for complex **1** is given in Fig. 2.16.

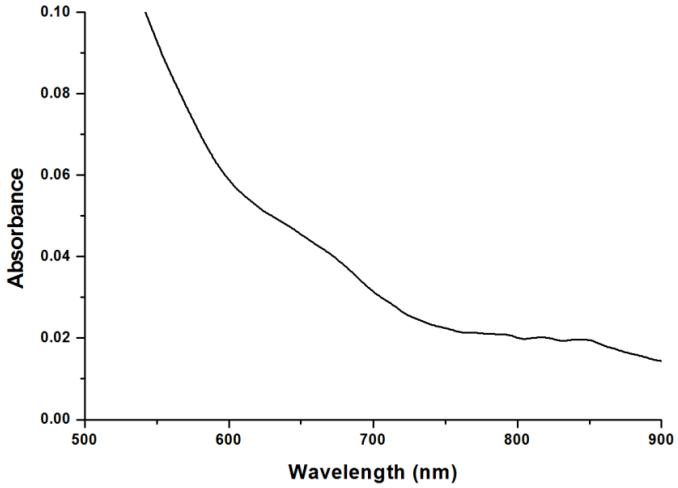

Fig. 2.16. Visible spectrum of $[VO(bsct)H_2O]_2$ (**1**).

Complex **2** gave absorption due intraligand transitions with maximum absorption at 345 nm ($\varepsilon = 7.23 \times 10^4$ M^{-1} cm^{-1}) and 360 nm ($\varepsilon = 6.56 \times 10^4$ M^{-1} cm^{-1}) respectively. The LMCT transitions due Ni←O or Ni←N were observed as a broad band with maximum absorption at 405 nm with molar absorptivity 3.06×10^4 M^{-1} cm^{-1} [45]. The electronic spectra for $H_2bsct \cdot 0.5CH_3CN$ and complex **2** are depicted in Fig. 2.17.

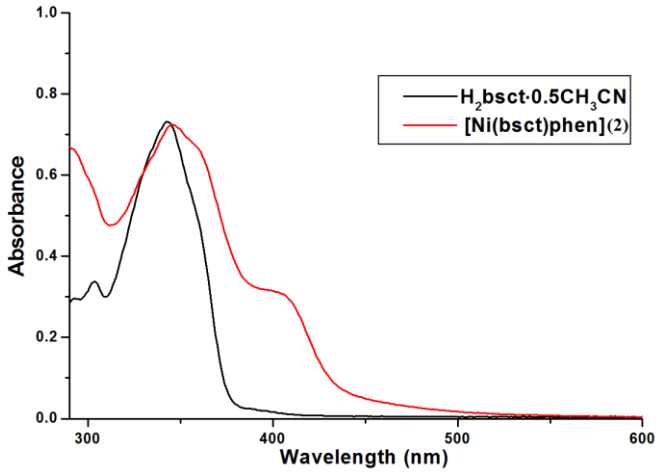

Fig. 2.17. Electronic spectra of H_2bsct·0.5CH_3CN and complex **2**.

Complexes **3** and **4** give almost similar electronic spectra but show shift from that of H_2bsct·0.5CH_3CN. The molar absorptivity of complex **4** is found to be greater than that of complex **3**, may be due different environment around the central metal ion. Complex **3** gives two absorption maxima at 323 and 379 nm with a shoulder at 312 nm (ε = 6.78×10^4, 7.60×10^4 and 6.43×10^4 $M^{-1}cm^{-1}$). For complex **4** two absorption maxima at 324 and 380 nm ($\varepsilon = 2.54 \times 10^4$ M^{-1} cm^{-1} and 2.75×10^4 M^{-1} cm^{-1}) were observed. These absorptions were assigned to intraligand transitions. Both complexes gave a shoulder at around 395 and 396 nm is attributed to LMCT transitions of type Cu←N and Cu←O [46]. Fig. 2.18 gives electronic spectra for H_2bsct·0.5CH_3CN, complexes **3** and **4**.

The d^9 Cu(II) complex is expected to show $^2E_g \leftarrow {}^2T_{2g}$ electronic transition in the visible region. Jahn-Teller distortion lead to splitting of these levels and resulted in transitions of the type $^2A_{1g} \leftarrow {}^2B_{1g}$, $^2A_{1g} \leftarrow {}^2B_{2g}$ and $^2E_g \leftarrow {}^2B_{2g}$ [47]. As these levels were close to each other only a broad band was obtained having absorption maxima at 574 nm and molar absorptivity 203 $M^{-1}cm^{-1}$.

In addition to this a shoulder with maximum absorption at 735 nm and absorptivity of 104 M^{-1} cm^{-1} was also observed for complex **3**. Similarly a broad band with maximum absorption at 569 nm and molar absorptivity 117 $M^{-1}cm^{-1}$ was observed for complex **4**. The visible spectra for both the Cu(II) complexes are depicted in Fig. 2.19.

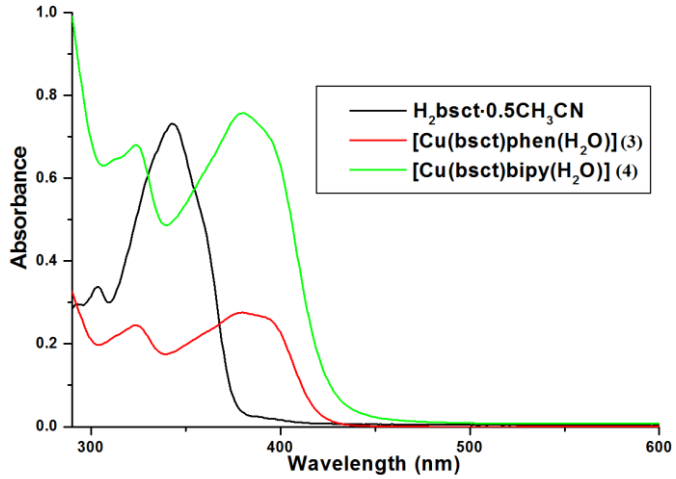

Fig. 2.18. Electronic spectra of H_2bsct·0.5CH_3CN, complexes **3** and **4**.

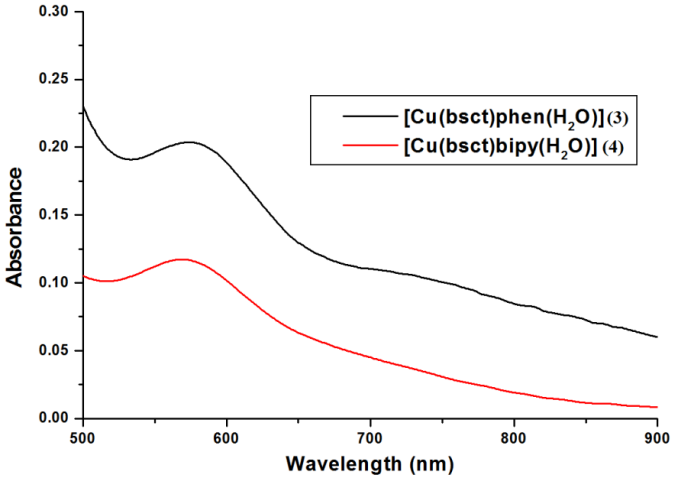

Fig. 2.19. Visible spectra of complexes **3** and **4.**

The electronic spectra of complexes **5** and **6** give two highly intense bands corresponding to intraligand transitons, which mask the LMCT transitions possible for complexes. These absorption are observed at λ_{max} of 301 and 342 nm for complex **5** with molar absorptivity 4.48×10^4 and 7.54×10^4 M^{-1} cm^{-1} respectively. Correspondingly the complex **6** also exhibit bands showing maximum absorption at 304 and 341 nm with molar absorptivity 5.74×10^4 and 8.77×10^4 M^{-1} cm^{-1}. The electronic spectra of H_2bsct·0.5CH_3CN, complexes **5** and **6** are illustrated in Fig. 2.20.

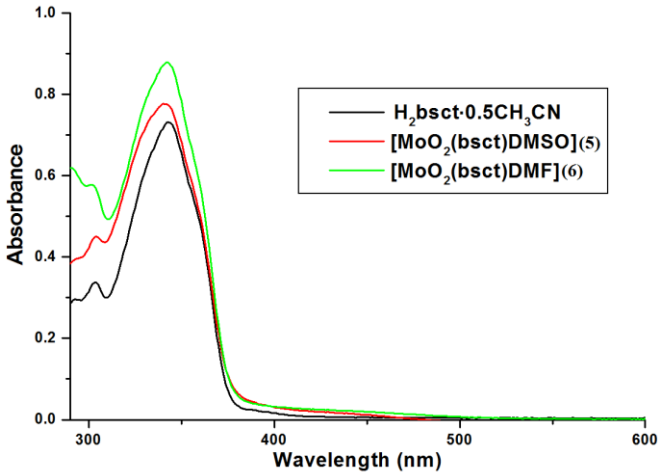

Fig. 2.20. Electronic spectra of H_2bsct·0.5CH_3CN, complexes **5** and **6**.

The palladium complex **7** gives two absorptions with maximum at 349 and 381 nm with molar absorptivity 6.38×10^4 and 7.28×10^4 M^{-1} cm^{-1} respectiely, assigned to intraligand transitions, accompanying a shoulder at 394 nm (ε=681 M^{-1} cm^{-1}), as a result of LMCT transitions [48]. The electronic spectra for H_2bsct·0.5CH_3CN and complex **7** are represented in Fig. 2.21.

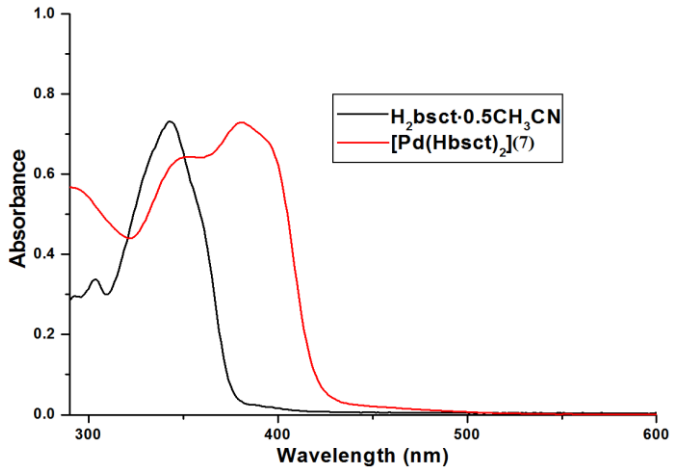

Fig. 2.21. Electronic spectra of H_2bsct and complex **7**.

The electronic spectrum of complex **8** give three absorption maxima at 307, 319 and 367 nm with molar absorptivity 2.96×10^4, 3.04×10^4 and 7.41×10^4 M^{-1} cm^{-1} respectively designated to intraligand transitions. The last broad band, with a shoulder, was due to MLCT transition. Fig. 2.22 represents the electronic spectra for H_2bsct·0.5CH_3CN and complex **8**.

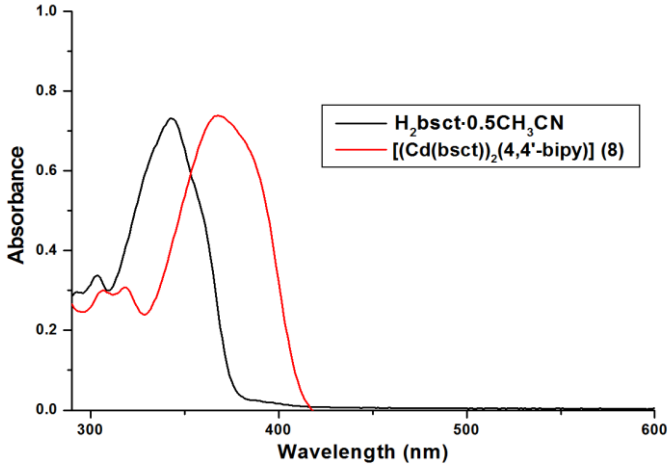

Fig. 2.22. Electronic spectra of H_2bsct·0.5CH_3CN and complex **8**.

2.3.2.4. ^{1}H NMR spectra

An NMR spectrum for a complex provides information regarding the coordination sites of the ligand that coordinate to a metal centre. The NMR spectrum of complexes **7** and **8** were recorded and compared with the NMR spectrum of $H_2bsct{\cdot}0.5CH_3CN$. NMR spectra of the complexes were recorded in DMSO-d_6 solution.

^{1}H NMR spectra of $H_2bsct{\cdot}0.5CH_3CN$ and complex **7** are illustrated in Fig. 2.23. There is a marked shift in the peaks for complex **7** as compared to $H_2bsct{\cdot}0.5CH_3CN$. The phenolic proton shows marked down field shift (δ=11.29 ppm) attributed to the extended electron delocalization generated as a result of complex formation. The absence of any proton corresponding to N(2)–H (δ=9.76 ppm) in the complex, which is present near to the phenolic proton in $H_2bsct{\cdot}0.5CH_3CN$ justifies the coordination of thiosemicarbazone as thio-iminolate form.

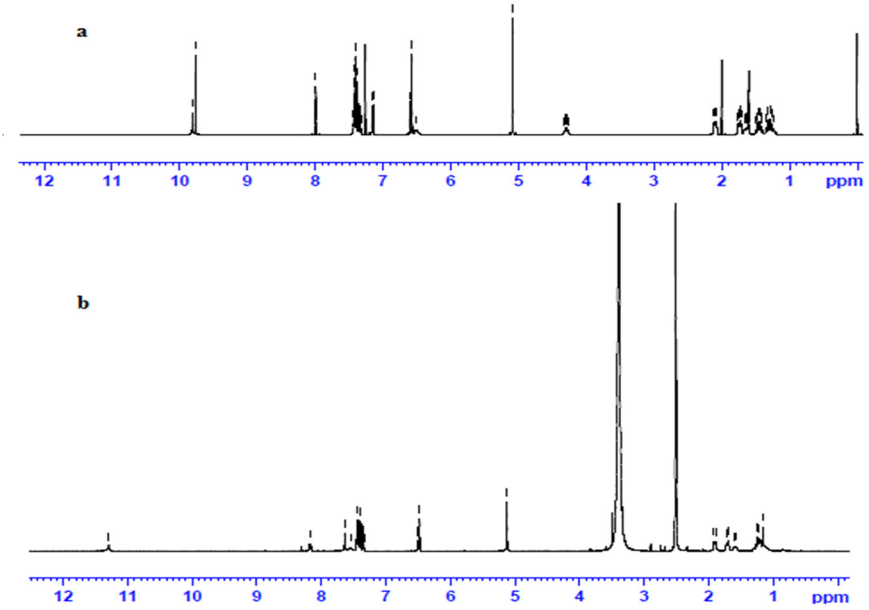

Fig. 2.23. ^{1}H NMR spectra of a) $H_2bsct{\cdot}0.5CH_3CN$ b) $[Pd(Hbsct)_2]$ (**7**) in DMSO-d_6 solution.

The ^{1}H NMR spectrum of complex **8** clearly indicate absence of phenolic proton and N(2)–H proton (δ=9.81 and δ=9.76 ppm). This justifies the coordination of H_2bsct·0.5CH_3CN in the doubly deprotonated form. The shift in the values for other protons also supports these observations. The ^{1}H NMR spectra for H_2bsct·0.5CH_3CN and complex **8** are presented in Fig. 2.24.

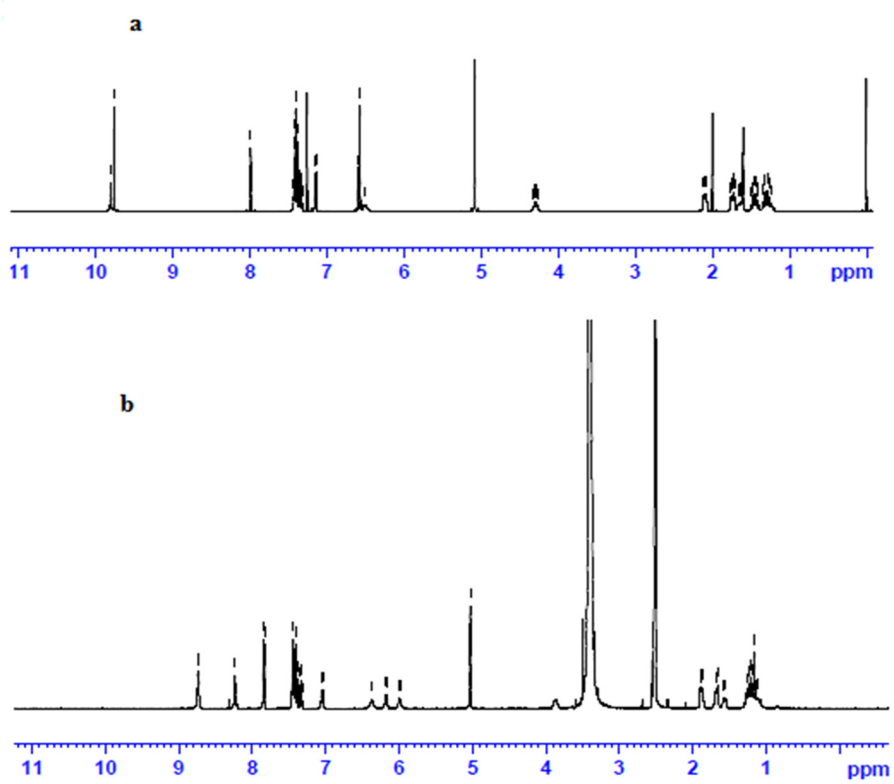

Fig. 2.24. ^{1}H NMR spectra of a)H_2bsct·0.5CH_3CN b) [(Cd(bsct))$_2$4,4′-bipy] (**8**) in DMSO-d_6 solution.

2.3.2.5. EPR spectra

Electron Paramagnetic Resonance spectroscopy is a powerful tool that helps to study the electronic structure of a paramagnetic metal ion, where by one could understand and establish the geometry and bonding

interactions in metal complexes. The condition to give EPR spectra is the presence of a paramagnetic metal with nuclear spin $I \neq 0$, such that the spectrum will split into hyperfine lines which is a characteristic of the metal. The spectra for the complexes were recorded in X band, using 100 kHz field modulation and 9.1 GHz microwave frequency. Generally a metal ion with one unpaired electron, like VO(II) and Cu(II) present in this chapter, with S=½ exist in a degenerate state in the absence of magnetic field. Whereas in the presence of magnetic field, this ground state degeneracy is lost and will split into two levels *viz* m_s= +½ and -½ (Fig. 2.25) [49,50]. The energy difference between these level is given by $\Delta E = g\beta B$, where g is the Lande splitting factor, g = 2.00233 for free electron, β is the electronic Bohr magneton and B is the magnetic field.

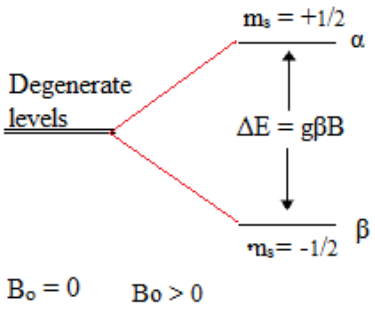

Fig. 2.25. Splitting of spin levels in presence of magnetic field.

Thus when electron under magnetic field absorbs suitable microwave frequency we get an absorption band corresponding to it. These bands depend not only on the spin of the electron but also on the nuclear spin of a particular metal ion, which lead to further splitting of these absorption bands and are characteristic of the metal ion.

2.3.2.5.1. EPR spectrum of $[VO(bsct)H_2O]_2$ (1)

In complex **1** vanadium exist in +4 oxidation state and has a d^1 electronic configuration. The g values of vanadium obtained from EPR

spectrum is usually less than free electron value of 2.00233. Vanadium has a nuclear spin I = 7/2 and when this nuclear spin interact with electronic spin the spectrum further splits into 2nI + 1 energy levels. As a result of this eight lines are expected for VO(II) ion. When the coordinating ^{14}N interact with nuclear spins this lines may further split to give hyperfine lines, which is not observed here as the single electron present on the metal resides in the sigma non-bonding orbital and is away from the thiosemicarbazone nullifying any chance of interaction.

The EPR spectrum for complex **1** was recorded in DMF solution at at 77 K. It gave axial spectrum comprising of two sets of eight lines are expected for VO(II) ion. The g values and hyperfine constants were calculated from the simulation of the spectrum using Easy Spin 4.0.0 package [51] and is presented in Fig. 2.26. The g values for the complex were found to be $g_{||}$ = 1.95 and $g_{\perp}$=1.98 and the hyperfine coupling constants obtained are A_{ll}=171×10^{-4} and $A_{\perp}$=64×10^{-4} cm^{-1}. The $g_{\perp} > g_{||}$ and $A_{ll} > A_{\perp}$ are characteristic of an axially compressed d^1_{xy} configuration [52]. The anisotropic parameters A_{av} and g_{av} were calculated using equations:

$$A_{av} = \tfrac{1}{3}(A_{ll} + 2A_{\perp}) \text{ and } g_{av} = \tfrac{1}{3}(g_{||} + 2\, g_{\perp})$$

For complex **1** the parameters are A_{av} = 99 10^{-4} cm^{-1} and g_{av} = 1.97.

The molecular orbital coefficients α^2 and β^2 for the complexes were calculated using the following equations:

$$\alpha^2 = \frac{(2.00277 - g_{\parallel})E_{d-d}}{8\lambda\beta^2}$$

$$\beta^2 = \frac{7}{6}\left[\left(\frac{-A_{\parallel}}{P}\right)+\left(\frac{A_{\perp}}{P}\right)+\left(g_{\parallel}-\frac{5}{14}g_{\perp}\right)-\frac{9}{14}g_e\right]$$

where, P=128×10^{-4} cm^{-1}, λ=135 cm^{-1} and $E_{d\text{-}d}$ is the electronic transition energy for the transition $^2E \leftarrow {}^2B_2$. The values obtained for complex **1** are α^2 = 0.792 and β^2 = 0.928. The lower value for α^2 than β^2 indicate in plane σ bonding is more covalent than in-plane π bonding [53]. As per Gangadharmath *et al.*, to get positive values for α^2 and β^2, the hyperfine constant values A_{ll} and $A_{\perp}$ were taken as negative [54].

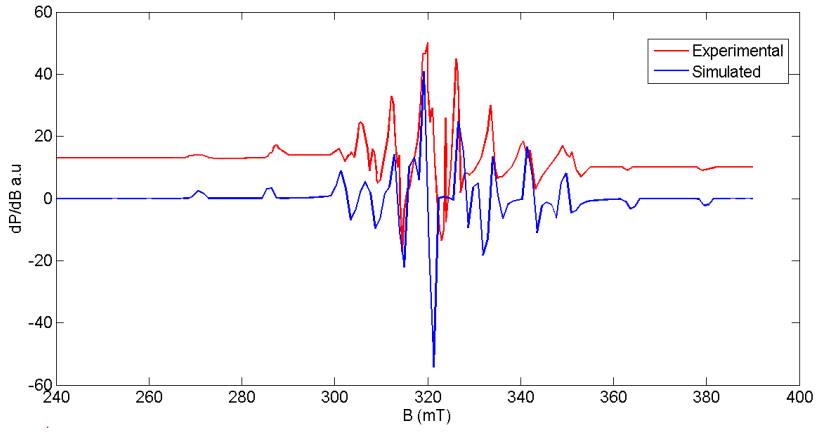

Fig. 2.26. EPR spectrum of [VO(bsct)H_2O]$_2$ (**1**).

2.3.2.5.2. EPR spectrum of [Cu(bsct)bipy(H_2O)] (4)

The EPR spectrum of the complex **4** was recorded in the polycrystalline state at 298 K and in DMF solution at 77 K. The complex [Cu(bsct)bipy(H_2O)] **(4)**, in the polycrystalline state as well as frozen state give axial spectra with two g values. The spin Hamiltonian for Cu(II) with B_{1g} ground state is given by [55,56]

$$\hat{H} = \beta[g_{\parallel}B_zS_z + g_{\perp}(B_xS_x + B_yS_y)] + A_{\parallel}I_zS_z + A_{\perp}(I_xS_x + I_yS_y)$$

The EPR spectrum for Cu(II) is important as this species can show a large number of coordination geometries like elongated octahedron, square pyramidal or square planar. The correct geometry is determined on the

basis of the ground state of the ion. It is reported that the ground state is found to be $d_{x^2-y^2}$ for an elongated octahedron, square pyramidal or square planar geometry. The value of *g* tensor gives an idea about the ground state of the electron in the metal ion [57].

The g_{iso} for the complex **4** in the polycrystalline was calculated from the simulated spectrum of the complex using Easy Spin 4.0.0 package. Best fitted experimental (red) and simulated (blue) spectra is given in Fig. 2.27. The *g* parameters for the complex were given as $g_{\perp}$ = 2.06 and $g_{\parallel}$ = 2.19 and g_{av} = 2.10. The geometric parameter in the polycrystalline state G is calculated using equation

$$G = (g_{\parallel} - 2.0023)/(g_{\perp} - 2.0023)$$

It is found that if $G > 4.4$, there is negligible exchange interaction between metal centre and ligand and if $G < 4.4$, considerable exchange interaction is present in the solid state [58]. The value of *G* for complex **4** is found to be 3.25.

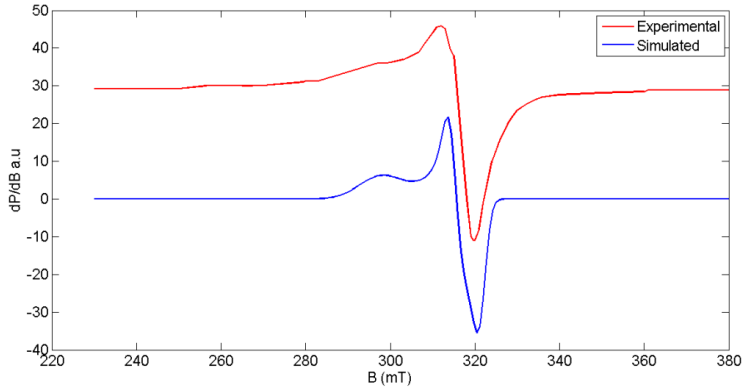

Fig. 2.27. EPR spectrum of complex **1** in polycrystalline state at 298 K.

The odd electron in the Cu(II) ion couples with the nuclear spin, $I \neq 0$, results in hyperfine interaction leads to further splitting of the energy levels $\Delta E = g\beta B_0 + SAI$, where S is the total spin quantum number, A is the hyperfine coupling constant and I is the nuclear spin quantum number [50]. The number of hyperfine lines obtained is calculated using the equation $(2nI+1)$. In the case of a complex with Cu(II) ion, $I = {}^3/_2$, four hyperfine lines are expected. In DMF solution at 77 K, complex **4** gave an axial spectrum with four hyperfine lines having g tensors $g_\perp = 2.05$ and $g_\parallel = 2.19$ and hyperfine coupling constants $A_\parallel = 172 \times 10^{-4}$ cm^{-1}. Fig. 2.28 elucidates the EPR spectrum of the complex **4** in DMF solution at 77 K.

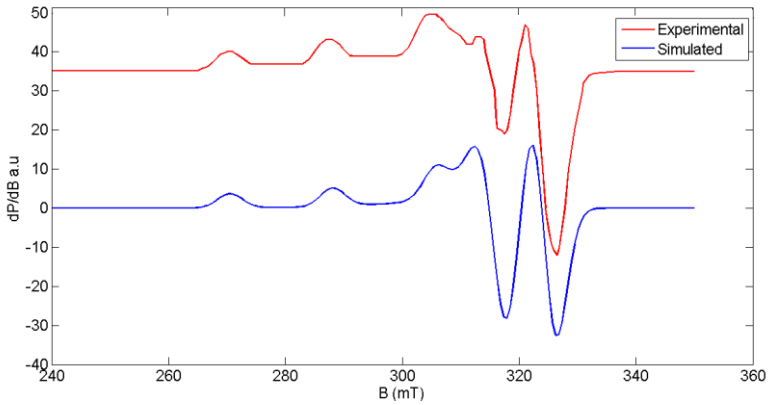

Fig. 2.28. EPR spectrum of complex **4** in DMF at 77 K.

The observations of G and $g_\parallel > g_\perp > 2.0023$, consistent with $d_{x^2-y^2}$ ground state for a square planar complex. The g_{av} calculated using equation $g_{av} = \frac{1}{3}(g_\parallel + 2g_\perp)$, is found to be $g_{av} = 2.09$. When $g_\parallel < 2.3$, there is a significant covalent character to the M–L bond and if $g_\parallel > 2.3$

indicate ionic character [56]. In the present case $g_{\|} < 2.3$ and hence Cu–L bond is having a significant covalent character.

Other bonding parameters like α^2 (covalence of the in-plane σ-bonds), β^2 (covalence of in-plane π-bonds) and γ^2 (covalence of out-of-plane π-bonds) can be calculated from the values of $g_{\|}$, $g_{\perp}$, $A_{\|}$ and energy of *d-d* transition. The value of α^2 gives the fraction of σ-bonding by Cu(II) ion. This can be calculated from the equation,

$$\alpha^2 = -A_{\|}/0.036 + (g_{\|}-2.00233) + 3/7(g_{\perp}-2.00233) + 0.04$$

If the value of α^2 is unity, the M–L bond is purely ionic and it is purely covalent if $\alpha^2 = 0.5$ [58,59]. The two later parameters can be calculated from expression,

$$K_{\|} = \alpha^2\beta^2 \text{ and } K_{\perp} = \alpha^2\gamma^2$$

$$\text{Where } K_{\|}^2 = (g_{\|}-2.00233)E_{d\text{-}d}/8\lambda_o$$

$$K_{\perp}^2 = (g_{\perp}-2.00233)\, E_{d\text{-}d}/2\lambda_o$$

Here $K_{\|}$ and $K_{\perp}$ are orbital reduction factors and λ_o the one electron spin coupling constant, which is equal to 828 cm^{-1} [57, 38]. For pure σ bonding $K_{\|} \approx K_{\perp} \approx 0.77$, for in plane π-bonding $K_{\|} < K_{\perp}$ and for out-of-plane π-bonding, $K_{\perp} < K_{\|}$.

For compound **4** these parameters were found to be $\alpha^2 = 0.79$, $\beta^2 = 0.88$, $\gamma^2 = 0.90$, $K_{\|} = 0.70$ and $K_{\perp} = 0.71$ suggests that the complex is having a significant σ bonding accompanied by an in plane π-bonding.

2.3.2.6. TG-DTA analysis

The thermal stability of a compound can be established using TG-DTA analysis. The presence of solvent molecules (in the lattice/coordinated) can be easly predicted by this method. The TG-DTA analysis of complexes **1**, **3**, **4** and **8** were done in a temperature range of 50-700 °C in nitrogen atmosphere.

In complex **1** the weight loss of (found (calc.)) 3.2 (3.7)% at 217 °C, is assigned to loss of two coordinated water molecules from the complex.

In the complex **3** two weight losses were observed, one at 233 °C with a weight loss of found(calcd.) 2.7 (2.9)% was designated to removal of a coordinated water molecule. The second at 256 °C with a weight loss of (found (calc.)) 44.4 (43.5)%, corresponds to removal of a molecule of 1,10-phenanthroline and a molecule of toluene.

A weight loss 2.7% equal to calculate weight loss of 2.9% at a temperature 176 °C corresponds to loss of a molecule of coordinated water in complex **4**. The weight loss at 202 °C (found 24.2%, calcd. 25.8%) corresponds to loss of 2,2′-bipyridine.

The complex **8** shows a single weight loss at 254 °C as a consequence of loss of 4,4′-bipyridine and a Cd(bsct) unit with a weight loss of 41.4% having a calculate weight loss of 42.6%. All the complexes show a weight loss after this and the decomposition is not complete even after 700 °C. The thermograms of the complexes 1, 3, 4 and 8 with differential thermal analysis are depicted in Fig. 2.29.

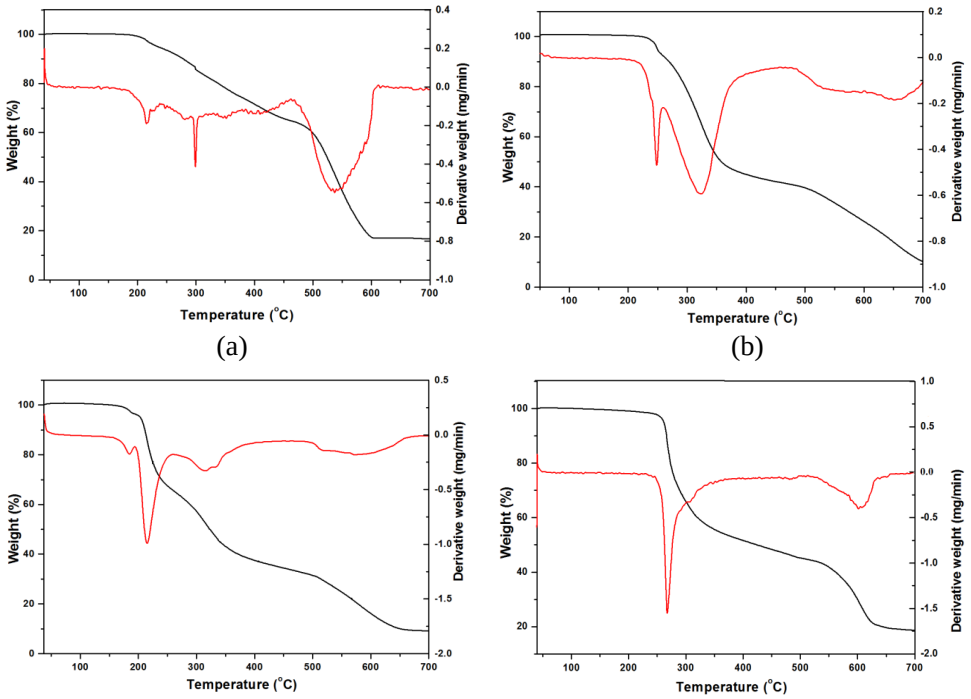

Fig. 2.29. Thermograms of a) $[VO(bsct)H_2O]_2$ (**1**), b) $[Cu(bsct)phen(H_2O)]$ (**3**), c) $[Cu(bsct)bipy(H_2O)]$ (**4**) d) $[(Cd(bsct))_2$4,4′-bipy] (**8**).

2.3.2.7. Single crystal X-ray diffraction studies

2.3.2.7.1. Single crystal X-ray diffraction studies of $[MoO_2(bsct)DMSO]$ (5)

The single crystals of $[MoO_2(bsct)DMSO]$ (**5**) were grown by slow evaporation from dimethyl sulfoxide solution. A dark orange block shaped crystals of complex **5** with size 0.22 × 0.12 × 0.08 mm^3 was mounded on a Rigaku Oxford Diffraction diffractometer on a nylon loop as illustrated in Fig. 2.30.

Fig. 2.30. Nylon looped single crystal of $[MoO_2(bsct)DMSO]$ (**5**).

All non-hydrogen atoms of the complex were refined anisotropically. The hydrogen atoms attached to C atoms were refined with riding coordinates and placed in calculated positions with the help of difference map, with bond distances of 0.95-0.99 Å. The hydrogen attached to N was located from difference map and the bond distance was constrained to 0.88 Å. Whereas the idealised methyl groups are refined as rotating groups, with $U_{iso}=1.2U_{eq}$ for all hydrogens except methyl group, for which the $U_{iso}=1.5U_{eq}$. The crystallographic data and refinement parameters are represented in Table 2.7.

Table 2.7. Crystal data and refinement parameters for $[MoO_2(bsct)DMSO]$ (**5**)

Parameters	**$[MoO_2(bsct)DMSO]$ (5)**
Empirical formula	$C_{23}H_{29}MoN_3O_5S_2$
Formula weight	587.55
Color	Orange
Temperature/K	173.2 (2)
Crystal system	Orthorhombic
Space group	*P*bca
Cell parameters	
a (Å)	12.074(12)
b (Å)	16.47301(19)
c (Å)	25.4339(3)
$\alpha = \beta = \gamma$(°)	90
Volume ($Å^3$)	5059.03(9)
Z	8
Calculated density, ρ (g cm^{-3})	1.543
F(000)	2416
Crystal size (mm^3)	0.22 x 0.12 x 0.08
θ range for data collection (°)	2.31 to 71.44
Limiting indices	$-9 \le h \le 14$, $-20 \le k \le 20$, $-31 \le l \le 29$
Reflections collected	36675
Independent reflections	4896 [R_{int} = 0.0467, R_{sigma} = 0.0223]
Data/restraints/parameters	4896/0/309
Goodness-of-fit on F^2	1.059
Final R indexes [I > 2σ (I)]	R_1 = 0.0313, wR_2 = 0.0787
Final R indexes [all data]	R_1 = 0.0349, wR_2 = 0.0821
Largest diff. peak and hole (e $Å^{-3}$)	0.78/-0.38

$R_1 = \Sigma||F_o| - |F_c|| / \Sigma|F_o|$

$wR_2 = [\Sigma w(F_o^2-F_c^2)^2 / \Sigma w(F_o^2)^2]^{1/2}$

The complex **5** crystallizes into orthorhombic *P*bca space group. The asymmetric unit of the complex consists of a single molecule. The H_2bsct undergoes double deprotonation and coordinates to MoO_2(II) moiety as an ONS donor tridentate ligand giving a distorted octahedral geometry around Mo(VI). Of six coordination sites of Mo(VI) two were occupied by O(3) and O(4) of MoO_2 moiety. The other four sites were filled by N(1), S(1) and O(1) of the H_2bsct and O(2) of DMSO. The ORTEP diagram of the complex **5** with numbering scheme is presented in Fig. 2.31.

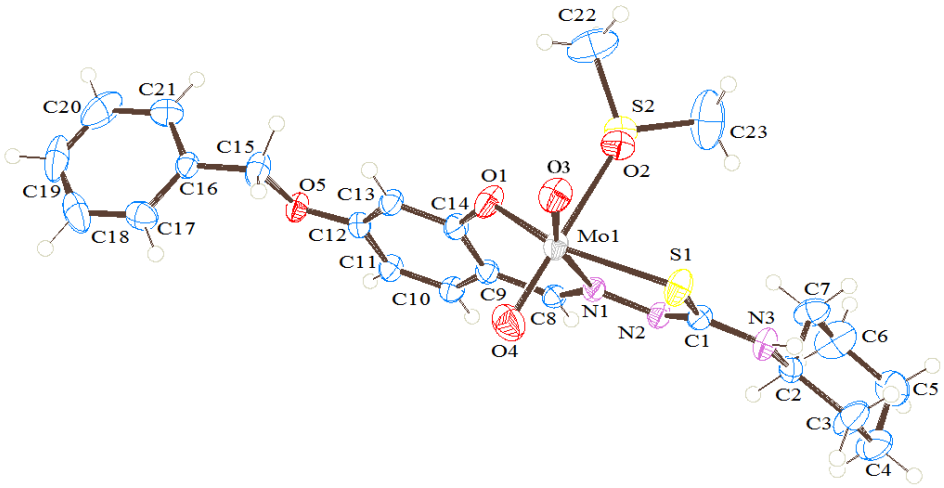

Fig. 2.31. ORTEP diagram of [MoO_2(bsct)DMSO] (**5**) with 50% ellipsoid probability.

The Mo(1)–O(2) bond length, equal to 2.364(17) Å, indicates that the DMSO molecule is weakly coordinated to metal centre [38]. It is found that Mo(1)–S(1) bond length is also longer (2.411(6) Å) than expected due to the *trans* effect from the oxo group [59]. The phenolic C–O bond length C(14)–O(1) in the complex **5** is found to be equal to 1.331(3) Å which is less than the C(10)–O(2) bond length 1.355(2) Å of H_2bsct·0.5CH_3CN, evidently due to extended conjugation of C–O bond during coordination to Mo(VI) ion. The longer C(1)–S(1) bond length (1.756(2) Å) of the complex

5, than that of H_2bsct·0.5CH_3CN (C(15)–S(1) (1.683(17) Å)) convince the transformation of C=S to C–S. The C(1)–N(2) bond length 1.31(3) Å of the complex **5** is lower than that of the ligand H_2bsct·0.5CH_3CN (C(15)–N(2) (1.35(2) Å)), indicate the generation of C=N from C–N. These observations confirm the coordination of H_2bsct to the metal in the thio-iminolate form.

The bond angles O(2)–Mo(1)–O(4), O(1)–Mo(1)–S(1) and O(3)–Mo(1)–N(1), 171.5(8), 150.6(6) and 159.7(8)° respectively revel that the complex **5** is deviating from perfect octahedral geometry. The MoO_2(II) unit adopt a *cis* arrangement in the complex. The complex formation changes the configuration of H_2bsct·0.5CH_3CN from *E* to *Z* about N(2)–C(1) bonds evident from the N(1)–N(2)–C(1)–S(1) torsion angles of 1.7(3)°, which enables the coordination of the thiosemicarbazone to the metal centre *via* N(1) and S(1). The coordination of H_2bsct·0.5CH_3CN to *cis*-MoO_2(II) creates two chelate rings, a five membered ring involving atoms S(1), C(1), N(2), N(1), Mo(1) and a six membered ring involving atoms O(1), C(14), C(9), C(8), N(1), Mo(1) and are twisted from each other by a dihedral angle 11.32(7)°. The phenyl ring (C(9)–C(10)–C(11)–C(12)–C(13)–C(14)) adjacent to the chelate ring O(1)–C(14)–C(9)–C(8)–N(1)–Mo(1) is found to be twisted from each other by a dihedral angle 12.56(7)°. The ring puckering analysis and least square plane calculations show that the cyclohexyl ring C(2)–C(3)–C(4)–C(5)–C(6)–C(7) is puckered with a puckering amplitude Q_T = 0.58(3) Å, which suggest that the ring adopt a chair conformation in the complex [60,61]. The bond lengths, bond angles and torsion angles for complex **5** are given in Table 2.8.

Table 2.8. Selected bond lengths (Å), bond angles (°) and torsion angles (°) for complex **5**

Bond length (Å)		**Bond angle (°)**	
Mo(1)–O(1)	1.945(17)	O(1)–Mo(1)–N(1)	80.74(7)
Mo(1)–O(2)	2.364(17)	O(3)–Mo(1)–O(4)	105.59(9)
Mo(1)–O(3)	1.711(17)	O(2)–Mo(1)–N(1)	81.14(6)
Mo(1)–O(4)	1.692(2)	O(4)–Mo(1)–N(1)	91.38(8)
Mo(1)–N(1)	2.287(6)	O(4)–Mo(1)–S(1)	100.12(7)
Mo(1)–S(1)	2.411(6)	O(1)–Mo(1)–O(3)	107.08(8)
C(8)–N(1)	1.295(3)	O(2)–Mo(1)–O(3)	82.55(7)
N(1)–N(2)	1.393(3)	O(4)–Mo(1)–O(1)	97.97(10)
N(2)–C(1)	1.306(3)	O(1)–Mo(1)–O(2)	76.96(17)
C(1)–S(1)	1.756(2)	O(2)–Mo(1)–O(4)	171.51(8)
C(14)–O(1)	1.331(3)	O(1)–Mo(1)–S(1)	150.66(6)
S(2)–O(2)	1.525(17)	O(3)–Mo(1)–N(1)	159.77(8)

The packing of molecules in complex **5** enabled *via* various intermolecular interactions as given in Table 2.9. The N(3)–H(3) form a bifurcated hydrogen bonding to O(2) and O(3) of the next molecule with a D···A distance of 3.094(3) and 3.189(3) Å respectively. The O(3) further strengthen the interaction with the aid of another hydrogen bonding C(15)–H(15A)···O(3) with D···A distance 3.290(3) Å. These hydrogen bonding interactions lead to form a one dimensional polymer in the '*a*' axis. The Fig. 2.32 illustrates the various hydrogen bonding interactions present in the complex **5**.

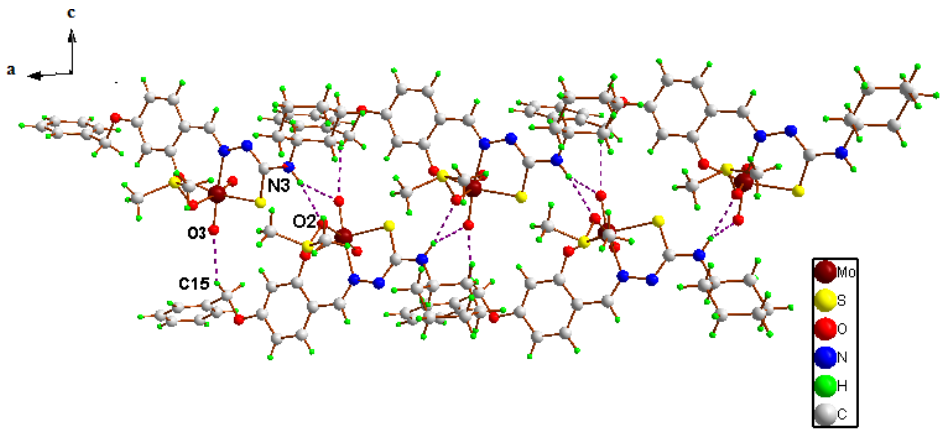

Fig. 2.32. Hydrogen bonding interactions present in complex **5**.

The packing of molecules in the unit cell are effective using C–H···π interactions of the type C(23)–H(23B) ···Cg(5) with C ···Cg distance 3.61(5) Å. The C–H···π interaction in complex **5** is represented in Fig. 2.33.

Table 2.9. Interaction parameters for complex **5**

Hydrogen bonding interactions				
D–H···A	D–H (Å)	H···A (Å)	D···A (Å)	D–H···A (°)
N(3)–H(3)···O(2)[a]	0.88	2.25	3.094(3)	160.0
N(3)–H(3)···O(3)[a]	0.88	2.54	3.189(3)	130.8
C(15)–H(15A)···O(3)[b]	0.99	2.52	3.290(3)	134.8
C–H···π interactions				
C–H···Cg	C–H (Å)	H···Cg (Å)	C···Cg (Å)	C–H···Cg (°)
C(23)–H(23B)···Cg(5)[c]	0.99	2.91	3.61(5)	130

A = -½ + x, y, ³⁄₂ +z; b= -½ + x, y, ³⁄₂ -z;

Cg(5)= C(16), C(17), C(18), C(19), C(20), C(21); D= donor, A= acceptor, Cg= centroid

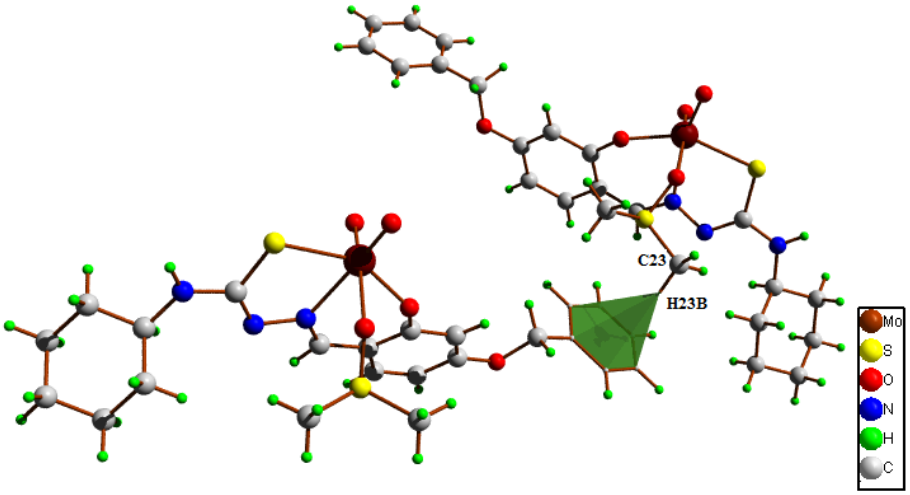

Fig. 2.33. C–H···π interaction in [MoO_2(bsct)DMSO] (**5**).

The packing of the complex **5** in the crystal lattice viewed along '*c*' axis is represented in the Fig. 2.34. The crystal packing extends the molecules through '*a*' axis giving rise to a 1D polymer.

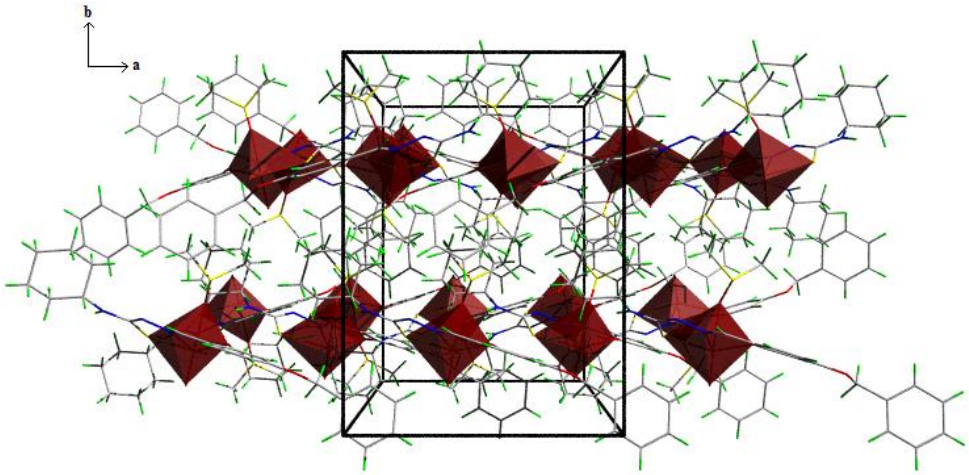

Fig. 2.34. Packing diagram of complex **5** exhibiting coordination polyhedra.

2.3.2.7.2. Single crystal X-ray diffraction studies of [MoO_2(bsct)DMF] (6)

Dark orange coloured block shaped crystals of complex **6** with 0.35×0.30×0.25 mm^3 was mounted on a Bruker SMART APEXII CCD diffractometer, equipped with monochromatic Mo Kα (λ = 0.71073 Å) radiation. Anisotropic refinement was used for refining all non-hydrogen atoms. With the help of difference map all hydrogen atoms were placed in calculated positions with C–H distances 0.93-0.99 Å. U_{iso} for the hydrogen atoms were assigned as U_{iso}=1.2U_{ij}, except methyl, for which U_{iso}=1.5U_{ij}. The cyclohexyl ring, with atoms C(16), C(17), C(18), C(19), C(20), C(21) was disorded. The two units of the disordered components have occupancy of 60 and 40% respectively. The equivalent atoms were generated using symmetry command SYMM with symmetry, -X, ½+Y, -Z. By assuming that the atoms connected to one another will have similar movement in similar direction with almost same amplitudes, the SIMU command was used to restrain these atoms with same U_{ij} components. The distance between N(13)–C(16) made same to N(13)–C(16A) using relative distance restrain command SADI [62]. The refinement methods and parameters are described in Table 2.10.

The complex **6** crystallize into monoclinic $P2_1$ space group. The Mo(VI) ion generates a distorted octahedral geometry around it with the coordination sited were enveloped by the tridentate ONS donor H_2bsct, two oxo groups and oxygen form DMF molecule. The distorted fashion of the octahedral geometry is evident from the O(3)–Mo(1)–O(5), O(2)–Mo(1)–S(1) and O(4)–Mo(1)–N(1) bond angles, 169.3(2), 151.4(14) and 162.3(19)° respectively. It is expected that the solvent DMF might be loosely bound to the metal centre. The M–L bond lengths for Mo(1)–O(5), to that of the ligand is found to be 2.28(4) Å. Whereas the Mo(1)–S(1) involving the thiosemicarbazone moiety and the metal is found to be 2.41(14) Å. This difference in bond lengths than that expected is due to the strong *trans* effect from O(2) [60]. The ORTEP diagram of the complex **6** with 50%

probability is presented in Fig. 2.35 (The disordered component of the cyclohexyl ring is represented and hydrogen atoms are omitted for clarity).

Table 2.10. Crystal diffraction parameters and crystal data for $[MoO_2(bsct)DMF]$ (**6)**

Parameters	**$[MoO_2(bsct)DMF]$ (6)**
Empirical formula	$C_{23}H_{29}MoN_3O_5S_2$
Formula weight	580.50
Color	Orange
Temperature/K	296(2)
Crystal system	Monoclinic
Space group	$P2_1$
Cell parameters	
a (Å)	9.5412(6)
b (Å)	12.1918(8)
c (Å)	11.7420(9)
$\alpha = \gamma$(°)	90
β(°)	109.103(3)
Volume (Å^3)	1290.66(16)
Z	2
Calculated density, ρ (g cm^{-3})	1.543
F(000)	596
Crystal size (mm^3)	0.35 x 0.30 x 0.25
θ range for data collection (°)	2.40 to 28.28
Limiting indices	$-12 \leq h \leq 10$, $-15 \leq k \leq 16$, $-9 \leq l \leq 15$
Reflections collected	10173
Independent reflections	10173 [$R_{int} = 0.0212$]
Data/restraints/parameters	5659/188/372
Goodness-of-fit on F^2	1.010
Final R indexes [$I > 2\sigma(I)$]	$R_1 = 0.0406$, $wR_2 = 0.1095$
Final R indexes [all data]	$R_1 = 0.0446$, $wR_2 = 0.1140$
Absolute structure parameter	-0.024(17)
Extinction coefficient	0.0079(19)
Largest diff. peak and hole (e Å^{-3})	1.82/-0.481

$R_1 = \Sigma||F_o| - |F_c|| / \Sigma|F_o|$
$wR_2 = [\Sigma w(F_o^2-F_c^2)^2 / \Sigma w(F_o^2)^2]^{1/2}$

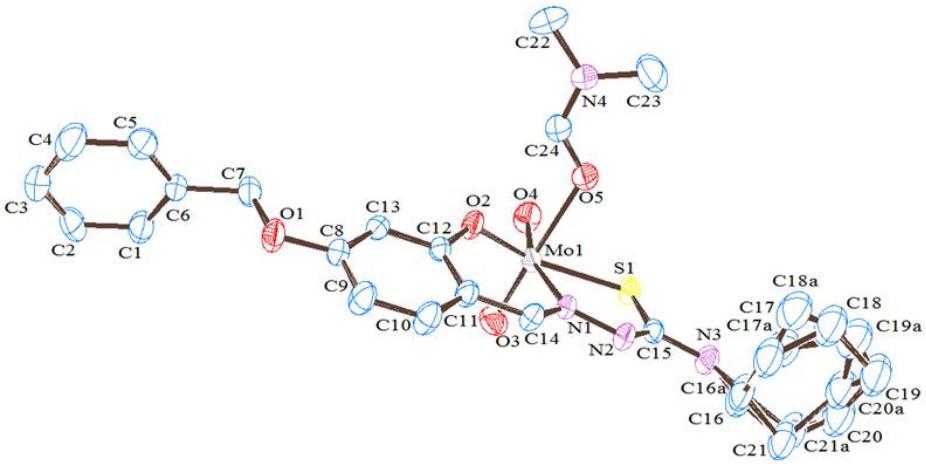

Fig. 2.35. ORTEP diagram of complex [MoO_2(bsct)DMSO] (**6**) with 50% ellipsoid probability.

It is found that the C(12)–O(2) bond length 1.332(6) Å in complex **6** is lower than C(10)–O(2) bond length of 1.355(2) Å in H_2bsct·CH_3CN. The C(14)–N(1) bond length (1.271(2) Å) is slightly less than that of H_2bsct·CH_3CN (1.281(2) Å). The coordination of H_2bsct as thio-iminolate form is evident from the change of C(15)–S(1) bond length from 1.683(17) Å to 1.748(6) Å upon complexation [37]. Further the C(15)–N(2) and N(1)–N(2) bonds show a shift form 1.346(2) and 1.379(19) to 1.303(7) and 1.390(6) Å respectively, is an evidence for the conversion of C–N single bond to C=N. The N(1)–N(2)–C(15)–S(1) torsion angle 3.6(7)° confirms the *Z* conformation of S(1) with respect to N(1) which was otherwise *trans* in H_2bsct·CH_3CN.

The coordination of H_2bsct to Mo(VI) leads to form two rings on a six membered and other is a five membered ring constituting atoms Mo(1)–O(2)–C(12)–C(11)–C(14)–N(1) and Mo(1)–S(1)–C(15)–N(2)–N(1) and these rings are twisted slightly from one another by a dihedral angle of 7.89(19)°. The benzene rings C(1)–C(2)–C(3)–C(4)–C(5)–C(6) and C(8)–C(9)–C(10)–C(11)–C(12)–C(13) are twisted from one another by a

dihedral angle of 83.7(3)°. The rings Mo(1)–O(2)–C(12)–C(11)–C(14)–N(1) and C(8)–C(9)–C(10)–C(11)–C(12)–C(13) adjacent to each other are twisted away from each other with a dihedral angle of 13(3)°. These deviations are the reason for loss of perfect octahedral geometry for the complex. The least square plane calculations and puckering analysis show that the ring C(16)–C(17)–C(18)–C(19)–C(20)–C(21) and the disordered component are puckered with amplitude Q_T= 0.44(2) and 0.55(2) Å respectively. This results indicate that the cyclohexyl ring exist in chair conformation [63]. Important bond parameters for complex **6** are given in Table 2.11.

Table 2.11. Selected bond lengths (Å), bond angles (°) and torsion angles (°) for complex **6**

Bond length (Å)		**Bond angle (°)**	
Mo(1)–O(2)	1.934(4)	O(2)–Mo(1)–O(3)	97.3(2)
Mo(1)–O(3)	1.678(4)	O(2)–Mo(1)–O(4)	104.8(2)
Mo(1)–O(4)	1.701(4)	O(2)–Mo(1)–O(5)	76.9(2)
Mo(1)–N(1)	2.284(6)	O(2)–Mo(1)–N(1)	82.1(2)
Mo(1)–S(1)	2.406(4)	O(4)–Mo(1)–O(5)	84.8(2)
C(14)–N(1)	1.271(7)	O(3)–Mo(1)–O(4)	105.2(1)
N(1)–N(2)	1.390(6)	O(4)–Mo(1)–N(1)	162.4(2)
C(15)–S(1)	1.748(6)	O(3)–Mo(1)–S(1)	100.4(2)
C(12)–O(2)	1.332(6)	O(5)–Mo(1)–O(3)	169.3(2)
C(24)–O(5)	1.242(7)	O(5)–Mo(1)–S(1)	81.8(2)
		S(1)–Mo(1)–O(2)	151.4(11)
		S(1)–Mo(1)–N(1)	75.9(11)

Intermolecular interactions always give additional strength to molecules to be held in the crystal lattice. The complex **6** exhibits two intermolecular interactions *viz* C(24)–H(24)···S(1) and C(1)–H(1)···O(3) with D···A distance of 3.833(7) and 3.261(9) Å respectively. The crystal packing is more effective through two different types of C–H···π interactions with C···Cg distance of 3.757(17) and 3.838(12) Å respectively. Figs. 2.36 and

2.37 gives the hydrogen bonding and C–H···π interactions in complex **6**. As a result of various intermolecular interactions the crystal lattice of complex **6** shows a linear polymeric chain extended along *b* axis (hydrogen atoms from the disordered molecule is omitted to simplify the structure). Table 2.12 contain all types of interactions present in complex **6.**

Table 2.12. Interaction parameters for complex **6**

Hydrogen bonding interactions				
D–H···A	D–H (Å)	H···A (Å)	D···A (Å)	D–H···A (°)
C(24)–H(24)···S(1)[a]	0.93	2.97	3.83(7)	155.6
C(1)–H(1)···O(3)[b]	0.93	2.52	3.27(9)	138
C–H···π interactions				
C–H···Cg	C–H (Å)	H···Cg (Å)	C···Cg (Å)	C–H···Cg(°)
C(23)–H(23A) ··Cg(4)[c]	0.96	2.90	3.828(12	164
C(18)–H(18B)···Cg(3)[d]	0.97	2.83	3.757(17)	159

a=--x, y-½, −z; b= 1-x, -½+y, -z; c=-1+x, 1+y, z; d=-1+x, y, z

Cg(4)= C(8), C(9), C(10), C(11), C(12), C(13); Cg(3)= C(1), C(2), C(3), C(4), C(5), C(6); D= donor, A= acceptor, Cg= centroid

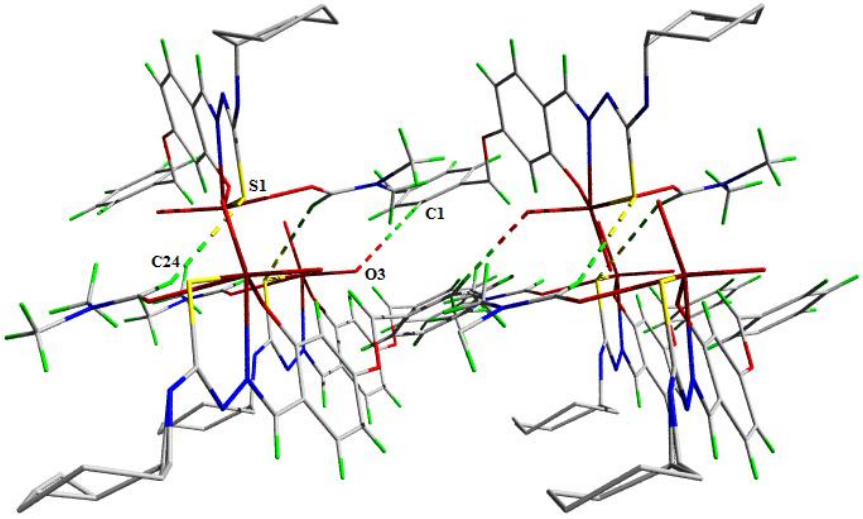

Fig. 2.36. Hydrogen bonding interaction in complex **6**.

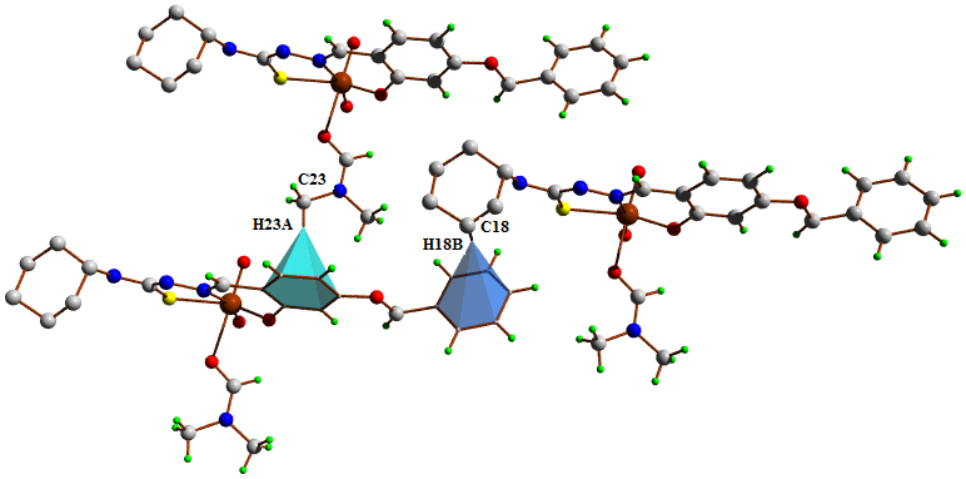

Fig. 2.37. C–H···π interactions in complex **6**.

The molecules in the crystal lattice adopt a zig-zag arrangement with the aid of various intermolecular interactions as given in Fig. 2.38. The crystal packing diagram involving the coordination polyhedra when viewed along '*b*' axis is represented in Fig.2.39.

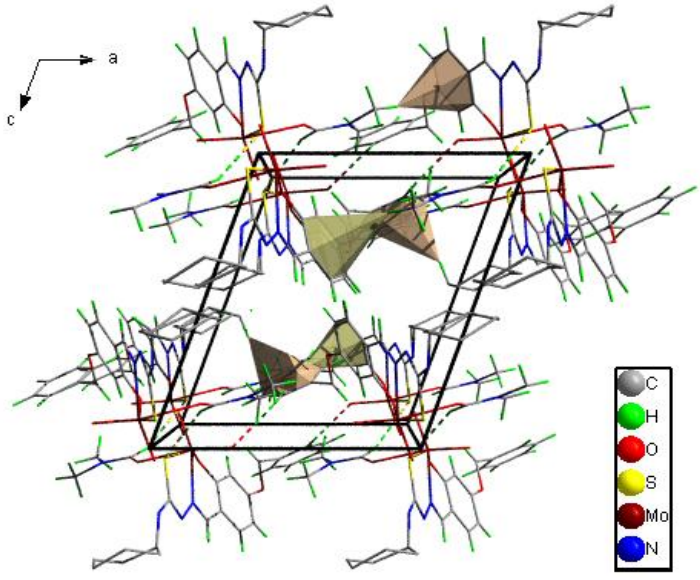

Fig. 2.38. The zig-zag arrangement in molecules of complex **6**.

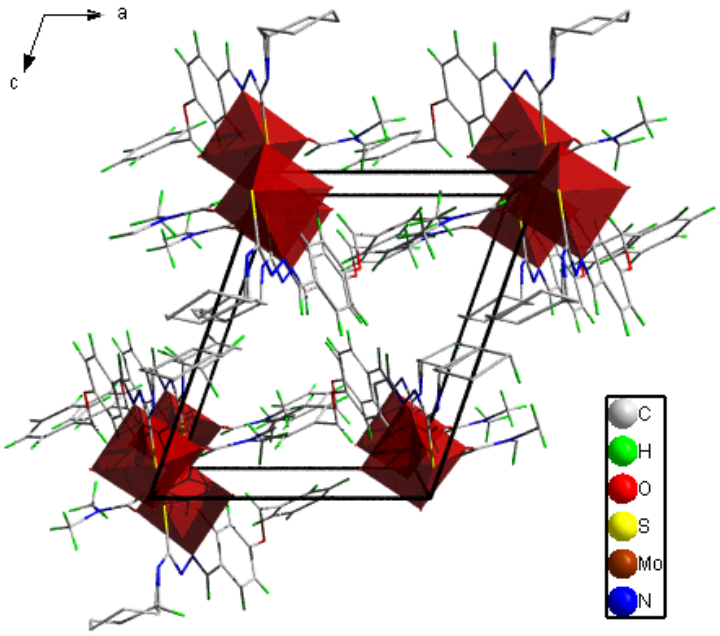

Fig. 2.39. Packing diagram of complex **6** viewed along '*b*' axis with coordination polyhedra.

2.4 Conclusion

The thiosemicarbazone H_2bsct·0.5CH_3CN was proved to be a good ONS donor ligand. We could synthesis eight complexes of using H_2bsct·0.5CH_3CN six different metals. In all the complexes the thiosemicarbazone was acting as an dianionic ONS donor ligand except in complex 7. In [Pd(Hbsct)$_2$] (7), H_2bsct·0.5CH_3CN coordinate as a monoprotonated molecule. Of eight complexes complex **1** (*via* oxygen atom within the molecule) and complex **8** (*via* the heterocyclic base 4,4′-bipyridine) are dimers. The Most of the complexes were octahedral except [Ni(bsct)phen] (**2**) and [(Cd(bsct)$_2$)$_2$(4,4′-bipy)] (**8**). Various spectroscopic methods were used to verify the structures of complexes are in agreement with the tentative structures as described in Fig. 2.40. The single crystal X-ray diffraction studies of complexes **5** and **6** give an insight into the conformation of the tentative structures, as in both

the complexes H_2bsct seems to change its configuration in order to facilitate complex formation. TG-DTA analysis of some complexes were performed upto a temperature of 700 °C, from this it was observed that the complexes were thermally stable.

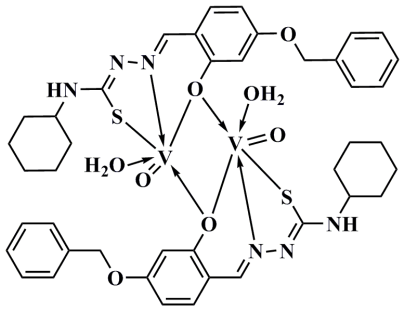

[VO(bsct)H_2O]$_2$ (1)

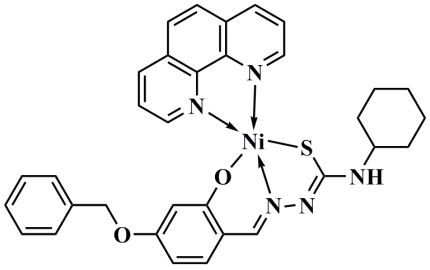

[Ni(bsct)phen] (2)

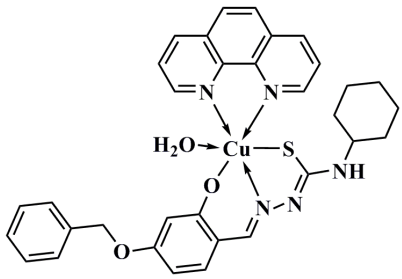

[Cu(bsct)phen(H_2O)] (3)

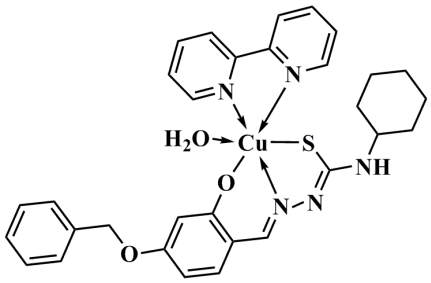

[Cu(bsct)bipy(H_2O)] (4)

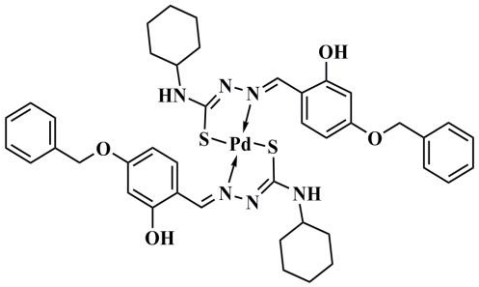

[Pd(Hbsct)$_2$] (7)

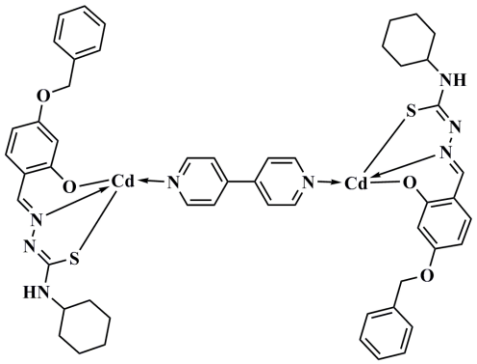

[(Cd(bsct))4,4′-bipy] (8)

Fig. 2.40. Tentative structures for complexes.

Referances

[1] S.M. Kumar, J. Rajesh, K. Anitha, K. Dhahagani, M. Marappan, N.I. Gandhi, G. Rajagopal, Spectrochem. Acta 142 (2015) 292.

[2] D. Rogolino, A. Bacchi, L. De Lucca, G. Rispoli, M. Sechi, A. Slevaert, L. Naesens, M. Carcelli, J. Biol. Inorg. Chem. 20 (2015) 1109.

[3] M.A. Ali, M.H. Khabir, M.N. Nazimuddhin, S.M.M.H. Majumder, M.T.H. Tarafder, M.A. Khair, Indian J. Chem. A27 (1988) 1064.

[4] P. Bindu, M.R.P. Kurup, T.R. Satyakeerty, Polyhedron 18 (1999) 321.

[5] T.S. Lobana, S. Indoria, H. Sood, D.S. Arora, B.S. Randhawa, I.G. -Santos, V.A. Smoinski, J.P. Jaisnski, Inorg. Chim. Acta 461 (2017) 248.

[6] S.M. Kumar, K. Dhahangi, J. Rajesh, K. Anitha, G. Chakkaravarthi, N. Kanakachalam, M. Marappan, G. Rajagopal, Polyhedron 85 (2015) 830.

[7] M.A. Hussein, T.S. Guan, R.A. Haque, M.B.K. Ahamed, A.M.S.A. Majid, Polyhedron 85 (2015) 93.

[8] A. Maiti, S. Ghosh, J. Inorg. Biochem. 36 (1989) 131.

[9] P.C. de Sousa, P.I.S. Maia, H.B. de Barros, C.Q.F. Leite, V.M. Deflon, F.R. Pavan, Curr. Clin. Pharmacol. 1 (2015) 66.

[10] P.I.S. Maia, F.R. Pavan, C.Q.F. Leite, S.S. Lemos, G.F. de Sousa, A.A. Batista, O.R. Nascimento, J. Ellena, E.E. Castellano, E. Niquet, V.M. Deflon, Polyhedron 28 (2009) 398.

[11] C. Umadevi, P. Kalaivani, H. Pushmann, S. Murugan, P.S. Mohan, R. Prabhakaran, J. Photobiol. Photochem. B 67 (2017) 45.

[12] G. Kalaiarasi, R. Jain, H. Pushman, S.P. Chandrika, K. Preethi, R. Prabhakaran, New J. Chem. 41 (2017) 2543.

[13] G. Kalaiarasi, R. Jain, A. Shanmugapriya, H. Pushman, P. Kalaivani, R. Prabhakaran, Inorg. Chim. Acta 462 (2017) 174.

[14] J.M. Jacob, M.R.P. Kurup, Acta Cryst. E68 (2012) o836.

[15] N.R. Sajitha, M. Sithambaresan, M.R.P. Kurup, Acta Cryst. E70 (2014) o987.

[16] SMART and SAINT, Area Detector Software Package and SAX Area Detector Program, Bruker Analytical X-ray; Madison, WI, USA, 1997.

[17] SADABS, Area Detector Absorption Correction Program; Bruker Analytical X-ray; Madison, WI, 1997.

[18] a) Ridaku Oxford diffraction, CrysAlis PRO Ridaku Americas, The Woodlands, Texas, USA (2015).

b) O.V. Dolomanov, L.J. Bourhis, R.J. Gildea, J.A.K. Howard, H. Puschmann, J. Appl. Cryst. 42 (2009) 339.

[19] G.M. Sheldrick, Acta Cryst. C71 (2015) 3.

[20] G.M. Sheldrick, Acta Cryst. A71 (2015) 3.

[21] K. Brandenburg, Diamond Version 3.2g, Crystal Impact GbR, Bonn, Germany, 1997.

[22] L.J. Farrugia, J. Appl. Cryst. 45 (2012) 849.

[23] V. Suni, M.R.P. Kurup, M. Nethaji, Spectrochim. Acta A63 (2006) 174.

[24] D.L. Pavia, G.M. Lapman, G.S. Kris, J.R. Vyvyan, Introduction to Spectroscopy, Brooks/Cole, Cengage Learning, 4th edn., 2001.

[25] E.B. Seena, M.R.P. Kurup, E. Suresh, J. Chem. Crystallogr. 38 (2008) 93.

[26] F.H. Allen, O. Kennard, D.G. Watson, L. Brammer, A.G. Orpen, R. Taylor, J. Chem. Perkin. Trans. 2 (1987) S1.

[27] E.B. Seena, B.N.B. Raj, M.R.P. Kurup, E. Suresh, J. Chem. Crystallogr. 36 (2006) 189.

[28] G.A Jeffrey, Cryst. Rev. 9 (2003) 135.

[29] V.V. Zelentsov, Russ. J. Inorg. Chem. 1 (1962) 670.

[30] A. Syamal, Coord. Chem. Rev. 16 (1975) 309.

[31] R. Hahn, A. Nakamura, K.Tanaka, Y. Nakayama, Inorg. Chem. 32 (1995) 6562.

[32] N.A. Mangalam, S. Sivakumar, S.R. Sheeja, M.R.P. Kurup, E.R.T. Tiekink, Inorg. Chim. Acta 362 (2009) 4191.

[33] M.R. Maurya, A. Kumar, M. Abid, A. Azam, Inorg. Chim. Acta 359 (2006) 2439.

[34] K. Nakomoto, Infrared and Raman Spectra of Inorganic and Coordination Compounds, 6th ed. Wiely, New York (2009) 59.

[35] M. Aljahdali, A.A. El-Sherif, Inorg. Chim. Acta 407 (2013) 58.

[36] P.B. Sreeja, M.R.P. Kurup, A. Kishore, C. Jasmin, Polyhedron 23 (2004) 575.

[37] R.P. John, A. Sreekanth, V. Rajakannan, T.A. Ajith, M.R.P. Kurup, Polyhedron 23 (2004) 2549.

[38] E.B. Seena, M.R.P. Kurup, Polyhedron 26 (2007) 3595.

[39] R.M. El-Bahnasaway, L.M.S. El-Deen, A.S. El-Table, M.A. Wahba, A.E.I.A. El-Mensef, Eur. Chem. Bull. 3 (2014) 441.

[40] A.M. Asiri, S.A. Khan, Molecules 15 (2010) 4784.

[41] T.A. Reena, E.B. Seena, M.R.P. Kurup, Polyhedron 27 (2008) 1825.

[42] N.A. Mangalam, M.R.P. Kurup, Spectrochim. Acta 71 (2009) 2040.

[43] R.J.H. Clark, D. Brown, The Chemistry of Vanadium, Niobium, Tantalum, Pergamon press, Oxford 20 (1973) 550.

[44] C.J. Ballhausen, H.B. Grey, Inorg. Chem. 1 (1962) 111.

[45] A. Sreekanth, S. Sivakumar, M.R.P. Kurup, J. Molec. Struct. 655 (2003) 47.

[46] E.B. Seena, M.R.P. Kurup, Polyhedron 26 (2007) 829.

[47] N.A. Mangalam, S. Sivakumar, M.R.P. Kurup, E. Suresh, Spectrochim. Acta 75A (2010) 686.

[48] P. Kalaivani, C. Umadevi, R. Prabhakaran, F. Dallemer, P.S. Mohan, Inorg. Chim. Acta 438 (2015) 264.

[49] A.B.P. Lever, Inorganic electronic spectroscopy 2nd *Ed*^{n}. Elsevier, Amsteram (1984).

[50] M.J. Bew, B.J. Hathaway, R.R. Faraday, J. Chem. Soc. Dalton Trans. (1972) 1229.

[51] S. Stoll, Spectral Simulations in Solid-state Eletron Paramagnetic Resonance, Ph. D. Thesis, ETH, Zurich, 2003.

[52] C.E. Housecroft, A.G. Sharpe, Inorganic chemistry, 3rd *Ed*n. Pearson (Edn.) Ltd. (2008) 615.

[53] N. Raman, Y.P. Raja, A. Kulandaisamy, Indian Acad. Sci. 113 (2001) 183.

[54] U.B. Gangadharmath, S.M. Annigeri, A.D. Naik, V.K. Revankar, V.B. Mahale, J. Molec. Struct. (Theochem) 572. (2001) 61.

[55] A. Sreekanth, M.R.P. Kurup, Polyhedron 22 (2003) 3321-3332.

[56] D. Kivelson, R. Neiman, J. Chem. Phys. 35 (1961) 149

[57] E. Garribba, G. Micera, J. Chem. Educ. 83 (2006) 1229.

[58] L. Latheef, M.R.P. Kurup, Spectrochim. Acta. A70 (2008) 86.

[59] B.J. Hathaway, Structure and Bonding, Springer Verlag, Heidelberg (1973) 60.

[60] A. Ducort, B. Scattergood, B. Coulson, R.N. Perutz, A.K. Duhme-Klair, Eur. J. Inorg. Chem. 21 (2015) 3562.

[61] G.G. Evans, J.A. Boeyens, Acta Cryst. B45 (1989) 581.

[62] P. Muller, R. Herbst-Irmer, A.L. Spek, T.R. Schneider, M.R. Sawaya, Crystal Structure Refinement, Oxford University Press (2006).

[63] D. Cremer, J.A. Pople, J. Am. Chem. Soc. 97 (1975) 1354.

.....ꕥ.....

Chapter 3

4-BENZYLOXYSALICYLADEHYDE-N^4-METHYLTHIOSEMICARBAZONE AND ITS TRANSITION METAL COMPLEXES: SYNTHESIS, SPECTRAL AND STRUCTURAL CHARACTERIZATION

Contents

3.1 Introduction

Substituted thiosemicarbazones have proved to show a large variety of properties, which found application in various fields. When R_1 of the thiosemicarbazone in Scheme 3.1 was replaced by 4-benzyloxysalicylaldehyde, R_3 with methyl group, R_2 and R_4 with hydrogen, an ONS donor thiosemicarbazone with methyl substitution on N^4 position was designed.

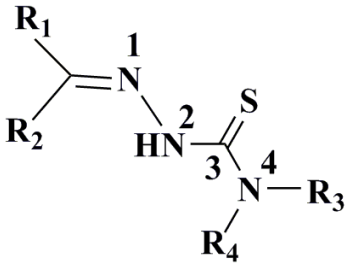

Scheme 3.1

The present chapter discusses the synthesis and characterization of a new salicylaldehyde N^4-substituted thiosemicarbazone and its VO^{2+}, Co(II), Ni(II), Cu(II) and MoO_2^{2+} complexes.

3.2. Experimental

3.2.1. Materials

4-Benzyloxysalicylaldehyde (Alfa Aesar), N^4-methylthiosemicarbazide (Sigma Aldrich), $VOSO_4 \cdot H_2O$ (Alfa Aesar), $CoCl_2$ (E-Merck), $NiBr_2$ (Sigma Aldrich), $Ni(NO_3)_2 \cdot H_2O$ (Alfa Aesar), $CuCl_2 \cdot 2H_2O$ (E-Merck), $MoO_2(acac)_2$ (Sigma Aldrich), $MoCl_5$ (Alfa Aesar), pyridine (S.D. Fine), CH_3OH (Spectrochem), CH_3CH_2OH (Spectrochem) and CH_3CN (Spectrochem) were of analar grade and used without further purification.

3.2.2. Syntheses of 4-benzyloxysalicylaldehyde-N^4-methylthiosemicarbazone (H_2bsmt)

A solution of N^4-methylthiosemicarbazone (0.1050 g, 1 mmol) in 10 ml acetonitrile was acidified with 1 drop of glacial acetic acid. To this an acetonitrile solution of 4-benzyloxysalicylaldehyde (0.2182 g, 1 mmol) was added and the reaction mixture was refluxed for 3 h under stirring (Scheme 3.2). The yellow colored solution obtained was kept for one week and the yellow block shaped crystals obtained were separated [1].

Yield: (0.084) 62.2%. m.p : 184 °C.
Elemental Anal. Found (Calcd)% : C 60. 77 (60.93); H 5.96 (5.43);
N 12.96 (13.32); S 10.20 (10.17).

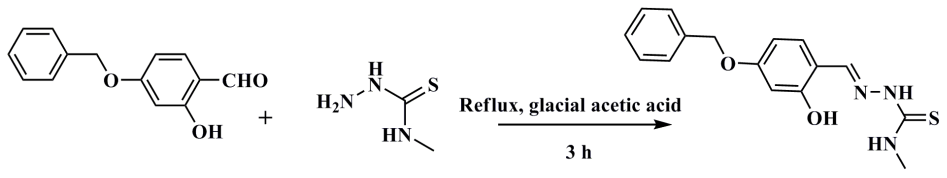

4-Benzyloxysalicylaldehyde **N^4-Methylthiosemicarbazone** **4-Benzyloxysalicylaldehyde-N^4-methylthiosemicarbazone**

Scheme 3.2

3.2.3. Syntheses of complexes

3.2.3.1. Synthesis of $[VO(bsmt)]_2$ (9)

The complex **9** was synthesized by refluxing a methanolic solution of vanadium sulfate monohydrate (0.162 g, 1 mmol) with H_2bsmt (0.315 g, 1 mmol) in methanol for 4 h. The green colored solution obtained was kept for 2 weeks. A brown compound obtained was filtered, washed with methanol and dried *in vacuo*.

Yield : (0.399 g) 52%.
Elemental Anal. Found (calcd)% : C 50.12 (50.53); H 4.02 (3.98); N 10.80 (11.05); S 8.00 (8.43).

3.2.3.2. Synthesis of $[Co(Hbsmt)_2]$ (10)

H_2bsmt (0.315 g, 1 mmol) was dissolved in 10 ml methanol and heated with stirring to ensure complete dissolution. To this hot solution, $CoCl_2 \cdot 2H_2O$ (0.085 g, 0.5 mmol) in methanol was added. The mixture was acidified with two drops of glacial acetic acid and refluxed for 4 h. The product formed was filtered, washed with methanol and dried *in vacuo*.

Yield : (0.331 g) 48%.
Elemental Anal. Found (calcd)% : C 55.46 (55.89); H 4.69 (5.02); N 12.12 (12.22); S 9.04 (9.33).

3.2.3.3. Synthesis of $[Ni(Hbsmt)_2]$ (11)

To a hot solution of H_2bsmt (0.315 g, 1 mmol) in acetonitrile, a solution of $NiBr_2$ (0.109 g, 0.5 mmol) in acetonirile was added with stirring and refluxed for 3 h. The resulting clear brown solution was kept for 3 weeks and the product obtained was separated by filtration, washed with methanol and dried *in vacuo*.

Yield : (0.448 g) 65%.
Elemental Anal. Found (calcd)% : C 55.90 (55.91); H 5.32 (4.69); N 11.74 (12.22); S 8.54 (9.33).

3.2.3.4. Synthesis of [Ni(bsmt)py] (12)

A solution of H_2bsmt (0.315 g, 1 mmol) in acetonitrile was heated under reflux with $Ni(NO_3)_2 \cdot 6H_2O$ (0.290 g, 1 mmol) for 2 h. To this hot solution, pyridine (0.079 g, 1 mmol) was added carefully with stirring. The product formed was filtered, washed with acetonirile and dried *in vacuo*.

Yield : (0.252 g) 55%.
Elemental Anal. Found (calcd)% : C 55.74 (55.90); H 4.30 (4.47); N 12.19 (12.42); S 6.78 (7.11).

3.2.3.5. Synthesis of [Cu(Hbsmt)Cl] (13)

This complex was synthesized by refluxing an ethanolic solution of H_2bsmt (0.315 g, 1 mmol), acidified with two drops of Con. HCl and $CuCl_2 \cdot 2H_2O$ (0.170 g, 1 mmol) in ethanol for 4 h. The resulted green colored solution was kept for 1 week and the product obtained was filtered, washed with ethanol and dried *in vacuo*.

Yield : (0.186 g) 45%.
Elemental Anal. Found (calcd)% : C 46.36 (46.49); H 3.99 (3.90); N 10.25 (10.16); S 7.89 (7.76).

3.2.3.6. Synthesis of [MoO_2(bsmt)py] (14)

To a methanolic solution of H_2bsmt (0.315 g, 1 mmol), $MoO_2(acac)_2$ (0.326 g, 1 mmol) dissolved in a mixture of methanol and DMF (1:1 v/v) was added and refluxed with stirring for 2 h. To this hot solution pyridine (0.079 g, 1 mmol) was added and further refluxed for 2 h. The orange solution obtained was kept for 1 week and the product obtained was separated, washed with methanol and dried *in vacuo*.

Yield : (0.315 g) 61%.
Elemental Anal. Found (calcd)% : C 49.23 (48.47); H 3.99 (3.87); N 10.25 (10.77); S 6.58 (6.16).

3.2.3.7. Synthesis of $[MoO_2(bsmt)H_2O]\cdot H_2O$ (15)

The complex was prepared by refluxing a solution of $MoCl_5$ (0.273 g, 1 mmol) in methanol with a methanolic solution of H_2bsmt (0.315 g, 1 mmol). The product formed after 2 h was separated, washed with methanol and dried *in vacuo*.

Yield : (0.260 g) 54%.
Elemental Anal. Found (calcd)% : C 40.65 (40.26); H 3.98 (4.01); N 8.45 (8.80); S 6.28 (6.72).

3.2.4. Physico-chemical techniques

3.2.4.1. Elemental analysis

Elemental analyses of the compounds were done on a Vario EL III CHNS elemental analyzer at the Sophisticated Analytical Instrument Facility, Cochin University of Science and Technology, Kochi-22, Kerala, India.

3.2.4.2. Magnetic susceptibility measurements

The magnetic susceptibility measurements of the complexes were taken on a Vibrating sample Magnetometer using $Hg[Co(SCN)_4]$ as a calibrant at the SAIF, Indian Institute of Technology, Madras.

3.2.4.3. Molar conductivity measurements

The conductivity measurements of the complexes were recorded in 10^{-3} M solution in DMF on a Systronic model 303 direct reading conductivity meter at room temperature.

3.2.4.4. Spectroscopic characterization

The infrared spectra of H_2bsmt and complexes **9-15** were recorded on a JASCP FT-IR-5300 spectrometer in the range 4000-400 cm^{-1} using KBr pellets. The electronic spectra of the prepared compounds were recorded in DMF solution (10^{-3} and 10^{-5} M) on Thermo Scientific Evolution

220 UV-vis Spectrophotometer in the 200-900 nm range ^{1}H NMR spectrum of H_2bsmt was recorded using Bruker AMX 400 FT-NMR Spectrometer at the Sophisticated Analytical Instrument Facility, Cochin University of Science and Technology, Kochi, India. The Electron Paramagnetic Resonance spectra of complexes **9** and **13** were recorded in the solid state at 298 K and at 77 K in DMF solution, on a Varian E-112 spectrometer, with 100 kHz modulation frequency, 2 G modulation amplitude and 9.1 GHz microwave frequency at the Sophisticated Analytical Instrumentation Facility, IIT Bombay, India.

3.2.4.5. Thermogravimetric analysis

The TG-DTA analysis of complex **9** was carried out using a Perkin Elmer Pyris Diamond TG-DTA analyzer in a nitrogen atmosphere. The compound was heated at a rate of 10 °C min^{-1} in the 50-700 °C range at the Sophisticated Analytical Instrument Facility, Cochin University of Science and Technology, Kochi, India.

3.2.5. Single crystal X-ray diffraction studies

The single crystal X-ray diffraction studies of the thiosemicarbazone H_2bsmt was done at 296(2) K using a Bruker SMART APEXII CCD diffractometer at the Sophisticated Analytical Instrumentation Facility, Cochin University of Science and Technology, Kochi, India. Data acquisition was done using Bruker SMART software and data integration using Bruker SAINT software [2]. Absorption corrections were carried out using SADABS based on Laue symmetry using equivalent reflections [3]. The structure was solved by direct methods and refined by full-matrix least-squares calculations with the SHELXL-2014/7 software package [4]. The graphic tools used were DIAMOND version 3.2g [5] and ORTEP-3 [6].

3.3. Results and discussion

Elemental analysis of H_2bsmt and its complexes were presented in Sections 3.2.3. and 3.2.3. The structures of the compound were assigned on the basis of this.

3.3.1. Characterization of 4-benzyloxysalicylaldehyde-N^4-methylthiosemicarbazone (H_2bsmt)

3.3.1.1. Infrared spectrum

Infrared spectrum of H_2bsmt was taken in 4000-400 cm^{-1} range using KBr pellets. The band at 3349 cm^{-1} was assigned to ν(O–H) stretching vibrations. The ν(C=N) stretching vibrations as a result of C=N bond formed by the condensation between thiosemicarbazide and aldehyde gives a band at 1625 cm^{-1} [7]. The bands at 1453 and 863 cm^{-1} corresponds to ν(C=S)/ν(C–S) stretching vibrations, which suggests that the compound exist in thio-amido form. This is justified by the absence of any band for ν(S–H) stretching vibration in the 2700-2500 cm^{-1} range [8]. The band at 1104 cm^{-1} is assigned to hydrazinic ν(N–N) stretching vibration. The ether C–O–C vibrations are observed at 1161 cm^{-1}. Fig. 3.1 represents the infrared spectrum of H_2bsmt.

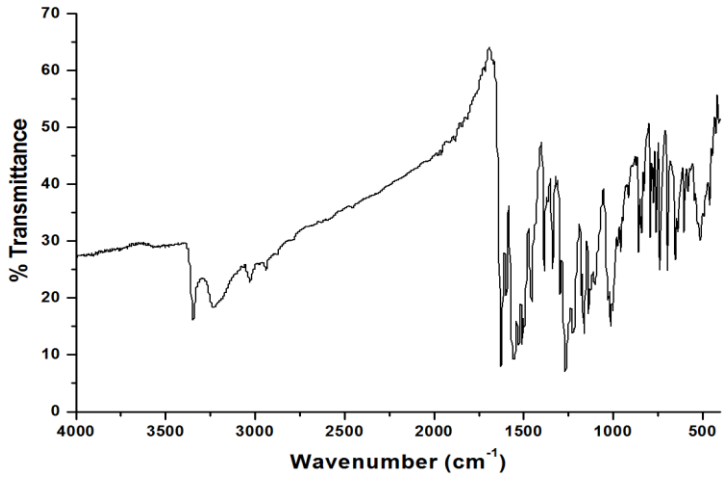

Fig. 3.1. Infrared spectrum of H_2bsmt.

3.3.1.2. Electronic spectrum

Electronic specta of organic compounds gave characteristic bands corresponds to n–π* and π–π* transitions. Electronic spectrum of H_2bsmt was recorded in 10^{-5} M solution of the compound in DMF. The compound gives bands with maximum absorption at 341 and 302 nm with molar absorptivity of 7.08×10^4 and 3.24×10^4 M^{-1} cm^{-1} respectively. These transitions are due to π–π* or n–π* transitions arised from benzene ring, imine and thiocarbonyl groups present in H_2bsmt. The electonic spectrum of H_2bsmt is given in Fig. 3.2.

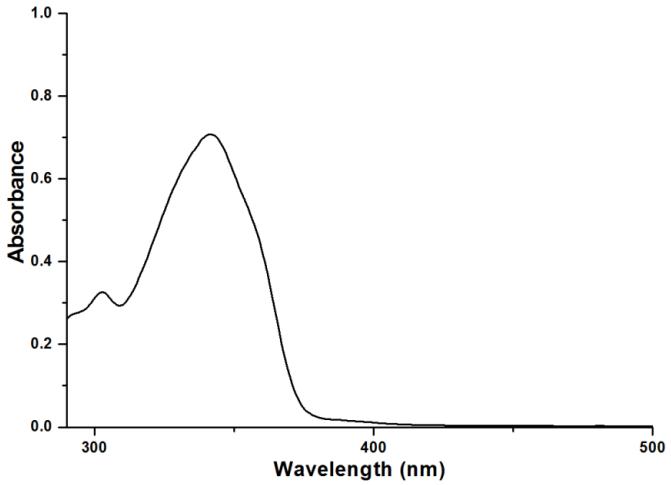

Fig. 3.2. Electronic spectrum of H_2bsmt.

3.3.1.3. ^{1}H NMR spectrum

The ^{1}H NMR spectrum of H_2bsmt was recorded in DMSO-d_6 with TMS as internal standard. Singlets at 11.25, 9.95 and 8.23 ppm were assigned to O(2)–H (s, 1H), N(2)–H (s, 1H) and N(3)–H (s, 1H) protons respectively. The absence of these peaks in the D_2O-^{1}H NMR spectrum indicates that these protons were exchanged in the D_2O. The down field shift for these protons are due to their involvement in hydrogen bonding (Fig. 3.5) [9]. The appearance of these peaks as singlet is a result of

absence of any coupling protons in the vicinity. The down field shift for this proton is due to involvement of intramolecular hydrogen bonding. Disappearance of this peak in the D_2O exchanged ^1H NMR spectrum, further confirms the presence of an exchangeable proton. The down field shift of C(14)–H (s, 1H) to 8.29 ppm was a result of conjugation with aromatic ring. The singlet at 5.12 ppm assigned to the O–C(7)–H (s, 2H) proton. The down field shift is due to deshielding of proton by hetro atom attached to the carbon atom. The methyl protons C(16)–H (s, 3H) appear at 3.00 ppm. The protons attached to aromatic ring assigned values in the 7.32-7.81 ppm range, which appear as a multipelt. ^1H NMR spectrum and D_2O exchanged ^1H NMR of H_2bsmt is presented in Fig. 3.3.

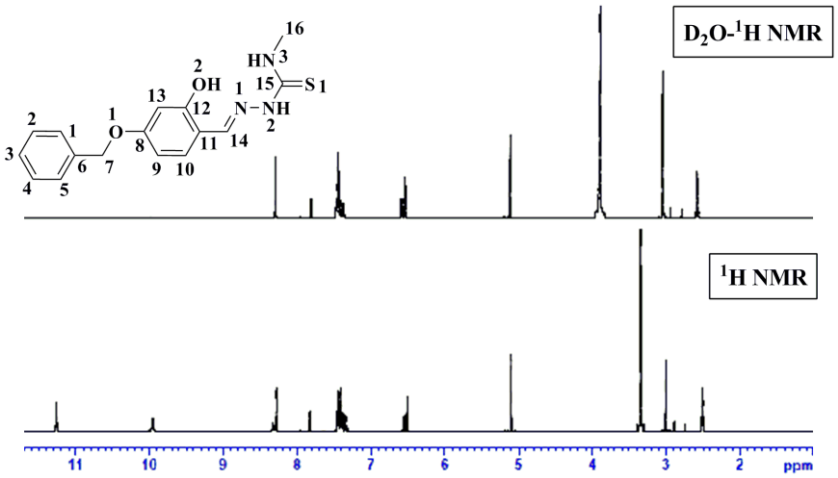

Fig. 3.3. ^1H NMR spectrum and D_2O exchange ^1H NMR spectrum of H_2bsmt.

3.3.1.4. Single crystal X-ray diffraction studies

Single crystals of H_2bsmt were isolated from acetonitrile by slow evaporation. The compound was crystallized into a monoclinic $P2_1/n$ space group. An yellow block shaped crystal of size 0.50 × 0.40 × 0.35 mm^3 was mounted on a Brucker Kappa APEXII CCD diffractometer equipped with graphite monochromated Mo Kα (λ = 0.71073 Å) radiation. The non-

hydrogen atoms were anisotropically refined and the C–H protons were placed in calculated positions guided by fourier map with a bond length of 0.93–0.96 Å. U_{iso} = 1.2U_{eq} (1.5 for Me) was assigned for H atoms. The N(2)–H(2′), N(3)–H(3′) and O(2)–H(2A) protons were located and the distances were restrained to 0.88±0.01 and 0.84±0.01 Å for N–H and O–H bonds respectively using DFIX instruction. The crystal data and refinement parameters are given in Table 3.1. The ORTEP diagram for H_2bsmt is given in Fig. 3.4.

Table 3.1. Crystal data and structure refinement parameters of H_2bsmt

Parameters	**H_2bsmt**
Empirical formula	$C_{16}H_{17}N_3O_2S$
Formula weight	315.39
Color	Yellow
Temperature/K	296(2)
Crystal system	monoclinic
Space group	$P2_1/n$
Cell parameters	
a (Å)	17.013(2)
b (Å)	5.9474(10)
c (Å)	17.542(4)
$\alpha = \gamma$(°)	90
β (°)	117.565(7)
Volume (Å^3)	1573.4(5)
Z	4
Calculated density, ρ (g cm^{-3})	1.331
Absorption coefficient, μ (mm^{-1})	0.216
F(000)	664
Crystal size (mm^3)	0.50 x 0.40 x 0.35
θ range for data collection (°)	2.28 to 28.17
Limiting indices	$-22 \le h \le 22$, $-7 \le k \le 4$, $-22 \le l \le 23$
Reflections collected	10845
Independent reflections	3827 [R_{int} = 0.0232]
Data/restraints/parameters	3827 / 3/ 212
Goodness-of-fit on F^2	1.016
Final R indexes [I>2σ (I)]	R_1 = 0.0428, wR_2 = 0.1074
Final R indexes [all data]	R_1 = 0.0719, wR_2 = 0.1280
Largest diff. peak and hole (e Å^{-3})	0.237/-0.240

$R_1 = \Sigma||F_o| - |F_c|| / \Sigma|F_o|$

$wR_2 = [\Sigma w(F_o^2-F_c^2)^2 / \Sigma w(F_o^2)^2]^{1/2}$

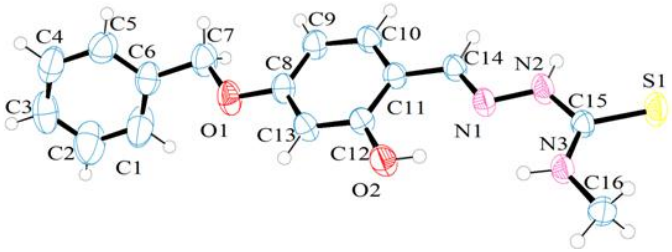

Fig. 3.4. ORTEP diagram of H_2bsmt with displacement ellipsoid of 50% probability.

The azomethine bond formd as a result of condensation between the aldehyde and thiosemicarbazide is evident from C(14)–N(1) bond length of 1.285(2) Å, which is near to the reported C=N bond length (1.276(3) Å) [10]. The C(15)–S(1) and C(15)–N(2) bond lengths were found to be equal to 1.683(14) and 1.346(2) Å respectively. These values are near to the reported C=S and C–N bond lengths [10]. These observations suggested that the compound H_2bsmt exists in thio-amido form in the solid state. The *E* conformation of the compound with respect to C(14)–N(1) bond, is evident from the C(11)–C(14)–N(1)–N(2) torsion angle 177.22(16)°. The N(1)–N(2)–C(15)–S(1) and N(1)–N(2)–C(15)–N(3) torsion angle 170.34(14) and 9.7(3)° respectively suggested that the thiol sulfur S(1) lies *trans* and N(3) lies *cis* with respect to N(1). The molecule as a whole is non-planar, with two benzene rings were twisted by a dihedral angle of 67.55(12)°. The hydrazine carbothioamide fragment N1/N3/C15/S1/C16 is planar with maximum deviation of 0.020(2) Å for N(3) [1]. Selected bond lengths and bond angles are given in Table 3.2.

Table 3.2. Selected bond parameters of H_2bsmt

Bond length (Å)		Bond angle (°)	
C(14)–N(1)	1.285(2)	C(11)–C(14)–N(1)	118.30(14)
C(15)–S(1)	1.326(2)	C(14)–N(1)–N(2)	114.92(14)
N(1)–N(2)	1.382(2)	N(2)–C(15)–N(3)	117.71(15)
C(15)–N(2)	1.346(2)	N(2)–C(15)–S(1)	118.49(12)

The special arrangement of atoms in the molecules gives rise to an intramolecular hydrogen bonding O(2)–H(2A)···N(1) with D···A distance of 2.690(2) Å [11]. The molecules in the unit cell are held together *via* intermolecular interactions N(3)–H(3)···S(1), N(2)–H(2)···O(2) and N(2)–H(2)···S(1) with D···A distances of 3.438(17), 3.094(2) and 3.485(17) respectively, where the H(2) atom involves in a bifurcated hydrogen bonding (Fig. 3.5). The hydrogen bonding interactions present in the crystal lattice are given in Table 3.4.

Table 3.3. Interaction parameters in H_2bsmt

Hydrogen bonding interactions				
D–H···A	D–H (Å)	H···A (Å)	D···A (Å)	D–H···A(°)
N(3)–H(3′)···S(1)	0.88(1)	2.84(2)	3.438(17)	127(2)
N(2)–H(2′)···O(2) [a]	0.88(1)	2.48(2)	3.094(2)	127(2)
N(2)–H(2′)···S(1) [b]	0.88(1)	2.77(2)	3.485(17)	139(2)
O(2)– H(2A)···N(1)	0.84(1)	2.00(2)	2.690(2)	140(3)
C–H···π interactions				
C–H···Cg	C–H (Å)	H···Cg (Å)	C···Cg (Å)	C–H···Cg(°)
C(2)–H(2)···Cg(2) [c]	0.93	2.93	3.64(15)	135

a = x, 1+y, z; b = 2 - x, 2 - y, 2 - z; c = 2-x, -y, 1-z;

Cg(2)= C(8), C(9), C(10), C(11), C(12), C(13); D= donor, A= acceptor, Cg= centroid

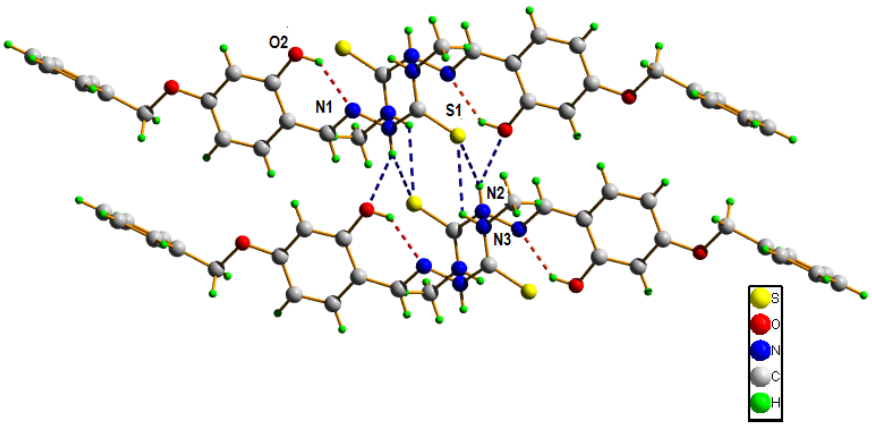

Fig. 3.5. Hydrogen bonding interactions in H_2bsmt.

The packing of molecules is further facilitated through C(2)–H(2)···π interaction with H···Cg distance of 3.64(4) Å [12]. Fig. 3.6 represents the packing of H_2bsmt when viewed along '*b*' axis. It is evident from the packing diagram that two units of the compounds had a parallel arrangement and connected to each other *via* C–H···π interaction.

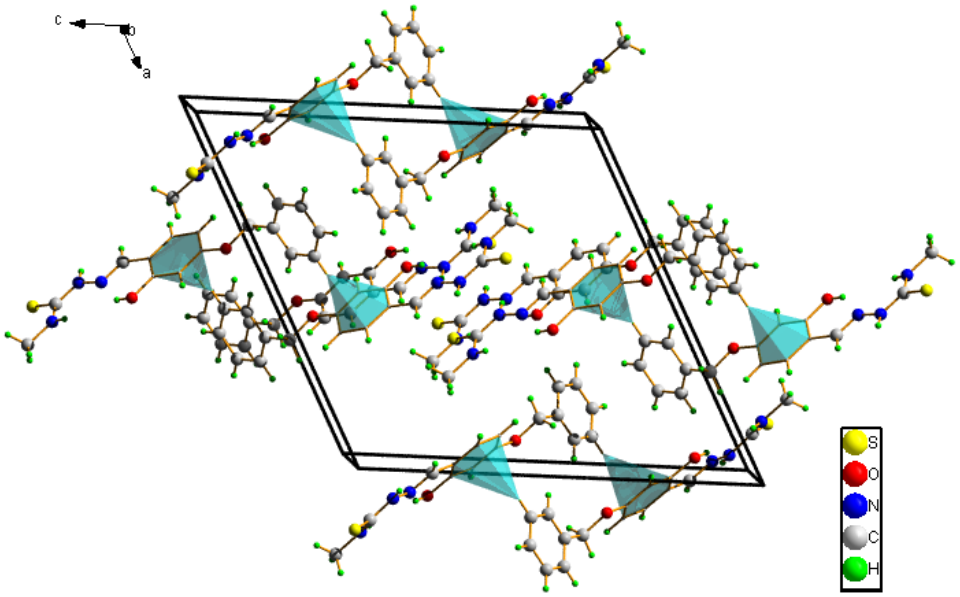

Fig. 3.6. C–H···π interaction in H_2bsmt facilitating molecular packing.

3.3.2. Characterization of complexes of H_2bsmt

The ONS donor thiosemicarbazone H_2bsmt is able to show a variety of coordination modes. Seven metal complexes of H_2bsmt were prepared. Complexes **9**, **13**, and **15** were prepared by refluxing H_2bsmt and metal salts in 1:1 ratio, whereas for synthesizing the complexes **10** and **11,** H_2bsmt and metal salts were used in the ratio 2:1. The complexes **12** and **14** were synthesized by refluxing H_2bsmt, metal salt and heterocyclic base pyridine in 1:1:1 ratio.

3.3.2.1. Molar conductivity and magnetic susceptibility measurements

Molar conductivity and magnetic susceptibility measurements give an insight into the coordination geometry and oxidation state of the metal in the complex. The molar conductivity measurements were taken in 10^{-3} M solutions of the complexes in DMF. All complexes were found to have molar conductivity in the range 2.1-43 ohm^{-1} cm^2 mol^{-1}, which was very much below the value for uni-univalent electrolyte (65-90 ohm^{-1} cm^2 mol^{-1}). This suggested that the complexes of H_2bsmt were non electrolytic in nature.

The magnetic susceptibility measurements of complexes **12, 14** and **15** suggest that these complexes are diamagnetic in nature. The diamagnetic nature of the complex **12** suggested that the Ni(II) in it adopted a square planar geometry, which lead to pairing of *d* electrons. The diamagnetic nature of complex **14** and **15** is a result of d^0 electronic configuration of Mo(VI). The complex **9** gave a subnormal magnetic moment value of 1.02 B.M., suggesting the complex exist in dimeric form. This result was in agreement with the values obtained for a series of dimeric VO(II) systems by Syamal [13]. The octahedral Co(II) complex was expected to had a magnetic moment value of 4.7-5.4 B.M.. The low magnetic momentum 2.5 B.M. for complex **10** was considered as an anomalous condition for Co(II) system as per literature [14]. The high spin electronic configuration of Ni(II) centre is evident from magnetic moment value of 2.9 B.M. for complex **11**, suggesting an octahedral arrangement of ligands around the metal center**.** The Cu(II) complex **13** gives a magnetic moment value of 1.73 B.M. corresponding to d^9 electronic configuration. The molar conductivity and magnetic susceptibility measurements results are tabulated in Table 3.4.

Table 3.4. Molar conductivity and magnetic moment values of complexes of H_2bsmt

Compound	λ_m (ohm^{-1} cm^2 mol^{-1})	μ_{eff} (B.M.)
$[VO(bsmt)]_2$ (**9**)	14.1	1.02
$[Co(Hbsmt)_2]$ (**10**)	2.5	2.5
$[Ni(Hbsmt)_2]$ (**11**)	4.8	2.9
[Ni(bsmt)py] (**12**)	2.1	0.14
[Cu(Hbsmt)Cl] (**13**)	4.6	1.73
$[MoO_2(bsmt)py]$ (**14**)	18	0
$[MoO_2(bsmt)H_2O]\cdot H_2O$ (**15**)	43	0

3.3.2.2 Infrared spectra

Infrared spectra of the complexes were recorded using KBr pellets in 400-4000 cm^{-1} range. Infrared spectra give information regarding extend of bond formation in a complex. This technique gives additional information with respect to the presence of heterocyclic base and solvent molecules in the coordination entity. The coordination of the ligand to the metal centre is evident from the shift of frequencies for coordinating functional groups as compared to that of the ligand. The tentative assignments of vibrational bands for metal complexes are given in Table 3.5.

Table 3.5. IR spectral assignments (cm^{-1}) of Hanpt and its metal complexes

Compound	ν(O–H)	ν(C=N)	ν(C=N)[a]	ν(C–O)	ν(C=S)/ ν(C–S)	ν(N–N)	ν(M=O) ν(M–O)	ν(M–N)
H_2bsmt	3349	1625	---	1263	1453, 863	1104	---	---
$[VO(bsmt)]_2$ (**9**)	---	1611	1594	1238	1415, 835	1125	967,514	469
$[Co(Hbsmt)_2]$ (**10**)	---	1613	---	1227	1420, 842	1028	557	426
$[Ni(Hbsmt)_2]$ (**11**)	---	1600	---	1222	1433, 836	1010	533	413
[Ni(bsmt)py] (**12**)	---	1607	1562	1215	1402, 842	1178	512	424
[Cu(Hbsmt)Cl] (**13**)	---	1621	---	1238	1410, 841	1033	439	447
$[MoO_2(bsmt)py]$ (**14**)	---	1618	1556	1218	1446, 830	1123	995,837	446
$[MoO_2(bsmt)H_2O]\cdot H_2O$ (**15**)	---	1600	1524	1231	1443, 823	1123	945,843	456

a- Newly formed C=N

Absence of ν(O–H) band in all complexes, which in turn present in free H_2bsmt, was an evidence for the coordination of the ligand *via* deprotonation of phenolic O–H. The band at 1625 cm^{-1} assigned to ν(C=N) vibration show a shift by 20-30 cm^{-1} confirms coordination of azomethine nitrogen to the metal center for all the complexes.

The appearance of a new band at 1594 cm^{-1} for $[VO(bsmt)]_2$ (**9**) corresponding to new ν(C=N), along with a shift in the ν(C=S)/ν(C–S) stretching vibrations for H_2bsmt from 1453 cm^{-1} to 1415 cm^{-1} in the complex **9** is an evidence for the coordination of the ligand in deprotonated form. The blue shift observed for ν(N–N) stretching support the imiolization of the ligand which results in extra stability of the complex [15]. The M–L characteristic vibrations are important for identifying complexating sites of a particular ligand. Maurya *et al.*, reported that a band in the region 756-804 cm^{-1} corresponds to ν(V–O–V) bridging vibration. In the present complex there was a band at 772 cm^{-1} corresponding to ν(V–O–V) vibration [16]. Along with absence of band corresponding to ν(O–H) a band appeared at 514 cm^{-1} is assigned to ν(V–O) stretching vibrations due to coordination through phenolate oxygen. This is further confirmed from the shift for ν(C–O) stretching vibration. The ν(V–N) stretching vibrations were observed as band at 469 cm^{-1} [17]. The terminal ν(V=O) stretching vibration designated by a band at 967 cm^{-1}. The infrared spectrum for complex **9** is illustrated in Fig. 3.7.

The ν(C=S)/ν(C–S) vibrations showed a blue shift for $[Co(Hbsmt)_2]$ (**10**) as compared to H_2bsmt support the coordination of the ligand through thiolate sulfur. Absence of any new band corresponding to ν(C=N) and a decrease in ν(N–N) stretching frequency to 1028 cm^{-1} attributed to the fact that the ligand coordinates in thio-amido form [18,19]. The ν(Co–O) and ν(Co–N) stretching vibrations are observed at 557 and 426 cm^{-1} respectively. Infrared spectrum of complex **10** is represented in Fig. 3.8.

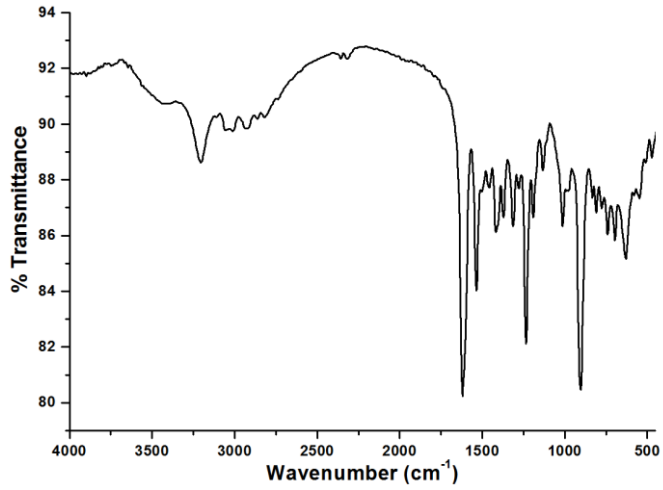

Fig. 3.7. Infrared spectrum of $[VO(bsmt)]_2$ (**9**).

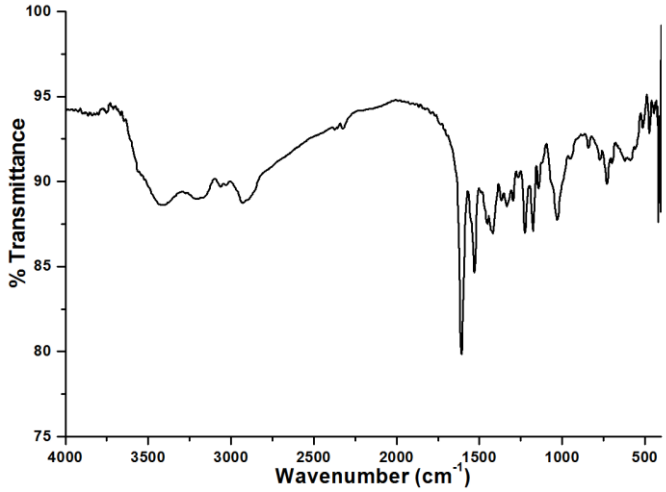

Fig. 3.8. Infrared spectrum of $[Co(Hbsmt)_2]$ (**10**).

Complexes [Ni(Hbsmt)$_2$] (**11**) and [Ni(bsmt)py] (**12**) gave bands at 1402 and 1433 cm^{-1} respectively corresponding to ν(C=S)/ν(C–S) vibrations. The blue shift observed for these bands indicate coordination of sulfur in H_2bsmt to Ni(II). The band corresponding to newly formed C=N bond was observed in the region 1562 cm^{-1} for complex **12,** was not observed for complex **11**. This suggests that the thiosemicarbazone coordinate in the thio-amido form in complex **11** and in the thio-iminolate form in complex **12.** This was confirmed from the ν(N–N) stretching vibrations 1010 and 1178 cm^{-1} respectively for complexes **11** and **12**. The increase in stretching frequency for complex **12** was due to extended conjugation due to deprotonation. The disappearance of ν(O–H) stretching frequency and a shift for the ν(C–O) stretching confirms the involvement of phenolic oxygen in the complex formation. The bands at 533 and 512 cm^{-1} were ascribed to ν(Ni–O) for complexes **11** and **12** respectively. The ν(Ni–N) stretching vibrations for complexes **11** and **12** appear at 413 and 424 cm^{-1} respectively. The coordination of heterocyclic base was observed at 1457 and 688 cm^{-1}. The infrared spectra for complexes **11** and **12** are depicted in Figs. 3.9 and 3.10 respectively.

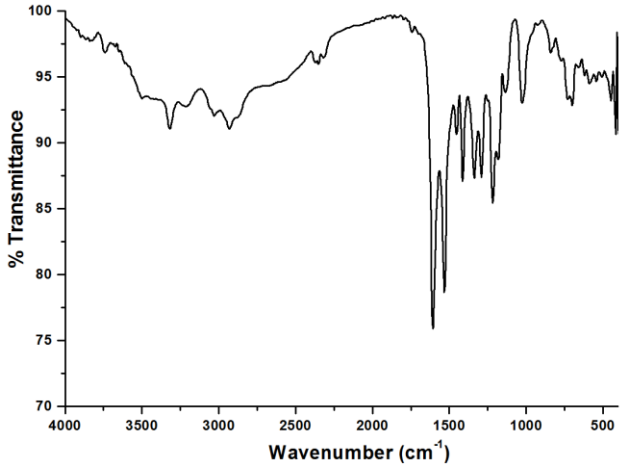

Fig. 3.9. Infrared spectrum of [Ni(Hbsmt)$_2$] (**11**).

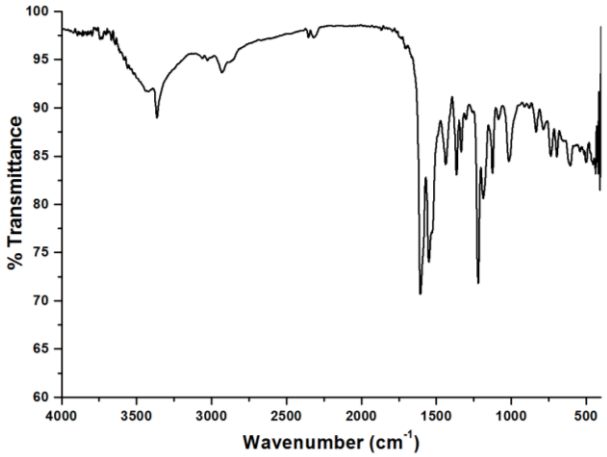

Fig. 3.10. Infrared spectrum for [Ni(bsmt)py] (**12**).

The shift for ν(C=S)/ν(C–S) vibrations to lower frequencies compared to H_2bsmt accompanied by a lower shift for ν(N–N) stretching vibrations by 70 cm^{-1} for complex [Cu(Hbsmt)Cl] (**13)** indicate the coordination of thiosemicarbazone in thio–amido form. The coordination of phenolic oxygen was confirmed form absence of ν(O–H) stretching vibrations and shift in ν(C–O) stretching vibration at1238 cm^{-1}. The bands at 439 and 447 cm^{-1} were ascribed to the ν(Cu–O) and ν(Cu–N) vibrations respectively [20]. The infrared spectrum of complex **13** is shown in Fig. 3.11.

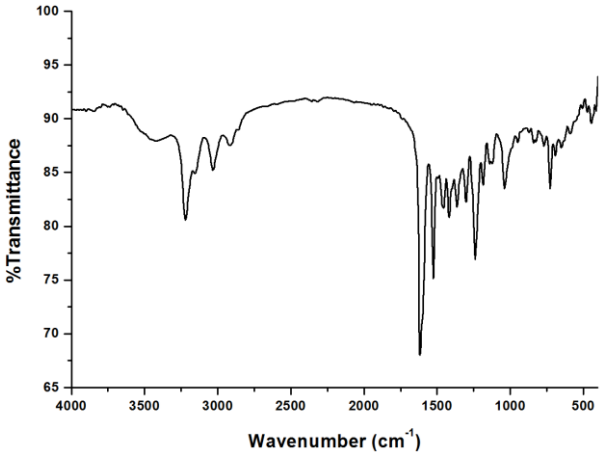

Fig. 3.11. Infrared spectrum of [Cu(Hbsmt)Cl] (**13)**.

Appearance of new bands at 1556 and 1524 cm^{-1} for complexes $[MoO_2(bsmt)py]$ (**14**) and $[MoO_2(bsmt)H_2O]\cdot H_2O$ (**15**) corresponds to the newly formed C=N bond. The shift in the stretching vibration of ν(C=S)/ν(C–S) along with a shift in ν(N–N) stretching vibrations (1123 cm^{-1}) adds to the existence of thiosemicarbazone in the doubly deprotonated state. The second proton was removed from the phenolic O–H, which was evident from the disappearance of ν(O–H) stretching vibration from 3349 cm^{-1}. The vibrations corresponding to *cis*-MoO_2 were observed at 995 and 837 cm^{-1} for complex **14**. Similarly complex **15** gave these vibrations at 945 and 843 cm^{-1}. The vibrations at 1453 and 697 cm^{-1} were ascribed to pyridine molecule coordinated to metal in complex **14**. The broad band at 3438 cm^{-1} for complex **15** is assigned to ν(O–H) stretching vibration for solvent water molecule. Infrared spectra of complexes **14** and **15** are given in Figs. 3.12 and 3.13.

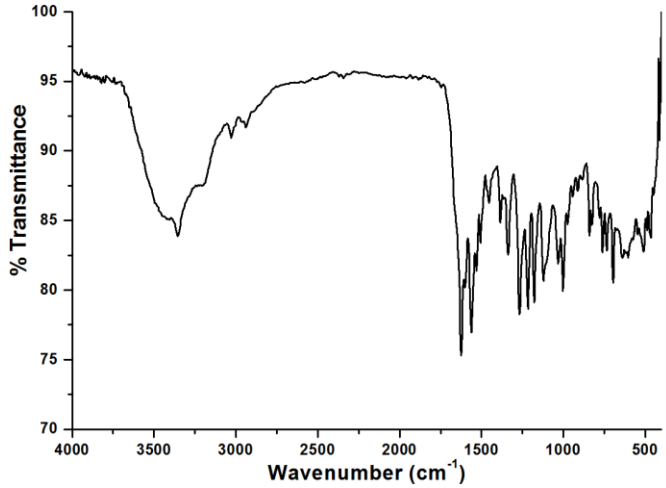

Fig. 3.12. Infrared spectrum of $[MoO_2(bsmt)py]$ (**14**).

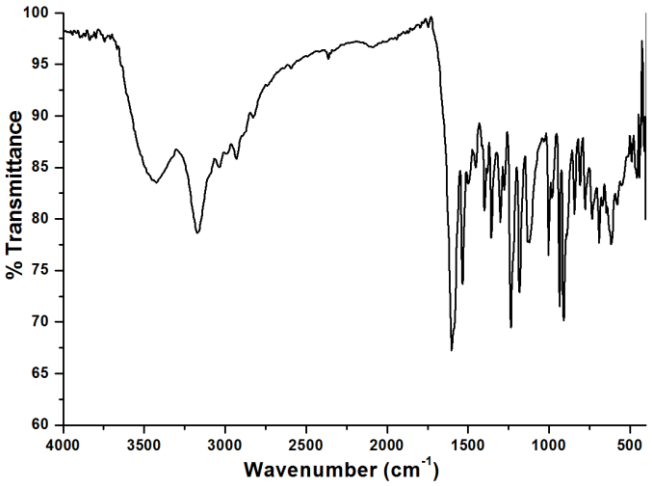

Fig. 3.13. Infrared spectrum of $[MoO_2(bsmt)H_2O]\cdot H_2O$ (**15**).

3.3.2.3. Electronic Spectra

Electronic spectra of the complexes were recorded in DMF (10^{-5} and 10^{-3} M) solution. The electronic spectral assignments of the complexes are given in Table 3.7. All the complexes gave characteristic electronic absorption corresponding to intraligand transitions in the range 292-369 nm. These transitions show a significant shift for the n-π* and π-π* transition as that of free H_2bsmt. All the complexes gave absorption at lower energy (large λ_{max}) region attributed to LMCT transitions from thiosemicarbazone to the metal.

Table 3.7. Electronic spectral assignments (nm) of and complexes

Compound	n–π*/ π–π* ($\varepsilon = 10^4$ M^{-1} cm^{-1})	LMCT ($\varepsilon = 10^4$ M^{-1} cm^{-1})	d-d (nm) (ε (M^{-1} cm^{-1}))
H_2bsct	302 (3.24), 341 (7.08)	---	---
$[VO(bsmt)]_2$ (**9**)	353 (7.88)	380 (7.6)	641 (46)
$[Co(Hbsmt)_2]$ (**10**)	358 (4.42),	402 (5.42), 417 (5.62)	509 (665), 672 (169)
$[Ni(Hbsmt)_2]$ (**11**)	343 (3.68), 358 (3.22)	407 (2.04)	476 (496), 597 (117)
[Ni(bsmt)py] (**12**)	295 (6.83), 369 (9.73)	405 (6.39)	476 (482), 601 (115)
[Cu(Hbsmt)Cl] (**13**)	324 (2.25), 377 (2.32)	393 (2.15)	489 (248), 624 (269)
$[MoO_2(bsmt)py]$ (**14**)	303 (6.89), 332 (8.93)	---	
$[MoO_2(bsmt)H_2O]\cdot H_2O$ (**15**)	292 (4.49), 304 (5.03)	341 (9.03)	

The electronic spectrum for complex **9** gave a broad band with maximum absorption at 353 nm ($\varepsilon = 7.88 \times 10^4$ M^{-1} cm^{-1}), was assigned to intraligand transitions. This transition showed a red shift with respect to the ligand absorption. The band with maximum absorption at 380 nm with molar absorptivity of 7.6×10^4 M^{-1} cm^{-1} was due to LMCT V←O from phenolic oxygen to vanadium [16]. The electronic spectra of H_2bsmt and complex **9** are depicted in Fig.3.14.

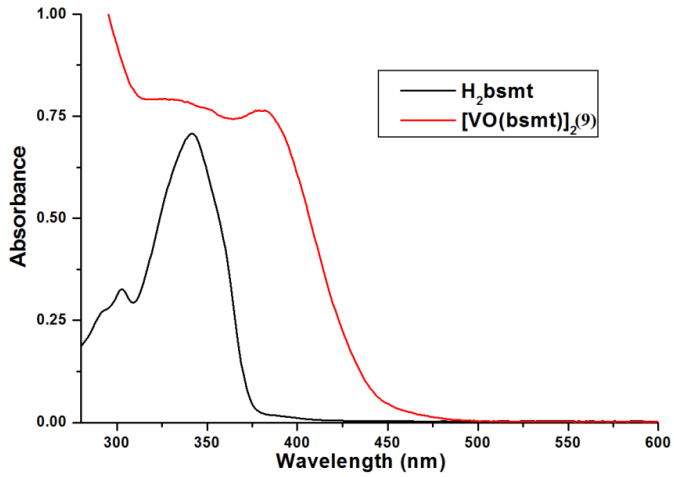

Fig.3.14. Electronic spectrum of H_2bsmt and complex **9**.

For a VO(II) complex, with vanadium in V(IV) oxidation state the visible spectrum is expected to give three different types of transitions *via* ${}^2E \leftarrow {}^2B_2$ ($d_{xy} \rightarrow d_{xz}, d_{yz}$), ${}^2B_1 \leftarrow {}^2B_2$ ($d_{xy} \rightarrow d_{x^2-y^2}$)and ${}^2A_1 \leftarrow {}^2B_2$ ($d_{xy} \rightarrow d_{z^2}$).

For complex **9** instead of three different transitions only one broad band is observed with maximum absorption at 641 nm with molar absorptivity of 46 M^{-1} cm^{-1}. The visible spectrum for complex **9** is given in Fig. 3.15.

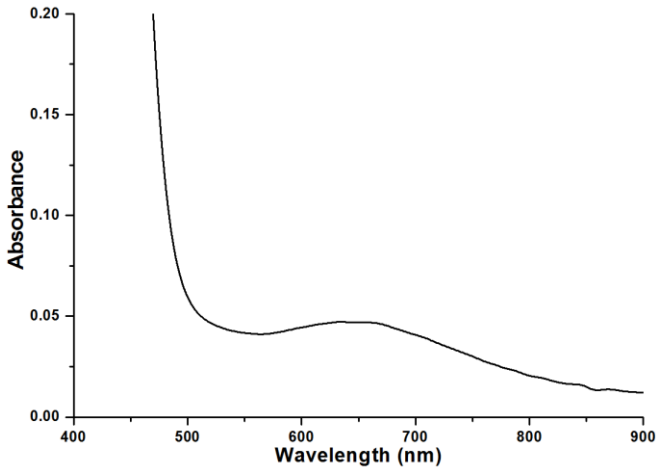

Fig. 3.15. Visible spectrum of $[VO(bsmt)]_2$ (**9**).

The intraligand transitions of $[Co(Hbsmt)_2]$ (**10**) were observed as a broad band with a maximum at 358 nm ($\varepsilon = 4.42 \times 10^4\ M^{-1}\ cm^{-1}$). The LMCT transitions resulted from Co←S and Co←O were observed at 402 nm ($\varepsilon = 5.42 \times 10^4\ M^{-1}\ cm^{-1}$) and 417 nm ($\varepsilon = 5.62 \times 10^4\ M^{-1}\ cm^{-1}$) respectively [21]. The electronic spectrum for complex **10** is given in Fig. 3.16.

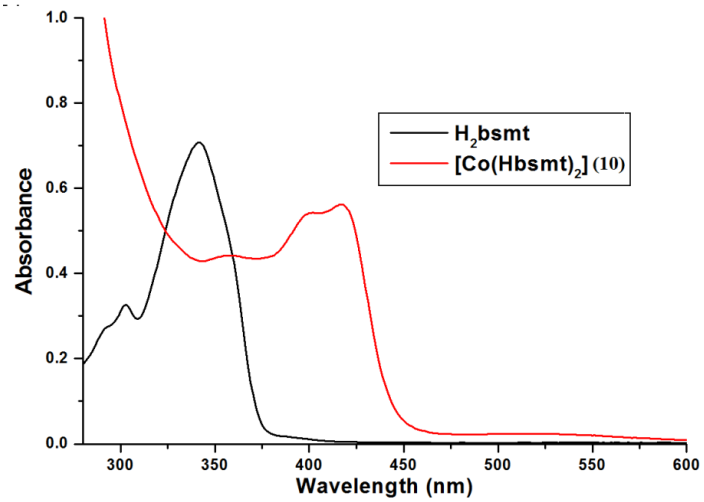

Fig. 3.16. Electronic spectrum of H_2bsmt and complex **10**.

An octahedral Co(II) complex is expected to give two absorptions due to $^4A_{1g}(F) \leftarrow {}^4T_{1g}(F)$ and $^4T_{1g}(P) \leftarrow {}^4T_{1g}(F)$ transitions in the visible region. The complex **10** showed two absorption maxima at 509 and 672 nm with molar absorptivity of 665 and 169 $M^{-1}\,cm^{-1}$ respectively, which is in agreement with the previous reports [21]. The visible spectrum for complex **10** is depicted in Fig. 3.17.

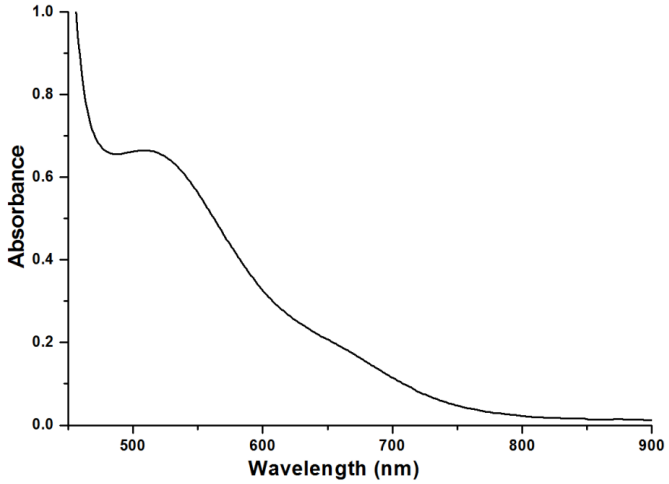

Fig. 3.17. Visible spectrum of $[Co(Hbsmt)_2]$ **(10)**.

Electronic spectra of complexes **11** and **12** exhibited bands with maximum absorption at 343 and 295 nm with $\varepsilon = 3.68\times10^4$ and 6.83×10^4 $M^{-1}cm^{-1}$ accompanied by intense broad band with λ_{max} of 358 nm ($\varepsilon = 3.22 \times 10^4$ $M^{-1}\,cm^{-1}$) and 369 nm ($\varepsilon = 9.73 \times 10^4$ $M^{-1}\,cm^{-1}$) respectively were due to intraligand transitions. The charge transfer transition from Ni←O is observed at λ_{max}= 407 and 405 nm ($\varepsilon = 2.04 \times 10^4$ and 6.39×10^4 $M^{-1}\,cm^{-1}$) respectively for complexes **11** and **12** [22,23]. Fig. 3.18 represents the electronic spectrum of H_2bsmt and complexes **11** and **12**.

The nickel complexes **11** and **12** gave visible spectrum as represented in Fig. 3.18. The complex **11** exhibited two shoulders at 476 and 601 nm (ε = 482 and 115 $M^{-1}\,cm^{-1}$) corresponding to $^3T_{2g} \leftarrow {}^3A_{2g}$, $^3T_{1g}(F) \leftarrow {}^3A_{2g}$,

$^3T_{1g}(P) \leftarrow {}^3A_{2g}$ transitions, observed for an octahedral Ni(II) complex [22]. The square planar Ni(II) complex **12** is expected to give absorptions corresponding to transitions $^1E_g \leftarrow {}^1A_{1g}$, $^1A_{2g} \leftarrow {}^1A_{1g}$ and $^1B_{1g} \leftarrow {}^1A_{1g}$. Instead of three absorption maxima the complex **12** gave two shoulders at 476 and 597 nm with ε = 496 and 117 $M^{-1}cm^{-1}$ respectively [24]. The visible spectra of complexes **11** and **12** are given in Fig. 3.19.

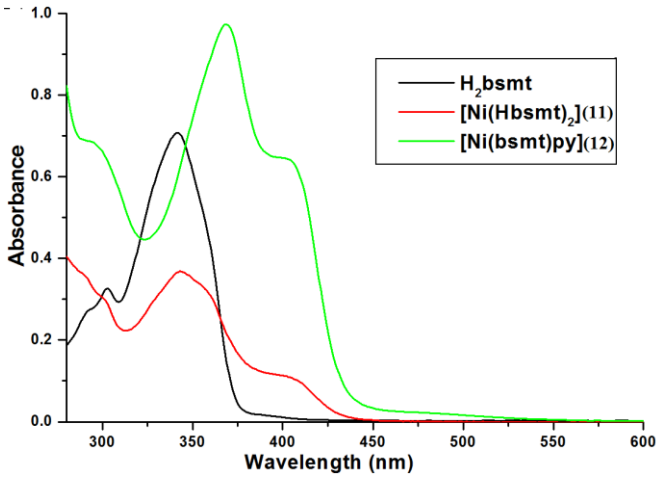

Fig. 3.18. Electronic spectra of H_2bsmt and complexes **11** and **12**.

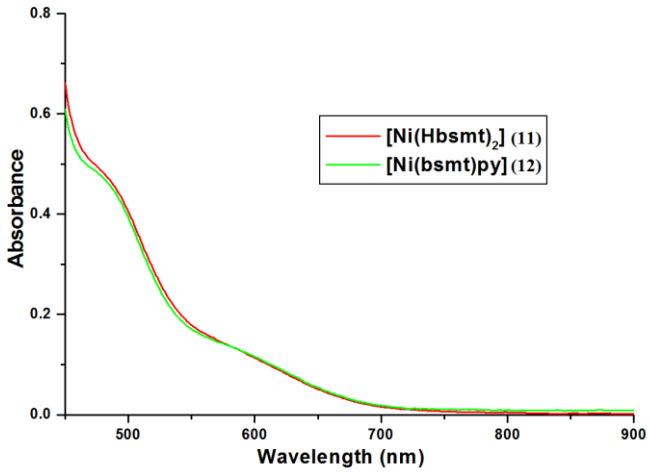

Fig. 3.19. Visible spectrum of complex **11** and **12**.

The electronic spectrum of complex **13** consist of broad band with maximum absorption at 303 nm with molar absorptivity 2.25 × 10^4 M^{-1} cm^{-1}, was assigned to intraligand transitions. The LMCT transitions of the type Cu←S and Cu←O were observed at an absorption maximum at 377 nm and 393 nm (ε = 2.32 × 10^4 and 2.15 × 10^4 $M^{-1}cm^{-1}$) respectively. Fig. 3.20 represents electronic spectra for H_2bsmt and complex **13**.

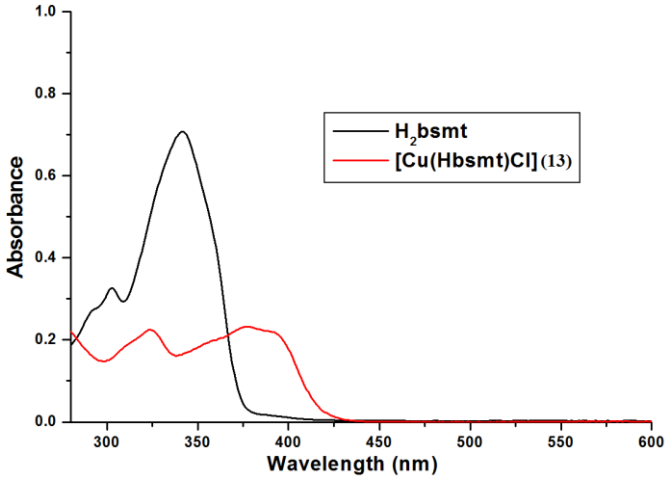

Fig. 3.20. Electronic spectra of H_2bsmt and complex **13**.

A square planar Cu(II) complex give three absorptions characteristic of the transitions $d_{x^2-y^2} \rightarrow d_{xy}$, $d_{x^2-y^2} \rightarrow d_{z^2}$ and $d_{x^2-y^2} \rightarrow d_{yz}$, d_{xy} ($^2B_{2g}$ ←$^2B_{1g}$, $^2A_{1g}$ ← ^2B1_g and ^2E_g ← $^2B_{1g}$). For complex **13** two absorptions were observed with an absorption maximum at 642 nm (ε = 269 M^{-1} cm^{-1}) and a shoulder at 489 nm (ε = 248 M^{-1} cm^{-1}) corresponding to these absorptions. The visible spectrum for complex **13** is given in Fig.3.21.

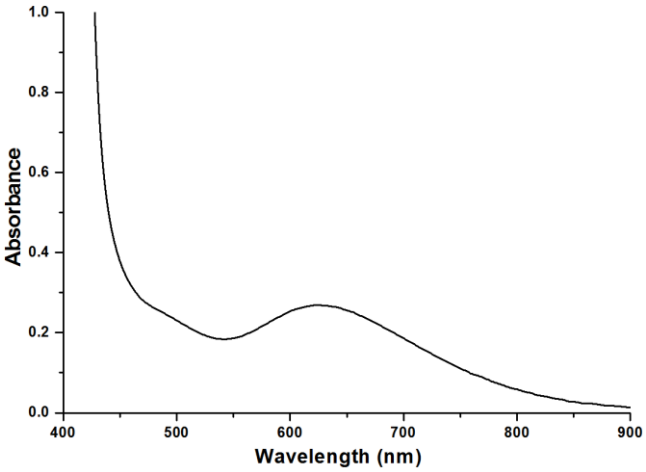

Fig. 3.21. Visible spectrum of [Cu(Hbsmt)Cl] (**13**).

The intraligand transitions for complexes **14** were observed at 303 and 332 nm (ε = 6.89 × 10^4 and 8.93 × 10^4 M^{-1} cm^{-1}). For complex **15** bands at 292 and 304 nm respectively with ε = 4.49 × 10^4 and 5.03 × 10^4 M^{-1} cm^{-1} corresponds to intraligand transtions. The spectrum was further characterized by very sharp absorption at 341 nm for complex **15** with ε = 9.03×10^4 M^{-1} cm^{-1} which corresponds to the LMCT transition from Mo ←O [25]. The combined electronic spectrum for complexes **14** and **15** accompanying H_2bsmt is given in Fig. 3.22.

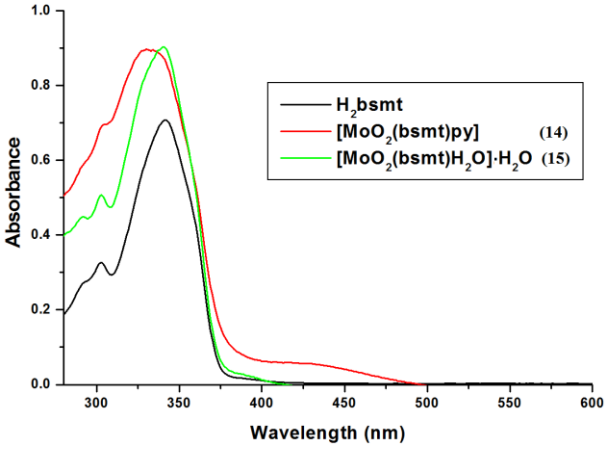

Fig. 3.22. Electronic spectra of H_2bsmt and complexes **14** and **15**.

3.3.2.4 EPR spectra

Complexes **9** and **13** were characterized by Electron Paramagnetic Resonance spectroscopy.

3.3.2.4.1 EPR spectrum of $[VO(bsmt)]_2$ (9)

Vanadium in complex **9** exist in VO(II) oxidation state with d^1 electronic configuration. The epr spectrum for complex **9** was recorded in DMF solution at 77 K. It gave axial spectra consisting of two sets of 8 lines (8 parallel and 8 perpendicular). The g values for the complex were found to be $g_{\parallel}$ = 1.95 and $g_{\perp}$ = 1.98. The hyperfine constants are $A_{\parallel}$ = 164 × 10^{-4} cm^{-1} and $A_{\perp}$ = 59 × 10^{-4} cm^{-1}. The $g_{\perp} > g_{\parallel}$ and $A_{\parallel} > A_{\perp}$, characteristic of an axially compressed d^1_{xy} configuration [26]. The anisotropic parameters A_{iso} and g_{iso} for complex **9** were found to be A_{iso}= 94 and g_{iso}= 1.97.

The molecular orbital coefficients α^2 and β^2 for the complexes are calculated by using the following equations:

$$\alpha^2 = \frac{(2.00277 - g_{\parallel})E_{d-d}}{8\lambda\beta^2}$$

$$\beta^2 = \frac{7}{6}\left[\left(\frac{-A_{\parallel}}{P}\right)+\left(\frac{A_{\perp}}{P}\right)+\left(g_{\parallel}-\frac{5}{14}g_{\perp}\right)-\frac{9}{14}g_e\right]$$

where, P=128×10^{-4} cm^{-1}, λ=135 cm^{-1} and E is the electronic transition energy for the transition $^2E \leftarrow {}^2B_2$. The values obtained for complex **9** are α^2 = 0.835 and β^2 = 0.912. The lower value for α^2 than β^2 indicate in plane σ bonding is more covalent than in-plane π bonding [27]. As per Gangadharmath *et al.*, to get positive values for α^2 and β^2, the values for $A_{\parallel}$ and $A_{\perp}$ were taken as negative [28]. The EPR spectrum of complex **9** in DMF at 77 K is given in Fig. 3.23.

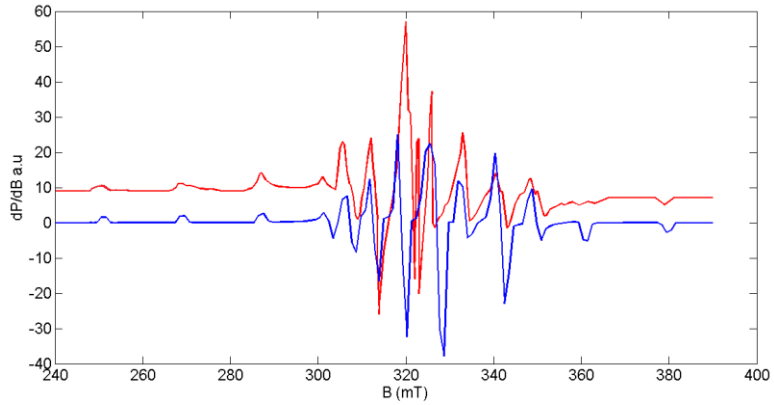

Fig. 3.23. EPR spectrum of complex **9** in DMF at 77 K.

3.3.2.4.2. EPR spectrum of [Cu(Hbsmt)Cl] (13)

The EPR spectrum of the [Cu(Hbsmt)Cl] (**13)**.was recorded in the polycrystalline state at 298 K and in DMF solution at 77 K. It is found that the complex with geometries like elongated octahedron, square pyramidal or square planar the ground state was $d_{x^2-y^2}$. The value of g tensor gives an idea about the ground state of the electron in the metal [29]

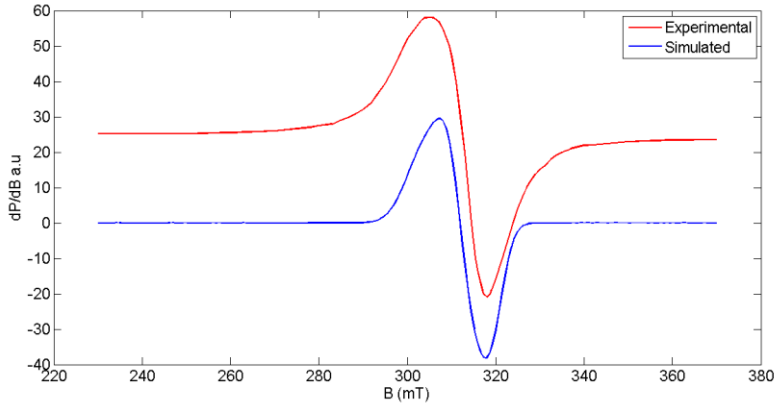

Fig. 3.24. EPR spectrum of complex **13** in polycrystalline state at 298 K.

The EPR spectrum of complex **13** in polycrystalline state was recorded at 298 K (Fig. 3.24). The EPR spectrum was simulated using

Easy Spin 4.0.0 package [30]. Best fitted experimental (red) and simulated (blue) spectra is given in Fig. 3.25. The complex **13** in polycrystalline state gave an isotropic spectrum with g_{iso} = 2.14.

In the case of a complex **13** Cu(II) ion, with $I = {}^3/_2$, gives four hyperfine lines. In frozen DMF at 77 K, complex **13** gave an axial spectrum with four hyperfine lines with g tensors $g_{\parallel}$ = 2.20 and $g_{\perp}$ = 2.04 and hyperfine coupling constants $A_{\parallel} = 186 \times 10^{-4}$ and $A_{\perp} = 35 \times 10^{-4}$ cm^{-1} [31]. Due to strong coordination with thiosemicarbazone with Cu(II), the perpendicular region gives superhyperfine lines with $A_{\perp(N)} = 19 \times 10^{-4}$ cm^{-1}. Fig. 3.25 depicts the EPR spectrum of the complex **13** in frozen DMF at 77 K. From the values of $A_{\parallel}$ and $A_{\perp}$ it is possible to calculate A_{av} using the equation $A_{av} = \frac{1}{3}(A_{\parallel} + 2A_{\perp})$. For the present complex its value is $A_{av} = 85.3\ 10^{-4}$ cm^{-1}.

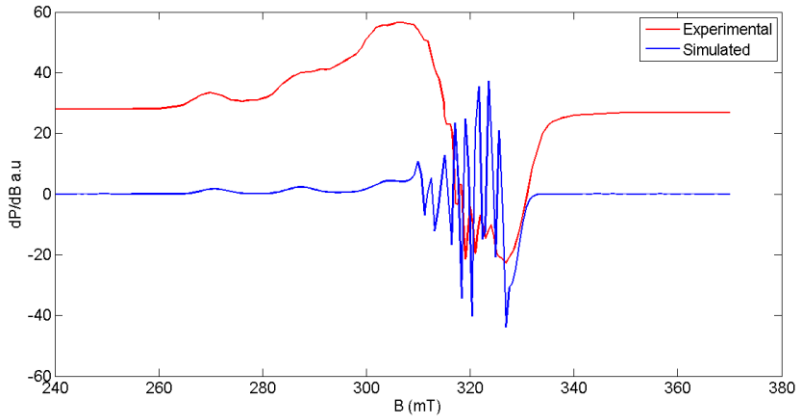

Fig. 3.25. EPR spectrum of [Cu(Hbsmt)Cl] (**13**).in DMF at 77 K.

The value for $g_{\parallel} > g_{\perp} > 2.0023$, consistent with $d_{x^2-y^2}$ ground state for a square planar complex. The g_{av} can be calculated using equation $g_{av} = \frac{1}{3}(g_{\parallel} + 2g_{\perp})$, here g_{av}= 2.14. When $g_{\parallel} < 2.3$, there is a significant covalent character to the M–L bond [32].

Other bonding parameters like α^2 (covalence of the in-plane σ-bonds), β^2 (covalence of in-plane π-bonds) and γ^2 (covalence of out-of-plane π-bonds) can be calculated from the values of $g_{\parallel}$, $g_{\perp}$, $A_{\parallel}$ and energy of *d-d* transition. The value of α^2 gives the fraction of σ-bonding by Cu(II) ion. This can be calculated from the equation

$$\alpha^2 = - A_{\parallel}/0.036 + (g_{\parallel} - 2.0023) + 3/7(g_{\perp} - 2.0023) + 0.04$$

If the value of α^2 is unity, the M–L bond is purely ionic and it is purely covalent if α^2 = 0.5 [20,33]. The two later parameters can be calculated from expression,

$$K_{\parallel} = \alpha^2\beta^2 \text{ and } K_{\perp} = \alpha^2\gamma^2$$

$$\text{Where } K_{\parallel}^2 = (g_{\parallel} - 2.0023)E_{d\text{-}d}/8\lambda_o$$

$$K_{\perp}^2 = (g_{\perp} - 2.0023)\, E_{d\text{-}d}/2\lambda_o$$

Here $K_{\parallel}$ and $K_{\perp}$ are orbital reduction factors and λ_o the one electron spin coupling constant, which is equal to 828 cm^{-1} [34,24]. For pure σ bonding $K_{\parallel} \approx K_{\perp} \approx 0.77$, for in plane π-bonding $K_{\parallel} < K_{\perp}$ and for out-of-plane π-bonding, $K_{\perp} < K_{\parallel}$.

For [Cu(Hbsmt)Cl] (**13**).these parameters were found to be α^2 = 0.71, β^2 = 0.89, γ^2= 0.78, $K_{\parallel}$ = 0.69 and $K_{\perp}$ = 0.61 suggests that the complex is having a significant σ bonding accompanied by an out of plane π-bonding.

3.3.2.5. TG-DTA analysis

Thermogravimetric analysis of $[MoO_2(bsmt)H_2O]\cdot H_2O$ **(15)** was recorded at a rate 10 °C min^{-1} in the 30-700 °C range in an atmosphere of nitrogen. The thermogram of complex **15** with differential thermogram is depicted in Fig. 3.26. The complex **15** shows a weight loss of 3.3% (calcd. 3.7%) at 104 °C, due to solvent H_2O molecule. The weight loss found

3.2% (calcd. 3.9%) at 175 °C is assigned for coordinated H_2O molecule. Loss of O_2 was clear from a weight loss of 7.6% (calcd. 3.9%) at 223 °C. The compound is stable after this temperature indicating stability of coordinated system.

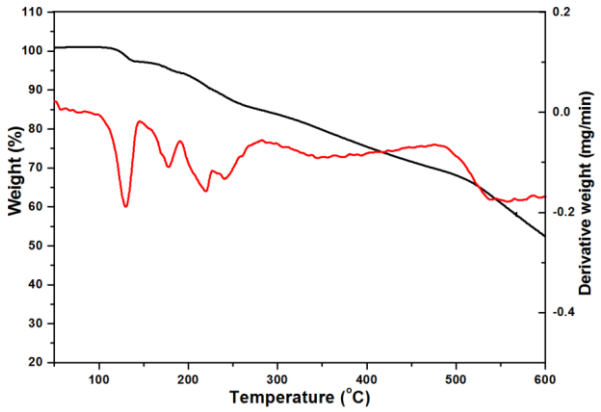

Fig. 3.26. Thermogram of $[MoO_2(bsmt)H_2O]\cdot H_2O$ **(15).**

3.4. Conclusion

The thiosemicarbazone H_2bsmt differ from H_2bsct only in the substitution at N^4 position. But it is observed that this thiosemicarbazone have given some complexes in the monoanionic form. The complexes $[Co(Hbsmt)_2]$ (**10**), $[Ni(Hbsmt)_2]$ (**11**) and [Cu(Hbsmt)Cl] (**13**) were formed with monodeprotonation of H_2bsmt. Complexes **10**, **11**, **14** and **15** give hexacoordinted complex. Complex **12** and **13** were four coordinated and complex **9** was a penta coordinated complex. This may be due to the acidic nature the solvent as compared to thiosemicarbazone. The physicochemical analyses of all the complexes are in agreement with the tentative structures given in Fig. 3.27.

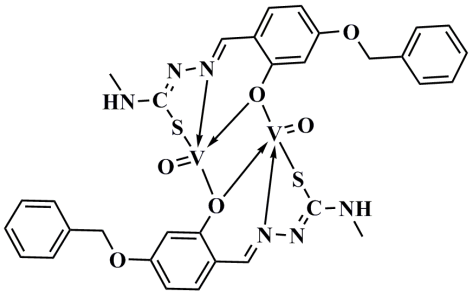

[VO(bsmt)]$_2$ **(9)**

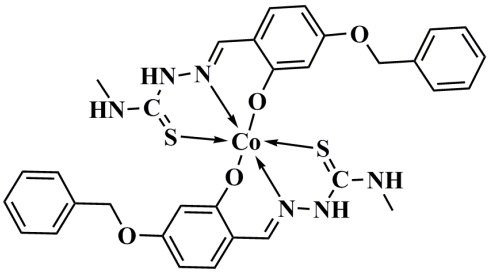

[Co(Hbsmt)$_2$] (**10**)

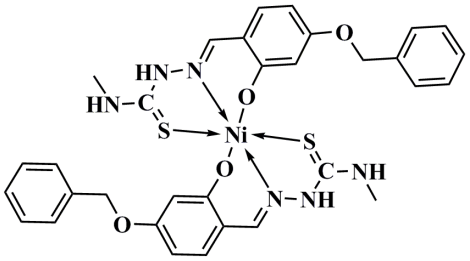

[Ni(Hbsmt)$_2$] (**11**)

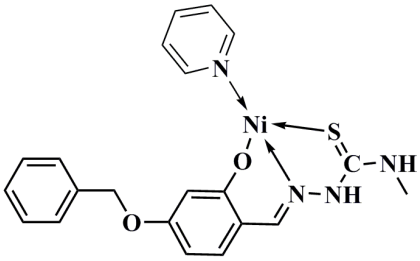

[Ni(bsmt)py] **(12)**

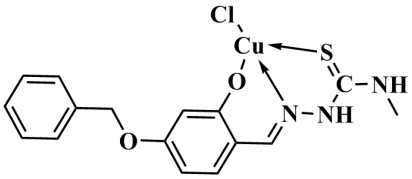

[Cu(Hbsmt)Cl] **(13)**

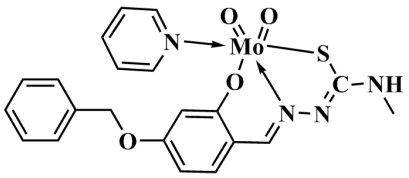

[MoO_2(bsmt)py]·(**14**)

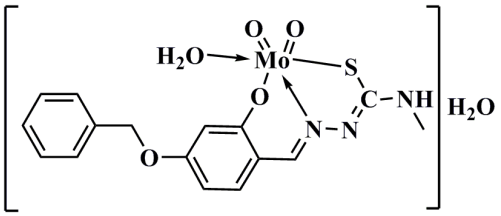

[MoO_2(bsmt)H_2O]·H_2O (**15).**

Fig. 3.27. Tentative structures for complexes of H_2bsmt.

Referances

[1] N. R. Sajitha, M. Sithambaresan, M. R. P. Kurup, Acta Cryst. E70 (2014) o112.

[2] SMART and SAINT, Area Detector Software Package and SAX Area Detector Program, Bruker Analytical X-ray; Madison, WI, USA, 1997.

[3] SADABS, Area Detector Absorption Correction Program; Bruker Analytical X-ray; Madison, WI, 1997.

[4] G.M. Sheldrick, Acta Cryst. C71 (2015) 3.

[5] K. Brandenburg, Diamond Version 3.2g, Crystal Impact GbR, Bonn, Germany, 1997.

[6] L.J. Farrugia, J. Appl. Cryst. 45 (2012) 849.

[7] M. Joseph, V. Suni, C.R. Nayar, M.R.P. Kurup, H.-K. Fun, J. Mol. Struct. 705 (2004) 63.

[8] R.P. John, A. Sreekanth, M.R.P. Kurup, H.-K. Fun, Polyhedron 24 (2005) 601.

[9] D.L. Pavia, G.M. Lapman, G.S. Kris, J.R. Vyvyan, Introduction to Spectroscopy, Brooks/Cole, Cengage Learning, 4th edn. (2001) 128.

[10] E.B. Seena, M.R.P. Kurup, E. Suresh, J. Chem. Crystallogr. 38 (2008) 93.

[11] G.A Jeffrey, Cryst. Rev. 9 (2003) 135.

[12] H.R. Khavasi, A.R. Salimi, H.E. Hosseini, M.M. Amini, Cryst. Eng. Comm. 13 (2011) 3710.

[13] A. Syamal, Coord. Chem. Rev. 16 (1975) 309.

[14] N.N. Jha, I.P. Ray, Asian J. Chem. 12 (2000) 703.

[15] B.S. Grag, M.R.P. Kurup, S.K. Jain, Y.K. Bhoon, Transit. Met. Chem. 13 (1988) 309.

[16] M.R. Maurya, A. Kumar, M. Abid, A. Azam, Inorg. Chim. Acta 359 (2006) 2439.

[17] N.A. Mangalam, M.R.P. Kurup, Spectrochim. Acta A71 (2009) 2040.

[18] B. Jeragh, A.A. El-Asy, Spectrochim. Acta A130 (2014) 546.

[19] A.K. El-Sawaf, D.X. West, R.M. El-Bahnasawy, F.A. El-Saied, Transit. Met. Chem. 23 (1998) 227.

[20] L. Latheef, M.R.P. Kurup, Spectrochim. Acta A70 (2008) 86.

[21] M.V. Angelusiu, S.-F. Barbuceanu, C. Draghici, G.L. Almajah, Europ. J. Med. Chem. 45 (2010) 2055.

[22] A. Sreekanth, S. Sivakumar, M.R.P. Kurup, J. Mol. Struct. 655 (2003) 47.

[23] V. Philip, V. Suni, M.R.P. Kurup, M. Nethaji, Polyhedron 23 (2004) 225.

[24] E.B. Seena, M.R.P. Kurup, Polyhedron 26 (2007) 3595.

[25] A.B.P. Lever, Inorganic Electronic Spectroscopy 2nd *Ed*^{n}. Elsevier, Amsteram (1984).

[26] C.E. Housecroft, A.G. Sharpe, Inorganic chemistry, 3rd *Ed*^{n}. Pearson (Eds.) Ltd. (2008) 615.

[27] N. Raman, Y.P. Raja, A. Kulandaisamy, Indian Acad. Sci. 113 (2001) 183.

[28] U.B. Gangadharmath, S.M. Annigeri, A.D. Naik, V.K. Revankar, V.B. Mahale, J. Molec. Struct. (Theochem) 572 (2001) 61.

[29] E. Garribba, G. Micera, J. Chem. Educ. 83 (2006) 1229.

[30] S. Stoll, Spectral Simulations in Solid-State Electron Paramagnetic Resonance, Ph. D. Thesis, ETH, Zurich, 2003.

[31] M.J. Bew, B.J. Hathaway, R.R. Faraday, J. Chem. Soc., Dalton Trans. (1972) 1229.

[32] D. Kivelson, R. Neiman, J. Chem. Phys. 35 (1961) 149

[33] B.J. Hathaway, Structure and Bonding, Springer Verlag, Heidelberg (1973) 60.

[34] E.B. Seena, M.R.P. Kurup, Polyhedron 26 (2007) 829.

.....ꕥ.....

Chapter 4

6-BROMOPYRIDINE-2-CARBALDEHYDE-N^4,N^4-DIMETHYLTHIOSEMICARBAZONE AND ITS TRANSITION METAL COMPLEXES: SYNTHESIS, SPECTRAL AND STRUCTURAL CHARACTERIZATION

Contents

4.1. Introduction

Thiosemicarbazones containing a pyridine ring have been of great interest for many decades in the research field, when it was found that these counterparts increase the biological activities of this class of compounds. Klayman *et al.* found that a large series of pyridine containing thiosemicarbazones with N^4-mono and disubstitution show enhanced antimalarial activity [1,2,3]. Triapine, a substituted pyridine containing thiosemicarbzone is an established anticancer drug [4,5]. Pyridine containing thiosemicarbazones have also found to act as good corrosion inhibitors for mild steel in acid media [6,7]. The present chapter discusses a substituted pyridine containing thiosemicarbazone that can be picturized by removing R_1 with 6-bromopyridine-2-carbaldehyde, R_3 and R_4 with methyl groups respectively (Scheme 4.1)

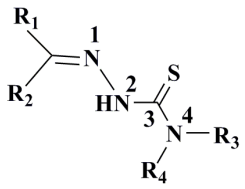

Scheme 4.1

This thiosemicarbazone can act as NNS donor ligand in the coordination complexes with the aid of nitrogen from pyridine ring and azomethine group as well as sulfur from thio group. The compound can either coordinate in the neutral form or in the monodeprotonated form. Being established biologically active compounds, transition metal complexes of pyridine containing thiosemicarbazones attracted much interest from scientists. Mn(II) complexes of thiosemicarbazones with substituted pyridine show antituberculosis activity [8]. Scovill *et al.* reported that Cu(II) complexes of substituted pyridine containing thiosemicrabazone showed antimalarial and antileukemic activities [9]. Later some of the reports showed that Cu(II) and Ni(II) complexes of benzoylpyridine and pyridine-2-formaldehyde thiosemicarbazones exhibit cytotoxic, antifungal, antioxidant, anticancer and antimicrobial properties [10-14]. Catalytic properties of Pd(II) complexes of 2-formylpyridine was reported by Paul *et al.* [15]. It was found that Cd(II) complexes of thiosemicarbazones containing pyridine as a substituent act as anitibacterial agents [16]. Taking inspiration from these findings we decided to synthesis a new substituted thiosemicarbazone and its metal complexes.

Thus the present chapter discusses the synthesis and characterization of 6-bromopyridine-2-carbaldehyde-N^4,N^4-dimethylthiosemicarbazone (Hbpdmt) and its complexes using Mn(II), Ni(II), Cu(II), MoO_2(II), Pd(II) and Cd(II) ions.

4.2. Experimental

4.2.1. Materials

6-Bromopyridine-2-carbaldehyde (Alfa Aesar), N^4,N^4-dimethylthiosemi carbazide (Sigma Aldrich), $Mn(OAc)_2 \cdot 4H_2O$ (Alfa Aesar), $NiBr_2$ (Sigma Aldrich), $Ni(OAc)_2 \cdot 4H_2O$ (Alfa Aesar), $Cu(NO_3)_2 \cdot 3H_2O$ (E-Merck), $MoO_2(acac)_2$ (Sigma Aldrich), $PdCl_2$ (Sigma Aldrich), $Cd(OAc)_2 \cdot 2H_2O$ (Alfa Aesar),

CH_3OH (Spectrochem), CH_3CN (Spectrochem) and DMF (Spectrochem) were of analar grade and used without further purification.

4.2.2. Syntheses of 6-bromopyridine-2-carbaldehyde-N^4,N^4-dimethylthiosemicarbazone (Hbpdmt)

The compound is synthesized by condenzation of 6-bromopyridine-2-carbaldehyde (0.186 g, 1 mmol) with N^4,N^4-dimethylthiosemicarbazide (0.138 g, 1 mmol) in ethanol (Scheme 4.2). The reaction was carried out in presence of three drops of glacial acetic acid to ensure completion of the reaction. Yellow colored solution obtained after 4 h reflection was kept under room temperature for three weeks. The yellow colored crystals of the compound obtained was separated, washed with ethanol and dried *in vacuo*.

Yield : (0.187 g) 65%. m.p: 162 °C.
Elemental Anal. Found (Calcd)% : C 37.16 (37.64); H 3.68 (3.86); N 19.05 (19.51); S 11.51 (11.17).

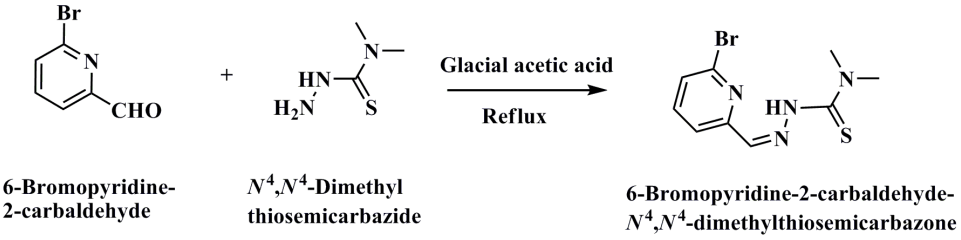

6-Bromopyridine-2-carbaldehyde | **N^4,N^4-Dimethyl thiosemicarbazide** | **6-Bromopyridine-2-carbaldehyde-N^4,N^4-dimethylthiosemicarbazone**

Scheme 4.1

4.2.3. Syntheses of complexes

4.2.3.1. Synthesis of $[Mn(bpdmt)_2]$ (16)

The complex **16** was synthesized by refluxing a hot methanolic solution of Hbpdmt (0.289 g, 1 mmol) with $Mn(OAc)_2 \cdot 4H_2O$ (0.122 g, 0.5 mmol) dissolved in methanol. Two drops of trimethylamine was added

prior to reaction. The contents were heated with stirring for about 6 h. The resultant clear solution was kept for 3 weeks. The product obtained was filtered, washed with methanol and dried *in vacuo*.

Yield : (0.348 g) 55%.
Elemental Anal. Found (Calcd)% : C 33.68 (34.24); H 3.43 (3.83);
N 17.50 (17.75); S 10.48 (10.16).

4.2.3.2. Synthesis of $[Ni(bpdmt)_2]\cdot DMF$ (17)

To synthesize complex **17**, the compound Hbpdmt (0.289 g, 1 mmol) was dissolved in 10 mL of acetonitrile and heated to ensure complete dissolution. To this hot solution, $NiBr_2$ (0.109 g, 0.5 mmol) in acetonitrile was added and refluxed for 2 h. The product obtained was separated by filteration, washed with acetonitrile and dried *in vacuo*. A small quantity of it was dissolved in 10 mL DMF and the resulted solution was kept for recrystallization. The brown blocked shaped crystals obtained after 3 weeks was separated and dried.

Yield : (0.393 g) 62%.
Elemental Anal. Found (Calcd)% : C 34.54 (34.26); H 2.82 (3.19);
N 17.20 (17.66); S 10.15 (10.16).

4.2.3.3. Synthesis of $[Ni(bpdmt)(OAc)(H_2O)_2]$ (18)

To a hot methanolic solution of Hbpdmt (0.289 g, 1 mmol), methanolic solution of $Ni(OAc)_2\cdot 4H_2O$ (0.248 g, 1 mmol) was added and refluxed for 4 h. The resultant hot solution was kept for 1 week and the compound obtained was separated, washed with methanol and dried *in vacuo*.

Yield : (0.203 g) 54.1%.
Elemental Anal. Found (Calcd)% : C 38.86 (38.43); H 5.29 (5.37);
N 17.18 (17.06); S 8.08 (8.55).

4.2.3.4. Synthesis of [Cu(bpdmt)$_2$] (19)

Hbpdmt (0.289 g, 1 mmol) dissolved in 10 ml of methanol and acetonirile. The mixture was refluxed for 4 h with $Cu(NO_3)_2 \cdot 3H_2O$ (0.121 g, 0.5 mmol). The brown product obtained was filtered, washed with methanol and dried *in vacuo*.

Yield : (0.302 g) 48%.
Elemental Anal. Found (Calcd)% : C 34.23 (34.00); H 3.27 (3.17); N 17.94 (17.62); S 10.43 (10.09).

4.2.3.5. Synthesis of [(MoO$_2$(bpdmt))$_2\mu^2$S] (20)

In order to synthesize complex **20**, a methanolic solution of Hbpdmt (0.289 g, 1 mmol) was refluxed with $MoO_2(acac)_2$ (0.326 g, 1 mmol), in 10 mL methanol. The reaction was carried out in the presence of two drops of triethylamine to ensure deprotonation of the thiosemicarbazone. After refluxing for 1 h, KNCS (0.101 g, 1 mmol) was added. The reaction was continued for 3 more hour. The product obtained was separated, washed with acetonitrile and dried *in vacuo.*

Yield : (0.365 g) 42%.
Elemental Anal. Found (Calcd)%: C 25.54 (25.13); H 2.16 (2.34); N 13.20 (13.03); S 10.82 (11.18).

4.2.3.6. Synthesis of [Pd(bpdmt)Cl] (21)

The complex **21** was synthesized by heating Hbpdmt (0.289 g, 1 mmol) dissolved in 10 mL acetonitrile with a hot methanolic solution of $PdCl_2$ (0.177 g, 1 mmol) under reflux for 6 h. The orange product obtained was separated by filtration, washed with acetonitrile and dried *in vacuo*.

Yield : (0.267 g) 62%.
Elemental Anal. Found (Calcd)% : C 25.55 (25.25); H 2.71 (2.35); N 13.16 (13.09); S 7.05 (7.49).

4.2.3.7. Synthesis of [Cd(bpdmt)$_2$] (22)

Synthesis of complex **22** was accomplished by reaction of Hbpdmt (0.289 g, 1 mmol) dissolved in 10 mL methanol with a methanolic solution of $Cd(OAc)_2 \cdot 2H_2O$ (0.133 g, 0.5 mmol) under reflux condition. The yellow colored solution obtained after 3 h, was kept for 2 weeks. The product obtained was filtered, washed with methanol and dried *in vacuo*.

Yield	:	(0.461 g) 67%.
Elemental Anal. Found (Calcd)%	:	C 30.73 (30.57); H 3.14 (2.94); N 16.40 (16.36); S 9.68 (9.37).

4.2.4. Physico-chemical techniques

4.2.4.1. Elemental analysis

Elemental analyses of the compounds were done on a Vario EL III CHNS elemental analyzer at the Sophisticated Analytical Instrument Facility, Cochin University of Science and Technology, Kochi-22, Kerala, India.

4.2.4.2. Magnetic susceptibility measurements

The magnetic susceptibility measurements of the complexes were taken on a Vibrating sample Magnetometer using $Hg[Co(SCN)_4]$ as a calibrant at the SAIF, Indian Institute of Technology, Madras.

4.2.4.3. Molar conductivity measurements

The conductivity measurements of the complexes were done in 10^{-3} M DMF solution on a Systronic model 303 direct reading conductivity meter at room temperature at the Department of Applied Chemistry, Cochin University of Science and Technology, Kochi, India.

4.2.4.4. Spectroscopic characterization

The infrared spectra of Hbpdmt and complexes **16-22** were recorded on a JASCO FT-IR-5300 spectrometer in 4000-400 cm^{-1} range using KBr

pellets. The electronic spectra of the prepared compounds were recorded in DMF solution (10^{-3} and 10^{-5} M) on a Thermo Scientific Evolution 220 UV-vis Spectrophotometer in the 200-900 nm range. ^{1}H NMR spectra of Hbpdmt and complexes **21** and **22** were recorded using Bruker AMX 400 FT-NMR Spectrometer at the Sophisticated Analytical Instrument Facility, Cochin University of Science and Technology, Kochi, India. The Electron Paramagnetic Resonance spectra of complex **19** were recorded in the solid state at 298 K and at 77 K in DMF on a Varian E-112 with 100 kHz modulation frequency, 2 G modulation amplitude and 9.1 GHz microwave frequency at the Sophisticated Analytical Instrumentation Facility, Indian Institute of Technology, Bombay, India.

4.2.4.5. Thermogravimetric analysis

The TG-DTA analysis of complex **18** was carried out using a Perkin Elmer Pyris Diamond TG-DTA analyzer in a nitrogen atmosphere. The compound was heated at a rate of 10 °C min^{-1} in the 50-700 °C range at the Sophisticated Analytical Instrument Facility, Cochin University of Science and Technology, Kochi, India.

4.2.5. Single crystal X-ray diffraction studies

The single crystal X-ray diffraction studies of Hbpdmt and complex **17** were carried out using a Bruker SMART APEXII CCD diffractometer at the Sophisticated Analytical Instrumentation Facility, Cochin University of Science and Technology, Kochi, India. Data acquisition was done using Bruker SMART software and data integration using Bruker SAINT software [17]. Absorption corrections were carried out using SADABS based on Laue symmetry using equivalent reflections [18]. The structure was solved by direct methods and refined by full-matrix least-squares calculations with the SHELXL-2014/7 software package [19]. The graphic tools used were DIAMOND version 3.2g [20] and ORTEP-3 [21].

4.3. Results and discussion

Analytical data of the compounds are presented in Sections 4.2.2 and 4.2.3, and structures of the compounds were assigned on this basis.

4.3.1. Characterization of 6-bromopyridine-2-carbaldehyde-N^4,N^4-dimethyl thiosemicarbazone (Hbpdmt)

4.3.1.1. Infrared spectrum

The formation of Hbpdmt through condensation of aldehyde with thiosemicarbazide was confirmed from the band at 1587 cm^{-1} which was assigned to azomethine C=N bond stretching vibration. The ν(C=S) vibrations are observed at 1434 and 887 cm^{-1}. The band at 1085 cm^{-1} corresponds to ν(N–N) bond. Absence of any band at 2600 cm^{-1} confirms that thiosemicarbazone exists in the thio-amido in solid state. The pyridine unit in the compound was observed as a band at 786 cm^{-1} [11]. The infrared spectrum of Hbpdmt is presented in Fig. 4.1.

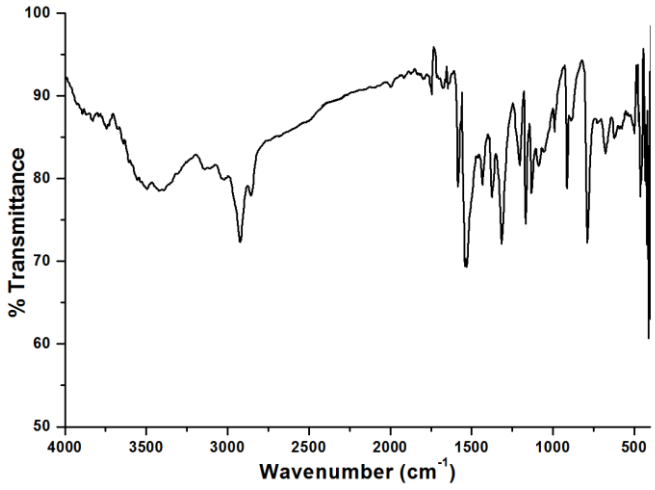

Fig. 4.1. Infrared spectrum of Hbpdmt.

4.3.1.2. Electronic spectrum

Electronic spectrum of Hbpdmt was recorded in 10^{-5} M solution in DMF. The compound gave a broad spectrum with maximum absorption at 317 nm with $\varepsilon = 7.2\times10^4$ was due to π–π^* and n– π^* transitions resulted from the pyridine group and aromatic ring. The electronic spectrum of Hbpdmt is given in Fig. 4.2.

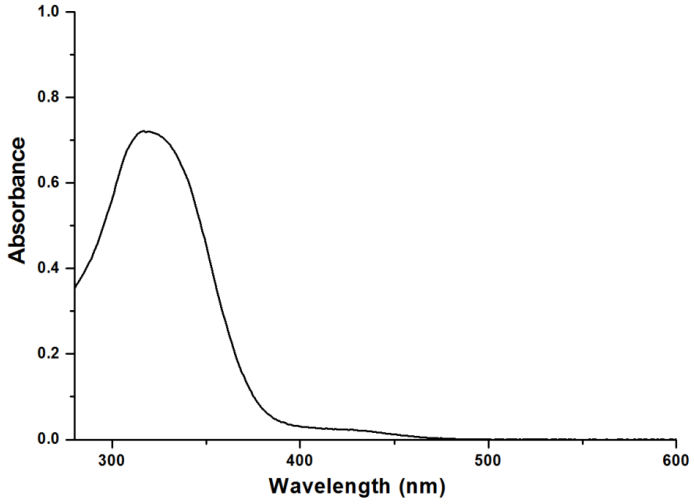

Fig. 4.2. Electronic spectrum of Hbpdmt.

4.3.1.3. ^{1}H NMR spectrum

^{1}H NMR spectrum of Hbpdmt was recorded in DMSO-d_6 using TMS as the internal standard. The N(3)–H proton shows a large downward shift to 11.28 ppm. This is resulted from the intramolecular hydrogen exhibited by this hydrogen, evident from the crystal structure. This singlet disappears in the D_2O exchanged ^{1}H NMR spectrum of the compound, confirmed the presence exchangeable proton. The aromatic protons gave a multiplet in the region 7.60-8.12 ppm. The methyl protons gave two singlets close to each other at 3.31 and 3.32 ppm, corresponds to 6 protons. The ^{1}H NMR and D_2O exchanged ^{1}H NMR spectra of Hbpdmt are given in Fig. 4.3.

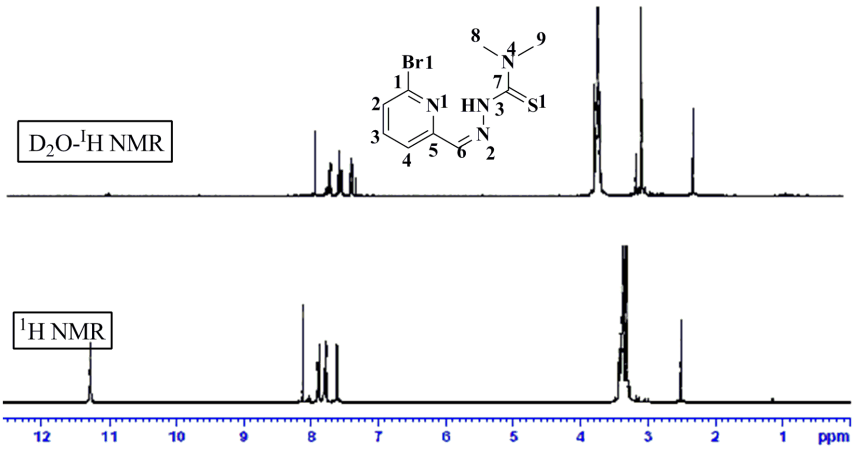

Fig. 4.3. ^{1}H NMR spectrum and D_2O exchanged ^{1}H NMR spectrum of Hbpdmt.

4.3.1.4. Single crystal X-ray diffraction studies

The compound Hbpdmt crystallized into yellow needle shaped crystals from the mother liquor. The compound crystallized into monoclinic space group *C*2/c. A crystal of size 0.40 × 0.20 × 0.15 mm^3, suitable for diffraction studies were isolated from the solution and mounted on Bruker SMART APEXII CCD diffractometer. The equipment is fitted with a graphite monochromated Mo Kα (λ = 0.71073 Å) radiation. The non-hydrogen atoms were refined anisotropically and the C–H protons were placed at a distance 0.93–0.96 Å guided by differece map. U_{iso}=1.2U_{eq} was assigned for all hydrogen atoms except, for methyl groups, for which U_{iso}=1.5U_{eq}. The N(3)–H(3) bond distance was restrained to 0.88±0.01 Å using DFIX instruction. Table 4.1 describes all the crystal refinement parameters and structure data.

Table 4.1. Crystal data and structure refinement parameters of Hbpdmt

Parameters	**Hbpdmt**
Empirical formula	$C_9H_{11}BrN_4S$
Formula weight	287.18
Color	Yellow
Temperature/K	296 (2)
Crystal system	monoclinic
Space group	$P2_1/n$
Cell parameters	
a (Å)	17.8225(11)
b (Å)	11.5372(11)
c (Å)	13.8030(11)
$\alpha = \gamma$ (°)	90
β (°)	128.593(6)
Volume (Å^3)	2218.3(4)
Z	8
Calculated density, ρ (g cm^{-3})	1.720
Absorption coefficient, μ (mm^{-1})	3.866
F(000)	1152
Crystal size (mm^3)	0.40 x 0.20 x 0.15
θ range for data collection (°)	2.925 to 28.375
Limiting indices	$-22 \le h \le 23$, $-13 \le k \le 15$, $-17 \le l \le 18$
Reflections collected	8287
Independent reflections	2779 [R(int) = 0.0347]
Data/restraints/parameters	2779 / 1 / 142
Goodness-of-fit on F^2	1.092
Final R indexes [I>2σ (I)]	R_1 = 0.0354, wR_2 = 0.0802
Final R indexes [all data]	R_1 = 0.0579, wR_2 = 0.0869
Largest diff. peak and hole (e Å^{-3})	0.280 / -0.794

$R_1 = \Sigma||F_o| - |F_c|| / \Sigma|F_o|$
$wR_2 = [\Sigma w(F_o^2-F_c^2)^2 / \Sigma w(F_o^2)^2]^{1/2}$

The ORTEP diagram of the compound with 50% probability is given in Fig. 4.4. The compound Hbpdmt adopts *Z* conformation with respect to C=N bond, confirmed from the C(5)–C(6)–N(2)–N(3) torsion angle of 0.2(4)°. The sulfur atom was found to adopt a *trans* conformation with respect to azomethine nitrogen in all the thiosemicarbazones in the present study. But for Hbpdmt the S(1) atom lies *cis* with respect to N(2), confirmed from N(2)–N(3)–C(7)–S(1) torsion angle 2.6(3)°. The C(6)–N(2) bond length 1.278(3) Å is close to C=N bond length of similar compounds [22]. Further the existence of Hbpdmt in the thioamido form is confirmed from C(7)–S(1) bond length of 1.670(2) Å, which is similar to the formal C=S bond length [23]. Selected bond lengths and bond angles are described in Table 4.2.

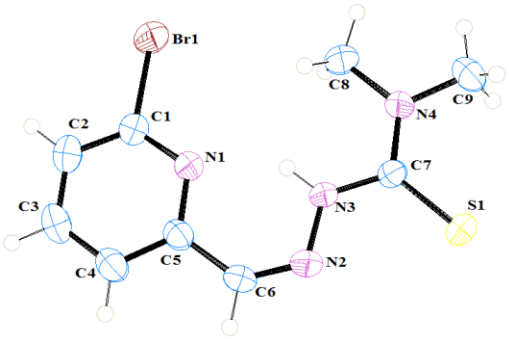

Fig. 4.4. ORTEP diagram for Hbpdmt with 50% ellipsoid probability.

Table 4.2. Selected bond parameters of Hbpdmt

Bond length (Å)		**Bond angle (°)**	
C(1)–Br(1)	1.886(2)	C(5)–C(6)–N(2)	131.6(2)
C(6)–N(2)	1.278(3)	C(6)–N(2)–N(3)	117.20(2)
N(2)–N(3)	1.352(3)	N(3)–C(7)–S(1)	122.68(16)
C(7)–S(1)	1.670(2)	N(3)–C(7)–N(4)	113.60(2)
C(7)–N(3)	1.361(3)		

The compound contains 8 molecules in the unit cell. Hbpdmt showed an intramolecular interaction N(3)–H(3)···N(1) with D···A distance of 2.661(3) Å, taking the benefit of *Z* conformation about C(6)–N(2) bond.

The adjacent molecules in the crystal lattice are connected with the aid of an intermolecular hydrogen bonding C(6)–H(3)···S(1) with a D···A distance of 3.728(3) Å. This hydrogen bonding interaction connects the molecules in the crystal lattice along '*b*' axis (Fig. 4.5). Different layers were linked to one another with the help of a π···π interaction between the pyridine rings with Cg···Cg distance of 3.746(18) Å. Thus the molecules in the crystal lattice were extended along *b* axis as shown in the packing diagram of Hbpdmt in Fig. 4.6. Table 4.3 gives various interactions present in Hbpdmt.

Table 4.3. Interaction parameters in Hbpdmt

Hydrogen bonding interactions				
D–H···A	D–H (Å)	H···A (Å)	D···A (Å)	D–H···A (°)
N(2)–H(2′)···S(1)[a]	0.88(9)	2.44(10)	3.30(16)	171(2)
N(5)–H(5′)···S(2)	0.88(9)	2.48(2)	3.35(16)	172(19)
π ···π interaction				
Cg(I)···Cg(J)	Cg···Cg (Å)	α (°)	β (°)	γ (°)
Cg(1)···Cg(1)[b]	3.746(18)	3	13.9	13.9

a = -x + ½ , y - ½, -z + ⅗ ; b = -x, y, ⅗ – z
Cg(1) = C(1), C(2), C(3), C(4), C(5), N(1); D= donor, A= acceptor, Cg= centroid
α (°) = Dihedral angle between planes I and J
β (°) = Angle between Cg(I)–Cg(J) vector and Cg(J) perp
γ (°) = Angle between Cg(I)–Cg(J) vector and Cg(I) perp

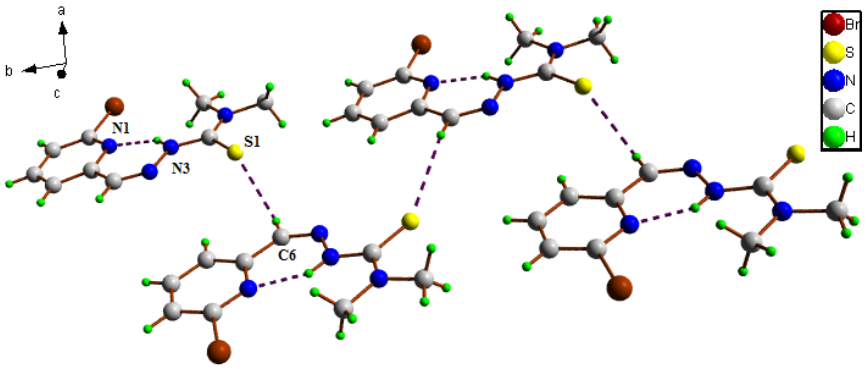

Fig. 4.5. Hydrogen bonding interactions in Hbpdmt.

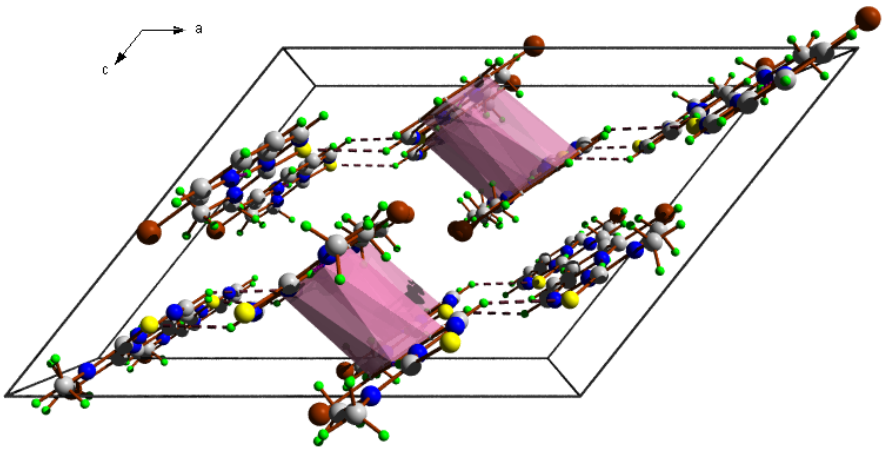

Fig. 4.6. Packing diagram of Hbpdmt viewed along '*b*' axis enclosing hydrogen bonding and π···π interaction.

4.3.2. Characterization of complexes of Hbpdmt

The thiosemicarbazone Hbpdmt acts as an NNS donor ligand in its complexes by the virtue of azomethine nitrogen, pyridine nitrogen and thiolate sulfur. The compound can either act as a neutral or monodeprotonated ligand. We synthesized seven complexes of transition metals like Mn(II), Ni(II), Cu(II), MoO_2(II), Pd(II) and Cd(II). Of these, complexes **16, 19** and **22** were synthesized by refluxing the ligand and the metal salt in 2:1 ratio. The complex **17** synthesized by refluxing ligand with the metal salt in 2:1 ratio followed by recrystallization form DMF. The complexes **18** and **21** were synthesized by refluxing the ligand and metal salt in 1:1 ratio. To synthesize complex **20** the ligand, metal salt and potassium thiocyanate were mixed in 1:1:1 ratio and refluxed.

4.3.2.1. Molar conductivity and magnetic susceptibility measurements

Molar conductivity as well as magnetic susceptibility measurements gave insight into the oxidation state of the metal in the complex, with which we could predict the coordination environment. The molar conductivity

measurements were taken in 10^{-3} M solution of DMF. It is observed that the compounds give a molar conductivity between 1.3-18 $ohm^{-1}cm^2mol^{-1}$, well below the value of uni-univalent electrolyte (60-90 $ohm^{-1}cm^2mol^{-1}$), justifies the non conducting nature of all the complexes.

The complex **16** gave a magnetic moment value of 5.24 B.M., indicate the presence of five unpaired electrons in the complex as the value is consistent with high spin Mn(II) ion [24]. The magnetic moments for complexes **17** and **18** are 2.92 and 2.96 B.M. respectively and are due to two unpaired electrons in the complex, indicating an octahedral geometry for Ni(II) complexes [25]. For $[Cu(bpdmt)_2]$ (**19**), the magnetic moment value of 1.72 B.M. which is consistent with presence of one unpaired electron in it [26]. Complexes **20, 21,** and **22** exhibited diamagnetic nature which is in agreement with the Mo(VI), low spin Pd(II) and d^{10} Cd(II) state of the metals in these complexes. The molar conductivity and magnetic moment values for the complexes are presented in Table 4.4.

Table 4.4. Molar conductivity and magnetic moment values of complexes of Hbpdmt

Compound	**λ_m (ohm^{-1} cm^2 mol^{-1})**	**μ_{eff} (B.M.)**
$[Mn(bpdmt)_2]$ (**16**)	1.3	5.24
$[Ni(bpdmt)_2]\cdot DMF$ (**17**)	17.8	2.92
$[Ni(bpdmt)(OAc)(H_2O)_2]$ (**18**)	16	2.96
$[Cu(bpdmt)_2]$ (**19**)	3.2	1.72
$[MoO_2(bpdmt)\mu^2S]$ (**20**)	9.9	0
[Pd(bpdmt)Cl] (**21**)	18	0.04
$[(Cd(bpdmt)_2]$ (**22**)	1.5	0

4.3.2.2. Infrared spectra

Infrared spectra of the complexes were recorded in the range 400-4000 cm^{-1} using KBr pellets. The infrared spectrum gives us insight into the nature of coordinating atoms of a complex. The tentative assignments of infrared stretching frequencies for various groups present in the complexes and a comparison with the ligand is listed in Table 4.5. The extend of shift in the vibrational frequencies for various groups compared to that of Hbpdmt justify coordination of Hbpdmt to metal centre.

Table 4.6. Infrared spectral assignments (cm^{-1}) of Hbpdmt and its complexes

Compound	ν(C=N)	ν(C=N)[a]	ν(C=S)/ ν(C–S)	ν(N–N)	ν(py)	ν(M–N_{azo})
Hbpdmt	1587	---	1434, 887	1085	621	---
[Mn(bpdmt)$_2$] (**16**)	1594	1491	1409, 868	1117	652	430
[Ni(bpdmt)$_2$]·DMF (**17**)	1581	1498	1403, 863	1110	640	468
[Ni(bpdmt)(OAc) (H_2O)$_2$] (**18**)	1556	1491	1409, 856	1117	633	424
[Cu(bpdmt)$_2$] (**19**)	1556	1486	1409,792	1123	652	462
[MoO_2(bpdmt)μ^2S] (**20**)	1575	1486	1415, 868	1161	671	462
[Pd(bpdmt)Cl] (**21**)	1576	1498	1415, 863	1161	665	468
[Cd(bpdmt)$_2$] (**22**)	1576	1491	1403, 894	1161	671	443

a = newly formed C=N

The manganese complex showed a shift in the stretching frequencies for ν(C=N) from 1587 cm^{-1} of Hbpdmt to 1594 cm^{-1} for [Mn(bpdmt)$_2$] (**16**), suggesting the coordination of azomethine nitrogen to the metal ion. The increase in the ν(N–N) stretching frequency and shift in the ν(C=S)/ν(C–S) stretching accompanying appearance of a new band at 1491 cm^{-1} correspond to newly formed ν(C=N), which indicate that Hbpdmt was coordinated to the metal ion in the deprotonated form [24]. The pyridine ring in the

complex gave a band at 652 cm^{-1}. This band showed blue shift as compared to free ligand, confirms the coordination of pyridyl nitrogen to the metal. The ν(Mn–N_{azo}) stretching gave a band at 430 cm^{-1}. The infrared spectrum of complex **16** is represented in Fig. 4.7.

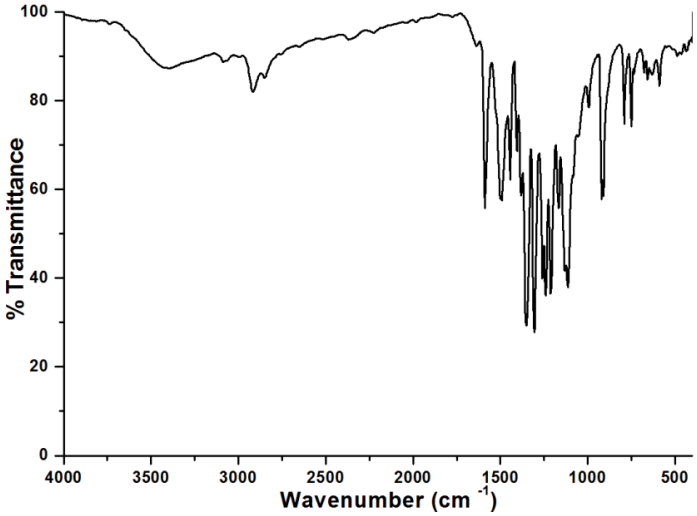

Fig. 4.7. Infrared spectrum of complex $[Mn(bpdmt)_2]$ (**16**).

Both $[Ni(bpdmt)_2]\cdot DMF$ (**17**) and $[Ni(bpdmt)(OAc)(H_2O)_2]$ (**18**) exhibited shift in the ν(C=N) stretching frequency to lower energy suggesting the coordination of metal *via* azomethine nitrogen. The coordination of ligand in the monodeprotonated form was confirmed from the shift in the ν(N–N) stretching frequency along with appearance of a new band at 1498 cm^{-1}. This was further confirmed from the shift in ν(C=S)/ν(C–S) stretching frequencies. The ν(Ni–N_{azo}) stretching were observed at 468 and 424 cm^{-1} respectively [27]. The infrared spectra for complexes **17** and **18** are presented in Figs. 4.8 and 4.9.

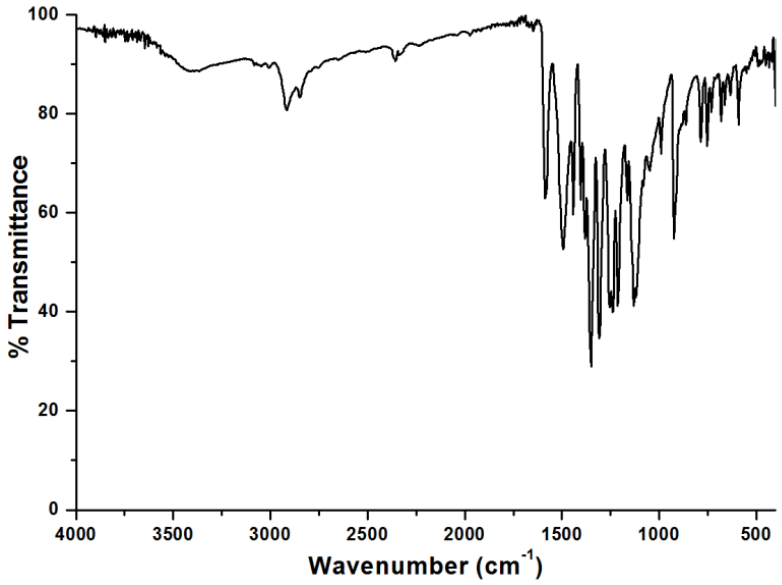

Fig. 4.8. Infrared spectrum for $[Ni(bpdmt)_2]\cdot DMF$ (**17**).

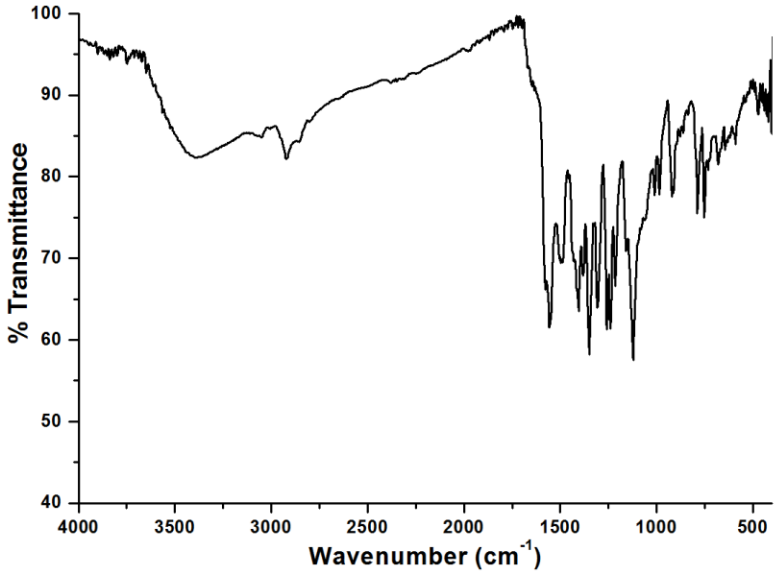

Fig. 4.9. Infrared spectrum for $[Ni(bpdmt)(OAc)\ (H_2O)_2]$ (**18**).

A shift in the ν(C=N) stretching vibration for Hbpdmt from 1587 cm^{-1} to 1556 cm^{-1} in the in $[Cu(bpdmt)_2]$ (**19**) gave an insight into coordination of azomethine nitrogen to Cu(II). Formation of a new C=N bond, gave a band at 1486 cm^{-1} accompanying a shift of ν(N–N) to higher and ν(C=S)/ν(C–S) to lower energies suggested the coordination of Hbpdmt in the monodeprotonated form. The coordination of pyridyl nitrogen is evident from the shift for pyridine stretching frequency to 652 cm^{-1} as that of free ligand (621 cm^{-1}). The Cu–N bond give a characteristic vibration at 462 cm^{-1} [14]. The infrared spectrum for complex **19** is presented in Fig. 4.10.

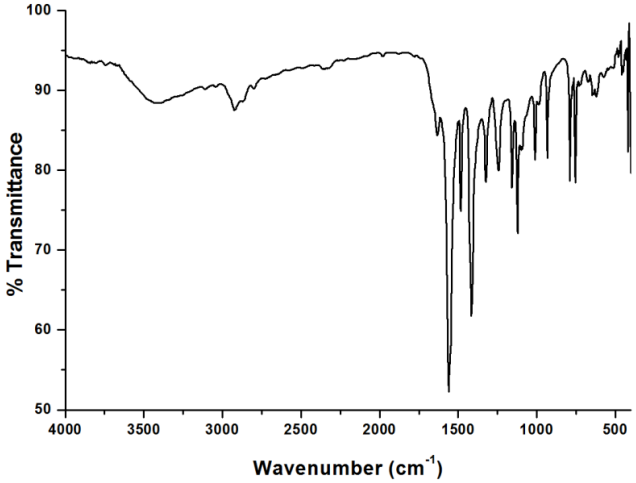

Fig. 4.10. Infrared spectrum of $[Cu(bpdmt)_2]$ (**19**).

The $[MoO_2(bpdmt)\mu^2S]$ (**20**) also showed a shift for the ν(C=N) and ν(C=S) stretching vibrations as that of other complexes. This indicates that Hbpdmt coordinates as monodeprotonated form in complex **20**. The *cis*-MoO_2(II) gives two vibrations at 860 and 940 cm^{-1} [28]. For complex **20**, these vibrations were observed at 868 and 964 cm^{-1}. Fig. 4.11 depicts the infrared spectrum for complex **20**.

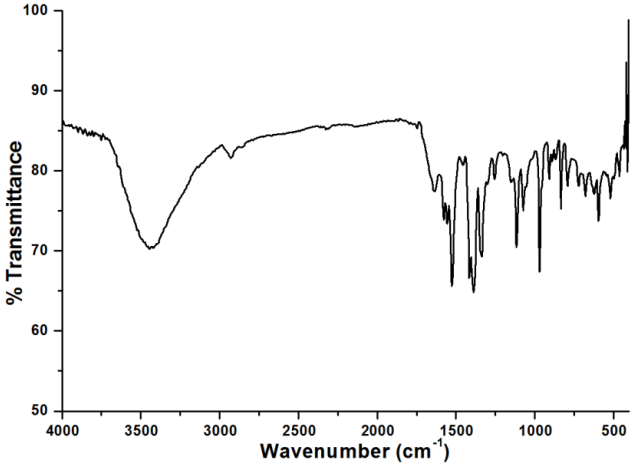

Fig. 4.11. Infrared spectrum of $[MoO_2(bpdmt)\mu^2S]$ (**20**).

The complexes [Pd(bpdmt)Cl] **(21)** and $[(Cd(bpdmt)_2]$ **(22)** exhibited a shift in the streching for ν(C=N) from 1587 of free Hbpdmt to 1576 cm^{-1} for both complexes, suggesting one of the coordination sites for metal was fulfilled by azomethine nitrogen. The presence of a new band at 1498 and 1491 cm^{-1} respectively for complexes **21** and **22** combined with a shift for the ν(N–N) stretching frequency to higher wavenumber (1161 cm^{-1}) suggested an extended electron delocalization in the whole molecule. This is possible only when the thiolate sulfur coordinate to the metal centre in the monodeprotonated state. The pyridine rings in the complex showed vibrations at 665 and 671 cm^{-1} for complexes **21** and **22** respectively and were showed a blue shift from that of free Hbpdmt [29]. The $M–N_{azo}$ bond formation gives a vibration at 468 cm^{-1} for complex **21** [30] and 443 cm^{-1} for complex **22** [31] corresponding to the coordination of azomethine nitrogen to metal ion. The infrared spectra of complexes **21** and **22** are presented in Figs. 4.12 and 4.13 respectively.

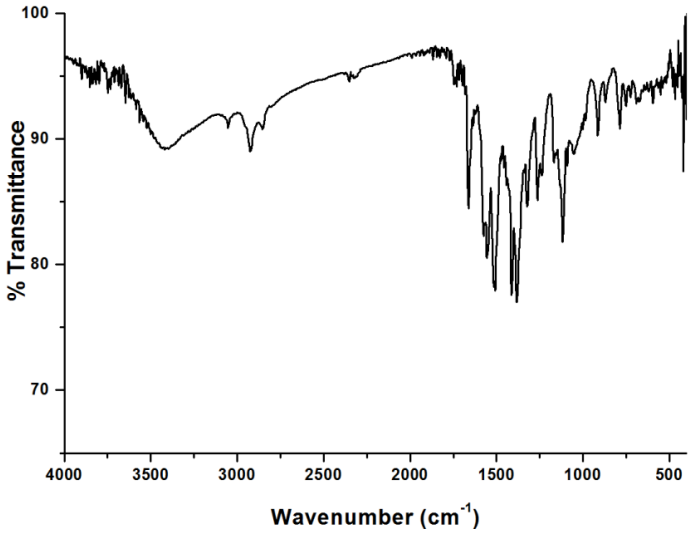

Fig. 4.12. Infrared spectrum of [Pd(bpdmt)Cl] **(21).**

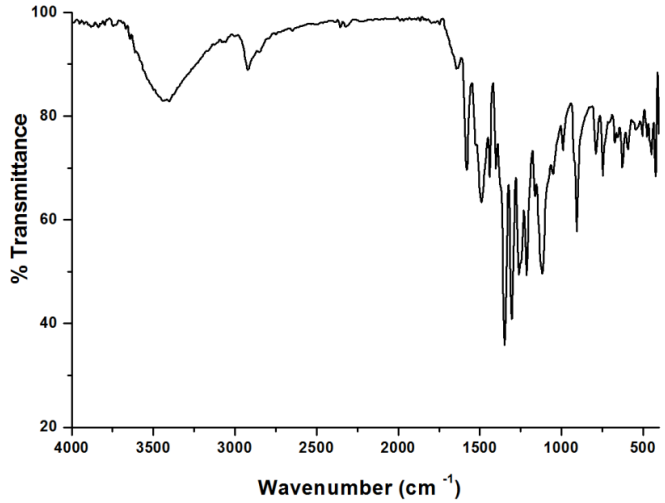

Fig. 4.13. Infrared spectrum of [(Cd(bpdmt)$_2$] **(22).**

4.3.2.3. Electronic spectra

The electronic spectra of the complexes were recorded in 10^{-3} and 10^{-5} M solution of DMF. The complex formation shifts the absorption of free Hbpdmt. This was ascribed to the elongation of C=S as well as

extended conjugation as a result of complexation [32]. The shift was also affected due to complexation *via* azomethine and pyridine nitrogen [33]. The complexes showed intralignad transitions with maximum absorption in the region 313-346 nm. The presence of unpaired electrons was confirmed from the *d-d* transitions exhibited by complexes **16** and **19**. The assignment of electronic absorption by Hbpdmt and its complexes are given in Table 4.6.

Table 4.6. Electronic spectral assignment (nm) of Hbpdmt and its complexes

Compound	**n–π*/ π–π*(nm) ($\varepsilon = 10^4$ M^{-1} cm^{-1})**	**LMCT (nm) ($\varepsilon = 10^4$ M^{-1} cm^{-1})**	**d-d (nm) (ε (M^{-1} cm^{-1}))**
Hbpdmt	317 (7.20)	---	---
[Mn(bpdmt)$_2$] (**16**)	328 (3.62)	437 (7.23)	674 (184)
[Ni(bpdmt)$_2$]·DMF (**17**)	325 (6.90), 372 (7.01)	400 (7.71),440 (8.51)	---
[Ni(bpdmt)(OAc) (H_2O)$_2$] (**18**)	345 (7.40)	444 (3.42)	---
[Cu(bpdmt)$_2$] (**19**)	346 (8.12)	---	583 (118)
[MoO_2(bpdmt)μ^2S] (**20**)	315 (9.05)	399 (4.10)	---
[Pd(bpdmt)Cl] (**21**)	313 (5.65), 382 (9.02)	488 (1.75)	---
[(Cd(bpdmt)$_2$] (**22**)	321 (3.42)	430 (7.94)	---

The complex [Mn(bpdmt)$_2$] (**16**) gave an absorption with maximum at 328 nm with molar absorption constant of 3.62×10^4 $M^{-1}cm^{-1}$ corresponding to intraligand transitions. The absorption showed marked shift from that of Hbpdmt confirming the formation of complex *via* coordination to $bpdmt^-$. The complex also gave ligand to metal charge transfer transition with maximum absorption at 437 nm with molar absorptivity 7.23×10^4 M^{-1} cm^{-1}. The electronic spectra of Hbpdmt and complex **16** are presented in Fig. 4.14. The Mn(II) complexes were expected to gave absorption in the visible region due to $^4E_g \leftarrow {}^6A_{1g}$ and $^4A_{1g}(^4G) \leftarrow {}^6A_{1g}$ transitions [24]. The complex **16** gave a broad band with maximum absorption at 674 nm (ε = 184 M^{-1} cm^{-1}). The visible spectrum of the complex **16** is depicted in Fig. 4.15.

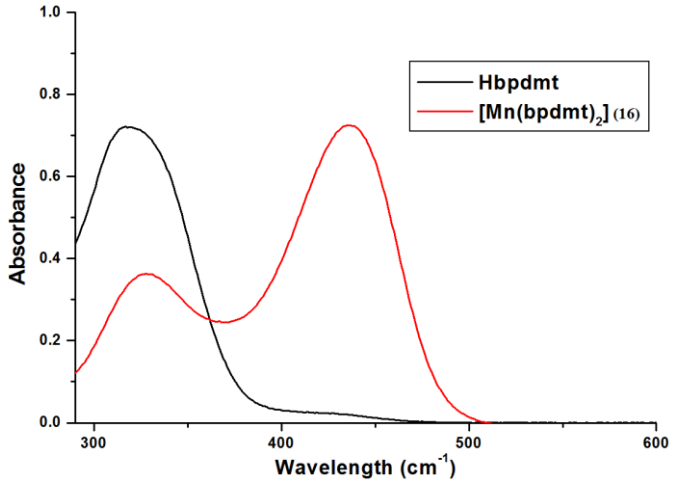

Fig. 4.14. Electronic spectra of Hbpdmt and complex **16**.

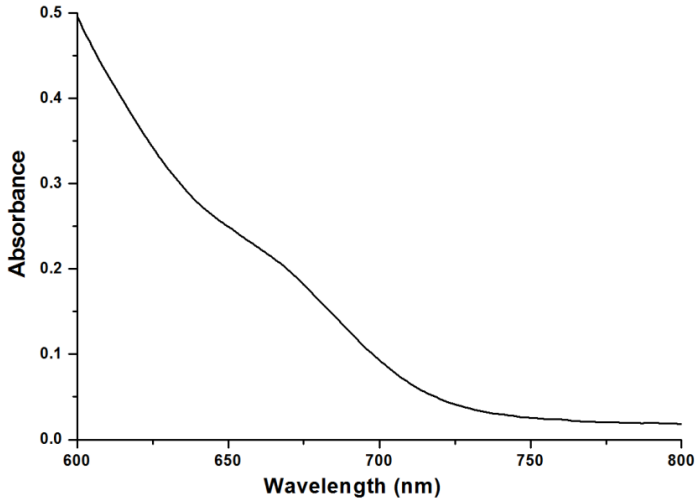

Fig. 4.15. Visible spectrum of $[Mn(bpdmt)_2]$ (**16**).

Electronic spectrum of $[Ni(bpdmt)_2]\cdot DMF$ (**17**) gave two absorption maxima 325 and 372 nm ($\varepsilon = 6.90 \times 10^4$ and 7.01×10^4 M^{-1} cm^{-1}) corresponding to intraligand transitions. However for the complex $[Ni(bpdmt)(OAc)(H_2O)_2]$ (**18**), a broad band with maximum absorption at 345 nm ($\varepsilon = 7.40 \times 10^4$ M^{-1} cm^{-1}) correspond to intraligand transitions.

These transitions were due to the unpaired electrons present in pyridine nitrogen and azomethine nitrogen, or due to the π electron cloud on pyridine ring. The electronic spectra of the complexes **17** and **18** along with Hbpdmt are presented in Fig. 4.16. The LMCT transitions for complexes **17** were observed at 400 and 440 nm (ε = 7.71 × 10^4 and 8.51 × 10^4 $M^{-1}cm^{-1}$), whereas for complex **18** this transition gave a broad band with absorptions maximum at 444 (ε = 3.40 × 10^4 $M^{-1}cm^{-1}$). These transitions were a result of transitions from pyridine and azomethine nitrogen to metal.

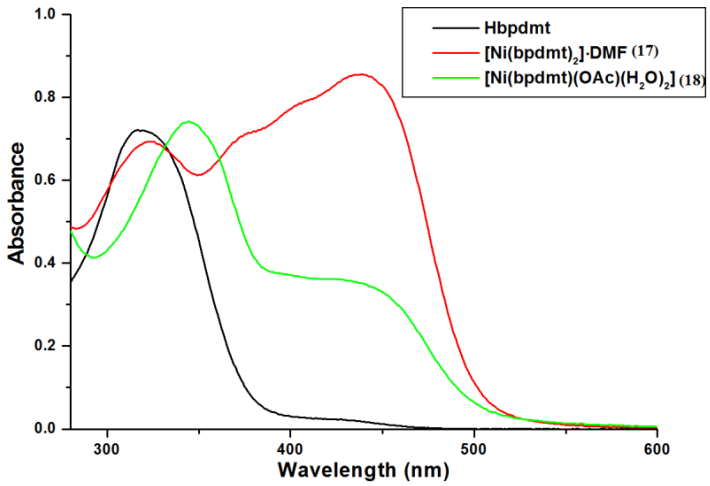

Fig. 4.16. Electronic spectra of Hbpdmt, complexes **17** and **18**

The intraligand transitions for $[Cu(bpdmt)_2]$ (**19**) gave a broad highly intense absorption due to highly intense LMCT transitions overlapping with intraligand transitions. A single band is observed at 346 nm with molar absorptivity 8.12 × 10^4 M^{-1} cm^{-1}. Fig. 4.17 depicts the electronic spectrum of complex **18** along with Hbpdmt. The *d-d* absorption in complex **19** appeared as a broad band with absorption maximum at 583 nm with molar absorptivity 118 M^{-1} cm^{-1}. The visible spectrum for complex **19** is presented in Fig. 4.18.

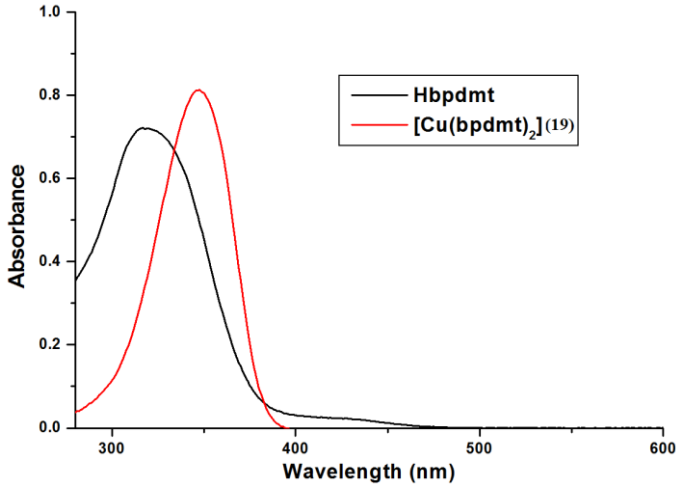

Fig. 4.17. Electronic spectrum of complex **19** and Hbpdmt.

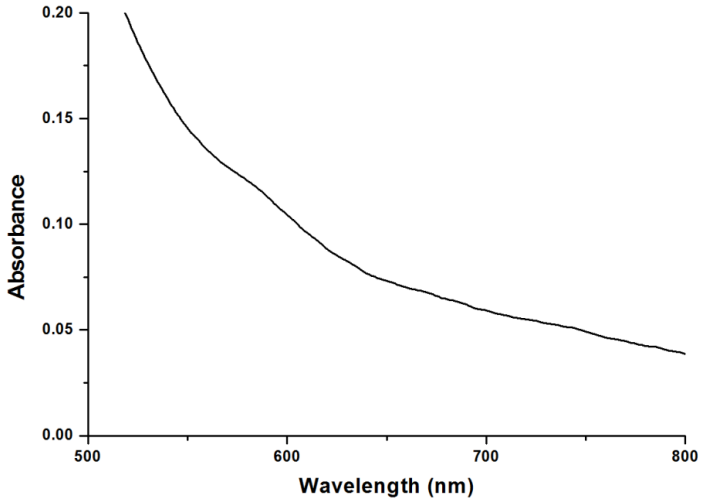

Fig. 4.18. Visible spectrum of $[Cu(bpdmt)_2]$ (**19**).

The electronic spectrum for complex **20**, depicted in Fig. 4.19 shows absorption maximum at 315 nm ($\varepsilon = 9.01 \times 10^4\ M^{-1}cm^{-1}$) corresponding to intraligand transitions due to unpaired and conjugated electrons in the complex. The absorption with a maximum at 399 nm with molar absorptivity $4.12 \times 10^4\ M^{-1}\ cm^{-1}$ was due LMCT transitions resulted from merging of Mo←S and Mo←N transitions.

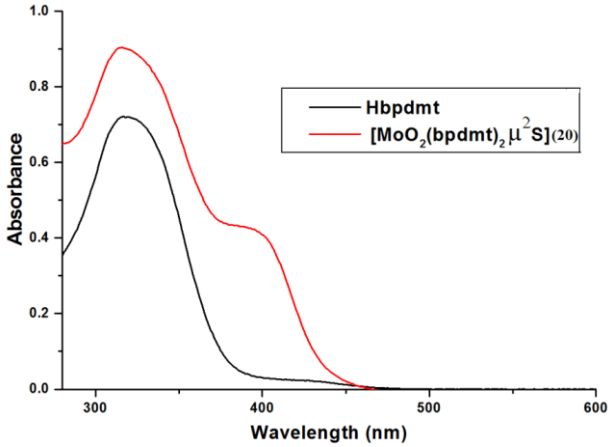

Fig. 4.19. Electronic spectrum of Hbpdmt and complex **20**.

The intraligand transitions for complex **21** accompany two transitions one with maximum absorption at 313 nm ($\varepsilon = 5.6 \times 10^4$ M^{-1} cm^{-1}) and another a broad band with absorption maximum at 382 nm ($\varepsilon = 5.6 \times 10^4$ M^{-1} cm^{-1}). These transitions were due to the presence of pyridine, azomethine nitrogen and conjugated π electrons in the complex. The complex gave absorption with maxima at 488 nm ($\varepsilon = 5.6 \times 10^4$ $M^{-1}cm^{-1}$) was assigned to LMCT transitions due to Pd←N and Pd←S. The electronic spectra for Hbpdmt and complex **21** are given in Fig. 4.20.

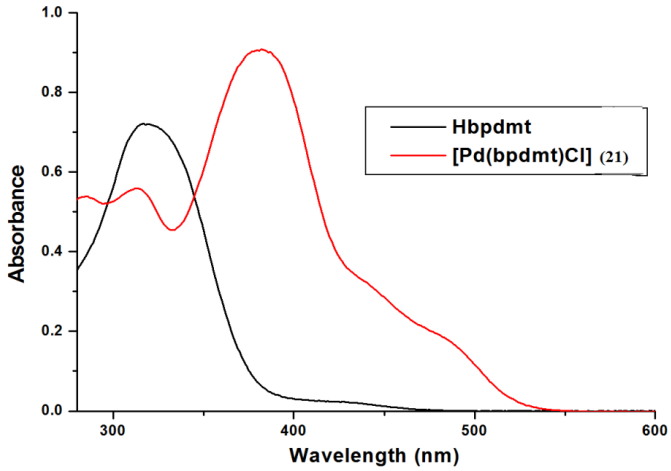

Fig. 4.20. Electronic spectra of Hbpdmt and complex **21**.

The complex **22** is characterized by a transition with maximum absorption at 321 nm with $\varepsilon = 3.4 \times 10^4$ M^{-1} cm^{-1} ascribed to intraligand transitions. There was a very intense absorption observed with absorption maximum at 430 nm with $\varepsilon = 7.9 \times 10^4$ M^{-1} cm^{-1} corresponding to MLCT transition. Fig. 4.21 shows the electronic spectra for complex **22** and Hbpdmt.

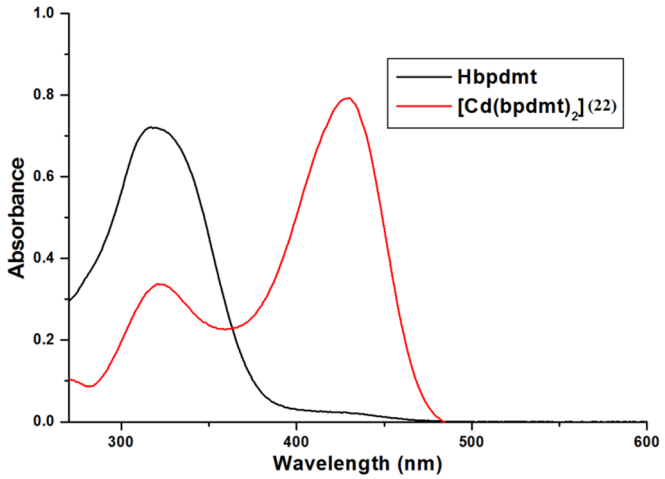

Fig. 4.21. Electronic spectra of complex **22** and Hbpdmt.

4.3.2.4. ^{1}H NMR spectra

The ^{1}H NMR spectra of complexes [Pd(bpdmt)Cl] (**21**) and [Cd(bpdmt)$_2$] (**22**) were recorded in DMSO-d_6 solution and compared with that of Hbpdmt. The observed spectra for both the complexes are presented in Figs. 4.22 and 4.23 respectively. It was found that the peak observed for N(3)–H at 11.28 ppm in the ^{1}H NMR spectrum of Hbpdmt (a) disappeared in the ^{1}H NMR spectrum of complex **21**. It was a confirmation for the complexation of Hbpdmt as a deprotonated ligand. There is a marginal shift observed for aromatic protons in the complex confirming the coordination of pyridyl nitrogen to the metal.

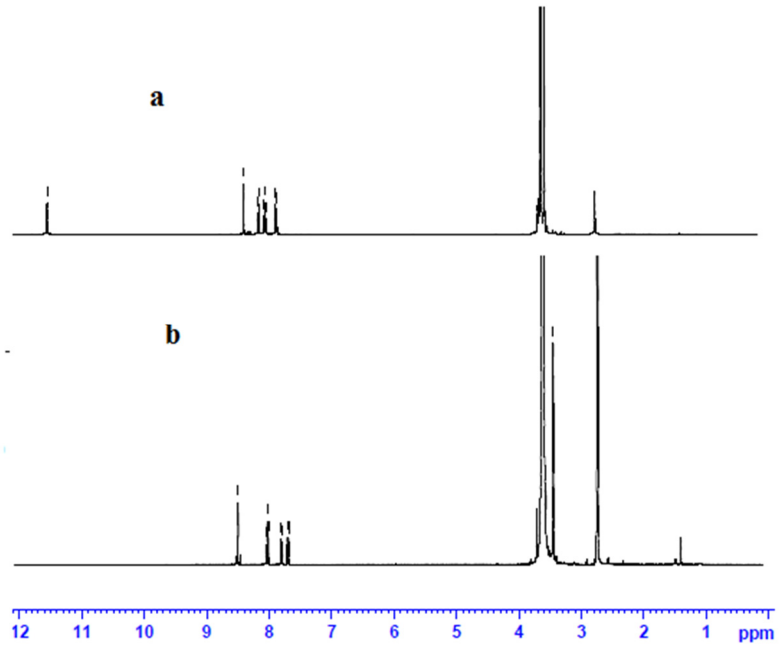

Fig. 4.22. ^{1}H NMR spectra of a) Hbpdmt b) complex **21** in DMSO-d_6 solution.

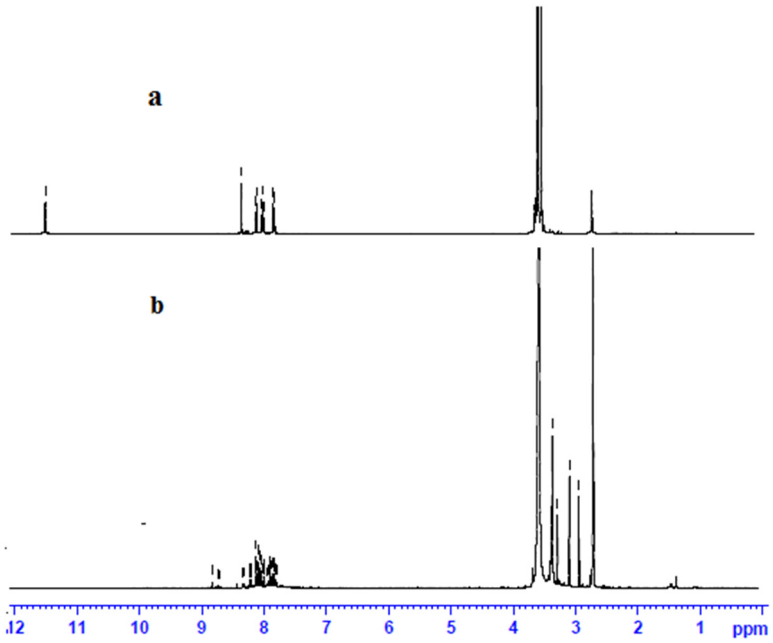

Fig. 4.23. ^{1}H NMR spectra of a) Hbpdmt b) complex **22** DMSO-d_6 solution.

The ^{1}H NMR spectrum for complex **22** gave a clear insight to the structure of the complex. The coordination of Hbpdmt in the monodeprotonated form was evident from the absence of a signal at 11.28 ppm, assigned to N(3)–H proton in the ligand. The presence of new bands is attributed to the presence of two bpdmt$^-$ in the complex **21**.

4.3.2.5. EPR spectrum for [Cu(bpdmt)$_2$] (19)

The EPR spectrum of the complex **19** was recorded in the polycrystalline state at 298 K and in DMF solution at 77 K. The EPR spectrum for complex **19** in the polycrystalline state as well as in DMF solution gives axial spectrum with two *g* values. The correct geometry is of Cu(II) determined on the basis of the ground state of the ion. It is reported that the ground state is found to be $d_{x^2-y^2}$ for an elongated octahedron, square pyramidal or square planar geometry. The value of *g* tensor gives an idea about the ground state of the electron in the metal ion [34].

The *g* pararmeters for the complex **19** in the polycrystalline was calculated from the simulated spectrum of the complex using Easy Spin 4.0.0 package [35]. Best fitted experimental (red) and simulated (blue) spectra is given in Fig. 2.24. The *g* parameters for the complex **19** were given as $g_\perp$ = 2.05 and $g_\parallel$ = 2.12 and g_{av} = 2.07.

The value of *G* for complex **19** is found to be 2.46 showing considerable interaction between metal centers [36]. The spectrum shows hyperfine splitting in the parallel as well as perpendicular region. The hyperfine coupling constants are calculated to as $A_\perp = 34 \times 10^{-4}$ cm^{-1} and $A_{II} = 182 \times 10^{-4}$ cm^{-1}. As a result of strong coordination of Hbpdmt to Cu(II) ion the hyperfine lines were further splitted to give superhyperfine lines with coupling constants $A_\perp$(N) = 23×10^{-4} cm^{-1} and A_{II}(N) = 29×10^{-4} cm^{-1}.

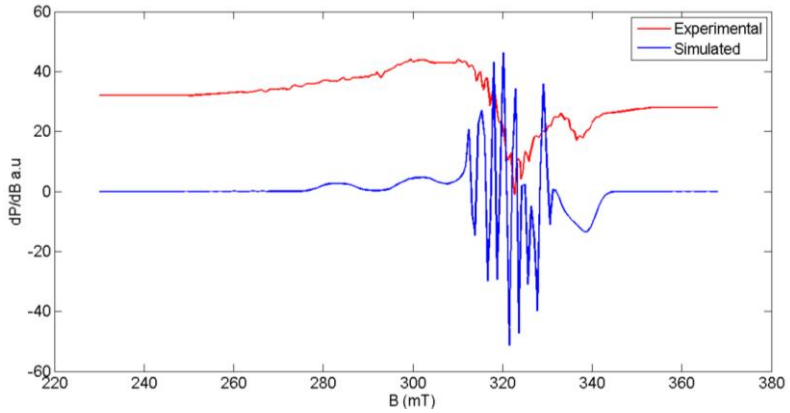

Fig. 2.24. EPR spectrum of complex **19** in polycrystalline state at 298 K.

In DMF solution at 77 K, complex **19** gives an axial spectrum with four hyperfine lines having g tensors $g_{\perp}$ = 2.02 and $g_{\parallel}$ = 2.15 and hyperfine coupling constants $A_{\perp}$ = 34 × 10^{-4} cm^{-1} and $A_{\parallel}$ = 192 × 10^{-4} cm^{-1}. As a result of strong coordination of nitrogen of pyridine and azomethine, these hyperfine lines were splitted further with coupling constants $A_{\perp}$(N) = 23 × 10^{-4} cm^{-1} and $A_{\parallel}$(N) =30 × 10^{-4} cm^{-1}. Fig. 4.25 elucidates the EPR spectrum of the complex **19** in DMF solution at 77 K.

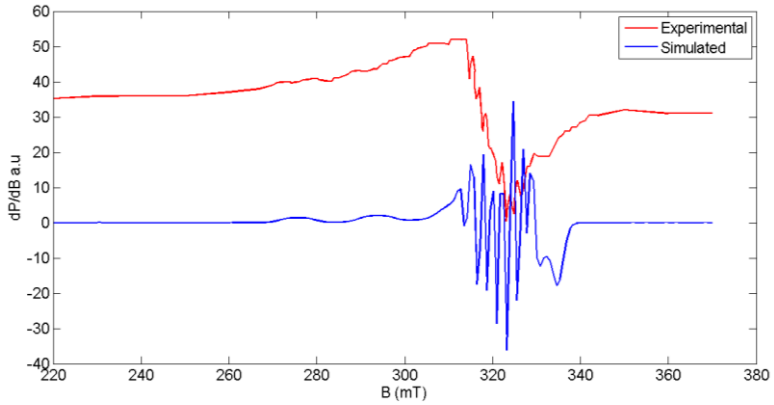

Fig.4.25. EPR spectrum of complex **19** in DMF at 77 K.

It is evident from the observation that the values for G as well as the condition $g_{\parallel} > g_{\perp} > 2.0023$, consistent with $d_{x^2-y^2}$ ground state for an

octahedral complex. The g_{av} calculated using equation $g_{av} = \frac{1}{3}(g_{\parallel} + 2g_{\perp})$, is found to be $g_{av} = 2.06$. In the present case $g_{\parallel} < 2.3$ and hence M–L bond is having a significant covalent character. [37]

For compound **19** α^2, β^2, γ^2, $K_{\parallel}$ and $K_{\perp}$ were found to be $\alpha^2 = 0.73$, $\beta^2 = 0.85$, $\gamma^2 = 0.58$, $K_{\parallel} = 0.62$ and $K_{\perp} = 0.43$ suggested that the complex was having a significant σ bonding accompanied by an out of plane π-bonding [38,39].

4.3.2.6. TG-DTA analysis

The thermal stability of a compound can be established using TG-DTA analysis. When solvent molecules are present in the complex, this method helps to determine whether the solvent is coordinated or not. The TG-DTA analysis of complex **18** was taken in a temperature range of 50-700 °C in nitrogen atmosphere. Fig. 4.26 represents thermogram for complex **19**. The complex shows a weight loss of 4.1% in the temperature range 205-336 °C with a calculated weight loss of 4.6% for 2 water molecules. At about 337 °C there was another weight loss of 9.7% corresponding to acetate unit with a calculated weight loss of 9.3%. It is found that the complex tends to decompose further with increase in temperature.

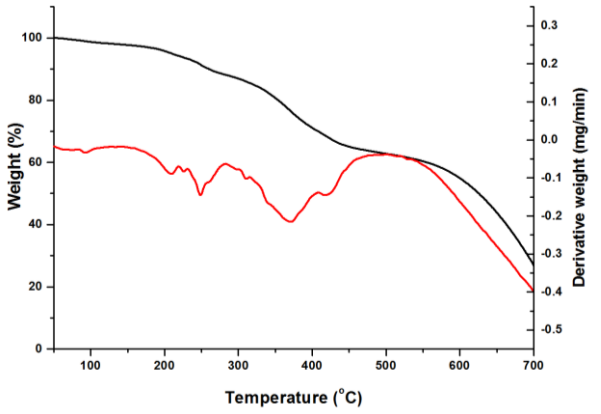

Fig. 4.26. Thermogram of complex **18**.

4.3.2.7. Single crystal X-ray diffraction studies of $[Ni(bpdmt)_2]\cdot DMF$ (17)

The single crystals suitable for X-ray diffraction studies were grown from DMF solution of the sample by slow evaporation at room temperature. A block shaped brown crystal of complex **17** of size 0.40 × 0.30 × 0.20 mm^3 was mounted on Bruker SMART APEXII CCD diffractometer. The crystal refinement data and other parameters are listed in Table 4.7. Non hydrogen atoms were refined anisotropically. The hydrogen atoms were identified from the Fourier map and were placed in idealized positions in the riding model approximation. The C–H distances were constrained to 0.93-0.96 with $U_{iso}(H) = 1.2U_{eq}$ and for methyl $U_{iso} = 1.5U_{eq}$.

The complex crystallized into monoclinic $P2_1/c$ space group. Two units of Hbpdmt coordinated to Ni(II) as NNS donor ligand giving rise to distorted octahedral geometry about the metal ion. The distorted geometry for the complex was evident from S(1)–Ni(1)–N(1), N(2)–Ni(1)–N(6) and N(5)–Ni(1)–S(2) bond angles of 157.15(14), 169.93(18) and 158.07(14)°, when a perfect octahedral complex was expected to show a bond angle of 180° [10]. The six coordination sites of the Ni(II) were occupied by atoms N(1), N(2), S(1) of the first unit and N(5), N(6) and S(2) of the second unit. A solvent unit was also present in the crystal lattice. The ORTEP diagram of the complex **17** with 50% probability is depicted in Fig. 4.27.

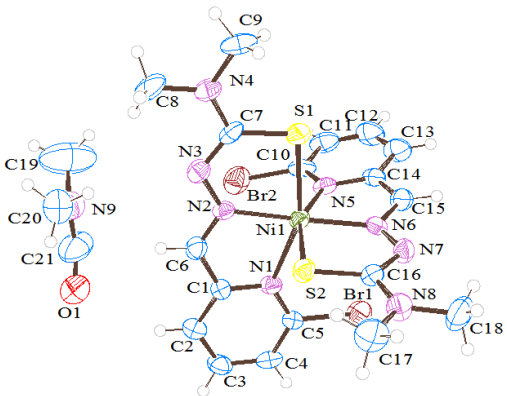

Fig. 4.27. ORTEP diagram for complex **17** with 50% probability.

Table 4.7. Crystal data and refinement parameters for $[Ni(bpdmt)_2]\cdot DMF$ (**17**)

Parameters	**$[Ni(bpdmt)_2]\cdot DMF$ (17)**
Empirical formula	$C_{21}H_{27}Br_2N_9NiOS_2$
Formula weight	704.16
Color	Brown
Temperature/K	296(2)
Crystal system	Monoclinic
Space group	$P2_1/c$
Cell parameters	
a (Å)	16.096(3)
b (Å)	9.8817(17)
c (Å)	18.151(4)
$\alpha = \gamma$ (°)	90
β(°)	108.871(11)
Volume (Å^3)	2731.8(9)
Z	4
Calculated density, ρ (g cm^{-3})	1.712
F(000)	1416
Crystal size (mm^3)	0.40 x 0.30 x 0.20
θ range for data collection (°)	2.378 to 28.305
Limiting indices	$-21 \leq h \leq 21$, $-13 \leq k \leq 12$, $-23 \leq l \leq 24$
Reflections collected	19319
Independent reflections	6802 [R(int) = 0.1529]
Data/restraints/parameters	6802 / 0 / 331
Goodness-of-fit on F^2	0.854
Final R indexes [I>2σ (I)]	$R_1 = 0.0524$, $wR_2 = 0.1025$
Final R indexes [all data]	$R_1 = 0.1709$, $wR_2 = 0.1337$
Largest diff. peak and hole (e Å^{-3})	0.765/-0.696

$R_1 = \Sigma||F_o| - |F_c|| / \Sigma|F_o|$
$wR_2 = [\Sigma w(F_o^2-F_c^2)^2 / \Sigma w(F_o^2)^2]^{1/2}$

The bond lengths increase in the order Ni(1)–$N(2)_{azo}$ < Ni(1)–$N(1)_{py}$ < Ni(1)–S(1) (1.996(5), 2.221(4) and 3.373(18) Å respectively). This trend is similar to that observed in previous reports [10]. The second unit of the ligand also exhibit similar results but the bond lengths are slightly less than the first unit of ligand (Table 4.9). The bond lengths for C(7)–S(1) and C(7)–N(3) were found to be 1.714(6) and 1.338(7) Å respectively which were nearly equal to C–S (1.82 Å) and C=N (1.29 Å) [40]. Similarly the second unit of the $bpdmt^-$ have C(16)–S(2) and C(16)–N(7) bond lengths 1.703(6) and 1.340(7) Å respectively. These observations are a clear evidence for both $bpdmt^-$ units to coordinate to the metal ion as a monodeprotonated form. The selected bond lengths and bond angles are listed Table 4.8.

Table 4.8. Selected bond parameters for complex **17**

Bond length (Å)		Bond angle (°)	
Ni(1)–S(1)	2.373(18)	N(2)–Ni(1)–S(2)	91.44(13)
Ni(1)–S(2)	2.368(17)	N(2)–Ni(1)–N(5)	110.18(19)
Ni(1)–N(1)	2.221(4)	N(6)–Ni(1)–S(2)	81.12(14)
N(1)–N(5)	2.203(4)	N(6)–Ni(1)–N(5)	77.82(19)
N(1)–N(2)	1.996(5)	S(1)–Ni(1)–S(2)	99.07(6)
N(1)–N(6)	2.012(5)	N(5)–Ni(1)–N(1)	90.14(16)
C(7)–N(3)	1.338(7)	N(2)–Ni(1)–N(6)	169.93(18)
N(3)–N(2)	1.350(6)	N(1)–Ni(1)–S(1)	157.15(14)
C(6)–N(2)	1.294(6)	N(5)–Ni(1)–S(2)	158.07(14)
C(16)–S(2)	1.703(6)	N(2)–Ni(1)–N(1)	78.40(18)
N(7)–C(16)	1.340(3)	N(2)–Ni(1)–S(1)	80.74(14)
N(6)–N(7)	1.338(6)	N(6)–Ni(1)–S(1)	93.66(13)
C(15)–N(6)	1.291(7)		

As a result of coordination of Hbpdmt to Ni(II) four new five membered rings were created *via* S(1)–C(7)–N(3)–N(2)–Ni(1), N(1)–C(1)–C(6)–N(2)–Ni(1), S(2)–C(16)–N(7)–N(6)–Ni(1) and N(5)–C(14)–C(15)–

N(6)–Ni(1). It is found that the adjacent rings S(1)–C(7)–N(3)–N(2)–Ni(1) /N(1)–C(1)–C(6)–N(2)–Ni(1) were twisted from each other by a dihedral angle of 4.6(2)° and the rings N(5)–C(14)–C(15)–N(6)–Ni(1)/N(5)–C(14)–C(15)–N(6)–Ni(1) were twisted with a dihedral angle of 5.8(2)°. It is also observed that the pyridine ring N(1)–C(1)–C(2)–C(3)–C(4)–C(5) and the ring N(1)–C(1)–C(6)–N(2)–Ni(1) were twisted by a dihedral angle of 6.3(3)°, as well as the rings N(5)–C(11)–C(12)–C(13)–C(14)–C(15) and the ring N(6)–C(15)–C(14)–N(5)–Ni(1) were also twisted by a dihedral angle of 8.8(3)°. This supports the fact that the complex is having a distorted octahedral geometry. Least square plane calculations and ring puckering studies show that the rings S(1)–C(7)–N(3)–N(2)–Ni(1) (Cg(1)), N(1)–C(1)–C(6)–N(2)–Ni(1) (Cg(3)) and N(5)–C(14)–C(15)–N(6)–Ni(1) (Cg(4)) were puckered. The ring Cg(1) adopts an envelope conformation with S(1) as the flap atom of the envelope with puckering parameters Q = 0.122(4) Å and φ = 181(3)°. The other two five membered rings also form an envelope confirmation with N(1) as the flap atom for ring Cg(3) and N(5) as the flap atom of the envelope for Cg(4) and have puckering amplitudes Q = 0.138(4) and 0.192(5) Å respectively and φ = 5(3) and 5(2)° respectively for Cg(3) and Cg(4).

Complex **17** show various interactions which facilitate the effective packing and thereby increase extend of crystal formation. The DMF molecule was connected to the complex *via* C(2)–H(2)···O(1) interaction with a D···A distance of 3.372(9) Å [40]. The adjacent crystal units were connected to each other, thus enhance efficiency of crystal packing through C(8)–H(8C)···S(1), C(19)–H(19C)···S(1) and C(18)–H(18B)···Br(1) hydrogen bonding with D···A distance of 3.891(7), 3.825(9) and 3.892(7) Å respectively [41]. Table 4.9 represents various intermolecular and intramolecular interactions in the complex **17**. The hydrogen bonding interactions are depicted in Fig. 4.28.

Table 4.10. Interaction parameters for complex **17**

Hydrogen bonding interactions				
D–H···A	D–H (Å)	H···A (Å)	D···A (Å)	D–H···A (°)
C(2)–H(2)···O(1)	0.93	2.53	3.372(9)	151
C(8)–H(8C)···S(1)[a]	0.96	2.95	3.891(7)	165.6
C(18)–H(18B)···Br(1)[b]	0.96	3.21	3.892(7)	129.5
C(19)–H(19C)···S(1)[c]	0.96	2.94	3.825(9)	153.3
C–H···π interactions				
C–H···Cg	C–H (Å)	H···Cg (Å)	C···Cg (Å)	C–H···Cg(°)
C(18)–H(18C)···Cg(5)[d]	0.96	2.94	3.676(7)	134

a = -x+2, -y, -z+1; b = -x+1, y-½, -z+½; c = x, -y+½, z+½; d = x, ½-y, -½+z
Cg(5)= N(1), C(1), C(2), C(3), C(4), C(5); D = donor, A = acceptor, Cg = centroid

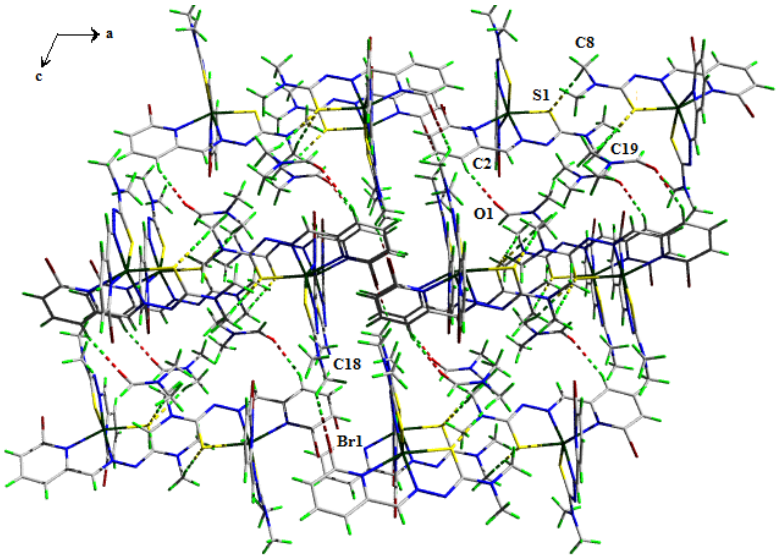

Fig. 4.28. Hydrogen bonding interactions in complex **17**.

The complex **17** also exhibits C–H···π interaction of the type C(18)–H(18C)···Cg(5) with H···Cg distance of 2.940 Å. This further strengthens the crystal packing by stitching various layers of the complex with each other as given in Fig. 4.29.

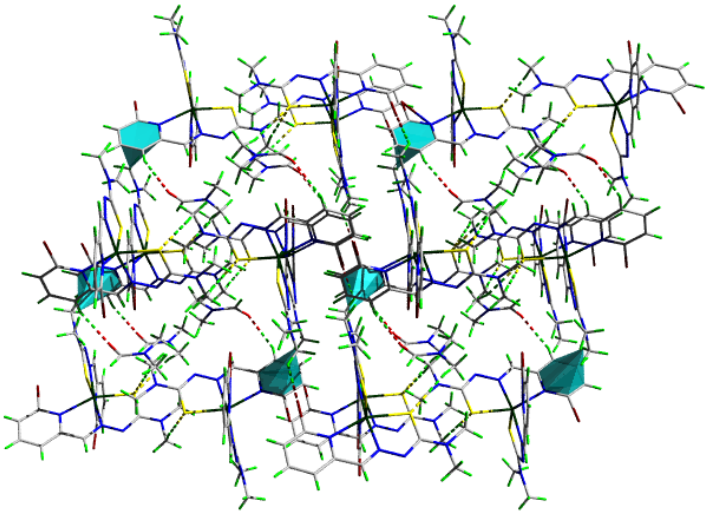

Fig. 4.29. C–H···π interaction along with hydrogen bonding interactions in complex **17**.

The packing diagram of the complex with crystallographic polyhedron is represented in Fig. 4.30. It is evident from the diagram that the complex units are aligned one over the other in a three dimensional fashion and give a clear image while viewing through '*b*' axis.

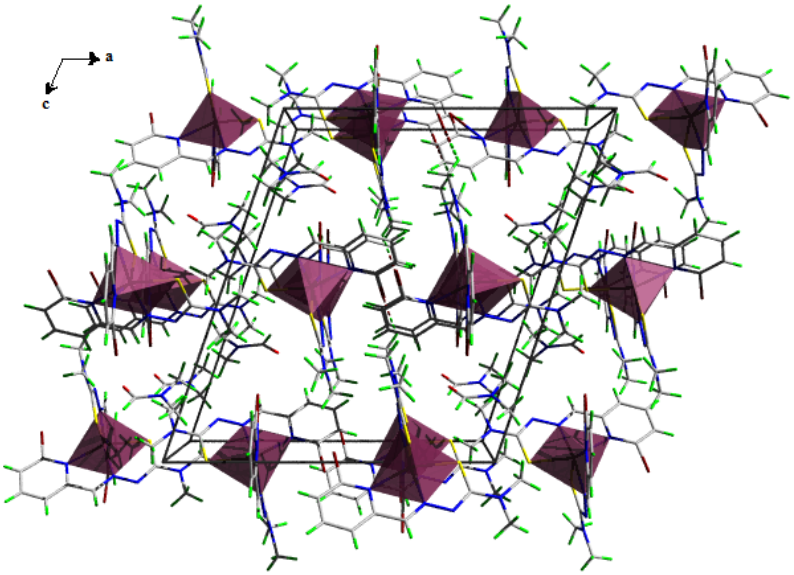

Fig. 4.30. Coordination polyhedron of complex **17** viewed along '*b*' axis.

4.4. Conclusion

Out of the five thiosemicarbazones included in this thesis only Hbpdmt is having a *cis* configuration about azomethine bond, resulted from intramolecular hydrogen bonding between pyridine nitrogen and N(3)–H. The ligand was found to coordinate in the monodeprotonated form in all of the complexes synthesized. Except complex **21**, all other complexes adopt a six coordinate geometry around the metal ions. The thiocyanate anion used in the synthesis of complex **20** lead to form a bridge through sulphur atom between two MoO_2(bpdmt) units. From various physicochemical studies the structures possible for complexes are given in Fig. 4.31.

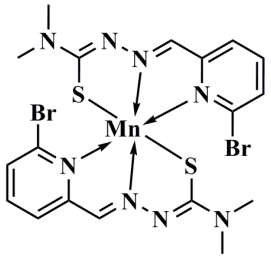

[Mn(bpdmt)$_2$] (16)

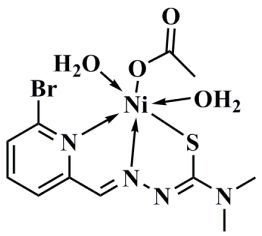

[Ni(bpdmt)(OAc)(H_2O)$_2$] (18)

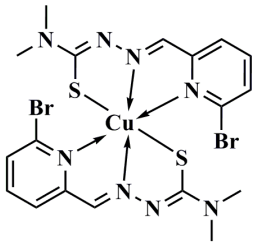

[Cu(bpdmt)$_2$] (19)

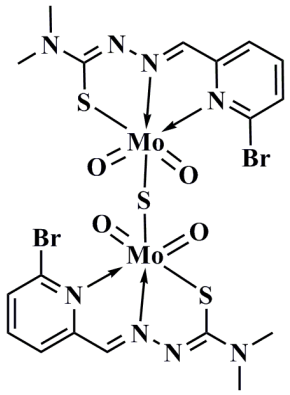

[MoO_2(bpdmt)μ^2-S] (20)

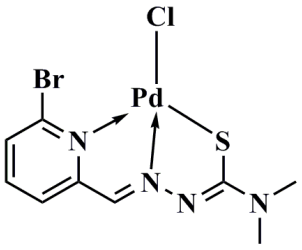

[Pd(bpdmt)Cl] (21)

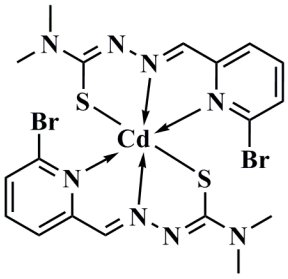

[Cd(bpdmt)$_2$] (22)

References

[1] D.L. Klayman, J.F. Bartosevich, S. Griffin, C.J. Manson, J.P. Scovill, J. Med. Chem. 22 (1979) 855.

[2] D.L. Klayman, J.P. Scovill, J.F. Bartosevich, C.J. Manson, J. Med. Chem. 22 (1979) 1367.

[3] J.P. Scovill, D.L. Klayman, C. Lambros, G.E. Childs, J.D. Notsch, J. Med. Chem. 27 (1984) 87.

[4] C.M. Nutting, C.M.L. van Herpen, A.B. Miah, Ann. Oncol. 20 (2009) 1275.

[5] B. Ma, B.C. Goh, E.H. Tan, K.C. Lam, R. Soo, S.S. Leong, L.Z. Wang, F. Mo, A.T. Chan, B. Zee, T. Mok, Invest New Drugs 26 (2008) 169.

[6] E.E. Ebenso, U.J. Ekpe, B.I. Ita, O.E. Offiong, U.J. Ibok, Mater. Chem. Phys. 60 (1999) 79.

[7] S.L.A. Kumar, M. Gopiraman, M.S. Kumar, A. Sreekanth, Ind. Eng. Chem. Res. 50 (2011) 7824.

[8] C.G. Oliveria, P.I. da S. Maia, P.C. Souza, F.R. Pavan, C.Q.F. Leite, R.B. Viana, A.A. Batista, O.R. Nascimento, V.M. Deflon, J. Inorg. Bio. Chem. 132 (2014) 21.

[9] J.P. Scovill, D.L. Klayman, C.F. Franchino, J. Med. Chem. 25 (1982) 1261.

[10] M. Muralisankar, J. Haribabu, N.S.P. Bhuvanesh, R. Karvembu, A. Sreekanth, Inorg. Chem. Acta 449 (2016) 82.

[11] D.X. West, J.S. Ives, J. Krejci, M.M. Salberg, T.L. Zumbahlen, G.A. Bain, A.E. Liberta, J.V. –Martinez, S.H. Ortiz, R.A. Toscano, Polyhedron 14 (1995) 2189.

[12] D.-C. Ilies, S. Shova, V. Radulescu, E. Pahontu, T. Rosu, Polyhedron 97 (2015) 157.

[13] Z.-Y. Ma, J. Shao, W.-G. Bao, Z.-Y. Qiang, J.-Y. Xu, J. Coord. Chem. 68 (2015) 277.

[14] M. Joseph, V. Suni, M.R.P. Kurup, M. Nethaji, A. Kishore, S.G. Bhat, Polyhedron 23 (2004) 3069.

[15] P. Paul, R.J. Butcher, S. Bhattacharya, Inorg. Chim. Acta 425 (2015) 67.

[16] R. Takjoo, M. Hakimi, M. Seyyedin, M. Abrishami, J. Sulfur Chem. 31 (2010) 415.

[17] SMART and SAINT, Area Detector Software Package and SAX Area Detector Program, Bruker Analytical X-ray; Madison, WI, USA, 1997.

[18] SADABS, Area Detector Absorption Correction Program; Bruker Analytical X-ray; Madison, WI, 1997.

[19] G.M. Sheldrick, Acta Cryst. C71 (2015) 3.

[20] K. Brandenburg, Diamond Version 3.2g, Crystal Impact GbR, Bonn, Germany, 1997.

[21] L.J. Farrugia, , J. Appl. Cryst. 45 (2012) 849.

[22] M. Joseph, V. Suni, C.R. Nayar, M.R.P. Kurup, H.-K. Fun, J. Molec. Struct. 704 (2004) 63.

[23] F.K. Allen, O. Kennard, D.G. Watson, L. Brammer, A.G. Orpen, R. Taylor, J. Chem. Soc. Perkin. Trans 2 (1987) S1.

[24] V. Philip, V. Suni, M.R.P. Kurup, M. Nethaji, Spectrochim. Acta 64A (2006) 171.

[25] E. Manoj, M.R.P. Kurup, Polyhedron 27 (2008) 275.

[26] V. Philip, V. Suni, M.R.P. Kurup, M. Nethaji, Polyhedron 24 (2005) 1133.

[27] V. Philip, V. Suni, M.R.P. Kurup, M. Nethaji, Polyhedron 23 (2004) 1225.

[28] E.B. Seena, M.R.P. Kurup, Polyhedron 26 (2007) 3595.

[29] A.P. Rebolledo, M. Vieites, D. Gambino, O.E. Piro, E.E. Castellano, C.L. Zani, E.M. Sauza-Fagundes, L.R. Teixeira, A.A. Batista, H. Beraldo, J. Inorg. Biochem. 99 (2005) 698.

[30] D.K –Demertzi, A. Domopoulou, M.A. Demertzis, G. Valle, A. Papageorgiou, J. Inorg. Biochem. 68 (1997) 147.

[31] T.A. Reena, E.B. Seena, M.R.P. Kurup, Polyhedron 27 (2008) 1825.

[32] I.-X. Li, H.-A. Tang, Y.-Z. Li, M. Wang, L.-F. Wang, C.-G. Xia, J. Inorg. Biochem. 78 (2000) 167.

[33] R.P. John, A. Sreekanth, M.R.P. Kurup, A. Usman, I.A. Razak, H.-K. Fun, Spectrochim. Acta A59 (2003) 1349.

[34] E. Garribba, G. Micera, J. Chem. Educ. 83 (2006) 1229.

[35] S. Stoll, Spectral Simulations in Solid-State Electron Paramagnetic Resonance, Ph. D. Thesis, ETH, Zurich, 2003.

[36] U.B. Gangadharmath, S.M. Annigeri, A.D. Naik, V.K. Revankar, V.B. Mahale, J. Molec. Struct. (Theochem) 572 (2001) 61.

[37] D. Kivelson, R. Neiman, J. Chem. Phys. 35 (1961) 149.

[38] B.J. Hathaway, Structure and Bonding, Springer Verlag, Heidelberg (1973) 60.

[39] K. Jayakumar, M. Sithambaresan, A.A. Aravinadakshan, M.R.P. Kurup, Polyhedron 75 (2014) 50.

[40] T. Steiner, Cryst. Rev. 9 (2003) 177.

[41] A. Sreekanth, S. Sivakumar, M.R.P. Kurup, J. Mol. Struct. 655 (2003) 47.

.....ꕥ.....

Chapter 5

6-BROMOPYRIDINE-2-CARBALDEHYDE-N^4-CYCLOHEXYLTHIOSEMICARBAZONE AND ITS TRANSITION METAL COMPLEXES: SYNTHESIS, SPECTRAL AND STRUCTURAL CHARACTERIZATION

Contents

5.1. Introduction

In the present chapter, we have designed the thiosemicarbazone by changing the substituent at the R_1 position with 6-bromopyridine and R_3 position with cylcohexyl group (Scheme 1).

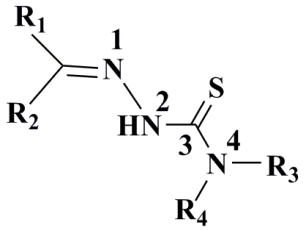

Scheme 5.1

This chapter includes synthesis and characterization of a new thiosemicarbazone, namely 6-bromopyridine-2-carbaldehyde-N^4-cyclohexyl thiosemicarbazone (Hbpct) and its transition metal complexes of Ni(II), Cu(II), Pd(II) and Cd(II) ions. All the compounds synthesized were characterized using various physico-chemical methods.

5.2. Experimental

5.2.1. Materials

4-Benzyloxysalicylaldehyde (Alfa Aesar), hydrazine monohydrate (98%) (Lancaster), cyclohexylisothiocyanate(Sigma Aldrich), $Ni(OAc)_2 \cdot 4H_2O$ (Alfa Aesar), $Ni(NO_3)_2 \cdot 6H_2O$ (Alfa Aesar), $Cu(OAc)_2 \cdot 2H_2O$ (E-Merck), $CuBr_2$ (Alfa Aesar), $PdCl_2$ (Sigma Aldrich), $Cd(OAc)_2 \cdot 2H_2O$ (Alfa Aesar), CH_3OH (Spectrochem), CH_3CH_2OH (Spectrochem), CH_3CN (Spectrochem) and DMF (Spectrochem) were of analar grade and used without further purification.

5.2.2. Synthesis of 6-bromopyridine-2-carbaldehyde-N^4-cyclohexylthiosemicarbazone (Hbpct)

Synthesis of Hbpct was carried out in a two-step process. The first step involve synthesis of N^4-cyclohexylthiosemicarbazide by reaction of cyclohexylisothiocyante (1.932 g, 14 mmol) with hydrazine hydrate (4.5 g, 90 mmol) in 20 ml methanol by stirring under room temperature. The colorless crystalline powder obtained was separated and washed with methanol and dried *in vacuo* (Scheme 5.2). In the later step, a solution of N^4-cyclohexylthiosemicarbazide (0.173 g, 1 mmol) in acetonitrile was refluxed under stirring with 6-bromopyridine-2-carbaldehyde (0.183 g, 1 mmol) in the presence few drops of glacial acetic acid. The colorless solution was kept for 2 weeks and colorless crystals of the compound obtained was separated, washed with acetonitrile and dried *in vacuo*.

Yield: 0.172 g (50%). m.p : 176 °C.
Elemental Anal. Found (Calcd)% : C 45.89 (45.71); H 5.44 (5.02); N 16.23 (16.42); S 9.56 (9.40).

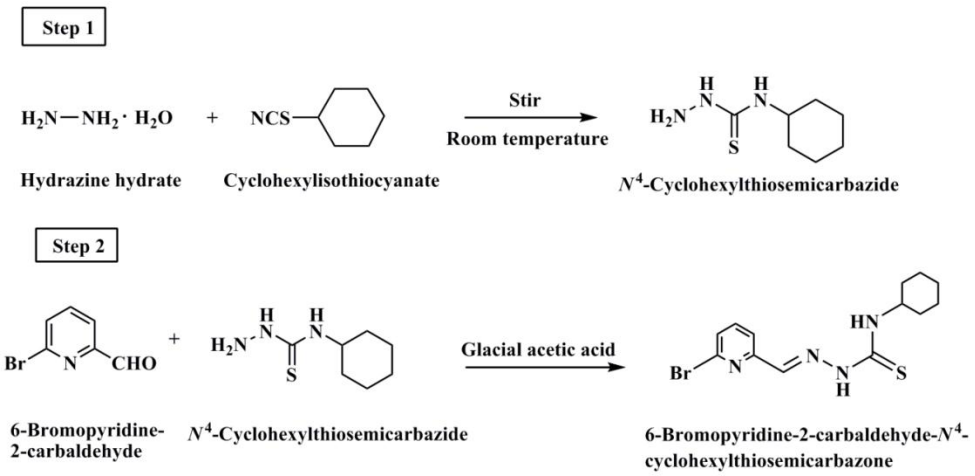

Scheme 5.2.

5.2.3. Syntheses of complexes

5.2.3.1. Synthesis of $[Ni(Hbpct)_2](NO_3)_2 \cdot H_2O$ (23)

A hot methanolic solution of Hbpct (0.341 g, 1 mmol) and $Ni(NO_3)_2 \cdot 6H_2O$ (0.145 g, 0.5 mmol) in methanol were mixed and stirred under reflux condition. The brown solution obtained after 2 h was allowed to stand for 3 weeks at room temperature for slow evaporation. The product obtained collected, washed with methanol and dried. The compound was dissolved in 10 mL DMF was allowed to evaporate slowly. The block shaped brown crystals obtained after 2 weeks was separated and dried.

Yield : (0.391 g) 45%.
Elemental Anal. Found (Calcd)% : C 35.21 (35.36); H 4.54 (4.11); N 6.23 (6.65); S 7.66 (7.26).

5.2.3.2. Synthesis of $[Ni(bpct)_2] \cdot DMF$ (24)

The complex **24** was prepared by refluxing Hbpct (0.341 g, 1 mmol) dissolved in 10 mL methanol with $Ni(OAc)_2 \cdot 4H_2O$ (0.124 g, 0.5 mmol) in

methanol. The product obtained was separated, washed with methanol and dried *in vacuo*. The small quantity of the compound was dissolved in 10 mL DMF and allowed to stand for 2 weeks and the brown block shaped crystals formed were separated.

Yield : (0.840 g) 52%.
Elemental Anal. Found (Calcd)% : C 43.64 (42.88); H 4.68 (4.84); N 15.55 (15.52); S 7.76 (7.89).

5.2.3.3. Synthesis of [Cu(bpct)Cl] (25)

Synthetic strategy of the complex **25** involves refluxing Hbpct (0.341 g, 1 mmol) in 10 mL methanol with $Cu(OAc)_2 \cdot 2H_2O$ (0.199 g, 1 mmol) in 10 mL methanol. A drop of con. HCl was added to the mixture and the content was refluxed for 1 h. The green product obtained was separated, washed and dried *in vacuo*.

Yield : (0.247 g) 56%.
Elemental Anal. Found (Calcd)% : C 34.58 (35.55); H 3.82 (3.67); N 12.45 (12.75); S 7.67 (7.30).

5.2.3.4. Synthesis of [Cu(bpct)Br] (26)

Complex **26** was prepared by refluxing Hbpct (0.341 g, 1 mmol) dissolved in 10 mL ethanol with $CuBr_2$ (0.223 g, 1 mmol) for 2 h. The product obtained was separated, washed and dried *in vacuo*.

Yield : (0.223 g) 46%.
Elemental Anal. Found (Calcd)% : C 32.41 (32.28); H 3.08 (3.33); N 11.71 (11.58); S 6.22 (6.63).

5.2.3.5. Synthesis of [Cu(bpct)(OAc)] (27)

To synthesize complex **27**, Hbpct (0.341 g, 1 mmol) was dissolved in 10 mL hot ethanol with stirring. To this hot solution, a solution of $Cu(OAc)_2 \cdot 2H_2O$(0.199 g, 1 mmol) in 1:1 mixture of ethanol and methanol was added. The contents were refluxed for 3 h and the product formed in brown color was separated and dissolved in 10 mL DMF. After 2 weeks, the complex obtained was separated, washed with methanol and dried *in vacuo.*

Yield : (0.282 g) 61%.
Elemental Anal. Found (Calcd)% : C 38.78 (38.92); H 4.35 (4.14); N 12.49 (12.10); S 6.72 (6.93).

5.2.3.6. Synthesis of [Pd(bpct)Cl] (28)

A mixture of hot methanolic solution of Hbpct (0.341 g, 1 mmol) and $PdCl_2$ (0.177 g, 1 mmol) were refluxed for about 4 h. The clear orange colored solution obtained was allowed to stand for 2 weeks and the product obtained was separated, washed with methanol and dried *in vacuo*.

Yield : (0.225 g) 46%.
Elemental Anal. Found (Calcd)% : C 32.50 (32.25); H 3.53 (3.75); N 11.44 (11.75); S 6.54 (6.62).

5.2.3.7. Synthesis of $[Cd(bpct)_2] \cdot DMF$ (29)

To a hot solution of $Cd(OAc)_2 \cdot 2H_2O$ (0.133 g, 0.5 mmol), a solution of Hbpct (0.341 g, 1 mmol) was added and refluxed under stir for 4 h. The crude yellow colored product obtained was separated from the content and dried. This product was dissolved in 10 mL DMF solution and allowed to stand for 2 weeks. Needle shaped crystals of complex **29** obtained were separated from the solution, washed with methanol and dried.

Yield : (1.177 g) 68%.
Elemental Anal. Found (Calcd)% : C 40.28 (40.22); H 4.62 (4.54); N 14.21 (14.56); S 7.76 (7.41).

5.2.4. Physico-chemical techniques

5.2.4.1. Elemental analysis

Elemental analyses of the compounds were done on a Vario EL III CHNS elemental analyzer at the Sophisticated Analytical Instrument Facility, Cochin University of Science and Technology, Kochi-22, Kerala, India.

5.2.4.2. Magnetic susceptibility measurements

The magnetic susceptibility measurements of the complexes were taken on a Vibrating sample Magnetometer using $Hg[Co(SCN)_4]$ as a calibrant at the SAIF, Indian Institute of Technology, Madras.

5.2.4.3. Molar conductivity measurements

The conductivity measurements of the complexes were recorded in 10^{-3} M solution in DMF on a Systronic model 303 direct reading conductivity meter at room temperature at Department of Applied Chemistry, Cochin University of Science and Technology, Kochi, India.

5.2.4.4. Spectroscopic characterization

The infrared spectra of Hbpct and complexes **23-29** were recorded on a JASCO FT-IR-5300 spectrometer in the 4000-400 cm^{-1} range using KBr pellets. The electronic spectra of the prepared compounds were recorded in DMF solution (10^{-3} and 10^{-5} M) on a Thermo Scientific Evolution 220 UV-vis Spectrophotometer in the 200-900 nm range. Hbpct and complex **28** were characterized by ^1H NMR techniques and was recorded using Bruker AMX 400 FT-NMR Spectrometer at the Sophisticated Analytical Instrument Facility, Cochin University of Science and Technology, Kochi, India. The Electro Paramagnetic Resonance spectra of complexes **25** and **27** were recorded in the solid state at 298 K and at 77 K in DMF solution on a Varian E-112 spectrometer, with 100 kHz modulation

frequency, 2 G modulation amplitude and 9.1 GHz microwave frequency at the Sophisticated Analytical Instrumentation Facility, Indian Institute of Technology, Bombay, India.

5.2.5. Single crystal X-ray diffraction studies

The single crystal X-ray diffraction studies of the thiosemicarbazone Hbpct was done on a Rigaku Oxford Diffraction diffractometer at 173(2) K equipped with a graphite crystal incident-beam monochromator, and a fine focus sealed tube with Cu Kα (λ = 1.54184 Å) as the X-ray source at the Department of Chemistry, Keene State College, 229 Main Street, Keene, NH. The unit cell dimensions were measured and the data collection was performed at 173(2) K. The structure was solved with the Superflip [1,2,3] structure solution program using Charge Flipping and was refined with the ShelXL [4] refinement package using Least Squares minimization. Whereas the single crystal X-ray diffraction studies of complexes **25**, **26** and **29** were carried out using a Bruker SMART APEXII CCD diffractometer at the Sophisticated Analytical Instrumentation Facility, CUSAT, Kochi, India. Data acquisition was done using Bruker SMART software and data integration using Bruker SAINT software [5]. Absorption corrections were carried out with SADABS based on Laue symmetry using equivalent reflections [6]. The structure was solved by direct methods and refined by full-matrix least-squares calculations with the SHELXL-2014/7 software package [4]. The graphic tools used were DIAMOND version 3.2g [7] and ORTEP-3 [8].

5.3. Results and discussion

Elemental analyses of the compounds were reported in Sections 5.2.2 and 5.2.3. The structures of the compounds were assigned on this basis.

5.3.1. Characterization of 6-bromopyridine-2-carbaldehyde-N^4-cyclohexylthiosemicarbazone (Hbpct)

5.3.1.1. Infrared spectrum

The condensation of 6-bromopyridine-2-carbaldehyde with N^4-cyclohexyl thiosemicarbazide leading to the formation of C=N gave a band at 1576 cm^{-1}. The infrared spectrum of the compound was characterized by bands at 3368 cm^{-1} due to the C–H stretching, which is accompanied by bands at 2929 and 2846 cm^{-1} assigned to N–H stretching. The C=S bond gives infrared absorption at 1441 and 887 cm^{-1}. The pyridine ring in the compound usually gave bands at 600 cm^{-1} [9]. Here the band for pyridine appears at 551 cm^{-1}. The N–N stretching vibration was identified from a band at 1072 cm^{-1}. The infrared spectrum for Hbpct is presented in Fig. 5.1.

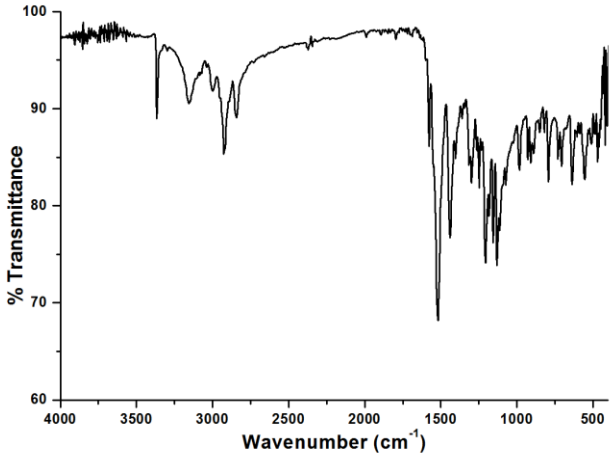

Fig. 5.1. Infrared spectrum of Hbpct.

5.3.1.2. Electronic spectrum

The electronic spectrum of Hbpct showed a broad band with maximum absorption at 335 nm with molar absorptivity of 6.88×10^4 M^{-1} cm^{-1}. This band is result of n→π* and π→π* transitions from the benefit of lone pairs

of electrons and π electrons present in the pyridine and aromatic rings. The electronic spectrum for compound Hbpct is depicted in Fig. 5.2.

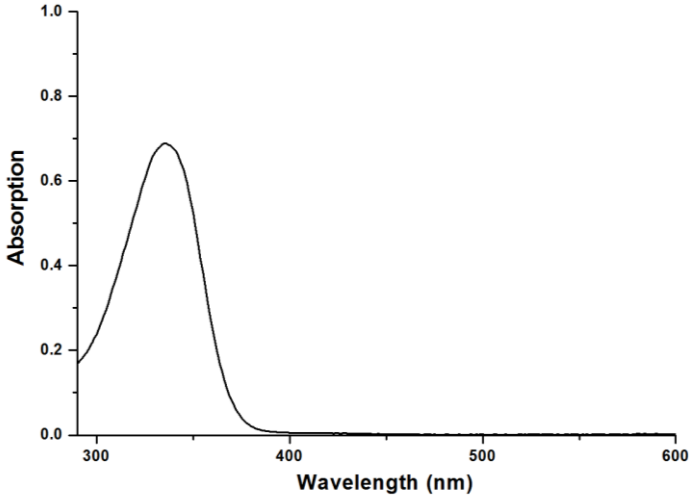

Fig. 5.2. Electronic spectrum of Hbpct.

5.3.1.3. ^{1}H NMR spectrum

The ^{1}H NMR as well as ^{1}H-D_2O exchange spectra of Hbpct were recorded in $CDCl_3$ solution, using TMS as standard. The ^{1}H NMR spectrum for Hbpct is shown in Fig. 5.3. The N(2)–H (Fig. 5.5) hydrogen gives a signal at 9.34 ppm with respect to TMS. This downfield shift attributed to the extended delocalization of electrons present in the thiosemicarbazone moiety. Disappearance of this shift in the D_2O exchanged ^{1}H NMR specrum confirms the presence of an exchangeable proton (Fig. 5.3). The multilpet appeared in the regions 1.22-2.16, 4.28-4.32 and 7.33-7.80 ppm were assigned to cyclohexyl protons, hydrogen on C(8) and aromatic protons respectively.

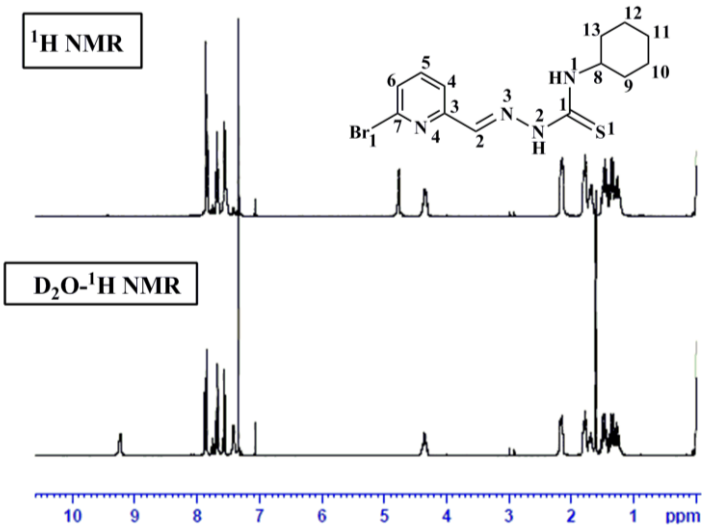

Fig. 5.3. ^{1}H NMR and D_2O exchanged ^{1}H NMR spectrum of Hbpct.

5.3.1.4. Single crystal X-ray diffraction

Single crystals of Hbpct suitable for X-ray diffraction studies were isolated from the mother liquor. A crystal with size 0.32 × 0.30 × 0.24 mm^3 was nylon looped and mounted on a Rigaku Oxford Diffraction diffractometer at 173(2) K as given in Fig. 5.4.

Fig. 5.4. Nylon looped single crystal of Hbpct.

The instrument was equipped with graphite monochromated Cu Kα (λ=1.54184 Å) radiation. All non-hydrogen atoms of the complex were refined anisotropically. The hydrogen atoms attached to C atoms were

refined with riding coordinates and placed in calculated positions with the help of difference map. Thereby all the C–H and N–H bond distances were constrained to 0.95-0.99 Å and 0.88 Å respectively. Hydrogen atoms were defined with U_{iso}=1.2 U_{eq}. The crystallographic data and refinement parameters are represented in Table 5.1.

Table 5.1. Crystal refinement descriptions for Hbpct

Parameters	**Hbpct**
Empirical formula	$C_{13}H_{17}BrN_4S$
Formula weight	341.27
Color	Brown
Temperature/K	173.2 (2)
Crystal system	Monoclinic
Space group	$P2_1/n$
Cell parameters	
a(Å)	14.3316(5)
b (Å)	7.26405(17)
c (Å)	15.5495(5)
$\alpha = \gamma$(°)	90
β (°)	111.542
Volume (Å^3)	1505.71(8)
Z	4
Calculated density, ρ (g cm^{-3})	1.505
F(000)	696.0
Crystal size (mm^3)	0.32 × 0.3 × 0.24
θ range for data collection (°)	3.59 to 71.162
Limiting indices	$-16 \le h \le 17$, $-8 \le k \le 8$, $-13 \le l \le 19$
Reflections collected	5436
Independent reflections	2863 [R_{int} = 0.0390, R_{sigma} = 0.0469]
Data/restraints/parameters	2863/0/172
Goodness-of-fit on F^2	1.052
Final R indexes [I>2σ (I)]	R_1 = 0.0425, wR_2 = 0.1087
Final R indexes [all data]	R_1 = 0.0482, wR_2 = 0.1148
Largest diff. peak and hole (e Å^{-3})	0.73/-0.62

$R_1 = \Sigma||F_o| - |F_c|| / \Sigma|F_o|$
$wR_2 = [\Sigma w(F_o^2-F_c^2)^2 / \Sigma w(F_o^2)^2]^{1/2}$

Hbpct crystallized into monoclinic $P2_1/n$ space group. The asymmetric unit of the compound contains a single unit of Hbpct. Formation of azomethine bond was evident from the C(2)–N(3) bond length of 1.278(4) Å, close to the formal C=N of 1.279 Å [10]. The C(1)–S(1) and C(1)–N(2) bond lengths were equal to 1.683(3) and 1.359(4) Å respectively. These bond lengths were close to C=S and C–N bond lengths [11], which confirmed the existence of Hbpct in the thio-amido form. Fig. 5.5 represents ORTEP diagram for Hbpct with 50% probability.

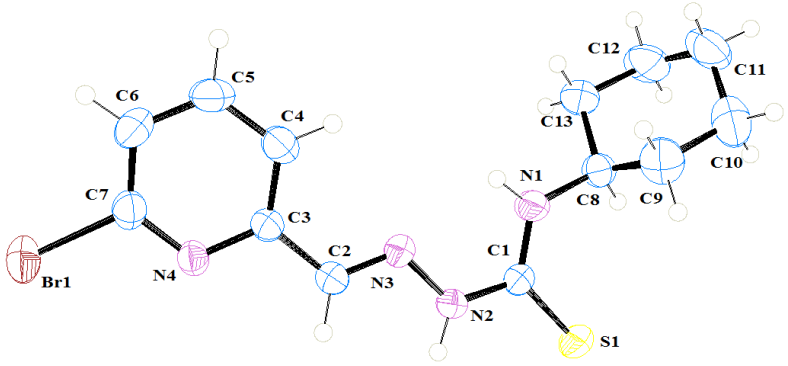

Fig. 5.5. ORTEP diagram of Hbpct with 50% ellipsoid probability.

The torsion angle of C(3)–C(2)–N(3)–N(2) was observed to be 177.7(2)°, affirms the *E* conformation of the thiosemicarbazone about the azomethine (C(2)=N(3)) bond. The torsion angles 176.6(2) and 3.3(4)° respectively for N(3)–N(2)–C(1)–S(1) and N(3)–N(2)–C(1)–N(1) suggest that N(3) lies *cis* with respect to N(1) and *trans* with respect to S(1), giving *Z* conformation about C(1)–N(2) bond, when thio (S(1)) unit is considered. The bonding parameters for Hbpct are listed in Table 5.2.

Table 5.2. Selected bond parameters of Hbpct

Bond length (Å)		Bond angle (°)	
C(2)–N(3)	1.278(4)	C(3)–C(2)–N(3)	119.80(2)
N(3)–N(2)	1.368(3)	C(2)–N(3)–N(2)	115.80(2)
C(1)–N(2)	1.359(4)	N(3)–N(2)–C(1)	119.50(2)
C(1)–S(1)	1.683(3)	N(2)–C(1)–S(1)	118.90(2)
		N(1)–C(1)–S(1)	124.70(2)

The ring puckering analysis shows that the cyclohexyl ring C(8)–C(9)–C(10)–C(11)–C(12)–C(13) is puckered with amplitude of Q_T = 0.576(4) Å. Molecules in the asymmetric unit were connected *via* N(2)–H(2)···N(4) intermolecular hydrogen bonding interactions with a D···A distance of 3.070(3) Å. There is a special halogen bond of the type C(1)–S(1)···Br(1) with a D···A distance of 3.212 Å in the crystal lattice [12]. These hydrogen bonds connected various molecules of Hbpct is extended along'*b*' axis forming a one dimensional chain (Table 5.3). The hydrogen bonding interactions in Hbpct are depicted in Fig. 5.6.

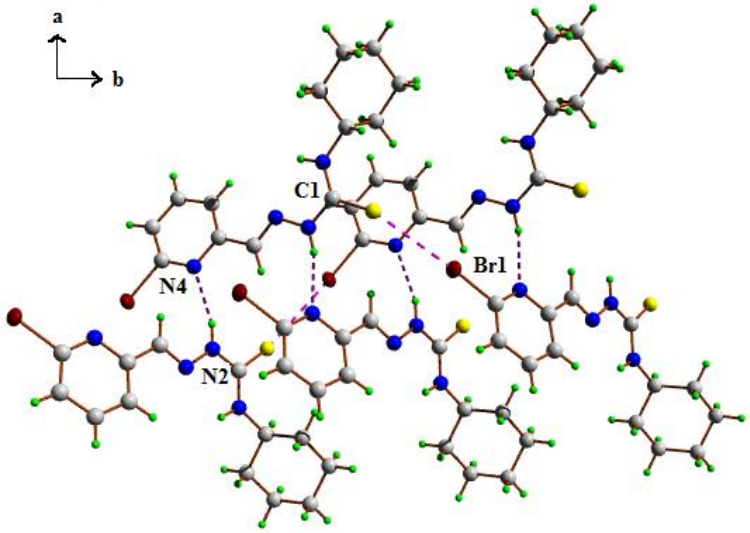

Fig. 5.6. Hydrogen bonding interactions in Hbpct.

Table 5.3. Interaction parameters in Hbpdmt

Hydrogen bonding interactions				
D–H···A	D–H (Å)	H···A (Å)	D···A (Å)	D–H···A (°)
N(2)–H(2)···N(4)[a]	0.88	2.22	3.070(3)	161.3
C(7)–Br(1)···S(1)[b]	1.902(3)	3.212(8)	3.968(2)	173.23(9)
π ···π interaction				
Cg(I)···Cg(J)	Cg···Cg (Å)	α (°)	β (°)	γ (°)
Cg(1)···Cg(1)[c]	3.578(16)	0.00(14)	14.7	14.7

a = ½-x , ½+y, ³⁄₂ -z; b = ½-x, ³⁄₂ +y, ³⁄₂ –z; c = 1-x, -y, -2-z

Cg(1) = C(3), C(4), C(5), C(6), C(7), N(4); D= donor, A= acceptor, Cg= centroid

α (°) = Dihedral angle between planes I and J

β (°) = Angle between Cg(I)–Cg(J) vector and Cg(J) perp

γ (°) = Angle between Cg(I)–Cg(J) vector and Cg(I) perp

The crystal was packed efficiently with the help of π–π interaction having Cg···Cg distance of 3.578(16) Å. The packing diagram of Hbpct, viewed along *b* axis, showing the hydrogen bonding interaction and π–π interaction leading to a three dimensional arrangement in the crystal lattice is given in Fig. 5.7.

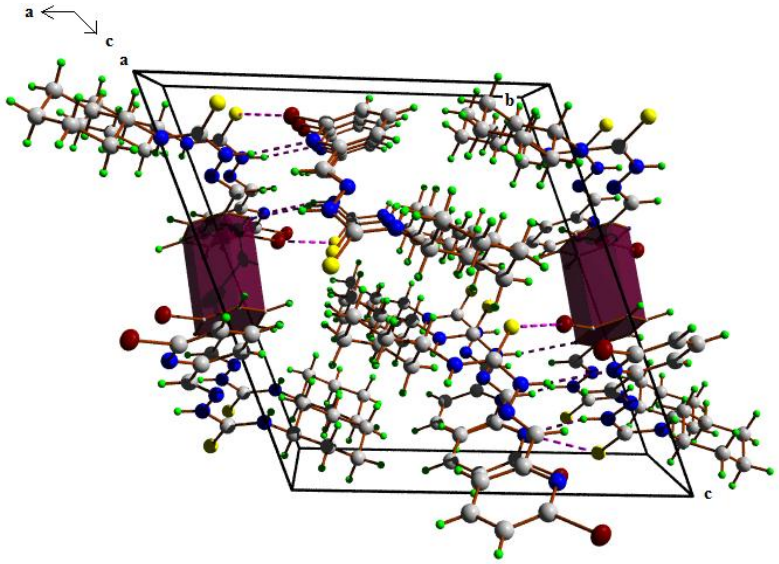

Fig. 5.7. Packing diagram of Hbpct viewed along '*b*' axis with hydrogen bonding and π–π interactions.

5.3.2. Characterization of complexes of Hbpct

The NNS donor thiosemicarbazone Hbpct could coordinate to the metal with the aid of azomethine nitrogen, pyridine nitrogen and thiolate sulfur, as a neutral or monodeprotonated ligand. We could synthesize seven metal complexes of transition metals like Ni(II), Cu(II), Pd(II) and Cd(II). Of these, complexes **23, 24** and **29** were synthesized by refluxing Hbpct and the metal salt in 2:1 ratio. Hbpct and metal salt were refluxed in the ratio1:1 to synthesize complexes **25, 26, 27** and **28**. Of these, the complexes $[Ni(Hbpct)_2](NO_3)_2 \cdot H_2O$ **(23)**, $[Ni(bpct)_2] \cdot DMF$ **(24)** and $[Cd(bpct)_2] \cdot DMF$ (**29**) were recrystallized from their solution in DMF.

5.3.2.1. Molar conductivity and magnetic susceptibility measurements

The molar conductivity measurements were taken in 10^{-3} M solution of DMF. It was observed that all complexes except $[Ni(Hbpct)_2](NO_3)_2 \cdot H_2O$ **(23)** gave a molar conductivity values between 2.3-27 $ohm^{-1}\ cm^2\ mol^{-1}$, well below the value of uni-univalent electrolyte (60-90 $ohm^{-1}\ cm^2\ mol^{-1}$), justifies the non conducting nature of the complexes. The molar conductivity of complex **23** is 170 $ohm^{-1}\ cm^2\ mol^{-1}$, lies in the range of a 2:1 electrolyte, giving an impression that Hbpct was coordinated to Ni(II) in the neutral form [13].

The magnetic moments for Ni(II) complexes **23** and **24** are 2.87 and 2.84 B.M. respectively, are close to magnetic moment for two unpaired electrons. This suggests that the geometries for these complexes are octahedral [14]. The magnetic moment values of 1.71, 1.74 and 1.72 B.M. for the Cu(II) complexes **25**, **26** and **27** are in agreement with the presence of one unpaired electron in the metal [15]. The diamagnetic nature of the complexes [Pd(bpct)Cl] **(28)** and $[(Cd(bpct)_2] \cdot DMF$ **(29)** were in agreement with low spin Pd(II) with a d^8 electronic configuration and d^{10} Cd(II) state of the metals in these complexes. The molar conductivity and magnetic moment values for the complexes are described in Table 5.4.

Table 5.4. Molar conductivity and magnetic moment values of complexes of Hbpct

Compound	λ_m(ohm^{-1}cm^{2}mol^{-1})	μ_{eff} (B.M.)
[Ni(Hbpct)$_2$](NO$_3$)$_2$·H$_2$O (**23**)	170	2.87
[Ni(bpct)$_2$]·DMF (**24**)	2.3	2.84
[Cu(bpct)Cl] (**25**)	14	1.71
[Cu(bpct)Br] (**26**)	27	1.74
[Cu(bpct)(OAc)] (**27**)	4.2	1.72
[Pd(bpct)Cl] (**28**)	4.2	0.04
[Cd(bpct)$_2$]·DMF (**29**)	5.2	0

5.3.2.2. Infrared spectra

Infrared spectra of the complexes were recorded in the 400-4000 cm^{-1} range using KBr pellets. The tentative assignments of infrared stretching frequencies for various groups present in the complexes and a comparison with the ligand is listed in Table 5.5.

Table 5.5. Infrared spectral assignments (cm^{-1}) of Hbpct and its complexes

Compound	ν(C=N)	ν(C=N)^a	ν(C=S)/ ν(C–S)	ν(N–N)	ν(py)	ν(M–N$_{azo}$)
Hbpct	1576	---	1441,887	1072	551	---
[Ni(Hbpct)$_2$](NO$_3$)$_2$ H$_2$O **(23)**	1524	---	1415, 818	1091	583	438
[Ni(bpct)$_2$]·DMF **(24)**	1526	1511	1422, 878	1123	576	435
[Cu(bpct)Cl] **(25)**	1524	1441	1423, 875	1155	589	459
[Cu(bpct)Br] **(26)**	1562	1511	1434,863	1155	587	466
[Cu(bpct)(OAc)] **(27)**	1530	1434	1422, 856	1148	567	472
[Pd(bpct)Cl] **(28)**	1523	1472	1428, 863	1174	583	474
[Cd(bpct)$_2$]·DMF **(29)**	1587	1536	1453, 863	1148	570	481

a = newly formed C=N

The shift in the ν(C=N) stretching frequencies for Hbpct in both the Ni(II) complexes at 1524-1526 cm^{-1} from 1576 cm^{-1} is an evidence for the complex formation though azomethine nitrogen. The complex [Ni(bpct)$_2$]·DMF **(24)**, gave a new band at 1511 cm^{-1} assigned to the newly

formed C=N, which is absent in $[Ni(Hbpct)_2](NO_3)_2 \cdot H_2O$ **(23)** suggesting the coordination of thiosemicarbazone to Ni(II) in the thio-amido form in complex **23** and thio-iminolate form in complex **24**. The above observation is further confirmed from the shift in the ν(N–N) stretching frequencies for complexes **23** and **24** to 1091 and 1123 cm^{-1} respectively from 1072 cm^{-1} as that of Hbpct. The small difference in the ν(N–N) stretching frequencies for complex **23** and a large difference for complex **24**, was due to the coordination of the former in neutral form. Whereas for later the deprotonation leads to an extended electron delocalization and hence an increase in ν(N–N) stretching frequency [16]. The formation of complex *via* sulfur atom in the thiosemicarbazone gives a shift in the ν(C=S)/ν(C–S) band from 1441cm^{-1} that of Hbpct to 1415and 1422 cm^{-1} respectively for complexes **23** and **24** may be due to the strong coordination to Ni(II). The pyridine counterpart in Hbpct, which a gave band at 551 cm^{-1} was shifted to 583 cm^{-1} for complex **23** and 576 cm^{-1} for complex **24** attributed to the coordination of pyridine nitrogen to metal ion. Both the complexes gave new bands at 438 and 435 cm^{-1} corresponding to $\nu(Ni–N_{azo})$ stretching vibration. The ν(Ni–S) and $\nu(Ni–N_{py})$ cannot be determined by the instrument used for the present study. The infrared spectrum for complex **24** is depicted in Figs. 5.8.

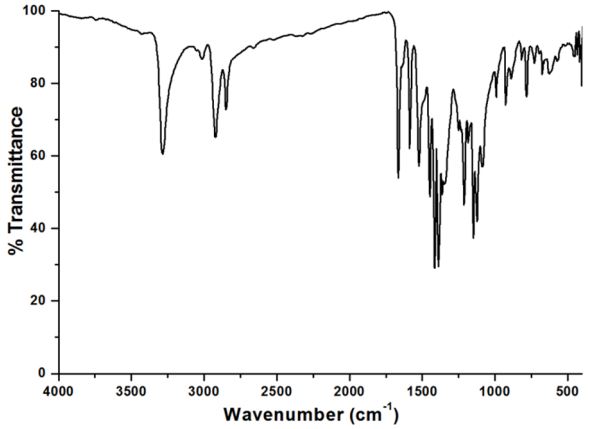

Fig. 5.8. Infrared spectrum of $[Ni(bpct)_2] \cdot DMF$ **(24).**

The Cu(II) complexes **25**, **26**, **27** gave a shift for the ν(C=N) stretching frequencies, for the coordinated Hbpct to a lower energy. The complexes [Cu(bpct)Cl] **(25),** [Cu(bpct)Br] **(26)** and [Cu(bpct)(OAc)] **(27)** exhibit new bands at 1441, 1511 and 1434 cm^{-1} respectively resulted from the formation of new C=N. Further the ν(N–N) stretching frequency is shifted to a higher frequency in the range 1155-1148 cm^{-1} from 1072 cm^{-1} of Hbpct [9]. From these observations, it was evident that the complex was formed by the coordination of the monodeprotonated Hbpct. The ν(Cu–N_{azo}) stretching vibrations were observed at 459, 466 and 472 cm^{-1} respectively for the complexes **25**, **26** and **27.** Shift observed for the stretching vibrations of pyridine unit justify the assumption of the coordinate complex formation with the aid of pyridine nitrogen [17]. The coordinated acetate ion gives a band at 1581 cm^{-1}. Figs. 5.9 and 5.10 gives the infrared spectra for complexes **26** and **27**.

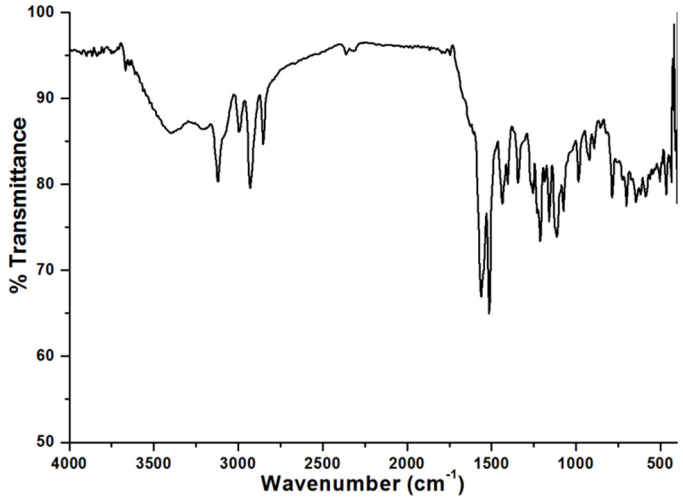

Fig. 5.9. Infrared spectrum for [Cu(bpct)Br] **(26).**

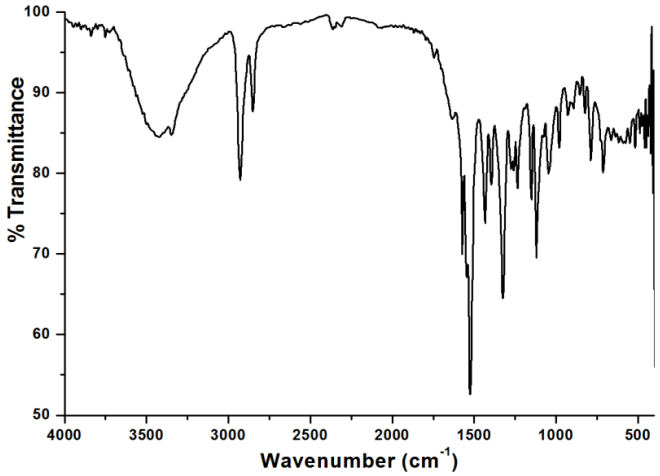

Fig. 5.10. Infrared spectrum for [Cu(bpct)(OAc)] **(27).**

In the complex [Pd(bpct)Cl] **(28),** the monodeprotonated Hbpct is coordinated to Pd(II) ion. This is evident from the shift in the ν(C=N) stretching frequency to 1523 cm^{-1} from 1576 cm^{-1} that of free ligand. Appearance of a new band at 1536 cm^{-1} corresponding to newly formed ν(C=N) and a shift of ν(N–N) to a higher frequency of 1148 cm^{-1} supported the observation. The ν(Pd–N_{py}) vibration was observed as band at 474 cm^{-1} [18]. The infrared spectrum of complex **28** is represented in Fig. 5.11.

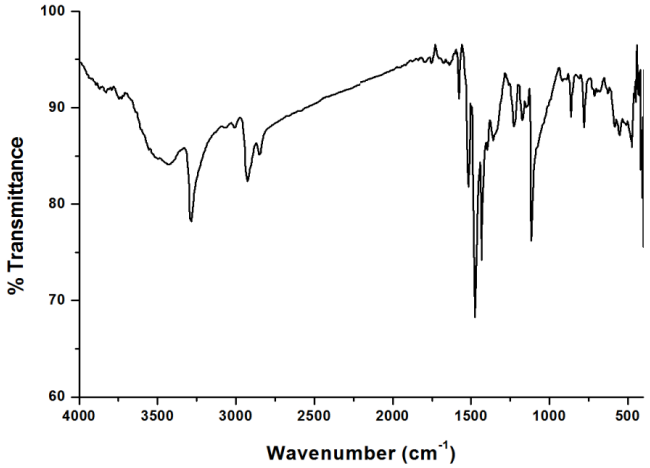

Fig. 5.11. Infrared spectrum for [Pd(bpct)Cl] **(28)**

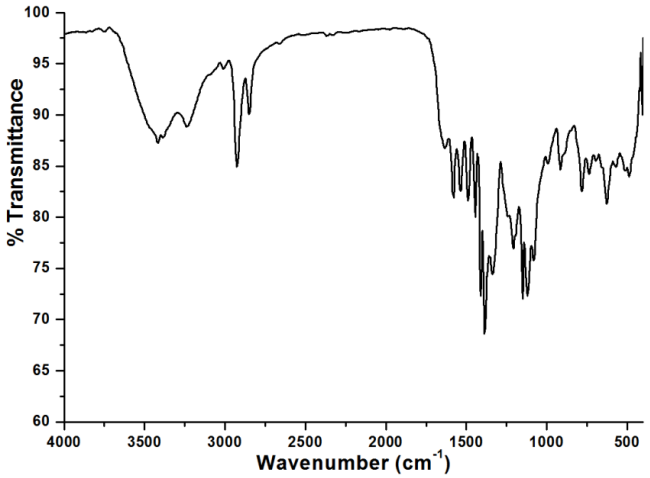

Fig. 5.12. Infrared spectrum for **[**Cd(bpct)$_2$]·DMF **(29)**.

The coordination of azomethine nitrogen and pyridine nitrogens in complex **29** was confirmed from the shift for ν(C=N) and ν(py) vibrations. The newly formed C=N bond give a vibration at 1536 cm^{-1}. The Cd–N bond formation was confirmed from a band at 481 cm^{-1} corresponding to ν(Cd–N$_{azo}$). The infrared spectrum of complex **[**Cd(bpct)$_2$]·DMF **(29)** is depicted in Fig. 5.12.

5.3.2.3. Electronic spectra

The complexes with 10^{-3} and 10^{-5} M solutions in DMF were employed to record the electronic spectra. The absorption bands for all the complexes showed shift as compared to free thiosemicarbazone. This is due to complexation *via* azomethine and pyridine nitrogens as well as elongation of C=S bond [19]. The assignment of electronic absorption by Hbpct and its complexes were given in Table. 5.6.

Table 5.6. Electronic spectral assignment (nm) of Hbpct and its complexes

Compound	n–π*/ π–π*(nm) ($\varepsilon = 10^4$ M^{-1} cm^{-1})	LMCT (nm) ($\varepsilon = 10^4$ M^{-1} cm^{-1})	*d-d* (nm) (ε (M^{-1} cm^{-1}))
Hbpct	335 (6.88)	---	---
$[Ni(Hbpct)_2](NO_3)_2 \cdot H_2O$ (**23**)	327 (6.64), 372 (6.29)	439 (7.05)	---
$[Ni(bpct)_2] \cdot DMF$ (**24**)	324 (5.58), 369 (5.29)	439 (5.87)	---
[Cu(bpct)Cl] (**25**)	319 (9.04)	410 (7.66)	683 (113)
[Cu(bpct)Br] (**26**)	334 (9.37)	416 (3.83)	667 (79)
[Cu(bpct)(OAc)] (**27**)	323 (7.43), 390 (8.49)	420 (7.08)	---
[Pd(bpct)Cl] (**28**)	312 (5.34), 385 (7.48)	447 (2.72), 488 (1.53)	---
$[Cd(bpct)_2] \cdot DMF$ (**29**)	328 (6.40)	422 (8.09)	---

The Ni(II) complexes $[Ni(Hbpct)_2](NO_3)_2 \cdot H_2O$ **(23)** and $[Ni(bpct)_2] \cdot DMF$ **(24)** gave three bands. Complex **23** exhibits bands at 327 (ε = 6.64 × 10^4 M^{-1} cm^{-1}) and 372 (ε =6.29×10^4 $M^{-1}cm^{-1}$) nm, are assignable to intraligand transitions. Whereas for complex **24** these bands appear at 324 (ε = 5.58 × 10^4 M^{-1} cm^{-1}) and 369 (ε = 5.29×10^4 M^{-1} cm^{-1}) nm. Both the complexes gave a characteristic LMCT transition with a maximum absorption at 439 nm with molar absorptivity 7.05 × 10^4 M^{-1} cm^{-1} for complex **23** and 5.87 × 10^4 $M^{-1}cm^{-1}$ for complex **24**. The electronic spectra for complexes **23** and **24** and Hbpct are presented in Fig. 5.13.

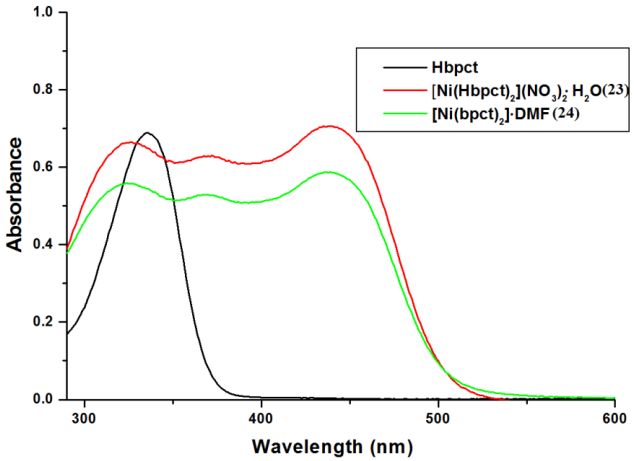

Fig. 5.13. Electronic spectra of Hbpct, complex **23** and **24**.

The electronic spectra of the Cu(II) complexes **25, 26** and **27** showed large differences from that of Hbpct. It is found that [Cu(bpct)Cl] **(25)** gave an absorption band with maximum at 319 nm $\varepsilon = 9.04 \times 10^4$ M^{-1} cm^{-1}. The complex [Cu(bpct)Br] **(26)** give a band with maximum absorption at 334 nm with molar absorptivity 9.37×10^4 M^{-1} cm^{-1}. Whereas the complex [Cu(bpct)(OAc)] **(27)** showed two absorptions with maximum at 323 and 390 nm ($\varepsilon = 7.43 \times 10^4$ and 8.49×10^4 $M^{-1}cm^{-1}$). These absorptions were assigned to intraligand transitions. The complexes **25, 26** and **27** gave LMCT transitions with maxima at 410, 416 and 420 nm with molar absorptivity 7.66×10^4, 3.83×10^4 and 7.08×10^4 M^{-1} cm^{-1} respectively. Fig. 5.14 gives electronic spectra for complexes **25, 26** and **27**. For a square planar Cu(II) complex with ground state $d_{x^2-y^2}$, three transitions expected are $d_{x^2-y^2} \rightarrow d_{xy}$, $d_{x^2-y^2} \rightarrow d_{x^2}$ and $d_{x^2-y^2} \rightarrow d_{yz}$, d_{xy} ($^2B_{2g} \leftarrow {}^2B_{1g}$, $^2A_{1g} \leftarrow {}^2B_{1g}$ and $^2E_g \leftarrow {}^2B_{1g}$) [20]. The visible spectra of complexes **25** and **26** give very broad spectrum as a result of closely spaced *d* orbitals, with a absorption maxima at 683 and 667 nm (ε = 133 and 79 $M^{-1}cm^{-1}$) respectively. The visible spectra for complexes **25** and **26** are depicted in Fig. 5.15.

The electronic spectra for Hbpct and [Pd(bpct)Cl] **(28)** as presented in Fig. 5.16 gave absorption maxima at 312 nm with molar absorptivity 5.34×10^4 $M^{-1}cm^{-1}$. The band with a maxima at 385 nm (ε = 443 M^{-1} cm^{-1}) was a broad band may be due to merging the highly intense LMCT with interaligand transitions. Accompanying these bands there are two shoulders with a maxima at 447 and 488 nm ($\varepsilon = 2.72 \times 10^4$ $M^{-1}cm^{-1}$ and 1.53×10^4 $M^{-1}cm^{-1}$). These low energy transitions were attributed to Pd←S and Pd←N_{py} transitions [21].

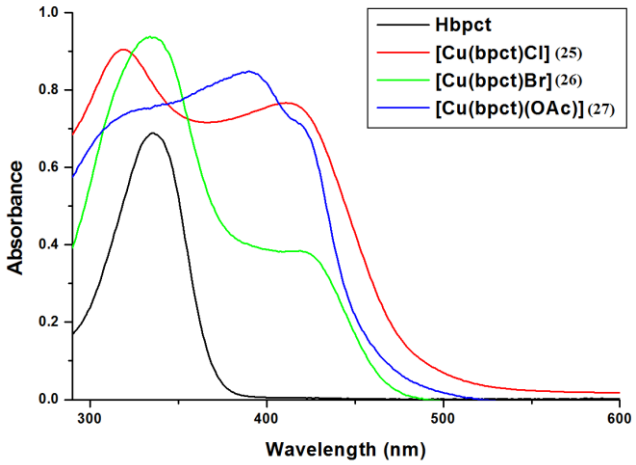

Fig. 5.14. Electronic spectra of Hbpct and complexes **25, 26** and **27**.

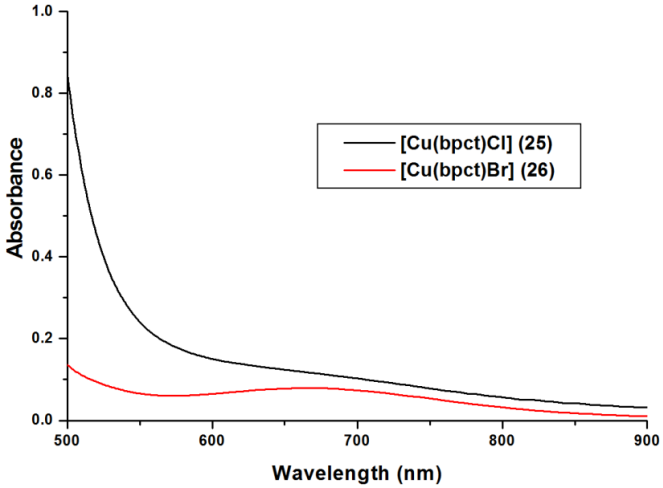

Fig. 5.15. Visible spectra of complexes **25** and **26**.

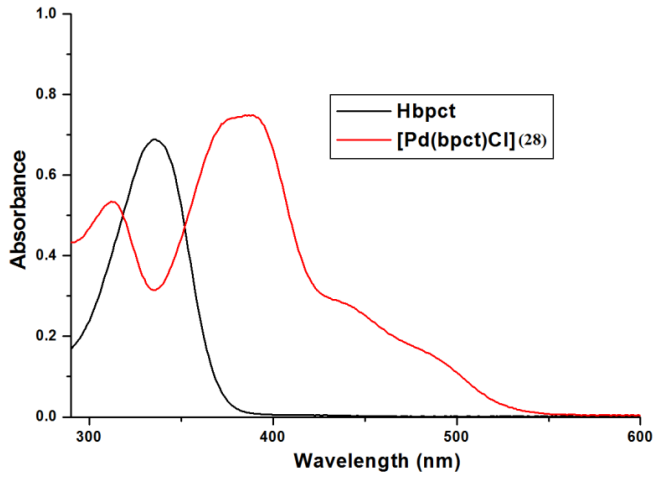

Fig. 5.16. Electronic spectra for Hbpct and complex **28**.

The electronic spectrum of $[Cd(bpct)_2]\cdot DMF$ **(29)** exhibited two maxima. The one with a maximum at 328 nm is a broad and strong band with molar absorptivity 6.4×10^4 M^{-1} cm^{-1}, accredited to intraligand transitions. The strong band with an absorption maximum at 422 nm with $\varepsilon = 8.09\times10^4$ M^{-1} cm^{-1} is due to LMCT transitions like Cd←N_{py} and Cd←S [22]. The electronic spectra for Hbpct and complex **29** depicted in Fig. 5.17.

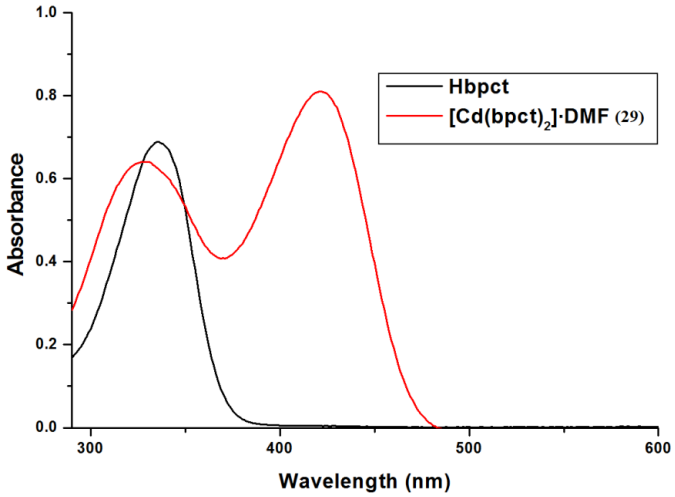

Fig. 5.17. Electronic spectra for Hbpct and complex **29**.

5.3.2.4. ^{1}H NMR spectra

The ^{1}H NMR spectrum of [Pd(bpct)Cl] **(28)** was recorded in DMSO-d_6 solution and compared with the ^{1}H NMR spectrum of Hbpct. The observed spectrum of the complex is presented in Figs. 5.18. It is found that the signal for N(2)–H at 9.33 ppm in the ^{1}H NMR spectrum of Hbpct has disappeared in the ^{1}H NMR spectrum of complex **28**. This is a confirmation for the complexation of Hbpct as a deprotonated mode. There is a marginal shift observed for aromatic protons in the complex confirming the coordination of pyridyl nitrogen to the metal.

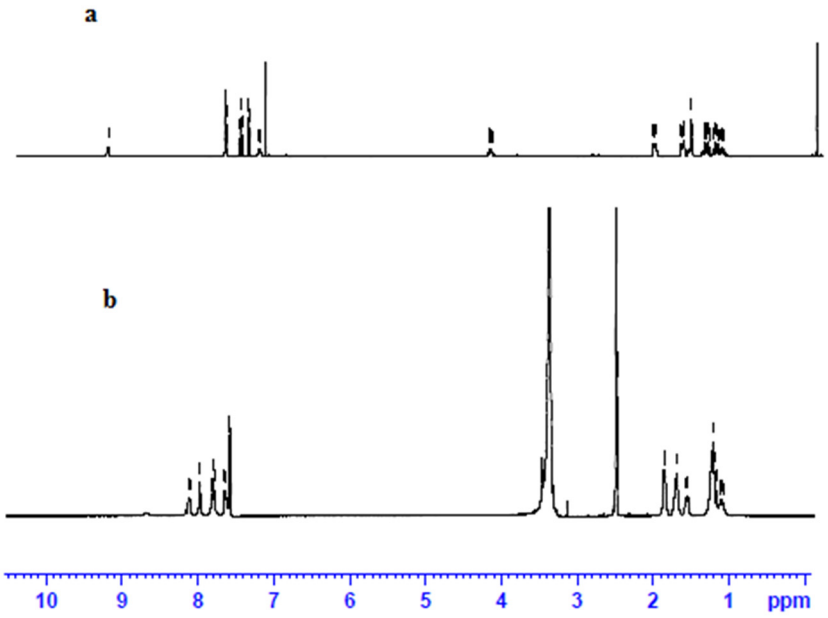

Fig. 5.18. ^{1}H NMR spectra for a)Hbpct and b) complex **28** In DMSO-d_6.

5.3.2.5. EPR spectra

The EPR spectrum of the complexes **25** and **27** were recorded in the polycrystalline state at 298 K and in DMF solution at 77 K. The EPR spectrum for complex **26** could not be resolved. The value of g tensor gives an idea about the ground state of the electron in the metal ion [23].

The g pararmeters for the complex [Cu(bpct)Cl] **(25)** in the polycrystalline was calculated from the simulated spectrum of the complex using Easy Spin 4.0.0 package [24]. Best fitted experimental (red) and a simulated (blue) spectra are given in Fig. 5.19. The g parameters for the complex **25** were given as $g_{\perp}$=2.05 and $g_{\|}$ =2.17 and g_{av}=2.09. The geometric parameter in the polycrystalline state G for complex **25** was found to be 3.51. The G values of the present complex was less than 4.4 suggest that there was a considerable interaction between the metal centres for complex **25** [25]. The EPR spectrum for complexes **25** in the polycrystalline state is represented in Fig. 5.19.

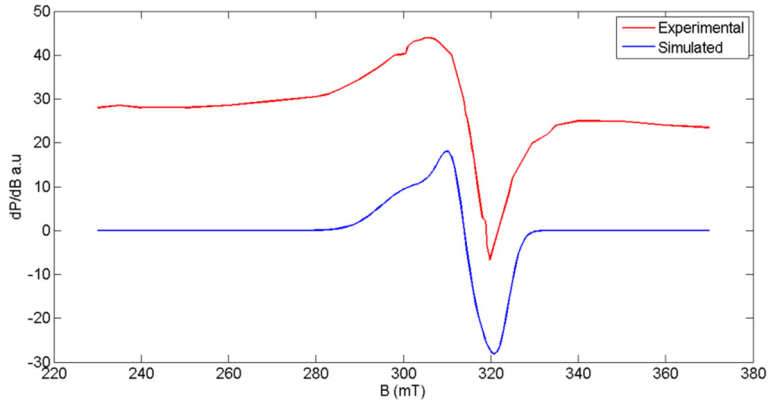

Fig. 5.19. EPR spectrum for complex **25** at 298 K.

The EPR spectrum for complex **25** in DMF solution at 77 K is given in Fig. 5.20. The g tensors for complex **25** give four hyperfine lines in DMF solution. The g parameters are $g_{\perp}$ = 2.04 and $g_{\|}$ = 2.19 with hyperfine constants of $A_{\|}$ = 186 × 10^{-4} cm^{-1} corresponding to splitting in the parallel region. We failed to get a best fitted simulated spectrum in the perpendicular region

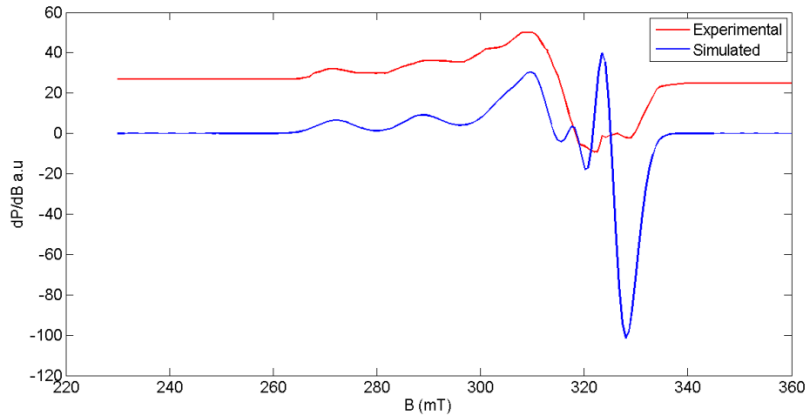

Fig. 5.20. EPR spectrum for complex **25** at 77 K.

The EPR spectral results for [Cu(bpct)(OAc)] **(27)** showed that the *g* parameters for complex **27** were found to be, $g_{\perp}$=2.05 and $g_{\parallel}$ =2.18 and g_{av}=2.09. The geometric parameter *G* for complex **27** is obtained as3.72. Since this value is less than 4.3, it was considered that there was a greater interaction between the metal centres. The EPR spectrum for complex **27** in the polycrystalline state at 298 K is given in Fig. 5.21.

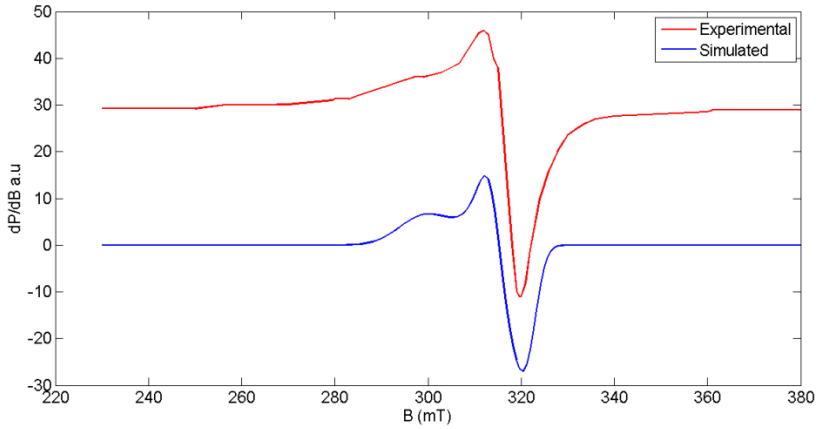

Fig. 5.21. EPR spectrum for complex **27** at 298 K.

The EPR spectrum for complex **27** at 77 K is represented in Fig. 5.22. The spectrum gave four hyperfine lines with g tensors as $g_{\perp} = 2.05$ and $g_{\parallel} = 2.19$ with hyperfine coupling constant $A_{\parallel} = 202 \times 10^{-4}$ cm^{-1}.

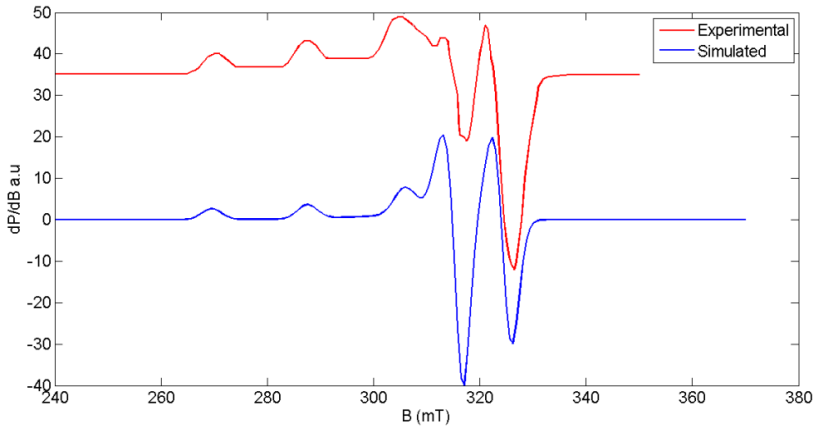

Fig. 5.22. EPR spectrum for complex **27**.

From the above observations it was found that for both complex **25** and **27,** the condition $g_{\parallel} > g_{\perp} > 2.0023$, consistent with $d_{x^2-y^2}$ ground state for an octahedral or square planar complex. The g_{av}, calculated using the equation $g_{av} = \frac{1}{3}(g_{\parallel} + 2g_{\perp})$, is found to be 2.14 and 2.09 respectively for complexes **25** and **27**. When $g_{\parallel} < 2.3$, there is a significant covalent character to the M–L bond and if $g_{\parallel} > 2.3$ indicate ionic character [26]. For complexes **25** and **27**, $g_{\parallel} < 2.3$ and hence M–L bond is having a significant covalent character.

The various bonding parameters for complex **25** are $K_{\parallel} = 0.644$, $K_{\perp} = 0.577$, $\alpha^2 = 0.760$, $\beta^2 = 0.846$ and $\gamma^2 = 0.758$, whereas for complex **27** $K_{\parallel} = 0.634$, $K_{\perp} = 0.640$, $\alpha^2 = 0.807$, $\beta^2 = 0.786$ and $\gamma^2 = 0.792$ [27,28]. The

presence of significant covalent character for the M–L bond is evident from the α^2 values. For complex **25**, it was observed that $K_{\perp}<K_{\parallel}$, which indicate the complex had an out-of plane π-bonding, whereas for complex **27** $K_{\parallel}< K_{\perp}$ suggesting an in-plane π-bonding.

5.3.2.6. Single crystal X-ray diffraction studies

5.3.2.6.1. Single crystal X-ray diffraction studies of $[Ni(Hbpct)_2](NO_3)_2\cdot H_2O$ (23)

Brown crystals, of complex **23** were isolated from mother liquor by slow evaporation after two weeks. The compound crystallized into monoclinic *C*2/c space group. A crystal of size 0.40 × 0.35 × 0.20 mm^3 were separated and mounted on SMART APEXII CCD diffractometer. The details regarding crystal refinement and other parameters are given in Table 5.7. The asymmetric unit of $[Ni(Hbpct)_2](NO_3)_2\cdot H_2O$ **(23)** contain one unit of the complex. The two nitrate units and one of the cyclohexyl units of the complex are disordered. The disordered atoms C(20), N(8), C(20B) and N(8B) were restrained to lie in the same plane as that of atoms N(7) and S(1) with the help of FLAT instruction [29]. The ORTEP diagram of the molecule with 50% ellipsoid probability describes the disorder clearly (Fig. 5.23). The cyclohexyl ring is disordered over two sites with occupancy of 56 and 44% respectively. The non-hydrogen atoms in the molecule were refined anisotropically and with the help of difference map the C–H bond distances were constrained to 0.93-0.97 Å, with hydrogen assigned U_{iso} = 1.2*U*eq.

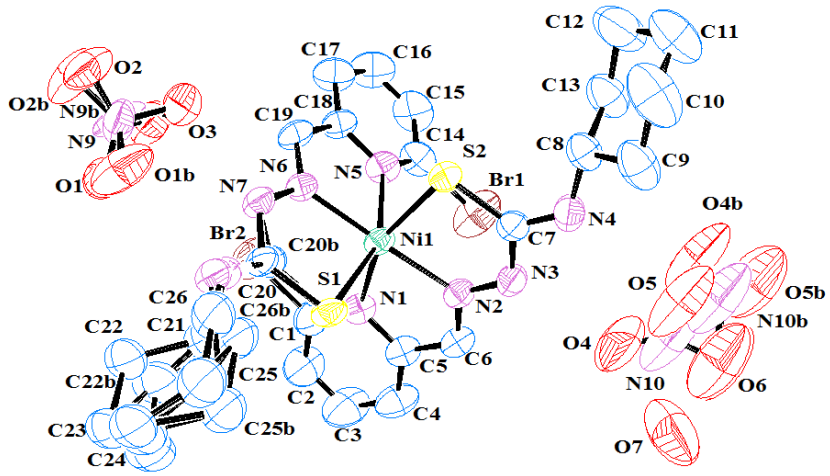

Fig. 5.23. ORTEP diagram for $[Ni(Hbpct)_2](NO_3)_2 \cdot H_2O$ **(23)** with 50% ellipsoid probability (hydrogen atoms are omitted for clarity).

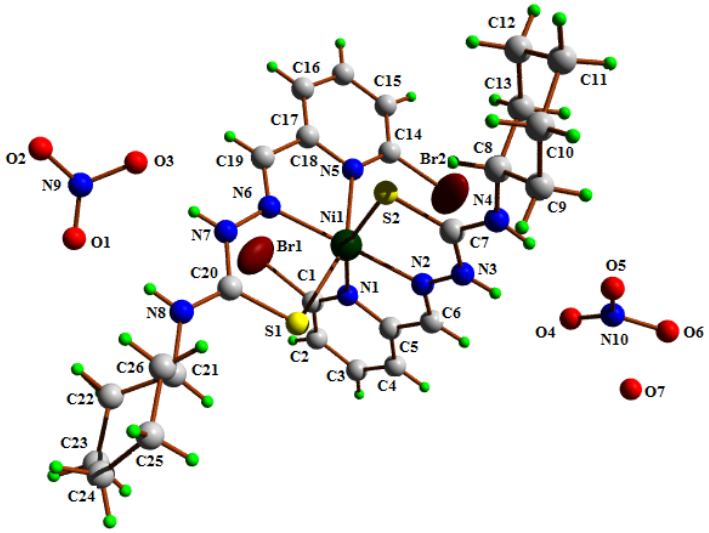

Fig. 5.24. Numbering scheme for complex **23** (omitting the disordered components).

The atoms from N(9) to O(3B) and N(10) to O(6B) were restrained to move in the same direction with same U_{ij} (nitrate units). The bonds C(20)–N(7) and C(20B)–N(7) were restrained to have same distance as

that of C(7)–N(3) with in a default standard uncertainty of 0.02 Å. The atoms from C(20) to C(26B) were refined anisotropically with same U_{ij} (disordered cyclohexyl ring). The numbering scheme for the complex (omitting the disordered components) is represented in Fig. 5.24.

Table 5.7. Crystal data and structure refinement parameters of $[Ni(Hbpct)_2](NO_3)_2 \cdot H_2O$ **(23)**

Parameters	**$[Ni(Hbpct)_2](NO_3)_2 \cdot H_2O$ (23)**
Empirical formula	$C_{26}H_{34}Br_2N_8NiO_{6.34}S_2$
Formula weight	870.73
Color	Brown
Temperature/K	293 (2)
Crystal system	monoclinic
Space group	*C*2/c
Cell parameters	
a(Å)	14.511(11))
b (Å)	21.842(2)
c (Å)	23.786(3)
α = γ (°)	90
β (°)	102.474(3)
Volume ($Å^3$)	7361.1(12)
Z	8
Calculated density, ρ (g cm^{-3})	1.571
Absorption coefficient, μ (mm^{-1})	2.864
F(000)	3526
Crystal size (mm^3)	0.40 x 0.35 x 0.20
θ range for data collection (°)	1.713 to 28.192
Limiting indices	$-19 \le h \le 11$, $-28 \le k \le 28$, $-25 \le l \le 31$
Reflections collected	29624
Independent reflections	8845 [R(int) = 0.0504]
Data/restraints/parameters	9064 / 524 / 580
Goodness-of-fit on F^2	1.060
Final R indexes [I>2σ (I)]	R_1 = 0.0918, wR_2 = 0.2090
Final R indexes [all data]	R_1 = 0.0579, wR_2 = 0.0869
Largest diff. peak and hole (e $Å^{-3}$)	0.280 / -0.794

$R_1 = \Sigma||F_o| - |F_c|| / \Sigma|F_o|$
$wR_2 = [\Sigma w(F_o^2-F_c^2)^2 / \Sigma w(F_o^2)^2]^{1/2}$

The disorder observed in the cyclohexyl and nitrate groups made the structure description of the complex tedious. So the disordered components are not included in the discussion of the structure as well as interactions in the molecule. The bond angles N(6)–Ni(1)–N(2), S(1)–Ni(1)–N(5) and S(2)–Ni(1)–N(1) were found to be 169.90(2)°, 156.53(15)° and 157.34(12)° respectively. From this observation, it was clear that the Ni(II) ion is having a distorted octahedral geometry with the six corners were engrossed by N(1), N(2) and S(2) of the first ligand and N(5), N(6) and S(1) of the second ligand, with opposite sides have been decorated by N(6) and N(2), S(1) and N(5) finally S(2) and N(1) atoms. This justifies the coordination of Hbpct as NNS donor ligand for complex **23**.

The variation in the bond lengths of free ligand as compared to that of the complex is a further evidence for the formation of a bond between the ligand and metal centre. It is found that the azomethine bond lengths C(6)–N(2) and C(19)–N(6) are 1.297(8) and 1.277(7) Å respectively. These values are slightly greater for former and lower for later, than that of Hbpct [1.278(4) Å], suggesting strong coordination of N(6) and N(2) to Ni(II) ion. This is further supported from the Ni(1)–N(2) and Ni(1)–N(6) bond lengths of 2.028(5) and 2.032(5) Å respectively. The C(7)–S(2) and C(20)–S(1) bond lengths 1.707(6) and 1.720(2) Å are longer than C(1)–S(1) [1.683(3) Å] bond length of free ligand. This advocates the coordination of sulfur atom to Ni(II) ion. Selected bond lengths and bond angles of the complexes are reported in Table 5.8.

Table 5.8. Selected bond parameters for complex **23**

Bond length (Å)		Bond angle (°)	
Ni(1)–S(1)	2.418(16)	N(1)–Ni(1)–N(2)	76.70(12)
Ni(1)–S(2)	2.392(19)	N(2)–Ni(1)–S(2)	81.59(16)
Ni(1)–N(1)	2.192(15)	N(5)–Ni(1)–S(2)	90.28(16)
Ni(1)–N(5)	2.418(16)	N(6)–Ni(1)–N(5)	76.30(19)
Ni(1)–N(2)	2.028(5)	S(1)–Ni(1)–S(2)	98.25(7)
Ni(1)–N(6)	2.032(5)	N(6)–Ni(1)–S(1)	81.72(13)
C(6)–N(2)	1.297(8)	N(5)–Ni(1)–N(1)	91.2(2)
N(3)–N(2)	1.346(7)	N(6)–Ni(1)–N(2)	169.9(2)
C(19)–N(6)	1.277(7)	S(1)–Ni(1)–N(5)	156.53(15)
C(7)–S(2)	1.707(6)	S(2)–Ni(1)–N(1)	157.34(12)
N(3)–C(7)	1.354(7)		
N(6)–N(7)	1.361(7)		
C(20)–N(7)	1.372(2)		
C(20)–S(1)	1.720(2)		

The torsion angles C(5)–C(6)–N(2)–N(3) and C(18)–C(19)–N(6)–N(7) [180.0(5) and 179.3(10)°] propose that the thiosemicarbazone moiety is *trans* with respect to azomethine bond. The *Z* conformation of sulfur [S(1) and S(2)] with respect to azomethine nitrogen [N(2) and N(6)] is evident from the torsion angles of 1.4(7) and -2.1(10)° for N(2)–N(3)–C(7)–S(2) and N(5)–C(18)–C(19)–N(6) respectively. Whereas in free ligand the sulfur atom is *trans* with respect to azomethine nitrogen [N(3)–N(2)–C(1)–S(1) torsion angle is 176.6 (2)°].

Because of complex formation four and five membered chelate rings were generated. The adjacent rings Ni(1)–N(5)–C(18)–C(19)–N(6) and Ni(1)–N(6)–N(7)–C(20)–S(1) are twisted with a dihedral angle of 5.2(3)°. Similarly the rings Ni(1)–N(1)–C(5)–C(6)–N(2) and Ni(1)–N(2)–N(3)–C(7)–S(2) are twisted with a dihedral angle of 3.6(2)°, confirming the

distortion in the octahedral geometry about Ni(II) ion. The pyridine rings N(5)–C(14)–C(15)–C(16)–C(17)–C(18) and N(1)–C(1)–C(2)–C(3)–C(4)–C(5) are twisted from their adjacent chelating rings Ni(1)–N(5)–C(18)–C(19)–N(6) and Ni(1)–N(1)–C(5)–C(6)–N(2) with a dihedral angle of 4.1(3) and 6.9(4)° respectively.

The ring puckering analysis and least square plane calculations show that the five membered chelate ring Ni(1)–N(6)–N(7)–C(20)–S(1) is twisted about N(6)–Ni(1) bond with Q(2) = 0.089(7) Å and Φ(2) = 345(8)°. As for ring Ni(1)–N(1)–C(5)–C(6)–N(2), Q(2) = 0.105(5) Å and Φ(2) = 192(4)° and is twisted about Ni(1)–N(1) bond [31]. The ring Ni(1)–N(5)–C(18)–C(19)–N(6) is found to adopt an envelope conformation with N(5) as the flap atom puckering amplitude Q(2) = 0.113(4) Å and Φ(2) = 173(3)°. The six membered rings C(8)–C(9)–C(10)–C(11)–C(12)–C(13) and C(21)–C(22)–C(23)–C(24)–C(25)–C(26) adopt a chair conformation with a puckering amplitude Q_T = 0.577(10) and 0.582(17) Å, θ = 177.8(10)° and 29.5(18)° respectively [11].

Complex **23** showed a large number of hydrogen bonding interactions as represented in Fig. 5.25 [Table 5.9]. The bifurcated hydrogen bond C(17)–H(17) connects the O(6) and O(7) of second nitrate with a D···A distances of 3.428(15) and 3.160(3) Å respectively. The N(10) and O(4) atoms on the first nitrate unit within the asymmetric unit is involved in another bifurcated hydrogen bonding interaction N(2)–H(3A)···N(10) and N(2)–H(3A)···O(4) with D···A distances of 3.480(18) and 2.715(12) Å respectively. The O(5) atom is involved in a bifurcated type hydrogen bonding interaction C(4)–H(4)···O(5) and N(4)–H(4N)···O(5) with D···A distances of 3.223(18) and 2.918(15) Å respectively. Here the former one is an intermolecular hydrogen bonding tend to connect the neighboring complex unit to the nitrate molecule, while the later is an intramolecular hydrogen bonding interaction. The

interamolecular interactions N(8)–H(8A)···O(1) and N(7)–H(7)···O(3) further strengthen the stability of the complex. Other intermolecular interactions that stabilizes the crystal lattice are C(26)–H(26B)···Br(1) and C(19)–H(19)···O(6) with D···A distance of 3.849(17) and 3.137(13) Å respectively. It is interesting to note that all the oxygen atoms on the nitrate unit are involved hydrogen bonding interactions.

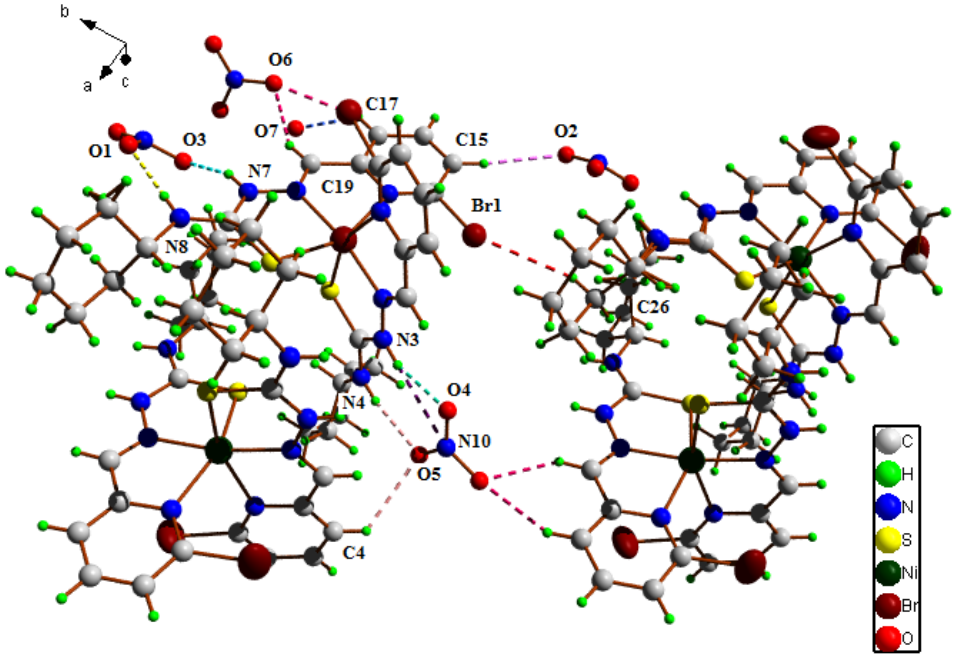

Fig. 5.25. Hydrogen bonding interactions in complex **23**.

The various hydrogen bonding interactions connect molecules such that a cluster of the compound is generated and thus a three dimensional figure is generated in the packing of the complex.

Table 5.9. Hydrogen bonding interactions in complex **23**.

Hydrogen bonding interactions				
D–H···A	D–H (Å)	H···A (Å)	D···A (Å)	D–H···A (°)
C(4)–H(4)···O(5)[a]	0.93	2.60	3.223(18)	125.2
N(4)–H(4N)···O(5)	0.86	2.07	2.918(15)	170.8
C(15)–H(15)···O(2)[b]	0.93	2.66	3.580(3)	169.1
C(17)–H(17)···O(6)[c]	0.93	2.66	3.428(15)	140.8
C(17)–H(17)···O(7)[c]	0.93	2.43	3.160(3)	135.7
C(19)–H(19)···O(6)[c]	0.93	2.29	3.137(13)	151.2
N(8)–H(8A)···O(1)	0.86	1.99	2.850(3)	177.3
C(26)–H(26B)···Br(1)[d]	0.97	3.02	3.849(17)	144.4
N(3)–H(3A)···N(10)	0.86	2.67	3.480(18)	157.8
N(3)–H(3A)···(O4)	0.86	1.88	2.715(12)	162.2
N(7)–H(7)···O(3)	0.86	1.92	2.726(15)	155.8

Equivalent positions : a = -x+2, y, -z+ ⅗ ; b = x-½, y+½, z; c = x+ ⅗ , y-½, -z+ ⅗ ; d = x+½, y-½, z.

5.3.2.6.2. Single crystal X-ray crystallographic studies of $[Ni(bpct)_2]\cdot DMF$ (24)

The complex **24** was isolated as brown crystals from a DMF solution of compound. The complex is found to crystallize into monoclinic *C*2/c space group. The asymmetric unit of the complex contains only half of the molecule. The DMF unit was disordered with the disordered component was be generated upon growing the fragment. The crystal lattice was embedded with some other atoms, which made the crystal refinement a tedious process. We in the end decided to confine our self to the structure come in agreement with other analysis. The disordered components from C(7) to C(14B) were restrained to lie in the same plane [29]. The N(4)–H(4A) and N(4B)–H(4B) distances were fixed to 0.86 Å. The atoms on the solvent were restrained to occupy same plane using SADI instruction [29]. The bond distances C(16)–N(5) and C(17)–N(5) were fixed to have a value of 1.5 Å, whereas for C(15)–O(1) the distance was fixed to 1.3 Å.

The C–H bonds were calculated to have values between 0.93-0.98 Å, with the aid of difference maps. The hydrogen atoms were given $U_{iso} = 1.2U_{eq}$ (1.5 for Me). The crystal refinement details are listed in Table 5.10.

Table 5.10. Crystal refinement details of $[Ni(bpct)_2]\cdot DMF$ **(24)**

Parameters	**$[Ni(bpct)_2]\cdot DMF$ (24)**
Empirical formula	$C_{55}H_{71}Br_4N_{18}Ni_2O_4S_4$
Formula weight	1613.52
Color	Brown
Temperature/K	296(2)
Crystal system	monoclinic
Space group	*C*2/c
Cell parameters	
a(Å)	15.4690(9)
b (Å)	18.9553(9)
c (Å)	12.6341(6)
α = γ(°)	90
β (°)	108.584(4)
Volume ($Å^3$)	3511.4(3)
Z	2
Calculated density, ρ (g cm^{-3})	1.526
Absorption coefficient, μ (mm^{-1})	2.986
F(000)	1638
Crystal size (mm^3)	0.50 x 0.50 x 0.45
θ range for data collection (°)	2.114 to 28.303
Limiting indices	$-19 \le h \le 20$, $-25 \le k \le 25$, $-16 \le l \le 16$
Reflections collected	13278
Independent reflections	4380 [R(int) = 0.0497]
Data/restraints/parameters	4316 / 333 / 344
Goodness-of-fit on F^2	0.926
Final R indexes [I>2σ (I)]	$R_1 = 0.0597$, $wR_2 = 0.1579$
Final R indexes [all data]	$R_1 = 0.1309$, $wR_2 = 0.2024$
Extinction coefficient	0.0012(3)
Largest diff. peak and hole (e $Å^{-3}$)	0.825 and -0.708

$R_1 = \Sigma||F_o| - |F_c|| / \Sigma|F_o|$

$wR_2 = [\Sigma w(F_o^2-F_c^2)^2 / \Sigma w(F_o^2)^2]^{1/2}$

The Br atom disordered with occupancy of 53 and 47% for each disordered component. Similarly the atoms from C(7) to C(14) were also disordered to two components with an occupancy of 64% and 36% respectively for each. The asymmetric unit of the complex **24** with an ellipsoid probability of 50% is given in Fig. 5.26.

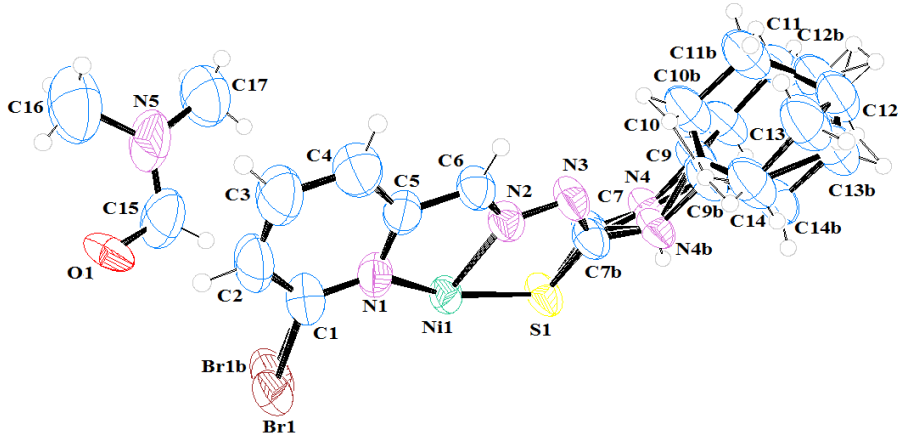

Fig. 5.26. ORTEP diagram for asymmetric unit of $[Ni(bpct)_2]\cdot DMF$ **(24)** with 50% ellipsoid probability.

Since the asymmetric unit of the complex **24** contains half of the molecule, discussion is restricted to only one portion. The bond angles N(1)–Ni(1)–S(1), N(1)–Ni(1)–N(1)$^{\#}$ and N(1)$^{\#}$–Ni(1)–S(1)$^{\#}$ (# = 2-x, y, ½-z) were found to be 158.6(11)°, 172.4(2)° and 158.6(11)° respectively. These bond angles suggest that bpct^{-} is coordinated to Ni(II) *via* N(1), S(1) and N(2) atoms and thus behaves as an NNS type ligand.

The azomethine, C(6)–N(2) bond length 1.276(6) Å found to be vary from that of free ligand indicating coordination of azomethine nitrogen to Ni(II). The N(3)–C(7) and C(7)–S(1) bond lengths 1.320(3) and 1.760(3) Å, are different from the corresponding bond lengths of free Hbpct [1.278(4) and 1.683(3) Å], suggesting coordination of ligand to Ni(II) as a monodeprotonated ligand. Selected bond lengths, bond angles and torsion

angles are listed in Table 5.11. The torsion angle N(1)–C(5)–C(6)–N(2) observed to be 6.08(11)° suggests that N(1) is lying *cis* to N(2). The thiosemicarbazone moiety in the complex is found to have a *E* configuration with respect to azomethine bond and is evident from the C(5)–C(6)–N(2)–N(3) torsion angle of 179.3(2)°. The *trans* conformation of S(1) with respect to N(2) in the ligand changes to *cis* in the complex. This is confirmed from and N(3)–N(2)–C(1)–S(1) torsion angle of 176.60(2)° in the ligand and N(2)–N(3)–C(5)–C(6) torsion angle 3.2(3)° in the complex

Table 5.11. Selected bond parameters for complex **24**

Bond length (Å)		**Bond angle (°)**	
Ni(1)–S(1)	2.364(14)	N(1)–Ni(1)–N(2)	77.78(16)
Ni(1)–N(1)	2.205(4)	N(2)–Ni(1)–S(1)	81.59(11)
Ni(1)–N(2)	2.020(4)	N(1)–Ni(1)–S(1)	158.60(11)
C(6)–N(2)	1.297(8)	N(1)–Ni(1)–N(1)$^{\#}$	92.90(2)
N(3)–N(2)	1.346(7)	N(2)–Ni(1)–N(2)$^{\#}$	172.4(2)
C(7)–S(1)	1.760(3)	N(1)$^{\#}$–Ni(1)–S(1)$^{\#}$	158.60(11)
N(3)–C(7)	1.320(3)		

Equivalent position coordinate, # = 2-x, y, ½-z

Two five membered chelating rings are generated as a result of complex formation and these rings Ni(1)–N(2)–C(6)–C(5)–N(1) (Cg(1)) and Ni(1)–N(2)–N(3)–C(7)–S(1) (Cg(2)) are twisted from each other with a dihedral angle of 4.2(8)°. The adjacent rings Ni(1)–N(2)–C(6)–C(5)–N(1) (Cg(1)) and N(1)–C(1)–C(2)–C(3)–C(4)–C(5) (Cg(3)) were twisted with a dihedral angle of 13.8(14)° from each other. Least square plane calculations and ring puckering analysis show that the five memebred rings Cg(1) and Cg(2) are puckered with Q(2) = 0.163 Å and φ(2) = 15.43° and Q(2) = 0.055 Å and φ (2) = 152.56°. These findings suggest that the former ring is having an envelope conformation about Ni(1) and the later

have a twist conformation about Ni(1)–N(2). The chair conformation of the cyclohexane ring Cg(4) is clear from Q(2) = 0.1165 Å, Q(3) = 0.6110 Å, φ(2) = 173.63° and ring puckering amplitude Q_T = 0.622 Å and φ(2) = 10.80° [30].

Complex **24** is characterized by three intermolecular interactions (Fig. 5.27, Table 5.12). The Br(1) is involved in bifurcated type of interaction C(6)–H(6)···Br(1) and C(14)–H(14B)···Br(1) with D···A distance of 3.707(4) and 3.794(11) Å respectively. The hydrogen bonding N(4)–H(4)···S(1) with D···A distance 3.424(8) Å further strengthen the crystal packing.

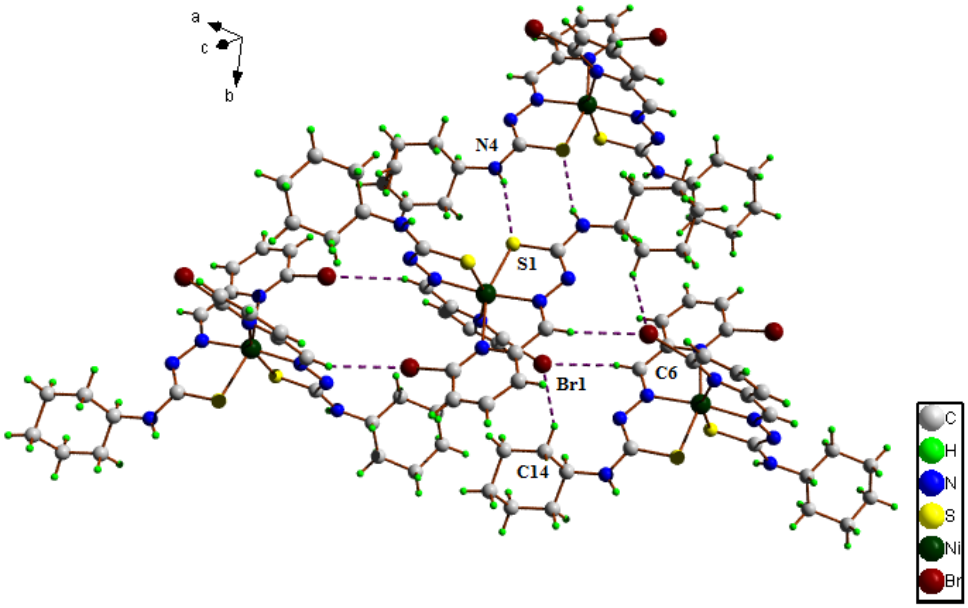

Fig. 5.27. Hydrogen bonding interactions in complex **24**, disordered components are omitted for clarity.

Table 5.12. Hydrogen bonding interactions in complex **24**

Hydrogen bonding interactions				
D–H···A	D–H (Å)	H···A (Å)	D···A (Å)	D–H···A (°)
C(6)–H(6)···Br(1)[a]	0.93	2.96	3.707(4)	138.1
C(14)–H(14B)···Br(1)[a]	0.97	3.13	3.794(11)	127.1(5)
N(4)–H(4)···S(1)[b]	0.87(19)	2.60(3)	3.424(8)	159(5)

a = x-½, -y+½, z-½; b = -x+2, -y, -z

5.3.2.6.3. Single crystal X-ray crystallographic studies of $[Cd(bpct)_2]\cdot DMF$ (29)

Yellow block shaped crystal of complex **29** of size 0.50 0.30 × 0.20 mm^3 was separated and mounted on a SMART APEXII CCD diffractometer. The complex crystallizes into monoclinic $P2_1$ space group. The asymmetric unit contains two molecules [set 1 and set 2] of the complex and two DMF units. The complex formed around Cd(2) is disordered about cyclohexane groups as well as atoms S(4), C(46) and N(16) to two components and are refined with 54% and 46% occupancy for each [set 1]. The pyridine ring N(9)–C(27)–C(28)–C(29)–C(30)–C(31) and Br(3) is also disordered to two parts and are refined with 64% and 36% occupancy for each components [set 2]. The disordered components are refined by placing the atoms in the same plane as that of N(15) and C(32) respectively for each set of disorder. All non-hydrogen atoms were refined anisotropically. The hydrogens attached to carbon were identified and placed in positions with the aid of difference map with C–H bond distances 0.93-0.98 Å and $U_{iso} = 1.2U_{eq}$ for hydrogen atom ($1.5U_{eq}$ for CH_3). The details of crystal refinement are summed up in Table 5.13.

Table 5.13. Crystal refinement parameters for $[Cd(bpct)_2]\cdot DMF$ **(29)**

Parameters	**$[Cd(bpct)_2]\cdot DMF$ (29)**
Empirical formula	$C_{58}H_{73}Br_4Cd_2N_{18}O_2S_4$
Formula weight	1727.02
Color	Yellow
Temperature/K	293(2)
Crystal system	Monoclinic
Space group	$P2_1$
Cell parameters	
a(Å)	10.6711(7)
b (Å)	25.601(2)
c (Å)	13.6227(12)
$\alpha = \gamma$ (°)	90
β (°)	104.287(4)
Volume ($Å^3$)	3606.5(5)
Z	2
Calculated density, ρ ($g\ cm^{-3}$)	1.590
Absorption coefficient, μ (mm^{-1})	2.973
F(000)	1726
Crystal size (mm^3)	0.50 x 0.30 x 0.20
Θ range for data collection (°)	3.086 to 28.462
Limiting indices	$-14 \leq h \leq 13$, $-34 \leq k \leq 34$, $-15 \leq l \leq 18$
Reflections collected	30182
Independent reflections	16302 [R(int) = 0.0616]
Data/restraints/parameters	9305 / 703 / 944
Goodness-of-fit on F^2	0.979
Final R indexes [$I>2\sigma(I)$]	$R_1 = 0.0645$, $wR_2 = 0.1491$
Final R indexes [all data]	$R_1 = 0.1298$, $wR_2 = 0.1762$
Largest diff. peak and hole (e $Å^{-3}$)	2.342 and -1.100

$R_1 = \Sigma||F_o| - |F_c|| / \Sigma|F_o|$

$wR_2 = [\Sigma w(F_o^2-F_c^2)^2 / \Sigma w(F_o^2)^2]^{1/2}$

ORTEP diagram with 50% ellipsoid probability for complex $[Cd(bpct)_2]\cdot DMF$ **(29)** is given in Fig. 5.28. The geometry around both Cd(1) and Cd(2) are distorted octahedral. This is supported by the bond angles 136.7(3)°, 138.3(3)° and 169.0(4)° respectively for N(1)–Cd(1)–S(1), N(5)–Cd(1)–S(2) and N(2)–Cd(1)–N(6) for the first complex and 137.5(4)°, 140.3(6) and 169.1(4)° respectively for N(9)–Cd(2)–S(3), N(13)–Cd(2)–S(4) and N(10)–Cd(1)–N(14) for the second complex. The above findings give an insight to the coordinating atoms in both the complexes to be N(1), S(1), N(5), S(2), N(2) and N(6) around Cd(1) and N(9), N(10), N(13), N(14), S(3) and S(4) around Cd(2).

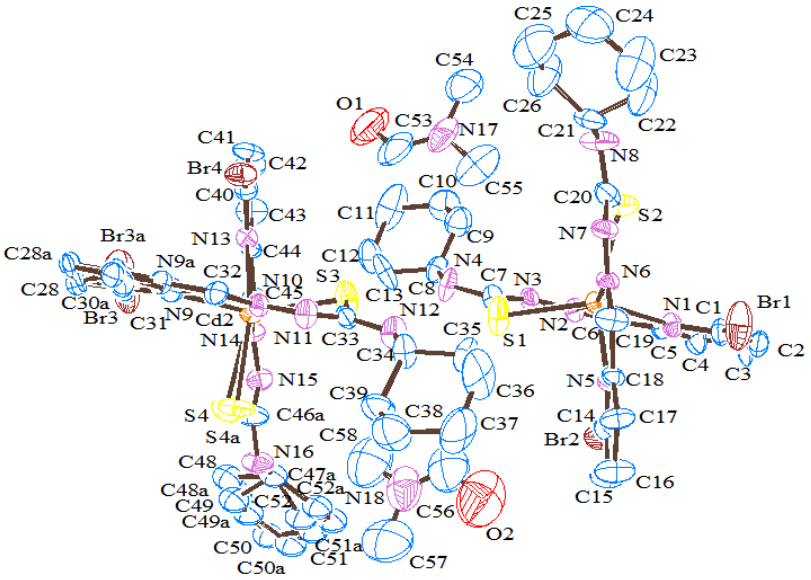

Fig. 5.29. ORTEP diagram with 50% probability for complex **29** (hydrogen atoms are omitted for clarity).

Since the bonding natures of both complexes are almost the same, the discussion is limited to only one of the complex molecule. The disordered components are also omitted from discussion as these components have a minor occupancy. The azomethine bond for both bpct⁻

units, C(6)–N(2) and C(19)–N(6) were found to be 1.294(17) and 1.282(16) Å respectively, show deviation from that of metal free Hbpct. The bond lengths 1.723(12) and 1.693(16) Å for the bonds C(7)–S(1) and C(20)–S(2) are longer than C(2)–N(3) bond length of free ligand. The bond lengths for the bonds C(7)–N(3) and C(20)–N(7) were found to be 1.350(15) Å and 1.343(18) Å respectively are shorter than the corresponding C(1)–N(2) bond length (1.359(4) Å) of free ligand. This observation is an evidence for the complexation of the Hbpct as monodeprotonated form. Selected bond lengths and bond angles are presented in Table 5.14.

Table 5.14. Selected bond parameters for complex **29**

Bond length (Å)		**Bond angle (°)**	
Cd(1)–S(1)	2.560 (4)	N(2)–Cd(1)–N(6)	169.0(4)
Cd(1)–N(1)	2.491(10)	N(1)–Cd(1)–S(1)	136.7(3)
Cd(1)–N(2)	2.337(10)	N(5)–Cd(1)–S(2)	138.3(3)
Cd(1)–N(5)	2.436(10)	S(1)–Cd(1)–S(2)	111.82(17)
Cd(1)–N(6)	2.371(10)	N(10)–Cd(2)–N(14)	169.1(4)
Cd(1)–S(2)	2.568 (4)	N(9)–Cd(2)–S(3)	137.5(4)
Cd(2)– S(3)	2.570 (4)	N(13)–Cd(2)–S(4)	140.3(6)
Cd(2)– N(9)	2.371(17)	S(4)–Cd(2)–S(3)	113.1(9)
Cd(2)–N(10)	2.361(11)		
Cd(2)–N(13)	2.446(11)		
Cd(2)–N(14)	2.334(11)		
Cd(2)–S(4)	2.660 (4)		
C(7)–S(1)	1.723(12)		
C(20)–S(2)	1.693(16)		
C(7)–N(3)	1.350(15)		
C(6)–N(2)	1.294(17)		
C(19)–N(6)	1.282(16)		
C(46)–N(15)	1.330(5)		
C(33)–S(3)	1.734(14)		

The change in torsion angle of 6.6(17)° for N(2)–N(3)–C(7)–S(1) in the complex **29** from that of 176.6(2)° for N(3)–N(2)–C(1)–S(1) in the free ligand reveals a change configuration for sulfur to *cis* from *trans* with respect to N–C bond. The azomethine moiety adopts an *E* configuration both in free ligand and complex **29**, supported by the C(5)–C(6)–N(2)–N(3) torsion angle 174.9(12)° in complex **29** which is 177.7(2)° for C(3)–C(2)–N(3)–N(2) in the free Hbpct.

Four five membered chelating rings are generated around Cd(1) as a result of complex formation. The adjacent chelating rings Cd(1)–S(1)–N(2)–N(3)–C(7) and Cd(1)–N(1)–N(2)–C(5)–C(6) are twisted away from each other by a dihedral angle of 16.4(5)°. Similarly the rings Cd(1)–S(2)–N(6)–N(7)–C(20) and Cd(1)–N(5)–N(6)–C(18)–C(19) are twisted by a dihedral angle of 13.8(5)°. The pyridine ring is also twisted from the neighbouring chelate ring like N(1)–C(1)–C(2)–C(3)–C(4)–C(5) and Cd(1)–N(1)–N(2)–C(5)–C(6) are twisted by dihedral angle of 3.8(7)° and N(2)–C(14)–C(15)–C(16)–C(17)–C(18) are twisted by a dihedral angle of 1.3(7)°. The chelating rings around Cd(2) also exhibit same results.

Least square plane calculations and ring puckering analysis proved that the cyclohexyl rings Cg(13), Cg(14), Cg(3) and Cg(4) adopt chair conformations with puckering amplitude Q_T = 0.54(2), 0.52(3), 0.58(2) and 0.59(4) Å respectively. [Cg(13)= C(8)–C(9)–C(10)–C(11)–C(12)–C(13), Cg(14)= C(21)–C(22)–C(23)–C(24)–C(25)–C(26), Cg(3)= C(34)–C(35)–C(36)–C(37)–C(38)–C(39) and Cg(4)= C(47)–C(48)–C(49)–C(50)–C(51)–C(52)]. The chelating ring Cd(1)–S(1)–C(7)–N(3)–N(2) adopt an envelope conformation with S(1) as the flap atom and have puckering amplitude Q(2) = 0.378(9) Å and Φ(2) = 8.0(19)°. The ring Cd(1)–S(2)–C(20)–N(7)–N(6) is twisted about Cd(1)–S(2) bond with Q(2) = 0.320(8) Å and Φ(2) = 10.0(2)°.

Intermolecular interaction inculcates more effective packing in the complex. The complex **29** showed a large number of hydrogen bonding, π···π and C–H···π interactions. But except hydrogen bonding interactions all other were not significance due to large D···A distances. The hydrogen bonding interactions for complex **29** are listed in Table 5.15.

Table 5.15. Hydrogen bonding interactions in complex **29**

Hydrogen bonding interactions				
D–H···A	**D–H (Å)**	**H···A (Å)**	**D···A (Å)**	**D–H···A (°)**
C(6)–H(6)···Br(4)[a]	0.93	2.82	3.647(14)	148.9
C(8)–H(8)···Br(4)[a]	0.98	3.00	3.810(14)	140.6
C(34)–H(34)···Br(2)[b]	0.93	2.94	3.747(15)	140.4
C(17)–H(17)···O(1)[c]	0.93	2.31	3.160(3)	150.6
C(41)–H(41)···Br(1)[d]	0.93	3.07	3.721(16)	128.9
C(52)–H(52A)···S(2)[e]	0.97	2.94	3.700(4)	135.4
C(54)–H(54A)···S(4)[f]	0.96	2.99	3.900(5)	159.4

a = x-1, y, z; b = -x+1, y+½, -z+1; c = x+1, y, z; d = -x+1, y-½, -z+1;
e = x, y, z-1; f = x, y, z+1

The Br(4) is involved in bifurcated type intermolecular interaction with D···A distances of 3.647(14) and 3.810(14) Å respectively. The two adjacent complex units are connected with the aid of these interactions. The interactions C(34)–H(34)···Br(2) and C(17)–H(17)···O(1) with D···A distance 3.747(15) and 3.721(16) Å connected different complex units to each other (Fig. 5.29). The DMF molecule as well give strength to the effective packing of the complex **29** molecules *via* C(17)–H(17)···O(1) and C(54)–H(54A)···S(4) interactions with D···A distances of 3.160(3) and 3.900(5) Å. The cyclohexyl ring of the second unit of complex connects the first complex unit through hydrogen bonding of the type C(52)–H(52A)···S(2) with a D···A distance of 3.700(4) Å.

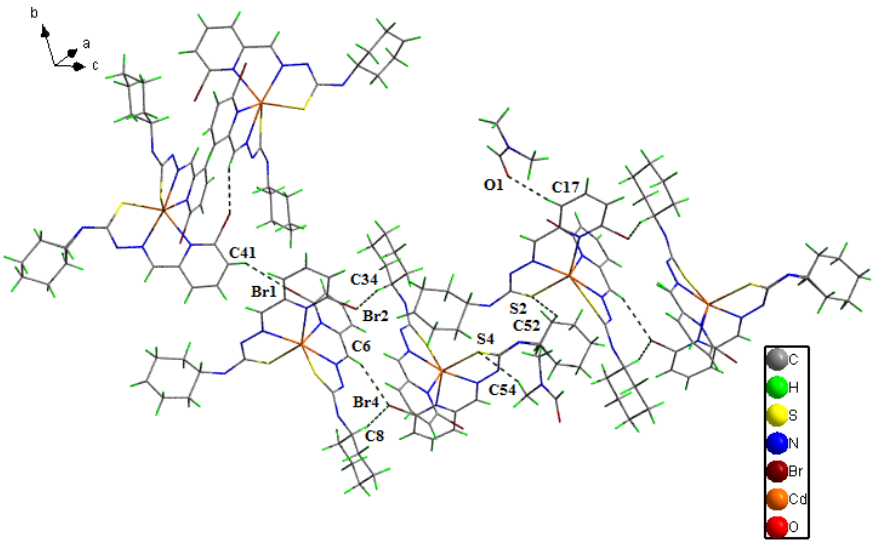

Fig. 5.29. Hydrogen bonding interactions in complex **29**.

The three dimensional packing of the complex **29** effected as a result of hydrogen bonding interations along with coordination polyhedra is represented in Fig. 5.31 when viewed along '*a*' axis.

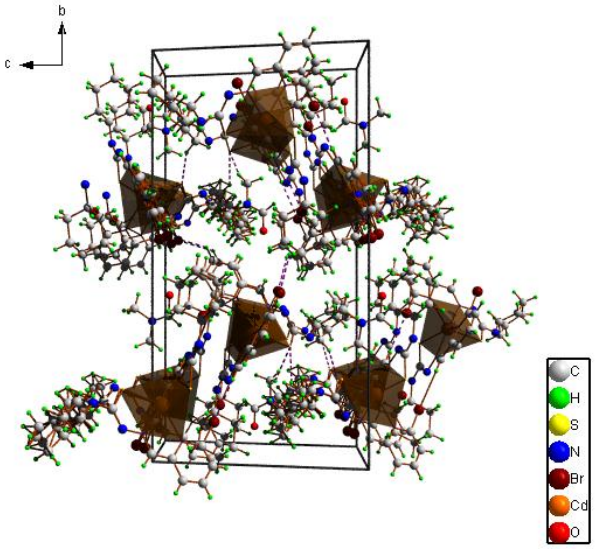

Fig. 5.31. Packing diagram for complex **29** when viewed along '*a*' axis.

5.4 Conclusion

This chapter deals with a thiosemicarbazone similar to Chapter 4 but the N^4 position is occupied by cyclohexyl ring. The Hbpct exhibited a special type of halogen bonding that is not exhibited by Hbpdmt [C(7)–Br(1)···S(1)]. Among the seven metal complexes prepared from Hbpct three of them could be isolated as single crystals. We could resolve all the disordered complexes more effectively as described. With the help of physicochemical studies the structure of the complexes **25, 26, 27** and **28** are assigned in Fig. 5.32.

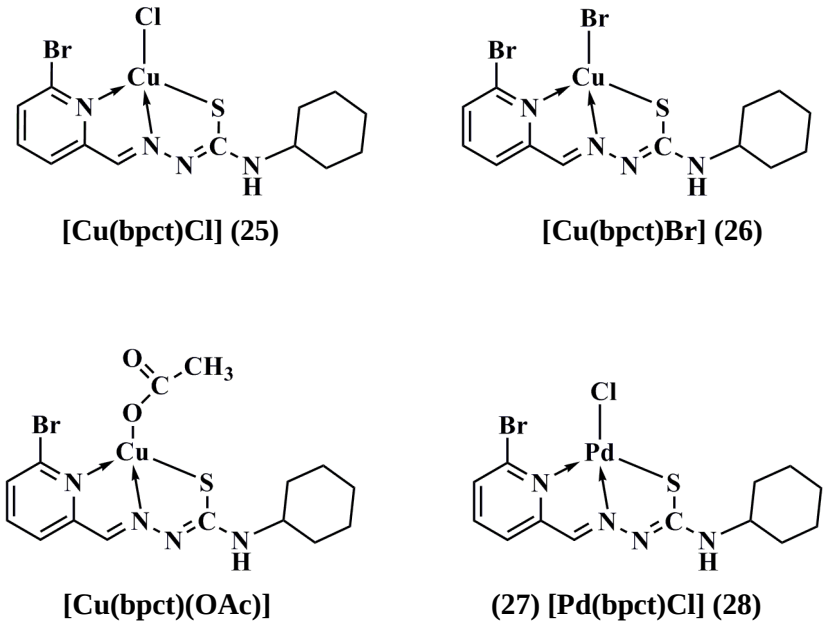

Fig. 5.32. Tentative structures for complexes **25, 26, 27** and **28** of Hbpct.

Reference

[1] L. Palatinus, G. Chapuis, J. Appl. Cryst., 40 (2007) 786.

[2] L. Palatinus, A. van der Lee, J. Appl. Cryst. 41 (2008) 975.

[3] L., Palatinus, S. J. Prathapa, S. van Smaalen, J. Appl. Cryst. 45 (2012) 575.

[4] G.M. Sheldrick, Acta Cryst. C71 (2015) 3.

[5] SMART and SAINT, Area Detector Software Package and SAX Area Detector Program, Bruker Analytical X-ray; Madison, WI, USA, 1997.

[6] SADABS, Area Detector Absorption Correction Program; Bruker Analytical X-ray; Madison, WI, 1997.

[7] K. Brandenburg, Diamond Version 3.2g, Crystal Impact GbR, Bonn, Germany, 1997.

[8] L.J. Farrugia, J. Appl. Cryst. 45 (2012) 849.

[9] D.X. West, J.S. Ives, J. Krejci, M.M. Salberg, T.L. Zumbahlen, G.A. Bain, A.E. Liberta, J.V. –Martinez, S.H. Ortiz, R.A. Toscano, Polyhedron 14 (1995) 2189.

[10] F.H. Allen, O. Kennard, D.G. Watson, L. Brammer, A.G. Orpen, R. Taylor, J. Chem. Soc. Perkin Trans. 2 (1987) S1.

[11] M. Joseph, V. Suni, C.R. Nayar, M.R.P. Kurup, H.-K. Fun, J. Mol. Struct. 705 (2004) 63.

[12] L. Koskinen, S.Jääskeläinen, P. Hirva, M. Haukka, Cryst. Growth Des. 15 (2015) 1160.

[13] R.P. Raphel, E. Manoj, M.R.P. Kurup, Polyhedron 26 (2007) 818.

[14] E. Manoj, M.R.P. Kurup, Polyhedron 27 (2008) 275.

[15] V. Philip, V. Suni, M.R.P. Kurup, M. Nethaji, Polyhedron 24 (2005) 1133.

[16] M. Muralisankar, J. Haribabu, NS.P. Bhuvanesh, R. Karvembu, A. Sreekanth, Inorg. Chim. Acta 449 (2016) 82.

[17] M. Joseph, V. Suni, M.R.P. Kurup, M. Nethaji, A. Kishore, S.G. Bhat, Polyhedron 23 (2004) 3069.

[18] P. Paul, R.J. Butcher, S. Bhattacharya, Inorg. Chim. Acta 425 (2015) 67.

[19] R.P. John, A. Sreekanth, M.R.P. Kurup, A. Usman, I.A. Razak, H.-K. Fun, Spectrochim. Acta A59 (2003) 1349.

[20] A.B.P. Lever, Inorganic Electronic Spectroscopy 2nd *Ed*n. Elsevier, Amsteram (1984).

[21] A.P. Rebolledo, M. Vieites, D. Gambino, O.E. Piro, E.E. Castellano, C.L. Zani, E.M. souza-Fagundes, L.R. Teixeira, A.A. Batista, H. Beraldo, J. Inorg. Biochem. 99 (2005) 698.

[22] R. Takjoo, M. Hakimi, M. Seyyedin, M. Abrishami, J. Sulfur Chem. 31 (2010) 415.

[23] E. Garribba, G. Micera, J. Chem. Educ. 83 (2006) 1229.

[24] S. Stoll, Spectral Simulations in Solid-State Electron Paramagnetic Resonance, Ph. D. Thesis, ETH, Zurich, 2003.

[25] U.B. Gangadharmath, S.M. Annigeri, A.D. Naik, V.K. Revankar, V.B. Mahale, J. Mol. Struct. (Theochem) 572. (2001) 61.

[26] B.J. Hathaway, Structure and Bonding, Springer Verlag, Heidelberg (1973) 60.

[27] K. Jayakumar, M. Sithambaresan, A.A. Aravinadakshan, M.R.P. Kurup, Polyhedron 75 (2014) 50.

[28] E.B. Seena, M.R.P. Kurup, Polyhedron 26 (2007) 829.

[29] P. Muller, R. Herbert-Irmer, A.L. Spek, T.R. Schneider, M.R. Sawaya, Crystal Structure Refinement, Oxford Science Publications, 2012.

[30] D. Cremer, J.A. Pople, J. Am. Chem. Soc. 97 (1975) 1354.

.....ൠ.....

Chapter 6

ACETONE-*N*4-(4-NITROPHENYL) THIOSEMICARBAZONE AND ITS TRANSITION METAL COMPLEXES: SYNTHESIS, SPECTRAL AND STRUCTURAL CHARACTERIZATION

Contents

6.1. Introduction

A bidentate thiosemicarbazone will coordinate *via* azomethane nitrogen and thio-amido/thio-iminol sulfur atom. These types of thiosemicarbazones are synthesized by condensation of carbonyl compounds with thiosemicarbazide. The thiosemicarbazone in the present chapter is designed by replacing R_1 and R_2 in the Scheme 6.1 with methyl groups, R_3 with 4-nitrophenyl group and R_4 position with hydrogen.

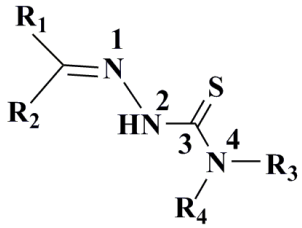

Scheme 6.1

This thiosemicarazone can act as an NS donor ligand in complexes. A large number of studies and structural characterizations were done on NS donor thiosemicarbazones. The possible geometries for an NS system were already discussed in Chapter 1. In most of the structural reports it was found that bis ligated acetone thiosemicarbazones tend to adopt a *cis* configuration around the metal centre [1]. Sn(IV) complexes of acetone thiosemicabazones were found to have biological properties [2]. There are reports on corrosion inhibition properties of acetone thiosemicarbazone on metal surface in phosphoric acid [3]. From the report of Ali *et al.*, it was proved that acetone thiosemicarbazones can show antineoplastic properties [4]. Metal complexes of acetone thiosemicarbzones with Cu(II) and Ni(II) are effective antifungal agents [5]. It is found that changing the environment around thiosemicarbazide through N^4 substitution a large variety of properties was observed for these compounds. Pd(II) complexes of N^4-phenylsubstituted acetone thiosemicarbazones were found to have cytotoxic properties on human tumor cells at very low micromolar concentrations [6].

Taking into consideration of the fact that by changing the substituent in the N^4 position and further complex formation lead to enhance the properties and applications of this class of thiosemicarbazone, we have synthesized and characterized five metal complexes of acetone-N^4-(4-nitophenyl)thiosemicarbzone. The transition metals used for the study are Co(II), Ni(II), Cu(II), Pd(II) and Cd(II).

6.2. Experimental

6.2.1. Materials

Acetone, 4-nitrophenylisothiocyante (Sigma Aldrich), hydrazine monohydrate (98%) (Lancaster), $CoBr_2$ (99%) (Sigma Aldrich), $Ni(NO_3)_2 \cdot 6H_2O$ (Alfa Aesar), $PdCl_2$ (Sigma Aldrich), $Cu(NO_3)_2 \cdot H_2O$ (Alfa

Aesar), $Cd(OAc)_2 \cdot 2H_2O$ (Alfa Aesar) and CH_3CN (Spectrochem) were used as received.

6.2.2. Synthesis of acetone-N^4-(4-nitrophenyl)thiosemicarbazone (Hanpt)

Synthesis of Hanpt involves a two step process. In the first step 4-nitrophenylisothiocyante (0.170 g, 4 mmol), dissolved in methanol was stirred with hydrazine hydrate monohydrate (0.180 g, 6 mmol) for 4 h. The yellow colored 4-nitrophenylthiosemicarbazide obtained was filtered washed with methanol and dried *in vacuo*. In the second step 4-nitrophenylthiosemicarbazide (0.230 g, 1 mmol) was dissolved in methanol and stirred with acetone (0.157 g, 20 mmol) for 4 h. The yellow colored solution resulted was kept for three weeks and the brown colored crystals obtained were separated (Scheme 6.2).

Yield : (0.122 g) 48%. m.p. 139 °C

Elemental Anal. Found (calcd) (%): C 48.42 (47.61); H 4.56 (4.79); N 22.68 (22.21); S 12.77 (12.71).

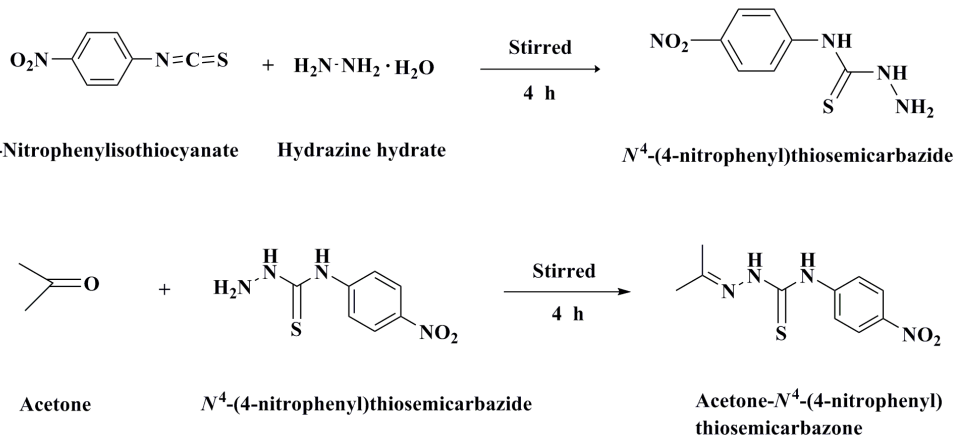

Scheme 6.2

6.2.3. Syntheses of complexes

6.2.3.1. Synthesis of $[Co(anpt)_2Br]$ (30)

The complex was synthesized by heating $CoBr_2$ (0.115 g, 0.5 mmol) with Hanpt (0.252 g, 1 mmol) in acetone under reflux condition. After refluxing for 1 h, the clear brown solution obtained was separated and kept at room temperature for 3 weeks. The product obtained was separated from the solution by filtration and dried *invacuo*.

Yield	:	(0.336 g) 52%.
Elemental Anal. Found (calcd) (%)	:	C 37.86 (37.22); H 4.76 (4.06); N 17.10 (17.36); S 9.02 (9.94)

6.2.3.2. Synthesis of $[Ni(anpt)_2]\cdot DMF$ (31)

The complex was synthesized by heating $Ni(NO_3)_2\cdot 6H_2O$ (0.145 g, 0.5 mmol) with Hanpt (0.252 g, 1 mmol) in 10 mL CH_3CN under reflux condition. After refluxing for 3 h, the clear brown solution obtained was separated and kept at room temperature for 3 weeks. The product obtained was separated and dissolved in 10 mL DMF solution and kept for recrystallization. The block shaped brown crystals obtained were separated and dried.

Yield	:	(0.290 g) 45%.
Elemental Anal. Found (calcd) (%)	:	C 43.72 (43.27); H 5.05 (5.21); N 19.32 (19.75); S 10.16 (10.05)

6.2.3.3. Synthesis of $[Cu(anpt)_2]\cdot DMF$ (32)

An acetonitrile solution of $Cu(NO_3)_2\cdot H_2O$ (0.120 g, 0.5 mmol) was refluxed with Hanpt (0.252 g, 1 mmol) in CH_3CN under reflux condition. After refluxing for 3 h, the clear brown solution obtained was separated and kept at room temperature for 3 weeks. The brown product obtained

was separated from the solution by filtration and dried *invacuo*. The compound was dissolved in 5 mL DMF solution and kept for slow evaporation. After 3 weeks the crystals of the compound obtained was separated washed and dried.

Yield : (0.330 g) 51%.
Elemental Anal. Found (calcd) (%) : C 42.56 (42.95); H 5.01 (5.17); N 19.14 (19.60); S 10.07 (9.97)

6.2.3.4. Synthesis of [Pd(Hanpt)Cl_2] (33)

The complex was synthesized by heating $PdCl_2$ (0.117 g, 1 mmol) with Hanpt (0.252 g, 1 mmol) in 10 mL CH_3CN under reflux condition. After refluxing for 3 h, the clear yellow solution obtained was separated and kept at room temperature for 3 weeks. The compound obtained was separated from the solution by filtration and dried *invacuo*.

Yield : (0.208 g) 48%.
Elemental Anal. Found (calcd) (%): C 27.90 (27.96); H 2.54 (2.82); N 13.15 (13.04); S 7.74 (7.46)

6.2.3.5. Synthesis of [Cd(anpt)$_2$] (34)

The complex was synthesized by heating $Cd(OAc)_2 \cdot 2H_2O$ (0.133 g, 0.5 mmol) with Hanpt (0.252 g, 1 mmol) in 15 mL acetone under reflux condition. After 1 h, the yellow product obtained was separated washed with acetone and dried *invacuo*.

Yield : (0.383 g) 62%.
Elemental Anal. Found (calcd) (%) : C 38.49 (39.06); H 3.80 (3.61); N 18.84 (18.22); S 9.94 (10.43)

6.2.4. Physico-chemical techniques

6.2.4.1. Elemental analysis

Elemental analyses of the compounds were done on a Vario EL III CHNS elemental analyzer at the Sophisticated Analytical Instrument Facility, Cochin University of Science and Technology, Kochi-22, Kerala, India.

6.2.4.2. Magnetic susceptibility measurements

The magnetic susceptibility measurements of the complexes were taken on a Vibrating sample Magnetometer using $Hg[Co(SCN)_4]$ as a calibrant at the SAIF, Indian Institute of Technology, Madras.

6.2.4.3. Molar conductivity measurements

The conductivity measurements of the complexes were recorded in 10^{-3} M solution in DMF on a Systronic model 303 direct reading conductivity meter at room temperature at the Department of Applied Chemistry, CUSAT, Kochi, India.

6.2.4.4. Spectroscopic characterization

The infrared spectra of Hanpt and complexes **33-35** were recorded on a JASCP FT-IR-5300 spectrometer in the range 4000-400 cm^{-1} using KBr pellets. The electronic spectra of the prepared compounds were recorded in DMF solution on a Thermo Scientific Evolution 220 UV-vis Spectrophotometer in the 200-900 nm range. ^1H NMR spectrum of Hanpt and complexes **33** and **34** were recorded using Bruker AMX 400 FT-NMR Spectrometer at the Sophisticated Analytical Instrument Facility, CUSAT, Kochi, India. The Electro Paramagnetic Resonance spectra of complex **32** was recorded in the solid state at 298 K and at 77 K in DMF on a Varian E-112 spectrometer, with 100 kHz modulation frequency, 2 G modulation amplitude and 9.1 GHz

microwave frequency at the Sophisticated Analytical Instrumentation Facility, IIT Bombay, India.

6.2.5. Single crystal X-ray diffraction studies

The single crystal X-ray diffraction studies of the thiosemicarbazone Hanpt was done on an Agilent, Eos, Gemini diffractometer both equipped with a graphite crystal incident-beam monochromator, and a fine focus sealed tube with Cu Kα (λ = 1.54184 Å) as the X-ray source at the Department of Chemistry, Keene State College, 229 Main Street, Keene, NH. The unit cell dimensions were measured and the data collection was performed at 173(2) K. The structure was solved with the Superflip [7,8,9] structure solution program using Charge Flipping and was refined using with the ShelXL [10] refinement package using Least Squares minimization. The single crystal X-ray diffracition studies of complexes **31** and **32** were carried out using a Bruker SMART APEXII CCD diffractometer at Sophisticated Analytical Instrumentation Facility, CUSAT, Kochi, India. Data acquisition was done using Bruker SMART software and data integration using Bruker SAINT software [11]. Absorption corrections were carried out using SADABS based on Laue symmetry using equivalent reflections [12]. The structure was solved by direct methods and refined by full-matrix least-squares calculations with the SHELXL-2014/7 software package [10]. The molecular and crystal structures were plotted by using Olex2 [13], DIAMOND version 3.2g [14] and ORTEP-3 [15].

6.3. Results and discussion

Elemental analysis of Hanpt and its complexes were given in Section 6.2.3. The structures of the complexes were proposed on this basis.

6.3.1. Characterization of Acetone-N^4-(4-nitrophenyl) thiosemicarbazone (Hanpt)

6.3.1.1. Infrared spectrum

Infrared spectrum of Hanpt was taken in a range 4000-400 cm $^{-1}$ using KBr pellets. The infrared spectrum of Hanpt gaves sharp bands in the region 3346-3267 cm^{-1} are assigned to ν(^{4}N–H) and ν(^{2}N–H) stretching frequencies [16]. A sharp band in the region 1600 cm^{-1} is assigned to ν(C=N) and confirms the azomethane bond formation through condensation of acetone with N^4-4-nitrophenylthiosemicarbzide [17]. Absence of any band in the 2800-2500 cm^{-1} region and the presence of bands at 1409 and 843 cm^{-1} due to ν(C=S)/ν(C–S), confirms the existence of only thioamido form in the solid state [17]. The nitro groups give bands in the region 1550-1500 and 1350-1290 cm^{-1} due to the N–O symmetric and asymmetric stretching modes of vibration. In Hanpt band at 1556 and 1333 cm^{-1} were assigned to ν(N–O) symmetric and asymmetric stretch respectively. The stretching vibration for hydrazinic N–N band was observed at 1110 cm^{-1}. The Fig. 6.1 represents the IR spectrum for Hanpt.

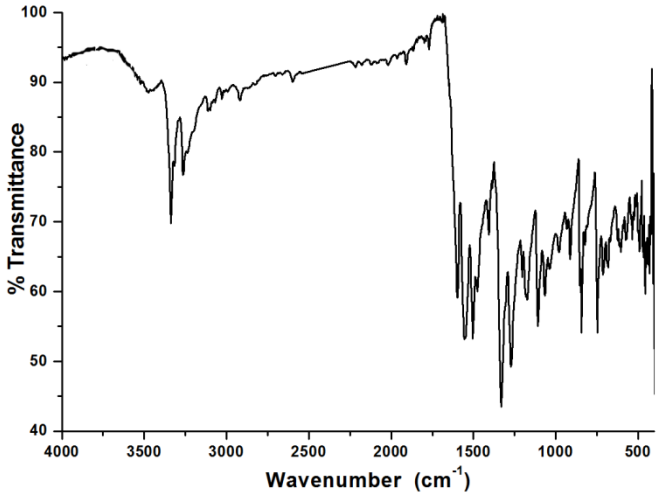

Fig. 6.1. Infrared spectrum of Hanpt.

6.3.1.2. Electronic spectrum

Electronic spectrum of Hanpt was taken in a 10^{-5} M DMF solution. A very broad band with a maximum at 344 nm with a $\varepsilon = 6.6 \times 10^{-4}$ L $M^{-1}cm^{-1}$. The broad band may be due to merging of aromatic and azido π–π* and n– π* transitions. The electronic spectrum for Hanpt is given in Fig. 6.2.

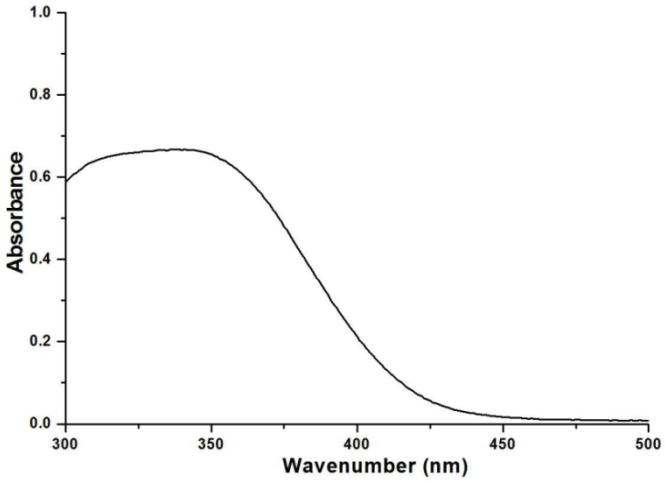

Fig. 6.2. Electronic spectrum for Hanpt.

6.3.1.3 ^{1}H NMR spectrum

The ^{1}H NMR spectrum of Hanpt was recorded in DMSO-d_6 solvent with TMS as the internal standard. Two singlets very close to each other at 2.01 ppm and 2.04 ppm correspond to the methyl groups on acetone, which clearly indicate magnetically independent CH_3 protons [18]. The multiplets distributed in a range from 8.06-8.12 ppm correspond to aromatic protons. Singlets at δ = 10.23 ppm and δ = 10.73 ppm were assigned to ^{2}N–H and ^{4}N–H protons respectively. The shift for ^{4}N–H was due to the highly electronegative conjugated system adjacent to it. These singlets disappear in the D_2O exchanged ^{1}H NMR spectrum for Hanpt, which confirms the presence of exchangeable protons on ^{2}N–H and ^{4}N–H (Fig. 6.3).

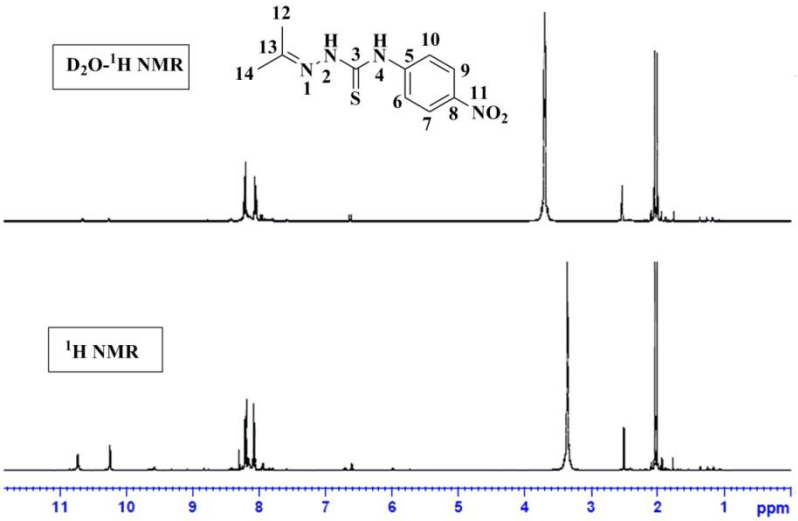

Fig. 6.3. ^{1}H NMR and D_2O exchanged ^{1}H NMR spectrum for Hanpt.

6.3.1.4. Single crystal X-ray diffraction studies

Single crystal suitable for X-ray diffraction studies was grown from mother liquor. A crystals with size 0.44 × 0.32 × 0.26 mm^3 was mounded on nylon loop on Rigaku Oxford Diffraction diffractometer at 173(2) K (Fig. 6.4).

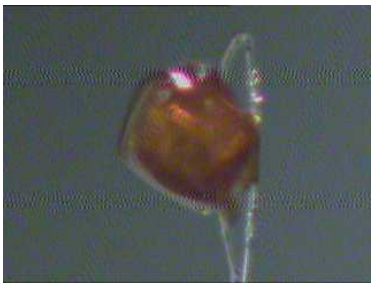

Fig. 6.4. Nylon looped single crystal on Hanpt.

Hanpt crystallizes into monoclinic space group *C*2/c. All non-hydrogen atoms were refined anisotropically. Aromatic hydrogen was refined with riding coordinates and idealized methyl hydrogen was refined as rotating

groups. The C–H bond distances were constrained to a value of 0.95-0.98 Å and that of N–H to a value of 0.88 Å. The crystallographic data along with details of refinement for structure solution are given in Table 6.1.

Table 6.1. Crystal data and structure refinement parameters of Hanpt

Parameters	**Hanpt**
Empirical formula	$C_{10}H_{12}N_4O_2S$
Formula weight	252.30
Color	Brown
Temperature (K)	173(2)
Wavelength (Cu Kα) (Å)	1.54184
Crystal system	monoclinic
Space group	*C*2/c
Cell parameters	
a(Å)	23.5940(7)
b(Å)	16.2081(4)
c(Å)	12.5673(3)
α = γ (°)	90
β(°)	101.326(3)
Volume ($Å^3$)	4712.3(2)
Z	16
Calculated density, ρ (g cm^{-3})	1.422
Absorption coefficient, μ (mm^{-1})	2.437
F(000)	2112.0
Crystal size (mm^3)	0.44 × 0.32 × 0.26
θ range for data collection (°)	3.329 to 71.233
Limiting indices	$-24 \le h \le 28$, $-19 \le k \le 12$, $-14 \le l \le 15$
Reflections collected	9350
Independent reflections	4493 [R_{int} = 0.0327, R_{sigma} = 0.0369]
Data/restraints/parameters	4493 / 0 / 311
Goodness-of-fit on F^2	1.024
Final R indexes [I>2σ (I)]	R_1 = 0.0416, wR_2 = 0.1114
Final R indexes [all data]	R_1 = 0.0459, wR_2 = 0.1160
Largest diff. peak and hole (e $Å^{-3}$)	0.30/-0.35

$R_1 = \Sigma||F_o| - |F_c|| / \Sigma|F_o|$

$R_2 = [\Sigma w(F_o^2-F_c^2)^2 / \Sigma w(F_o^2)^2]^{1/2}$

The molecular structure and numbering scheme of Hanpt is given in Fig. 6.5. The asymmetric unit of the compound contains two molecules of Hanpt. The bond length 1.283(2) Å for both C8a–N3a and C8b–N3b, suggest the formation of azomethine (C=N) bond [19]. The bond lengths 1.671(17) Å and 1.672(17) Å for C1a–S1a and C1b–S1b respectively suggest that the compound exist in thio-amido form in solid state [20,21]. Selected bond lengths and bond angles are given in Table 6.2.

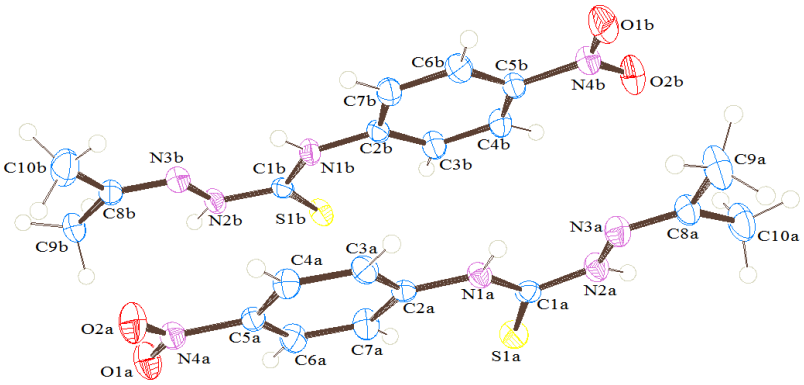

Fig. 6.5. Molecular structure of Hanpt.

Table 6.2. Selected bond parameters of Hanpt

Bond length (Å)		Bond angle (°)	
C8a–N3a	1.283 (2)	C8a–N3a–N2a	116.58 (14)
C8b–N3b	1.283 (2)	N3a–N2a–C1a	120.95 (14)
C1a–S1a	1.671 (17)	N2a–C1a–S1a	117.58 (12)
C1b–S1b	1.672 (17)	N1a–C1a–S1a	128.37 (12)
N2a–C1a	1.356 (2)	C8b–N3b–N2b	117.38 (15)
N2b–C1b	1.358 (2)	N3b–N2b–C1b	119.14 (13)
		N2b–C1b–S1b	119.47 (12)
		N1b–C1b–S1b	127.26 (12)

The torsion angles 178.47(15)° and 178.71(15)° for C8a/N3a/N2a/C1a and C8b/N3b/N2b/C1b respectively suggest that the molecules adopt a *E* configuration with respect to azomethine double bond. The N3a/N2a/C1a/S1a

and N3b/N2b/C1a/S1b torsion angles 175.70(12)° and 179.58(11)° respectively suggest that the thione sulfur S1a and S1b atoms are *trans* with respect to N3a and N3b respectively.

From conventional hydrogen bonding concepts [19], the compound showed a large number of hydrogen bonding interactions. The hydrogen bonding interactions along with parameters are given in Table 6.3. The intermolecular hydrogen bond C9b–H9bc···O1a with D···A distance 3.423(2) Å connects the two units of molecules present in the asymmetric unit give rise to a centrosymmetric dimer (Fig. 6.6).

Table 6.3. Hydrogen bonding interactions in Hanpt

D–H···A	D–H (Å)	H···A (Å)	D···A (Å)	D–H···A (°)
C(7a)–H(7a)···S(1a)	0.95	2.48	3.1748(18)	130.2
N(2b)–H(2b)···S(1b)[a]	0.88	2.84	3.4621(15)	129.3
C(3b)–H(3b)···S(1b)	0.95	2.54	3.2250(18)	128.7
C(6b)– H(6b)···O(2a)[b]	0.95	2.61	3.218(2)	122.4
C(7b)– H(7b)···O(2a)[b]	0.95	2.60	3.222(2)	123.4
C(9b)– H(9bc)···O(1a)	0.98	2.73	3.423(2)	128.3

a=1-x, +y, 1/2-z, b= 1-x, +y, 3/2-z

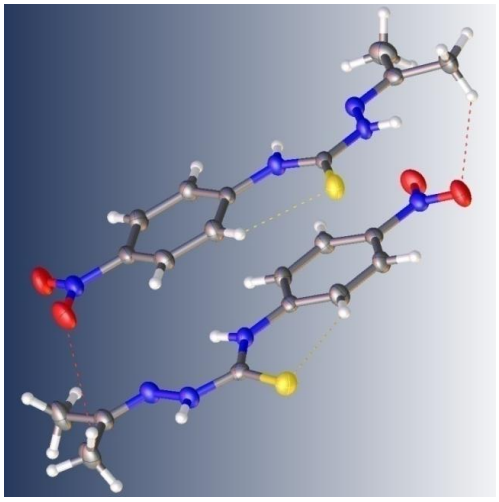

Fig. 6.6. Centrosymmetric dimer formed as a result of hydrogen bonding in Hanpt.

The interamolecular hydrogen bonding C7a–H7a···S1a and C3b–H3b···S1b with D···A distance 3.174(18) and 3.225(18) Å, gave rise to a six membered ring comprising atoms S1a, C1a, N1a, C2a, C7a, H7a and S1b, C1b, N1b, C2b, C3b, H3b respectively [22]. There were other hydrogen bonding interactions C6b–H6b···O2a, C7b–H7b···O2a and N2b–H2b···S1b with (D···A distances 3.218(2), 3.222(2) and 3.462(15) Å) connecting various units giving rise to a three dimensional packing in the crystal lattice. The hydrogen bonding interaction in the crystal lattice is depicted in Fig. 6.7.

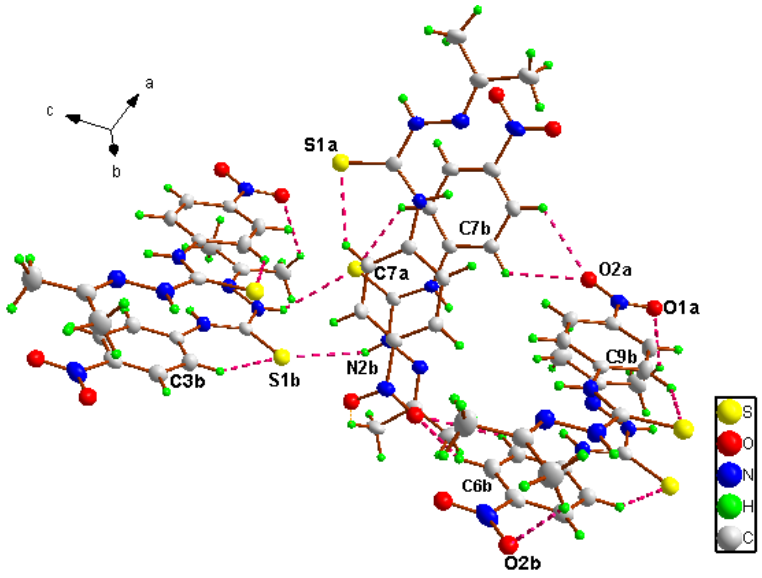

Fig. 6.7. Hydrogen bonding interaction in Hanpt.

The packing diagram of Hanpt when viewed along '*c*' axis is given in Fig.6.8. The supramolecular arrangement of Hanpt extends along '*b*' axis guided by intermolecular hydrogen bonding.

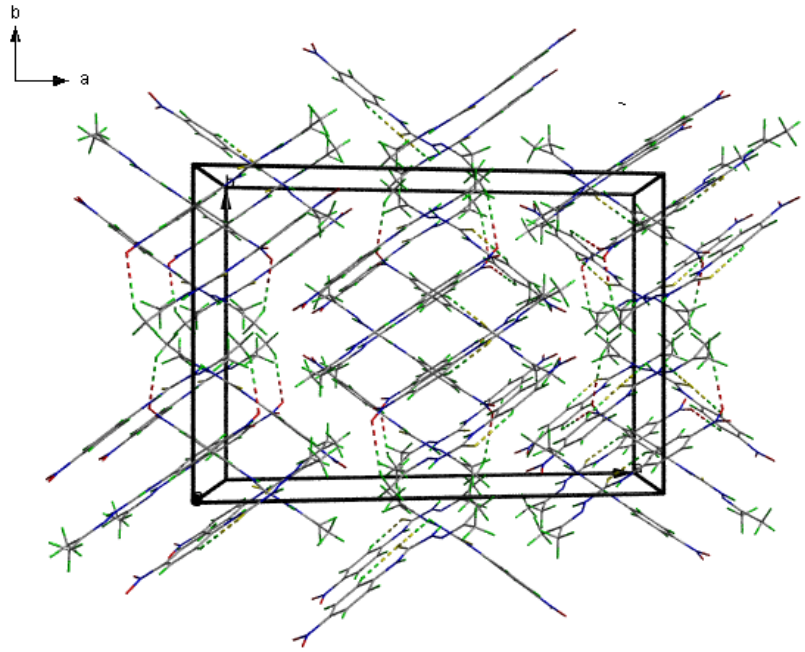

Fig. 6.8. Packing of Hanpt viewed along '*c*' axis.

6.3.2. Characterization of complexes of Hanpt

Hanpt act as bidentate NS donor ligand in its metal complexes. Five different complexes of Hanpt were prepared. Complex **33** was prepared by refluxing Hanpt and metal salts in 1:1 ratio, were as complexes **30**, **31**, **32** and **34** were prepared by refluxing metal salts with Hanpt in1:2 ratio.

6.3.2.1. Molar conductivity and magnetic susceptibility measurements

The molar conductivity measurements of the complexes of Hanpt were taken with 10^{-3} M solutions of complexes in DMF. All the complexes were found to have molar conductivity in the range 2-50 $ohm^{-1}cm^2mol^{-1}$, which is very much below the value for uni-univalent electrolyte (65-90 $ohm^{-1}cm^2mol^{-1}$). This suggested that the complexes of Hanpt were non electrolytic in nature.

The magnetic susceptibility measurements suggested that the metals in complexes were diamagnetic except complex **32**. The magnetic moment of $[Ni(anpt)_2]\cdot DMF$ **(31)** is very low suggesting a distorted square planar geometry for Ni(II). Very small values for such system are reported and for us very small value near to zero was obtained [23]. The diamagnetic nature of complex **30** suggests that cobalt in this complex exist in Co(III) oxidation state and hence adopt a low spin electronic configuration. Palladium in complex **33** also gave a diamagnetic behavior and was due to the low spin electronic configuration of d^8 Pd(II) system. The diamagnetic nature of complex **34** was in good agreement with the d^{10} configuration of Cd(II) metal in the system. For complex **32**, the magnetic moment value 1.73 B.M. is consistent with the single electron magnetic moment of d^9 system for copper in +2 oxidation state. The molar conductivity and magnetic susceptibility measurement results are tabulated in Table 6.4.

Table 6.4. Molar conductivity and magnetic moment values of complexes of Hanpt

Compound	λ_m(ohm^{-1} cm^2 mol^{-1})	μ_{eff} (B.M.)
$[Co(anpt)_2Br]$ (**30**)	5.8	0.12
$[Ni(anpt)_2]\cdot DMF$ (**31**)	2.8	0.53
$[Cu(anpt)_2]\cdot DMF$ (**32**)	9.3	1.73
$[Pd(Hanpt)Cl_2]$ (**33**)	49	0.04
$[Cd(anpt)_2]$ (**34**)	6.4	0

6.3.2.2. Infrared spectra

Infrared spectra of all the complexes were taken in the 4000-400 cm^{-1} range using KBr pellets. The characteristic IR bands with suitable assignment are given in Table 6.5. The IR spectra for all the complexes were expected to show a characteristic shift in stretching and bending frequency, attributed to coordination to the metal centre. The coordination

of metal through azomethine nitrogen decreases the ν(C=N) stretching frequency by 15-40 cm^{-1} as compared to free Hanpt. There is a new band formed in the region 1592-1598 cm^{-1} corresponds to newly formed C=N bond [24], which confirms coordination of the ligand in the anionic form. There is a shift in the ν(C=S) due to coordination *via* thio-iminolate sulfur, suggesting a change in bond order.

Table 6.5. Infraredspectral assignments (cm^{-1})of Hanpt and its metal complexes

Compound	**ν(C=N)**	**ν(C=N)[a]**	**ν(C=S)/ ν(C–S)**	**ν(N–N)**	**ν(M–N)**
H_2bsct	1600	---	1479, 843	1110	---
[Co(anpt)$_2$Br] (**30**)	1589	1596	1441, 842	1180	417
[Ni(anpt)$_2$]·DMF (**31**)	1551	1594	1411,840	1186	430
[Cu(anpt)$_2$]·DMF (**32**)	1549	1592	1454,818	1187	449
[Pd(Hanpt)Cl$_2$] (**33**)	1556	---	1451, 836	1199	430
[Cd(anpt)$_2$] (**34**)	1556	1598	1465, 835	1174	417

a- Newly formed C=N

The infrared spectrum for [Co(anpt)$_2$Br] (**30**) depicted in Fig. 6.9 gave a band at 1589 cm^{-1} corresponding to the azomethine stretching vibration. The large shift for this vibrations confirms the coordination of azomethine nitrogen to Co(III). The presence of a new band at 1596 cm^{-1} accompanying increase in ν(N–N) vibrations indicate extended double bond formation through chelation which confirms the coordination of sulfur in the thio-iminolate form. This is further confirmed from the shift in ν(C=S)/ν(C–S) stretching by 30 cm^{-1}. The frequency in the region 417-449 cm^{-1} corresponds to ν(Co–N) further justify the coordination of metal to thiosemicarbazone [25,26].

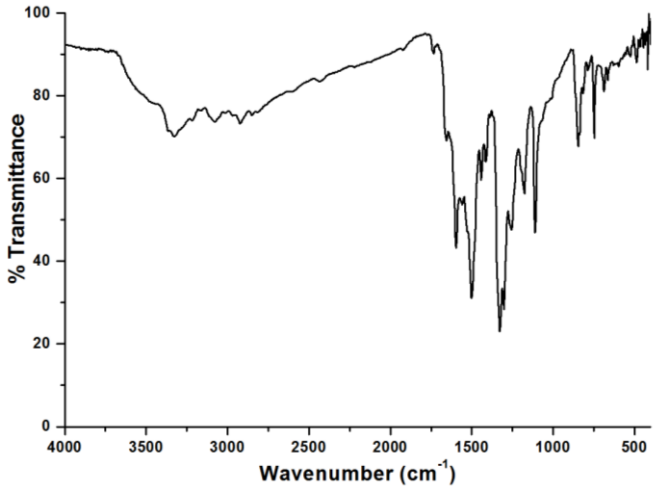

Fig. 6.9. Infrared spectrum of $[Co(anpt)_2Br]$ (**30**).

The $[Ni(anpt)_2]\cdot DMF$(**31)** gave a shift in the ν(C=N) stretching frequency to 1551 cm^{-1} from 1600 cm^{-1} that for the free Hanpt. This large shift is due to coordination of azomethine nitrogen to Ni(II). The coordination of sulfur atom to Ni(II) in the thio-iminolate form is confirmed from the shift in ν(C=S)/ν(C–S) to 1411 cm^{-1} and the appearance of a new band at 1594 cm^{-1} corresponding to newly formed C=N. The above observations are confirmed from the increase in ν(N–N) stretching as a result of partial double bond character created as a result of extended conjugation in the complex. Coordination of metal to azomethine nitrogen is further confirmed from the ν(Ni–N) stretching vibration observed at 430 cm^{-1}. Fig. 6.10 represents infrared spectrum of complex **31**.

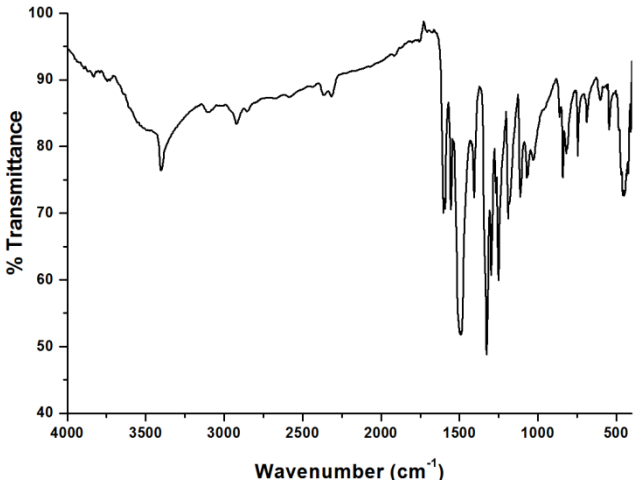

Fig. 6.10. Infrared spectrum of $[Ni(anpt)_2]\cdot DMF$ (**31**).

The complex **32** gave the azomethine stretching vibration at 1549 cm^{-1}, showing a large shift from that of free ligand. A new band at 449 cm^{-1}corresponding to ν(Cu–N) is also observed. These factors act as an evidence for the coordination of azomethine nitrogen to Cu(II).

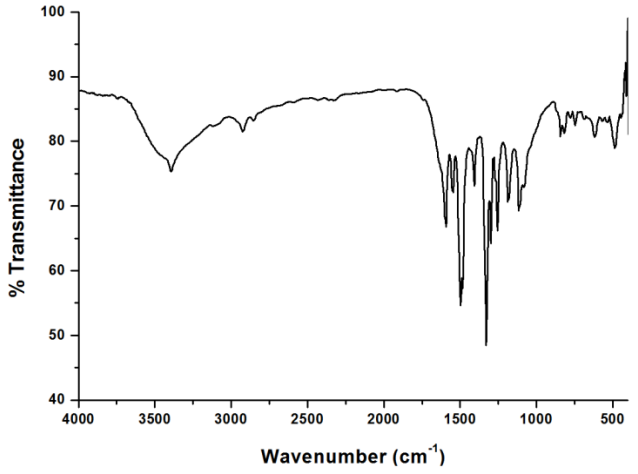

Fig. 6.11. Infrared spectrum of $[Cu(anpt)_2]\cdot DMF$ (**32**).

The coordination of thiosemicarbazone as a monodeprotonated form was confirmed from shift in ν(C=S)/ν(C–S) and ν(N–N) vibrations. This

was confirmed from appearance of a new band at 1592 cm^{-1} corresponding to the newly formed C=N bond. The infrared spectrum for complex $[Cu(anpt)_2]\cdot DMF$ (**32**) is given in Fig. 6.11.

The complex $[Pd(Hanpt)Cl_2]$ (**33**) gave only a single vibration at 1556 cm^{-1} corresponding to ν(C=N) vibration. The shift observed for this vibration was due to coordination of azomethine nitrogen to Pd(II) centre. This was further supported from the band at 430 cm^{-1} assigned to ν(Pd–N) stretching. The coordination of sulfur in the thio-amido form was evident from the absence of any new band ~ 1590 cm^{-1}. Thus the Hanpt coordinates as a neutral ligand in complex **33**. Theinfrared spectrum for complex **33** is presented in Fig. 6.12.

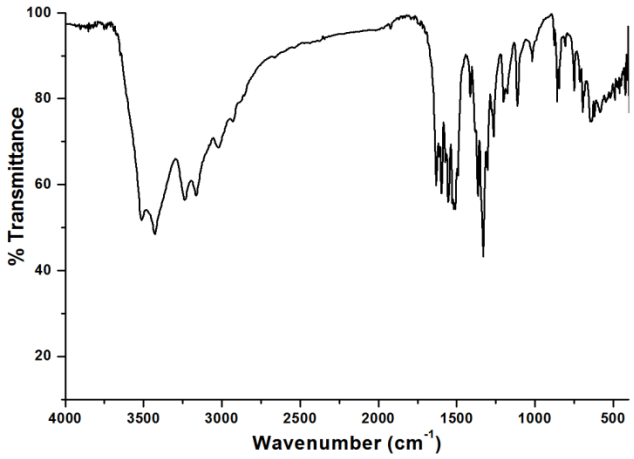

Fig. 6.12. Infrared spectrum of $[Pd(Hanpt)Cl_2]$ (**33**).

For complex $[Cd(anpt)_2]$ (**34**), a band at 1556 cm^{-1} assigned to ν(C=N) vibration is observed accompanying a new band at 1598 cm^{-1}. These factors suggest the coordination of azomethine nitrogen as well as monodeprotonated Hanpt to Cd(II) ion. The observation is supported by the shift in ν(C=S)/ν(C–S) and ν(N–N) stretching vibrations. The coordination of azomethine nitrogen to Cd(II) give a band at 417 cm^{-1}corresponding to ν(Cd–N) vibrational frequency. Fig. 6.13 represents infrared spectrum for complex **34**.

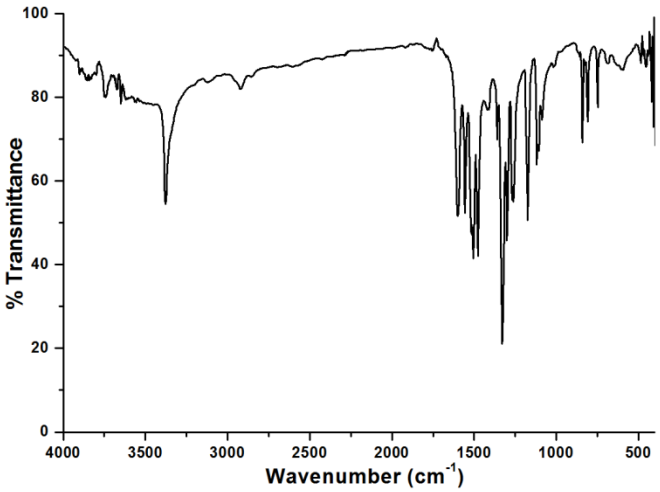

Fig. 6.13. Infrared spectrum of $[Cd(anpt)_2]$ (**34**).

6.3.2.3. Electronic spectra

Electronic spectra give information regarding the intraligand, charge transfer and d-d transitions in a complex. The electronic spectra were recorded in 10^{-3} and10^{-5} M solutions of complexes in DMF. The metal complexes of Hanpt show a shift in the transitions. Eventhough three bands are expected for all the metal complexes, like Hanpt a single band with high intensity of absorption was observed.

Table 6.6. Electronic spectral assignments (nm) of Hanpt and its transition metal complexes

Compound	**n–π*/ π–π* (nm) ($\varepsilon = 10^4$ $M^{-1}cm^{-1}$)**	**d-d (nm) (ε ($M^{-1}cm^{-1}$))**
Hanpt	339 (6.68)	
$[Co(anpt)_2Br]$ (**30**)	377 (7.47)	
$[Ni(anpt)_2]\cdot DMF$ (**31**)	382 (7.74)	593 (220)
$[Cu(anpt)_2]\cdot DMF$ (**32**)	370 (8.36)	620 (198)
$[Pd(Hanpt)Cl_2]$ (**33**)	374 (8.23)	
$[Cd(anpt)_2]$ (**34**)	388 (8.31)	

Complex **30** gave a broad band with maxima at 377 nm with molar absorption constant of 7.4×10^4 $M^{-1}cm^{-1}$ due to overlapping of intaligand and charge transfer transitions. The Fig. 6.14 represents electronic spectrum for Hanpt and complex **30**.

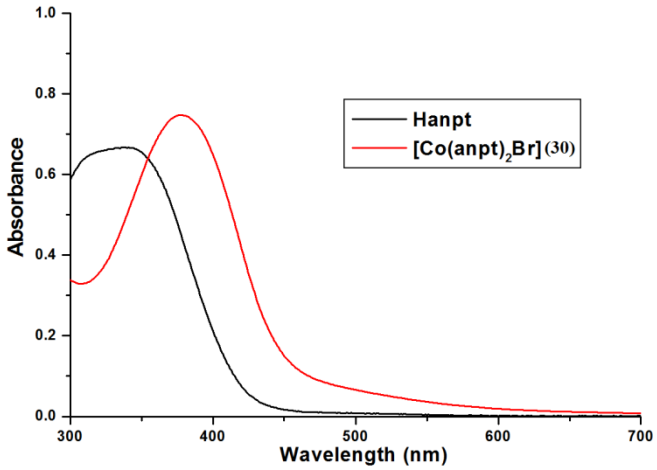

Fig. 6.14. Electronic spectrum of Hanpt and $[Co(anpt)_2Br]$ (**30**).

For complex **31** a highly intense absorption with maximum absorption at 382 nm ($\varepsilon = 7.74 \times 10^4$ $M^{-1}cm^{-1}$) was observed. The high intensity of the band is due to overlapping of charge transfer transitions with intraligand transitions. For a square planar Ni(II) complex a band in the visible spectrum is expected at 555 nm. The expected electronic transitions are for a square planar Ni(II) with bidentate lignd system are $d_{xy} \rightarrow d_{x^2-y^2}$, $d_{z^2} \rightarrow d_{x^2-y^2}$, d_{yz}, $d_{xy} \rightarrow d_{x^2-y^2}$ [$^1A_{1g} \leftarrow {}^1A_{2g}$, $^1A_{1g} \leftarrow {}^1B_{1g}$ and $^1A_{1g} \leftarrow {}^1E_g$] but for $[Ni(anpt)_2]\cdot DMF$ (**31**) a single band a with maximum absorption at 593 nm with molar absorptivity 220 $M^{-1}cm^{-1}$ complex **31** due to close spacing of these *d* orbitals only [28,29]. Figs. 6.15 and 6.16 represent electronic spectrum and visible spectrum of complex **31**.

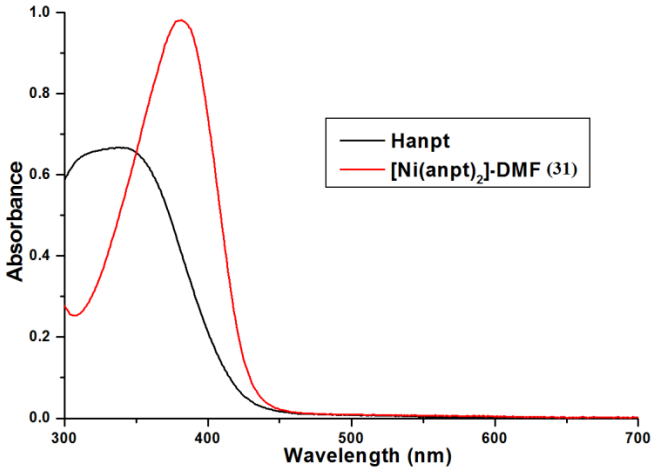

Fig. 6.15. Electronic spectra of Hanpt and $[Ni(anpt)_2]\cdot DMF$ (**31**).

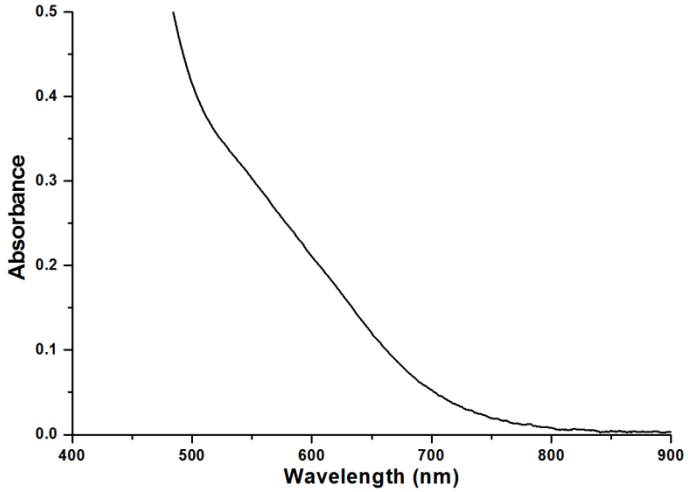

Fig. 6.16. Visible spectrum of $[Ni(anpt)_2]\cdot DMF$ (**31**).

For complex **32** a broad band with $\lambda_{max} = 370$ nm ($\varepsilon = 8.36 \times 10^4 M^{-1} cm^{-1}$) is observed corresponding to intraligand transition due to the presence of aromatic ring and non-bonding electrons in azomethine nitrogen. For a square planar Cu(II) complex with ground state $d_{x^2-y^2}$, three transitions are expected *via* $d_{x^2-y^2} \rightarrow d_{xy}$, $d_{x^2-y^2} \rightarrow d_{z^2}$ and $d_{x^2-y^2} \rightarrow d_{yz}$, d_{xy}

($^2B_{2g}\leftarrow{}^2B_{1g}$, $^2A_{1g}\leftarrow{}^2B_{1g}$ and $^2E_g\leftarrow{}^2B_{1g}$) [29]. The copper complex **32** gives a broad band with a maximum at 620 nm with ε = 198 $M^{-1}cm^{-1}$. This is because the *d* orbitals are very close to each other and it is difficult to isolate each of the transitions. Figs. 6.17 and 6.18 give electronic spectrum and visible spectrum for complex **32**.

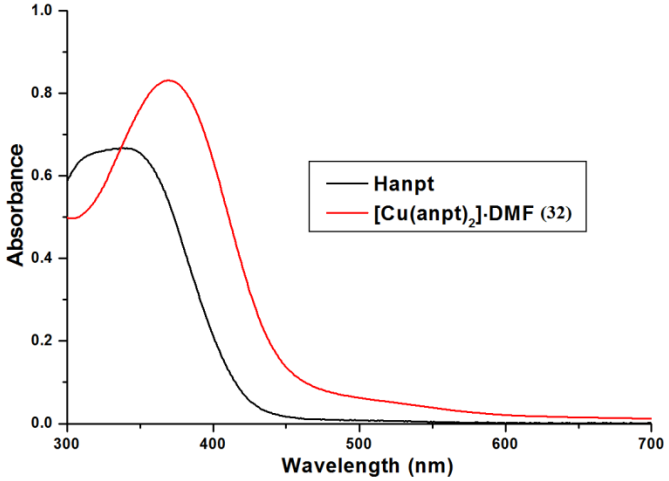

Fig. 6.17 Electronic spectra of Hanpt and $[Cu(anpt)_2]\cdot DMF$ (**32**).

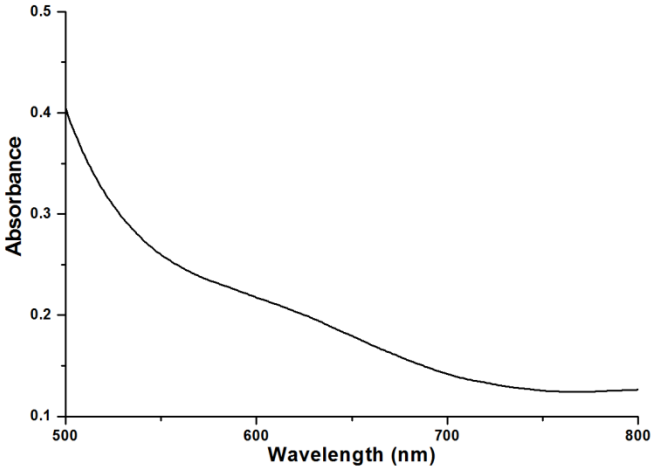

Fig. 6.18. Visible spectrum of $[Cu(anpt)_2]\cdot DMF$ (**32**).

The intraligand transitions tend to overlap with charge transfer transition in complexes **33** and **34** gave highly intense absorption with maxima at 374 and 388 nm with molar absorptivity 8.2 × 10^4 and 8.3 ×10^4 $M^{-1}cm^{-1}$ respectively. The electronic spectra for complexes **33** and **34** are given in Figs. 6.19 and 6.20.

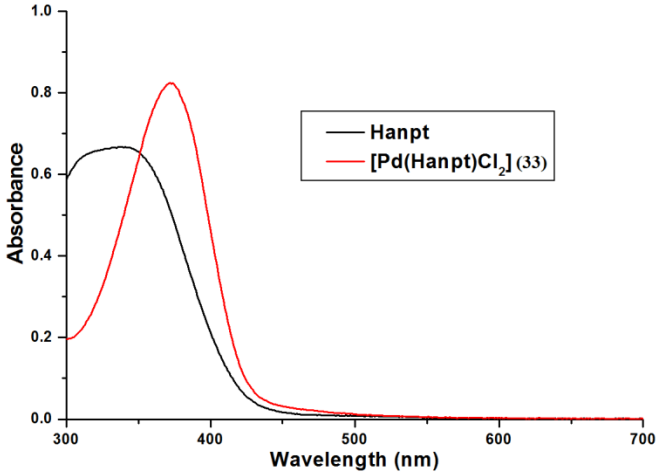

Fig. 6.19. Electronic spectra for Hanpt and $[Pd(Hanpt)Cl_2]$ (**33**).

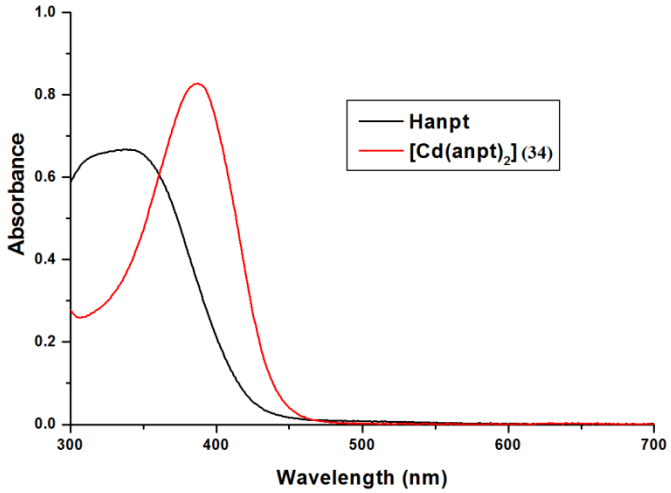

Fig. 6.20. Electronic spectra for Hanpt and $[Cd(anpt)_2]$ (**34**).

6.3.2.4. ^{1}H NMR spectra

^{1}H NMR spectra of complexes [Pd(Hanpt)Cl_2] **(33)** and [Cd(anpt)$_2$] **(34)** were taken in DMSO-d_6 with TMS as internal standard. The ^{1}H NMR spectra of the complexes are given in Figs. 6.22 and 6.23. All peaks in the ^{1}H NMR spectra shows a shift as compared to that of free ligand, confirms the complex formation. For complex **33,** the peaks at δ = 10.73 ppm (1H, s) and 10.24 ppm (1H, s) (Fig. 6.3) corresponding to ^{4}N–H and ^{2}N–H respectively show an upfield shift to δ = 9.84 ppm (1H, s) and 8.29 (1H, s), suggest that ligand is coordinated to the Pd(II). The aromatic protons show peaks in the region δ = 8.15-7.69 ppm and the methyl proton show an intense peak with δ = 2.4 ppm. The two peaks expected for magnetically nonequalent protons are not visible here suggesting that the bond strength and double bond character of C=N is reduced [30].

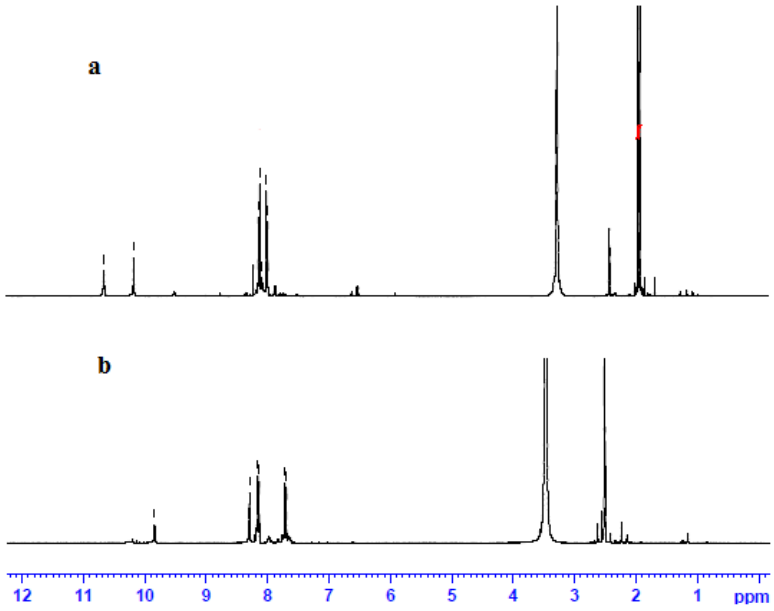

Fig. 6.21. ^{1}H NMR spectrum a) Hanpt b) for [Pd(Hanpt)Cl_2] **(33)**.

Complex **34** gave a peak at 9.61 ppm which corresponds to upfield shifted N^{4}–H proton. The aromatic protons give peaks in the region

8.14-7.93 ppm. The CH_3 protons, which appeared as closely spaced singlet (2.01 and 2.04 ppm), gave a peak at 2.56 ppm for the complex **34**. This indicates the coordination of Hanpt *via* azomethine nitrogen [31].

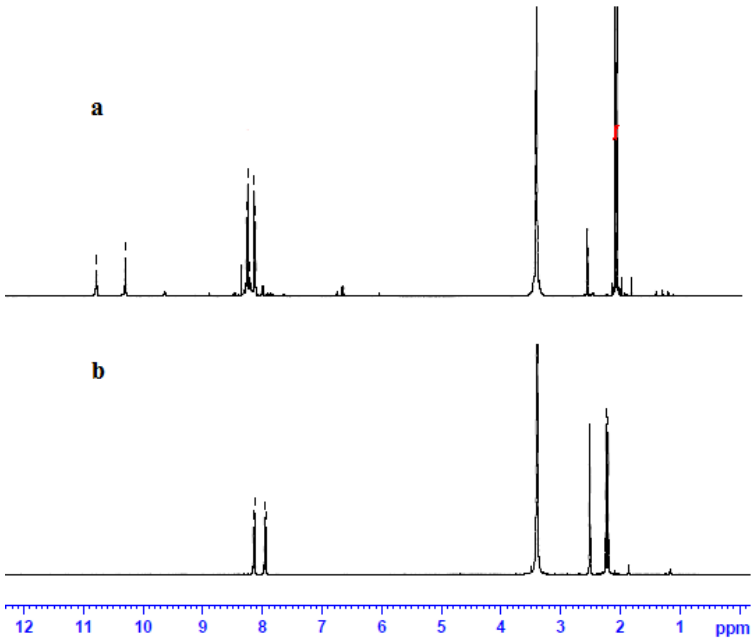

Fig. 6.22.^{1}H NMR spectrum for a) Hanpt and b) for $[Cd(anpt)_2]$ (**34).**

6.3.2.5. EPR spectrum of $[Cu(anpt)_2]\cdot DMF$ (32)

The EPR spectra of the $[Cu(anpt)_2]\cdot DMF$ (**32**) was recorded in the polycrystalline state at 298 K and in DMF solution at 77 K. The value of *g* tensor gives an idea about the ground state of the electron in the metal [32].

The EPR spectrum for complex **32** in the polycrystalline state was taken at 298 K. The EPR spectrum of the complex in the polycrystalline state was simulated using Easy Spin 4.0.0 package [33]. Best fit experimental (red) and simulated (blue) spectra are given in Fig. 6.23. The compound give an axial spectrum with $g_{\parallel} = 2.13$ and $g_{\perp} = 2.03$.

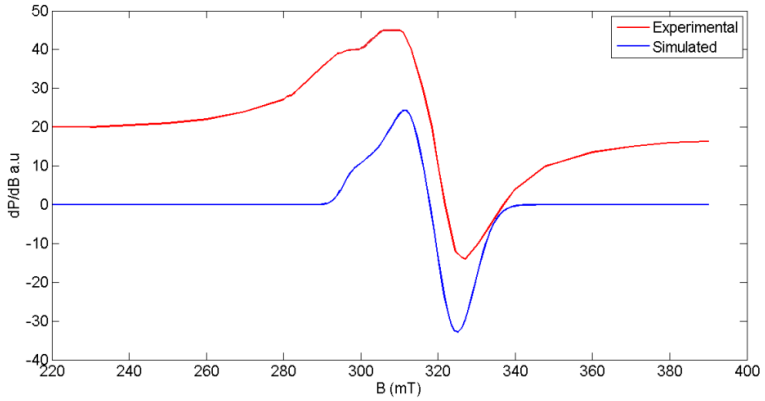

Fig. 6.23. EPR spectrum of $[Cu(anpt)_2]\cdot DMF$ (**32**) in polycrystalline state at 298 K.

In DMF solution at 77 K, complex **32** gives an axial spectrum with gives four hyperfine lines with g tensors $g_{\parallel} = 2.07$ and $g_{\perp} = 2.04$ and hyperfine coupling constants $A_{\parallel} = 51 \times 10^{-4}cm^{-1}$ and $A_{\perp} = 13 \times 10^{-4}\ cm^{-1}$. Fig. 6.24 gives the EPR spectrum of the complex **32** in DMF solution at 77 K. We failed to simulate completely the spectrum. From the values of $A_{\parallel}$ and $A_{\perp}$, it is possible to calculate A_{av} using the equation $A_{av} = \frac{1}{3}(A_{\parallel} + 2A_{\perp})$. For the present complex its value is $A_{av} = 25.6 \times 10^{-4}cm^{-1}$.

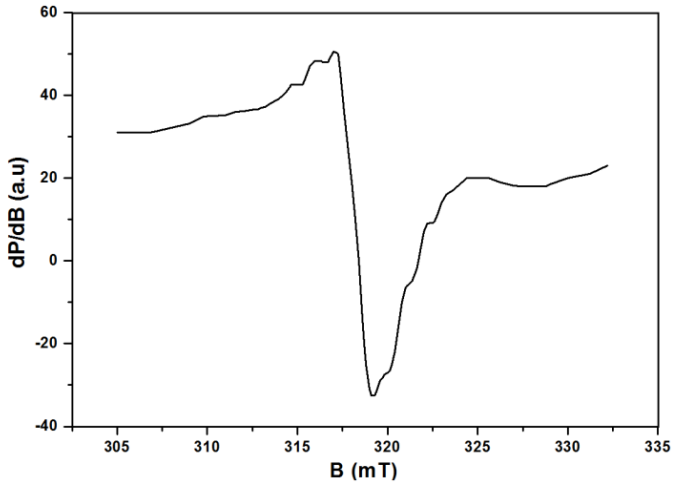

Fig. 6.24. EPR spectrum of $[Cu(anpt)_2]\cdot DMF$ (**32**) in frozen DMF at 77 K.

For complex **32,** G is found to have a value G = 7.21, which indicate a negligible interaction between metal centers in polycrystalline state[34,35]. The value for G> 2.014 and $g_{\parallel} > g_{\perp} > 2.0023$, consistent with $d_{x^2-y^2}$ ground state for a square planar complex. The g_{av} can be calculated using equation g_{av}= ⅓($g_{\parallel}$ + 2 $g_{\perp}$), here g_{av}= 2.06. When $g_{\parallel} < 2.3$, there is a significant covalent character to the M–L bond [36].

For complex **32,** bonding parameters α^2, β^2, γ^2,$K_{\parallel}$ and $K_{\perp}$ were found to be, α^2 = 0.4192, β^2 = 0.9685, γ^2 = 1.4456, $K_{\parallel}$ = 0.406 and $K_{\perp}$ = 0.606 suggests that the complex was having a significant σ bonding accompanied by an in-plane π-bonding [37,38].

6.3.2.6. Single crystal X-ray diffraction studies

6.3.2.6.1. Single crystal X-ray diffraction studies of [Ni(anpt)$_2$]·DMF (31)

Single crystals of [Ni(anpt)$_2$]·DMF (**31**) were isolated from DMF solution. Dark brown block shaped crystals with dimensions 0.35×0.25×0.20 mm^3 were mounted on a Bruker SMART APEXII CCD diffractometer. The non-hydrogen atoms were anisotropically refined and the C–H protons were placed in calculated positions guided by differance map with a distance 0.93 Å. The N(3)–H(3) proton was located from the difference map and the distance was restrained to 0.88±0.01 Å using DFIX instruction. The crystal data and refinement parameters are given in Table 6.7.

The complex crystallizes into monoclinic *C*2/c space group. The asymmetric unit comprises of half of the molecule and the other half is related by a two-fold screw axis, as a result of this only one part of the ligand is numbered. The bis ligated NS donor thiosemicarbazone form a four coordinate geometry about the Ni(II) ion accompanying a solvent

DMF molecule in the crystal lattice. ORTEP diagram for the complex **32** with 50% probability ellipsoid is given in Fig. 6.25.

Table 6.7. Crystal data and structure refinement parameters of $[Ni(anpt)_2]\cdot DMF$ (**31**)

Parameters	**$[Ni(anpt)_2]\cdot DMF$ (31)**
Empirical formula	$C_{26}H_{36}N_{10}NiO_6S_2$
Formula weight	707.48
Color	Brown
Temperature/K	296 (2)
Wavelength (Cu Kα) (Å)	0.71073
Crystal system	monoclinic
Space group	*C*2/c
Cell parameters	
a (Å)	27.7630(15)
b (Å)	7.8564(5)
c (Å)	17.1635(12)
$\alpha = \gamma$ (°)	90
β (°)	118.586(3)
Volume (Å^3)	3287.3(4)
Z	4
Calculated density, ρ (g cm^{-3})	1.429
Absorption coefficient, μ (mm^{-1})	0.772
F(000)	1480
Crystal size (mm^3)	0.35 × 0.25 × 0.20
Θ range for data collection (°)	2.72 to 27.50
Limiting indices	$-34 \le h \le 36$, $-10 \le k \le 8$, $-22 \le l \le 14$
Reflections collected	12093
Independent reflections	3777 [R_{int} = 0.0227]
Data/restraints/parameters	3771 / 1 / 212
Goodness-of-fit on F^2	1.042
Final R indexes [I>2σ (I)]	R_1 = 0.0349, wR_2 = 0.0933
Final R indexes [all data]	R_1 = 0.0470, wR_2 = 0.1031
Largest diff. peak and hole (e Å^{-3})	0.311/-0.343

$R_1 = \Sigma||F_o| - |F_c|| / \Sigma|F_o|$
$wR_2 = [\Sigma w(F_o^2-F_c^2)^2 / \Sigma w(F_o^2)^2]^{1/2}$

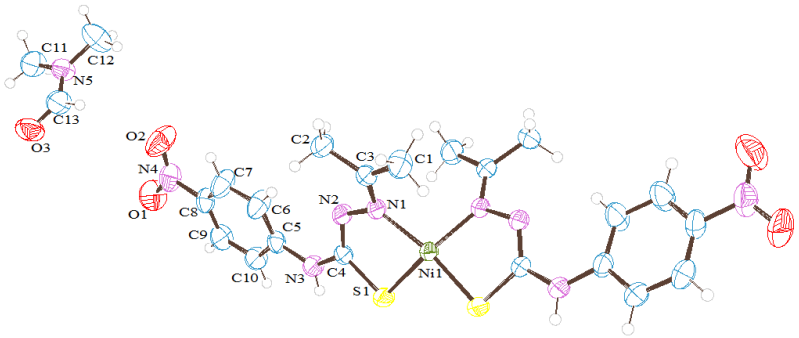

Fig. 6.25. ORTEP diagram for the complex $[Ni(anpt)_2]\cdot DMF$ (**31**) with 50% probability ellipsoid.

For a complex with coordination number four, two geometries were possible when the perfect alignment of atoms get disturbed and there is a chance for distortion from tetrahedral geometry or from square planar geometry. The actual distortion is calculated from the four coordinate geometry index using the equation $\tau_4=\frac{360-(\beta+\alpha)}{141}$, where β and α are the two largest angles around the metal. τ_4 = 1 for a perfect tetrahedral geometry and τ_4 = 0 for a perfect square planar geometry [39]. For complex **31** it is found that τ_4= 0.3, hence the molecule shows a distortion from square planar geometry. This is further confirmed from the N(1)–Ni(1)–S(1), N(1)–Ni(1)–N(1) and S(1)–Ni(1)–S(1) bond angles 86.18(5), 100.18(9) and 95.59(3)° respectively, which showed large deviation from square planar environment around Ni(II) ion.

The thiolate sulfur changes it confirmation with respect to azomethine nitrogen *E* to *Z*. This is evident from the N(1)–N(2)–C(4)–S(1) torsion angle which is equal to3.2(2)°, where as in ligand the N(3a)–N(2a)–C(1a)–S(1a) torsion angle is 175.7(12)°. Further the C(4)–S(1) bond length is 1.761(19) Å which is nearly equal to C–S single bond [40], this gives insight into the fact that the Hanpt ligand coordinate in the anionic form. This is further confirmed from the partial double bond character imparted to N(2)–C(4) bond which is equal to 1.28(2) Å [41].

The five membered chelate ring Ni(1)–S(1)–C(4)–N(2)–N(1) generated as a result of complex formation is puckered forming an envelope conformation with S(1) as the flap atom. The puckering parameters are Q(2)= 0.27(12) Å and φ(2)= 176.5(4)° [42] and both the rings about the metal centre are twisted away from each other with a dihedral angle 21.15(3)°. The benzene ring C(5)–C(6)–C(7)–C(8)–C(9)–C(10) and the ring Ni(1)–S(1)–C(4)–N(2)–N(1) makes an angle 21.95(6)° with each other. The selected bond lengths and bond angles are given in Table 6.8. The bond length of Ni(1)–S(1) and Ni(1)–N(1) were found to be 2.159(5) and 1.922(15) Å respectively are in good agreement with the previous reports [1,43,44]. It is suggested by Valdés-Martínez *et al.*, for a bis chelated compound with *cis* geometry the Ni–S bond length is shorter than expected is due to strong trans effect of sulfur over nitrogen that favour a *cis* geometry [1].

Table 6.8. Selected bond parameters for complex **31**

Bond length (Å)		Bond angle (°)	
N(1)–C(3)	1.290(2)	N(1)–Ni(1)–S(1)	86.17(5)
C(4)–S(1)	1.760(19)	N(1)–Ni(1)–S(1)$^{\#}$	158.24(5)
N(1)–N(2)	1.409(2)	N(1)–Ni(1)–N(1)$^{\#}$	100.18(9)
N(2)–C(4)	1.288(2)	S(1)$^{\#}$–Ni(1)–S(1)	95.59(3)
Ni(1)–S(1)	2.159(5)	C(3)–N(1)–N(2)	113.62(15)
Ni(1)–N(1)	1.922(15)	N(1)–N(2)–C(4)	112.04(15)

#- -x+2,y,-z+1/2

The solvent DMF molecule makes a strong hydrogen bonding interaction of the type N(3)–H(3)···O(3) [46] and C(10)–H(10)···O(3) with D···A distance 2.83 and 3.17(3) Å respectively. There is another intermolecular hydrogen bonding C(1)–H(1a)···N(1) with D···A distance of 3.07(3) Å between the acetone unit and the ligand on the other side. One intramolecular hydrogen bonding C(6)–H(6)···N(1) with D···A distance 2.839 Å is present within the ligand moiety. The hydrogen bonding

interactions present in the complex are presented in Fig. 6.26. One C–H···π interaction of the type C(11)–H(11c)···Cg(3) with X···C(g) distance 3.56(3) Å is also present in the molecule, where Cg(3) is the ring comprising of atoms C(5)–C(6)–C(7)–C(8)–C(9)–C(10). The C–H···π interaction is given in Fig. 6.27. Inter and intramolecular interactions present in the complex are given in Table 6.9.

Table 6.9. Interaction parameters in $[Ni(anpt)_2]\cdot DMF$ (**31**)

Hydrogen bonding interactions				
D–H···A	D–H (Å)	H···A (Å)	D···A (Å)	D–H···A (°)
C(1)–H(1a)···N(1)[a]	0.93	2.48	3.077(3)	120
N(3)–H(3)···O(3)[b]	0.88	1.98(18)	2.830(2)	164(3)
C(6)–H(6)···N(2)	0.93	2.25	2.839(3)	121
C(10)– H(10)···O(3)[b]	0.93	2.41	3.175(3)	139
C–H···π interactions				
C–H···Cg[c]	C–H (Å)	H···Cg (Å)	C···Cg (Å)	H···Cg(°)
C(11)–H(11c)···Cg(3)	[c]0.93	2.92	3.564(3)	126

a = 2-x, y, ½-z; b= x, -y, -½+z; c= x, 1-y, ½+z
Cg(3)= C(5), C(6), C(7), C(8), C(9), C(10)
D= donor, A= acceptor, Cg= centroid

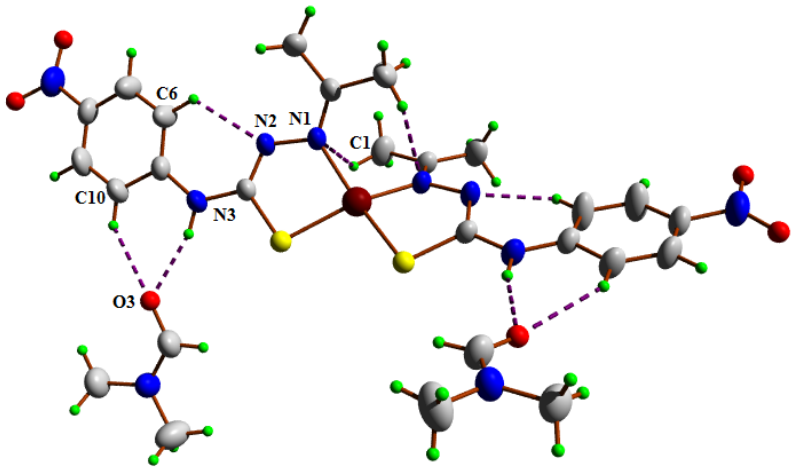

Fig. 6.26. Hydrogen bonding interactions in $[Ni(anpt)_2]\cdot DMF$ (**31**).

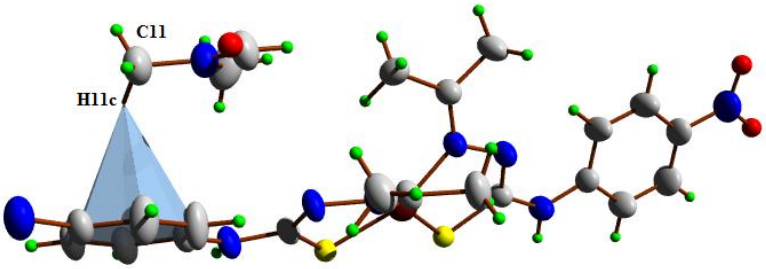

Fig. 6.27. C–H···π interaction in [Ni(anpt)$_2$]·DMF (**31**).

6.3.2.6.2. Single crystal X-ray diffraction studies of [Cu(anpt)$_2$]·DMF (32)

Single crystals of complex [Cu(anpt)$_2$]·DMF **(32)** were recrystallized from DMF solution of the crude sample. A dark green block shaped single crystal of size 0.35×0.30×0.25 mm^3 was mounted on a Bruker SMART APEXII CCD diffractometer for data collection. All non-hydrogen atoms were anisotropically refined and the C–H were placed in calculated positions guided by fourier map with distances 0.93-0.96. The N–H protons were fixed with a bond distance of 0.88±0.01 Å. The crystallographic data and structure refinement parameters are presented in Table 6.10.

Similar to complex **31** complex **32** is found to crystallize into monoclinic *C*2/c space group. The compound shows a four coordinate geometry around Cu(II) ion. The ORTEP diagram of complex **32** with 50% probability is given in Fig. 6.28. Four coordination cites of Cu(II) are occupied by the azomethine nitrogen and thiolate sulfur of the ligand Hanpt. The complex is a bis ligated Cu(II) complex with half of the molecule in the asymmetric unit. The Cu(II) ion have a half occupancy and the other half along with the second ligand unit is related to the first unit through a two folded screw axis. As a result of this, the numbering is restricted to one half of the molecule. A solvated DMF molecule is also found in the crystal lattice which facilitates the crystal formation.

Table 6.10. Crystal data and structure refinement parameters of $[Cu(anpt)_2]\cdot DMF$ (**32**)

Parameters	**$[Cu(anpt)_2]\cdot DMF$ (32)**
Empirical formula	$C_{26}H_{36}N_{10}CuO_6S_2$
Formula weight	712.32
Color	Dark green
Temperature/K	296 (2)
Wavelength (Å)	0.71073
Crystal system	monoclinic
Space group	C2/c
Cell parameters	
a (Å)	28.0650(3)
b (Å)	7.7967(7)
c (Å)	17.0100(12)
$\alpha = \gamma$ (°)	90
β(°)	118.585(7)
Volume ($Å^3$)	3268.4(6)
Z	4
Calculated density, ρ (g cm^{-3})	1.448
Absorption coefficient, μ (mm^{-1})	0.851
F(000)	1484
Crystal size (mm^3)	0.35 × 0.30 × 0.25
θ range for data collection (°)	2.72 to 28.37
Limiting indices	$-37 \le h \le 32$, $-10 \le k \le 9$, $-21 \le l \le 22$
Reflections collected	12221
Independent reflections	4098 [R_{int} = 0.0317]
Data/restraints/parameters	4098 / 1/ 212
Goodness-of-fit on F^2	1.030
Final R indexes [I>2σ (I)]	R_1 = 0.0381, wR_2 = 0.0964
Final R indexes [all data]	R_1 = 0.0649, wR_2 = 0.1083
Largest diff. peak and hole (e $Å^{-3}$)	0.319/-0.240

$R_1 = \Sigma||F_o| - |F_c|| / \Sigma|F_o|$

$wR_2 = [\Sigma w(F_o^2-F_c^2)^2 / \Sigma w(F_o^2)^2]^{1/2}$

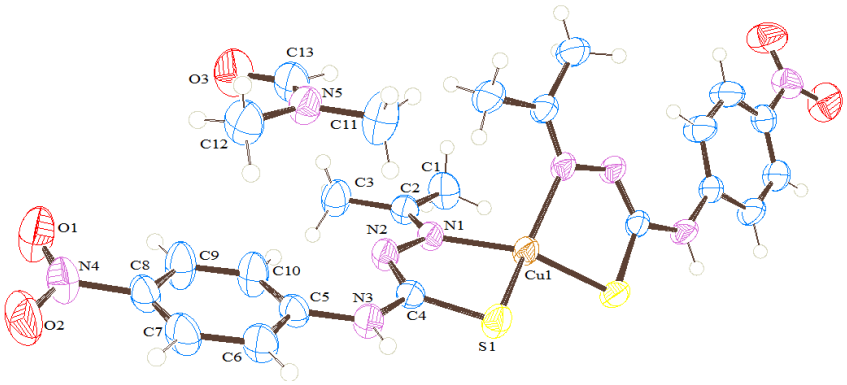

Fig. 6.28. ORTEP diagram of $[Cu(anpt)_2]\cdot DMF$ **(32)** with 50% probability ellipsoid.

The bond angles S(1)–Cu(1)–N(1), N(1)–Cu(1)–N(1), S(1)–Cu(1)–S(1) and N(1)–Cu(1)–S(1) are 147.59(6), 102.67(9), 103.89(3) and 85.73(5)° suggest that the complex deviate from a perfect square planar environment. Form the calculation it is found that τ_4= 0.42 for complex **32.** This confirms that the complex is having a distorted square planar geometry around Cu(II) ion. The Cu(1)–S(1), Cu(1)–N(1) bond lengths are 2.223(6) and 2.002(16) Å respectively are in close in agreement with already reported results [45,33].

The C(4)–S(1) bond length 1.752(2), which is nearly equal to C–S single bond supports the fact that the ligand coordinates in the anionic form. The shortening of C(2)–N(4) bond with a bond distance of 1.287(3) Å, which was 1.356(2) [C1a–N2a] for the ligand confirms the coordination of the ligand in the deprotonated mode. The *EE* conformation with respect to N1a–N2a and N2a–C1a respectively changes to *EZ* [with respect to N(1)–N(2) and N(2)–C(4)] as the sulfur atom changes its conformation from *E* to *Z* with respect to N(1) to facilitate coordination to Cu(II) ion. This is evident from the C(2)–N(1)–N(2)–C(4) and N(1)–N(2)–C(4)–S(1) torsion angles 168.7(2) and 2.3(3)° respectively. Selected bonding parameters are given in Table 6.11.

Table 6.11. Selected bond parameters of complex **32**.

Bond length (Å)		Bond angle (°)	
N(1)–C(2)	1.286(3)	N(1)–Cu(1)–S(1)	85.73(5)
C(4)–S(1)	1.752(2)	N(1)–Cu(1)–S(1)$^{\#}$	147.59(6)
N(1)–N(2)	1.399(2)	N(1)–Cu(1)–N(1)$^{\#}$	102.69(9)
N(2)–C(4)	1.287(3)	S(1)$^{\#}$–Cu(1)–S(1)	103.89(3)
Cu(1)–S(1)	2.223(6)	C(2)–N(1)–N(2)	114.29(16)
Cu(1)–N(1)	2.002(16)	N(1)–N(2)–C(4)	113.61(16)

#= -x, y, ½ -z

It is evident from the least square plane and puckering analysis, the five membered rings [Cu(1)–N(1)–N(2)–C(4)–S(1)] formed as a result of complex formation about the metal centre are puckered with Q = 0.2004(14) Å and φ = 356.6(6)° [42]. The benzene rings are twisted with a dihedral angle of 40.70(4)° with each other. The benzene ring and the chelating ring are twisted with a dihedral angle of 14.73(6)° suggest that the molecule as a whole is non planar.

The solvent DMF molecule in the crystal lattice is held to the complex *via* two intermolecular hydrogen bonding N(3)–H(3)···O(3) and C(6)–H(6)···O(3) with D···A distances 2.833(2) and 3.173(3) Å respectively and an intramolecular interaction, C(10)–H(10)···N(2) with a D···A distance of 2.838(3) Å. The is intermolecular interaction C(1)–H(1C)···N(1) with D···A distance 3.193(3) Å connects acetone of one ligand system to the next. The hydrogen bonding interactions are presented in Fig. 6.29. The molecular interaction include one C–H···π interaction between C(12)–H(12c) and Cg(3), where Cg(3) is the ring constituting atoms C(5)–C(6)–C(7)–C(8)–C(9)–C(10) with X···Cg distance 3.524(3) Å. The molecular interactions are given in Table 6.12. Fig. 6.30 depicts the C–H···π interaction present in the molecule.

Table 6.12. Interaction parameters in $[Cu(anpt)_2]\cdot DMF$ (**32**)

Hydrogen bonding interactions				
D–H···A	D–H (Å)	H···A (Å)	D···A (Å)	D–H···A (°)
C(1)–H(1c)···N(1)[a]	0.96	2.60	3.192(3)	120.1
N(3)–H(3)···O(3)[b]	0.87 (10)	1.98(11)	2.833(2)	167(2)
C(6)–H(6)···O(3) [b]	0.93	2.40	3.173(3)	140.3
C(10)– H(10)···N(2)	0.93	2.23	2.838(3)	121.9
C–H···π interactions				
C–H··· Cg	C–H (Å)	H···Cg (Å)	C···Cg (Å)	H···Cg(°)
C(12)–H(12c)···Cg(3)[c]	0.93	2.89	3.524(3)	124

a = x, y+1, z; b= -x+1, y, -z+3/2; c= x, y, z

Cg(3)= C(5), C(6), C(7), C(8), C(9), C(10)

D = donor, A= acceptor, Cg= centroid

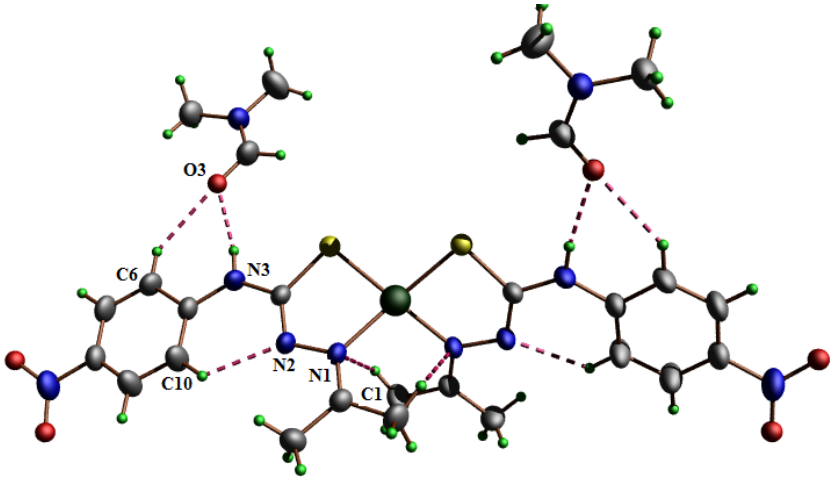

Fig. 6.29. Hydrogen bonding interactions in $[Cu(anpt)_2]\cdot DMF$ (**32**).

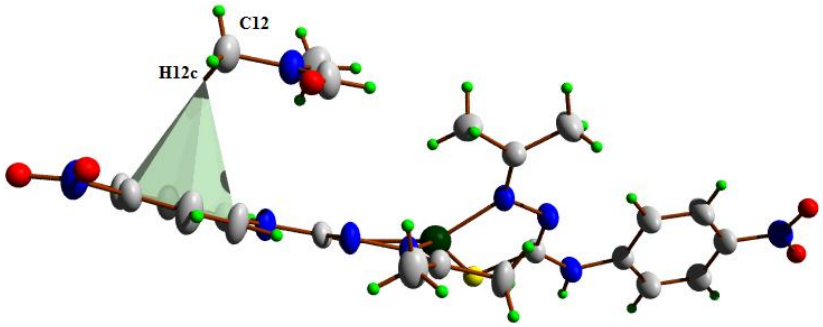

Fig. 6.30. C–H···π interaction in $[Cu(anpt)_2]\cdot DMF$ (**32**).

6.4. Conclusion

We could synthesize five metal complexes using Hanpt as the ligand. As already established an NS donor ligand give four coordinated complexes four of four of our complexes are four coordinated. Two of our complexes, Complex **31** and **32** could be isolated as single crystals. It is interesting to note that the conformation of the coordinating atoms in the ligand tend to change to enable coordinate bond formation. On the basis of physicochemical analysis the tentative structure for complexes **30**, **33** and **34** are assigned in Fig. 6.31.

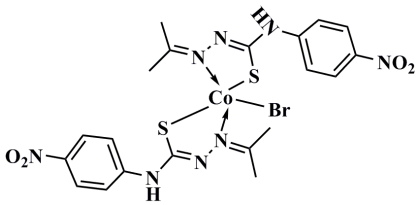

$[Co(anpt)_2Br]$ (**30**)

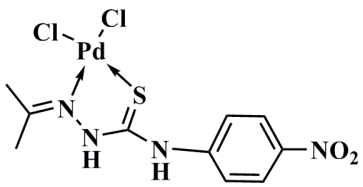

$[Pd(Hanpt)Cl_2]$ (**33**)

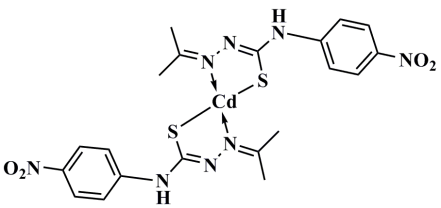

$[Cd(anpt)_2]$ (**34**)

References

[1] J.V. –Martínez, R.A. Toscano, M.S. –Gracía, M. Rubio, JG. –Lara, M.A. Vázquez-M, S. Carranza, Polyhedron 8 (1989) 727.

[2] S.-G. Teoh, S.-H. Ang, S.-B. Teo, H.-K. Fun, K.-L. Khew, C.-W. Ong, J. Chem. Soc., Dalton Trans. 4 (1997) 465.

[3] M.A. Ameer, E. Khamis, G. Al-Senani, Adsorp. Sci. Tecnol. 8 (2000) 177.

[4] M.M. Ali, M. Jesmin, M.K. Islam, F. Khatun, A.K. Azad, Med. J. Isl. W. Acad. Sci. 21 (2013) 97.

[5] B. Kpomah, S.H.O. Egboh, P.O. Agbaire, E.D. Kpomah, J. Pham. Appl. Chem. 2 (2016) 45.

[6] W. Hernández, J. Paz, F. Carrasco, A. Vaisberg, E. Spodine, J. Manzur, L. Hennig, J. Sieler, S. Blaurock, L. Beyer, Bioinorg. Chem. Appl. (2013).

[7] L. Palatinus, G. Chapuis, J. Appl. Cryst. 40 (2007) 786.

[8] L. Palatinus, A. van der Lee, J. Appl. Cryst. 41 (2008) 975.

[9] L., Palatinus, S. J. Prathapa, S. van Smaalen, J. Appl. Cryst. 45 (2012) 575.

[10] G.M. Sheldrick, Acta Cryst. C71 (2015) 3.

[11] SMART and SAINT, Area Detector Software Package and SAX Area Detector Program, Bruker Analytical X-ray; Madison, WI, USA, 1997.

[12] SADABS, Area Detector Absorption Correction Program; Bruker Analytical X-ray; Madison, WI, 1997.

[13] O.V. Dolomanov, L.J. Bourhis, R.J. Gildea, J.A.K. Howard & H. Puschmann, J. Appl. Cryst. 42 (2009) 339.

[14] K. Brandenburg, Diamond Version 3.2g, Crystal Impact GbR, Bonn, Germany, 1997.

[15] L.J. Farrugia, J. Appl. Cryst. 45 (2012) 849.

[16] K. Jayakumar, M. Sithambaresan, A.A. Aravindakshan, M.R.P. Kurup, Polyhedron 75 (2014) 50.

[17] V. Suni, M.R.P. Kurup, M. Nethaji, Spectrochim. Acta A63 (2006) 174.

[18] G.F. de Sousa, V.M. Deflon, E. Niquet, J. Mol. Struct. 687 (2004) 17.

[19] M. Joseph, V. Suni, C.R. Nayar, M.R.P. Kurup, H.-K. Fun, J Mol. Struct. 705 (2004) 63.

[20] G.R. Desiraju, Angew. Chem. Int. Ed. 50 (2011) 52.

[21] T. Steiner, Cryst. Rev. 9 (2003) 177.

[22] A. Sreekanth, H.-K. Fun, M.R.P. Kurup, J Mol. Struct. 737 (2005) 61.

[23] M. Mathew, G.J. Palenik, G.R. Clark, J. Inorg. Chem. 12 (1973) 446.

[24] P.F. Rapheal, E. Manoj, M.R.P. Kurup, E. Suresh, Poyhedron 26 (2007) 607.

[25] P. Bindu, M.R.P. Kurup, Ind. J. Chem. A38 (1999) 388.

[26] A.K. El-Sawaf, D.X. West, F.A. El-Saied, R.M. El-Bahnsawy, Transit. Met. Chem. 23 (1998) 565.

[27] Ş. Güveli, N. Özdemir, A. Koca, T. Bal-Demirci, B. Ülküseven, Inorg. Chim. Acta 443 (2016) 7.

[28] D.N. Sathyanarayana, Electronic Absorption Spectroscopy and related techniques, University press Ltd. (2001) 257.

[29] A.B.P. Lever, Inorganic electronic spectroscopy 2^{nd} *Ed*^{n}. Elsevier, Amsteram (1984).

[30] M.A. Demertzis, P.N. Yadav, D.K. Demertzi, Helv. Chim. Acta 89 (2006) 1959.

[31] M.M. Al-Mogren, A.N.-M.A. Alaghaz, Int. J. Electrochem. Sci. 8 (2013) 8669.

[32] E. Garribba, G. Micera, J. Chem. Educ. 83 (2006) 1229.

[33] S. Stoll, Spectral Simulations in Solid-State Electron Paramagnetic Resonance, Ph. D. Thesis, ETH, Zurich, 2003.

[34] L. Latheef, M.R.P. Kurup, Spectrochim. Acta A70 (2008) 86.

[35] M.J. Bew, B.J. Hathaway, R.R. Faraday, J. Chem. Soc., Dalton Trans. (1972) 1229.

[36] D. Kivelson, R. Neiman, J. Chem. Phys. 35 (1961) 149.

[37] B.J. Hathaway, Structure and Bonding, Springer Verlag, Heidelberg (1973) 60.

[38] E.B. Seena, M.R.P. Kurup, Polyhedron 26 (2007) 829.

[39] L. Yang, D.R. Powel, R.P. Houser, Dalton Trans. 9 (2007) 955.

[40] E. Manoj, M.R.P. Kurup, H.-K. Fun, A. Punnoose, Polyhedron 26 (2007) 4451.

[41] V. Suni, M.R.P. Kurup, M. Nethaji, Polyheron 26 (2007) 3097.

[42] D. Cramer, J.A. Pople, J. Am. Chem. Soc. 97 (1975) 1354.

[43] Ş. Güveli, N. Özdemir, T. Bal-Demirci, B. Ülküseven, Polyhedron 113 (2016) 16.

[44] G.A. Jeffrey, Crystallogr. Rev. 9 (2003) 135.

[45] M. Muralisankar, S. sujith, N.S.P. Bhuvanesh, A. Sreekanth, Polyhedron 118 (2016) 103.

Chapter 7

CORROSION INHIBITION STUDIES OF THIOSEMICARBAZONES ON MILD STEEL IN 1 M HCl

Contents

7.1. Introduction

Materials made up of metals find extensive application in domestic as well as industrial fields. The metals except noble metals are purified by reduction of ores, most of which is present as oxides. These metals always show a tendency to reverse the reaction, thus to form oxides whenever the surrounding factors become favorable. The chemical destruction of metals due to impact of surrounding factors is called corrosion. The term 'corrosion' is derived from Latin, where the word 'corrodere' means 'gnawing to pieces' [1].

Corrosion is a serious problem effecting life and money worldwide. One of the reports from Times of India in 2012 says that India losses about 2 lakh cores per year due to corrosion. According to another report, India loses about $70 billion equivalent to 4% of GDP (Gross Domestic Product) as a result of corrosion in the oil field alone. The companies around the world also face a similar situation. Because of the importance of prevention of corrosion, scientists around the world are working hard to develop new methods.

Corrosion in a metal may be due to,

- Impact, stress or exhaustion of materials
- Action of gases like oxygen, sulfur, fluorine *etc.*
- When the metal is immersed or is in contact with an electrolyte like water creation of electrochemical sites may result
- Action of microorganisms, which upon depositing on the surface of metals whereby creating 'live area' leading to corrosion [2]

Prevention measures for corrosion include cathodic protection, use of anticorrosive agents, use of corrosion inhibitors *etc.* In the present study we are interested in the use of corrosion inhibitors as a preventive measure.

Importance of studying acid corrosion…….

Acidizing is an important process in extraction of oils as they help in dissolving oils from rocks containing oil in the well. But uses of acids tend to destroy the metal pipes used for extraction of oils as a result of enhanced corrosion. Acids like HCl, HF, CH_3COOH, HCOOH *etc.* have been using for the purpose. HCl is the most commonly used among them [3]. To reduce the effect of acids on metal, retarded acid systems are used. This can be achieved by gelling the acid, chemically retarding the acid or emulsifying the acid. The present study deals only with chemically retarding the acid for the purpose of oil extraction. Effect of acids on metal can be controlled by using various chemicals like complexes of metals or organic compounds.

Corrosion inhibitors in acid medium:-A journey from the beginning

It was Herman Frasch first to discover a way to reduce corrosion due to acid with the help of lime stones in 1895 [4]. In 1915, Aupperle developed another method using antimony for steel as the galvanizing agent

[5]. Later a large number of materials were devised as corrosion inhibitors for steel in acid medium. It was in 1945, Hill used an aldehyde, H_2S reaction product as the first organic compound as a corrosion inhibitor [6]. Organic compound as a result of multicenters present in them facilitating coordination to the metal, forming a protective layer enable enhanced corrosion inhibition [7,8]. Therafter a large number of organic compounds were studied for the purpose. Use of thiourea derivatives as corrosion inhibitors was first reported by Cavallaro *et al.* in 1963 [9]. The effect of structure on corrosion inhibition action was first investigated by Granese *et al* in 1992 [10], when he used heterocyclic compounds like N-hexadecyl derivatives of pyridine, quinolene *etc.* as corrosion inhibitors. Quraishi *et al.* in 2000 [11] synthesized a series of thiosemicarbazides and hydrazides of long chain fatty acids and established them as good corrosion inhibitors in acid medium. The same group in 2001 synthesized 1-cinnamaldehyde thiosemicarbazone, that could act as a good corrosion inhibitor for carbon steel in HCl even at 60 °C [12]. From then on thiosemicarbazones were established as good corrosion inhibitors for mild steel in acid medium even at higher temperatures. In latest reports, anisoin and furoin N^4 substituted thiosemicarbazones as well as isatin based thiosemicarbazones were found to act as good corrosion inhibitors on mild steel in 1 M HCl [13,14].

Thiosemicarbazones act as good corrosion inhibitors due to its ability to coordinate to metal surface *via* sulfur and nitrogen. The quantitative structure activity studies by Lukovits suggested that the corrosion inhibition efficiency of thiosemicarbazones were a result of minimal excitation energy of these compounds [15].

As thiosemicarbazones were found to be an effective corrosion inhibition agent, we hereby present the investigation of corrosion inhibition

properties of five different thiosemicarbazones by weight loss, surface studies and electrochemical analysis methods.

7.2 Experimental

The synthesis and characterization of the thiosemicarbazones 4-benzyloxysalicylaldehyde-N^4-cyclohexylthiosemicarbazone (H_2bsct), 4-benzyloxysalicylaldehyde-N^4-methylthiosemicarbazone (H_2bsmt), 6-brom opyridinecarbaldehyde-N^4,N^4-dimethylthiosemicarbazone (Hbpdmt), 6-brom opyridine-N^4-cyclohexylthiosemicarbazone (Hbpct) and acetone-N^4-(4-nitrophenyl)thiosemicarbazone (Hanpt) used for the present chapter were discussed in Sections 2.2.2, 3.2.2, 4.2.2, 5.2.2 and 6.2.2. So the discussion is limited to corrosion inhibition studies.

7.2.1. Materials

7.2.1.1. Composition of material sample

The sample of mild steel whose chemical composition (weight %) is as follows: 0.20 C, 0.35 Mn, 0.024 P, 003 Si and remainder Fe was used for the study. Specimens were mechanically polished with fine grade emery paper in order to obtain a smooth surface, followed by ultrasonically degreasing in acetone, and then rinsed with distilled water, dried and weighed.

7.2.1.2. Hydrochloric acid

A stock solution of hydrochloric acid (1 M) was prepared using distilled water. The acid solution was prepared by diluting the appropriate volume of the concentrated chemically pure grade acid with distilled water. The concentration of the acid was checked by titration of an appropriately diluted portion with standard solution of Analar sodium carbonate.

7.2.2. Methods

The corrosion inhibition studies of the compounds were carried out *via* weight loss method, scanning electron microscopy, adsorption studies, infrared spectral analysis and electrochemical methods.

7.2.2.1. Weight loss method

Mild steel of the size 20×20×2 mm^3 were cut from a sheet of the mild steel. The sample was immersed in 100 ml, 1 M HCl solution at 30 °C. The average weight loss at a certain time for the tested samples was taken in mg cm^{-2}. The experiment was repeated with 1 M HCl solution containing various concentration of inhibitor (100, 200, 300, 400 and 500 ppm), for various time intervals (48, 96, 144, 192 and 336 h). The weight loss after each immersion was noted and weight loss per unit area was calculated from Eq. 7.1.

$$\Delta W = \frac{W1 - W2}{a} \quad \text{.....(7.1)}$$

where, $W1$ and $W2$ are the weights of a specimen before and after immersion, respectively, and a is the surface area in cm^2.

The corrosion inhibition efficiency and corrosion rate for each time interval could be calculated using Eq. 7.2 and Eq. 7.3 [16,17].

$$IE\ (\%) = \frac{\Delta W - \Delta Wi}{\Delta W} \times 100 \quad \text{..... (7.2)}$$

Here, ΔW and ΔWi are the weight losses per unit area in the absence and presence of the inhibitor, respectively.

$$CR = \frac{3.45 \times 10^6 \times W}{\rho A t} \quad \text{.....(7.3)}$$

CR is the corrosion rate, *W* is the weight loss (g), ρ is the density of the metal (g cm^{-3}), *A* is the area in cm^2 and *t* is exposure time (h).

7.2.2.2. Adsorption isotherm behavior

The inhibition of corrosion by organic compound can be well explained on the basis of adsorption studies, as adsorption plays an important role in corrosion inhibition. The adsorption of an organic molecule to a metal surface can be represented as the following displacement reaction [18].

$$\text{Organic (soln)} + n\text{H}_2\text{O(ads)} \longrightarrow \text{Organic (ads)} + n\text{H}_2\text{O (soln)}$$

Here n is the number of water molecules on the metal surface and depends up on the cross sectional area of the surface under study.

Three types of adsorption isotherms could be used to describe the adsorption of the organic compound to the metal surface [19]. They are Langmuir′s isotherm, Frumkin's isotherm and Temkin′s isotherm, each follow the relationship with surface coverage as given in Eq. 7.4, 7.5 and 7.6 respectively;

Langmuir′s isotherm: $\frac{\theta}{1-\theta} = KC$ ..... (7.4)

Frumkin's isotherm: $\frac{\theta}{1-\theta}e^{f\theta} = KC$ .....(7.5)

Temkin′s isotherm: $e^{f\theta} = KC$ ..... (7.6)

The values of surface coverage (θ) obtained from Eq. 7.7

$\theta = \frac{IE}{100}$,.....(7.7)

Were C is the concentration of the compound in mol L^{-1} and K is the equilibrium constant of adsorption process, IE is the percentage of inhibition efficiency [20].

The best fitted adsorption isotherm is obtained by plotting log $\frac{\theta}{1-\theta}$ versus log$C$ for Langmuir adsorption isotherm, log $\frac{\theta}{C(1-\theta)}$ versus θ for

Frumkin isotherm and θ versus log*C for* Temkin isotherm. The plot giving a straight line determines the adsorption isotherm.

On the basis of Langmuir isotherm, the standard free energy for adsorption can be calculated using the equation 7.8.

$$K_{ads} = \frac{1}{55.5} exp\left(\frac{-\Delta G^{\circ}_{ads}}{RT}\right) \quad \text{.....(7.8)}$$

On modifying Eq. 7.8, the expression for $-\Delta G^{\circ}_{ads}$ becomes,

$$-\Delta G^{\circ}_{ads} = 2.303RT \log(55.5K_{ads}) \quad \text{.....(7.9)}$$

Were, ΔG°_{ads} is the change in Gibbs free energy for adsorption, R is the universal gas constant and T is the absolute temperature. The value of K_{ads} could be calculated using the Eq. 7.10

$$K_{ads} = \frac{\theta}{C(1-\theta)} \quad \text{.....(10)}$$

Here K_{ads} is the equilibrium constant for adsorption process.

7.2.2.3. Surface analysis and spectroscopic techniques

SEM images of the metal surfaces used for corrosion studies were taken with a JEOL JSM–6390LV instrument at the Sophisticated Analytical Instrumentation Facility, Cochin University of Science and Technology. Samples for studies were prepared by immersing the metal in 1 M HCl in the presence and absence of an inhibitor for various time intervals. An image of the surface before immersion in 1 M HCl was also taken for comparison. The infrared spectrum of powder obtained from the surface of each sample after immersion of metal for a limited time interval was recorded on a JASCO FT-IR-5300 spectrometer in the range 4000-400 cm^{-1} using KBr pellets at Department of Applied chemistry, Cochin University of Science and Technology.

7.2.2.4. Electrochemical methods

Most of the corrosion process is electrochemical in nature. Where two electrodes *via*, the anode and cathode were generated within the metal surface (Fig. 7.1) and the following reactions occur in acid medium [21].

Anode: $Fe \rightarrow Fe^{2+} + 2e^-$

Cathode: $2H^+_{(acid)} + 2e^- \rightarrow H_2$

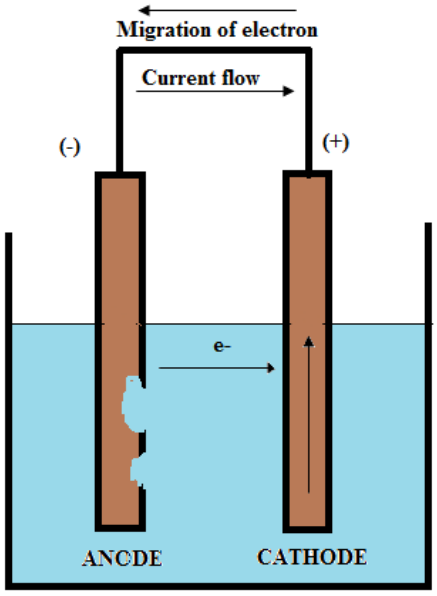

Fig. 7.1. Anodic and cathode process in corrosion cell.

The electrochemical reactions occurring on the mild steel surface were studied using standard three-electrode cell (Fig. 7.2). The counter electrode was a platinum wire of high purity (99.9%) and the reference electrode consisted of a saturated calomel electrode (SCE). The third electrode was the working electrode which was prepared from a sheet of mild steel. The exposed steel sample for the given solution was 2 cm^2. All tests were performed in open air at room temperature of 30±1 °C. Electrochemical testing was performed using an electrochemical analyzer (CH instrument model 680). The metal samples were exposed to

solutions with and without inhibitors with various concentrations (100-500 ppm by weight). Tafel polarization studies of the samples gave corrosion currents and corrosion rates. The corrosion inhibition actions of different thiosemicarbazones were compared using Nyquist plots and Bode plots and the measurements were carried out in the frequency range from 1 to 100000 Hz with a signal amplitude perturbation of 5 mV with an AC signal at OCP.

Fig. 7.2. Experimental setup for electochemical analysis.

7.2.2.4.1 Tafel Polarization studies

The kinetics of an electrochemical reaction can be described using the Butler-Volmer equation developed by Butler and Volmer [22,23]. The Butler–Volmer equation for current density when the electrode reactions occur under charge transfer control is given in Eq. 7.11

$$i = i_{corr}\left[exp\left[\frac{\alpha nF}{RT}\eta\right] - exp\left[\frac{-\beta n'F}{RT}\eta\right]\right] \quad \text{.....(7.11)}$$

where, $\eta = E - E_{corr}$, known as the over potential, E is the applied potential and E_{corr} is the corrosion potential, i and i_{corr} are the measured current and corrosion current density respectively. α and β are the coefficients related to the potential drop through the electrochemical double layer, F is the Faraday's constant, R is the Universal gas constant, T

is the absolute temperature and n and n′ are the number of electrons transferred in cathodic and anodic reactions. The Tafel equation is a simplified form of Butler-Volmer equation derived by Tafel [19].

For anodic polarization the measured current can be determined by Eq. 7.12

$$i = i_{corr}\left[exp\left[\frac{\alpha nF}{RT}\eta\right]\right] \quad \text{.....(7.12)}$$

or $$-\eta = -\frac{2.303RT}{\alpha F}logi_{corr} + \frac{2.303RT}{\alpha F}logi \quad \text{.....(7.13)}$$

For cathodic polarization the current can be determined from Eq. 7.14.

$$i = i_{corr}\left[exp\left[\frac{-\beta n'F}{RT}\eta\right]\right] \quad \text{..... (7.14)}$$

or $$-\eta = -\frac{2.303RT}{\beta F}logi_{corr} + \frac{2.303RT}{\beta F}logi \quad \text{.....(7.15)}$$

The equations 13 and 14 are called Tafel equations [21] and can be written as a general expression as given in Eq. 7.16.

$$|\eta| = a + b\ logi \quad \text{..... (7.16)}$$

Here a = $-\frac{2.303RT}{\alpha F}logi_{corr}$ and b = $\frac{2.303RT}{\alpha F}$ for anodic polarization and a = $-\frac{2.303RT}{\beta F}logi_{corr}$ and b = $\frac{2.303RT}{\beta F}$ for cathodic polarization. The graph obtained when electrode potential is plotted against current density is called the Tafel plot comprising of straight lines called Tafel lines Fig. 7.3 [22].

It is possible to calculate corrosion inhibition efficiency using corrosion current obtained from Tafel polarization graph using Eq. 7.17 [18].

$$IE\ (\%) = \frac{i_o - i}{i_o} \quad \text{.....(7.17)}$$

Where *IE* is the corrosion inhibition efficiency, i_o is the corrosion current in the absence of inhibitor and i is the corrosion current in the presence of inhibitor.

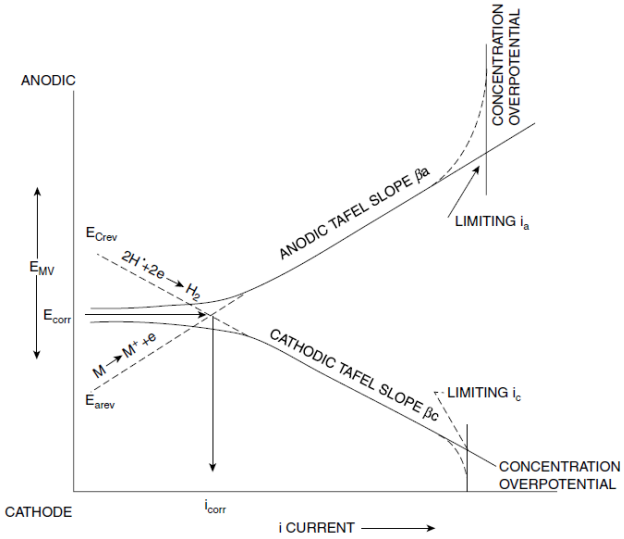

Fig. 7.3. Tafel plot describing various parameters.

7.2.2.4.2. Electrochemical impedance spectroscopy

Impedance (Z) is the resistance offered by the circuit to flow current through it. Electrochemical impedance spectroscopy is a technique where impedance is measured as a function of frequency of ac source [22]. Here the instrument records the real (resistance) and imaginary (capacitance) responses of the circuit under study. The frequency depended impedance $Z(\omega)$, can be represented by Eq. 7.18.

$$Z(\omega) = \frac{V(t)}{I(t)} = \frac{V_o \sin \omega t}{I_o \sin(\omega t + \theta)} = Z'(\omega) + jZ''(\omega) \quad \text{.....(7.18)}$$

Where, ω is the frequency, t is the time, $V(t)$ is the time dependent potential, $V_o \sin(\omega t)$ is the sinusoidal alternating potential signal, $I(t)$ is the

time dependent current response, $\sin(\omega t+\theta)$ is the sinusoidal alternating current response and θ is the angle between $V(t)$ and $I(t)$.

The graph obtained when the real component of impedance is plotted against imaginary component is called a Nyquist plot. When phase angle is plotted against frequency the graph obtained is called the Bode plot. A typical Nyquist plot is given in Fig. 7.4.

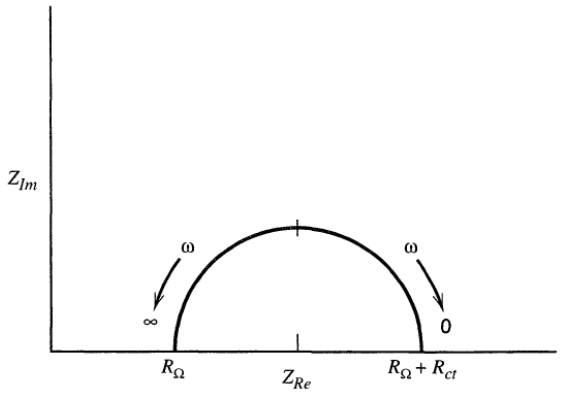

Fig. 7.4. A typical Nyquist plot with increasing frequency.

7.3 Results and discussion

7.3.1 Weight loss method

7.3.1.1 Weight loss per unit area

The weight loss per unit area for each sample of thiosemicarbazone H_2bsct, H_2bsmt, Hbpdmt and Hbpct and Hanpt were measured using Eq. 7.1. The weight losses per unit area for mild steel samples immersed in different concentrations of the thiosemicarbazones were reported in Table 7.1.

Table 7.1. Weight loss per unit area for mild steel

Sample	Concentration (ppm)	Time (h)				
		48	96	144	192	336
Blank		0.0152	0.0572	0.0606	0.0504	0.0280
H_2bsct	100	0.0022	0.0026	0.0069	0.0087	0.0122
	200	0.0012	0.0021	0.0064	0.0075	0.0118
	300	0.0011	0.0015	0.0052	0.0069	0.0078
	400	0.0017	0.0022	0.0061	0.0072	0.0089
	500	0.0019	0.0055	0.0063	0.0078	0.0102
H_2bsmt	100	00170	0.0024	0.0029	0.0042	0.0071
	200	0.0016	0.0019	0.0026	0.0030	0.0037
	300	0.0011	0.0015	0.0020	0.0025	0.0033
	400	0.0014	0.0019	0.0029	0.0020	0.0069
	500	0,0017	0.0020	0.0031	0.0046	0.0077
Hbpdmt	100	0.0032	0.0037	0.0054	0.0059	0.0085
	200	0.0025	0.0031	0.0041	0.0054	0.0082
	300	0.0027	0.0035	0.0047	0.0061	0.0090
	400	0.0028	0.0039	0.0049	0.0065	0.0102
	500	0.0031	0.0045	0.0053	0.0068	0.0120
Hbpct	100	0.0012	0.0021	0.0025	0.0029	0.0047
	200	0.0012	0.0019	0.0021	0.0024	0.0045
	300	0.0010	0.0014	0.0015	0.0017	0.0030
	400	0.0013	0.0015	0.0019	0.0024	0.0034
	500	0.0014	0.0017	0.0037	0.0037	0.0083
Hanpt	100	0.0035	0.0050	0.0090	0.0092	0.0131
	200	0.0034	0.0046	0.0052	0.0079	0.0130
	300	0.0033	0.0039	0.0050	0.0071	0.0126
	400	0.0035	0.0045	0.0051	0.0077	0.0127
	500	0.0036	0.0051	0.0066	0.0086	0.0144

In the absence of inhibitor the corrosion was drastic and the weight loss per unit area for mild steel for various time intervals was depicted in Fig. 7.5. There was a sharp increase in the weight loss up to a time period

of 144 h after that the weight loss is found to decrease. This could be explained on the basis of formation of a protective layer on the metal surface as time went on.

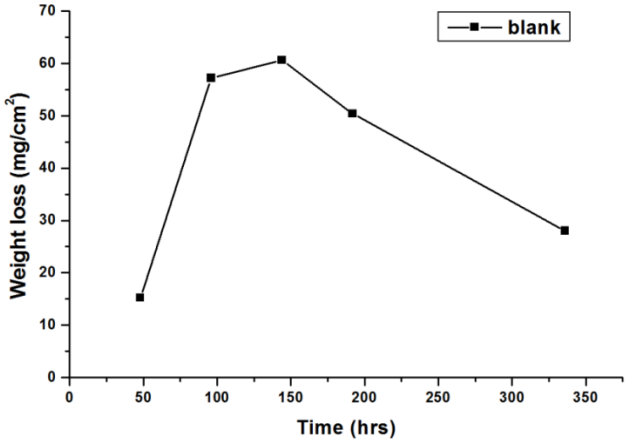

Fig. 7.5. Weight loss per unit area for mild steel in the absence of inhibitor.

It is found that the weight loss per unit area of the mild steel sample decreases when H_2bsct was used as the inhibitor, from a concentration of 100 ppm to 300 ppm followed by an increase upto 500 ppm. These weight losses were not showing much difference from each other in values but are very less as compared to that of weight loss for mild steel in the absence of inhibitor. This observation lead to a suggestion that corrosion inhibition had taken place on the surface of metal when H_2bsct was present in 1 M HCl solution. It is also observed that the weight loss per unit area increases with increase in time. The least weight loss was observed for the metal when immersed in a solution of 1 M HCl containing 300 ppm of H_2bsct for a time period of 48 h and maximum weight loss was observed when 100 ppm of the compound was present in 1 M HCl for a time period of 336 h. The weight loss per unit area for H_2bsct for various time intervals is given in Fig. 7.6

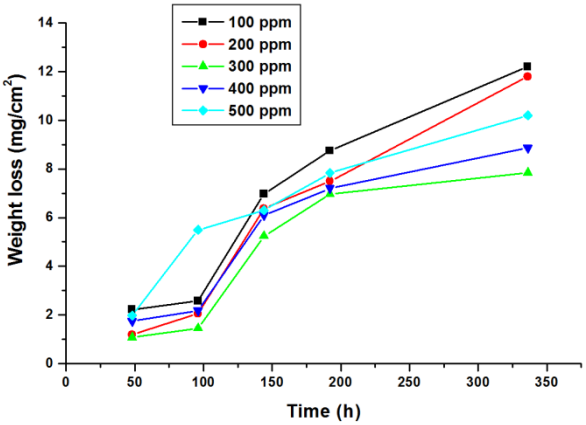

Fig. 7.6. Variation in weight loss for mild steel, when H_2bsct was used as inhibitor.

When the inhibitor used was H_2bsmt the weight loss per unit area for the mild steel observed is depicted in Fig. 7.6. It is evident from the figure that the inhibitor with concentration of 300 ppm was exhibiting minimum weight loss per unit area or was the optimum concentration of the inhibitor. Maximum weight loss was observed for 500 ppm concentration of H_2bsmt at 336 h. The value of weight loses for mild steel increase rapidly for all concentrations except 300 ppm of the sample, for which the weight loss show less variation.

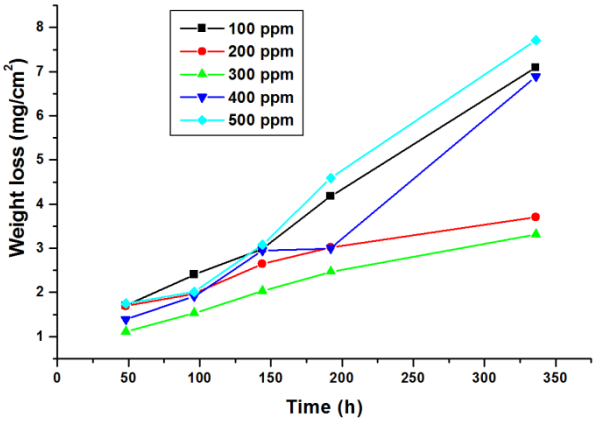

Fig. 7.7. Weight loss for mild steel in 1 M HCl when H_2bsmt was the inhibitor.

The trend in weight loss for mild steel in 1 M HCl in the presence of H_2bsmt as inhibitor is given in Fig. 7.7.

When Hbpdmt was used as the inhibitor for corrosion on mild steel in 1 M HCl, the weight loss of the sample is presented in Fig. 7.8. The minimum weight loss for the sample is observed when 200 ppm of Hbpdmt was mixed with 1 M HCl. There is a gradual increase in the weight loss per unit area of the metal. Maximum weight loss was observed for 500 ppm inhibitor at 336 h. At 100 ppm concentration of Hbpdmt, there was a deviation from the regular trend in the weight loss value. This may be due to the lower concentration of inhibitor in the solution.

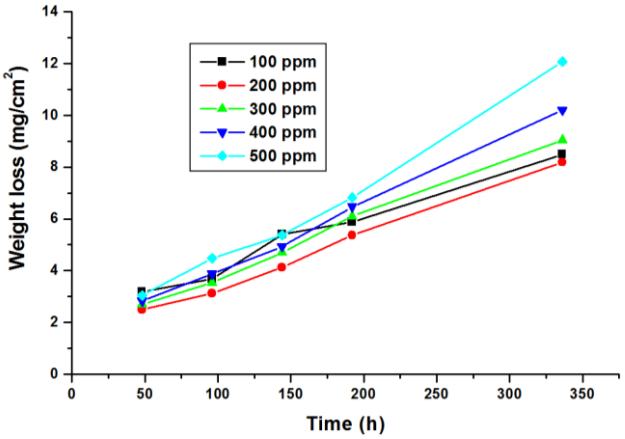

Fig. 7.8. Weight loss for mild steel in 1 M HCl when Hbpdmt was the inhibitor.

Weight loss for mild steel sample, when Hbpct was used as the inhibitor is graphically represented in Fig. 7.9. It was observed that 300 ppm of the inhibitor in 1 M HCl exhibit minimum weight loss of mild steel at all intervals of time. It is evident that the weight loss of mild steel varies with increase in time for all the concentrations, maximum deviation from a trend for the sample is observed when the inhibitor concentration was 500 ppm. This deviation from regular trend may be due to maximum layer formation and there by resisting the inhibition.

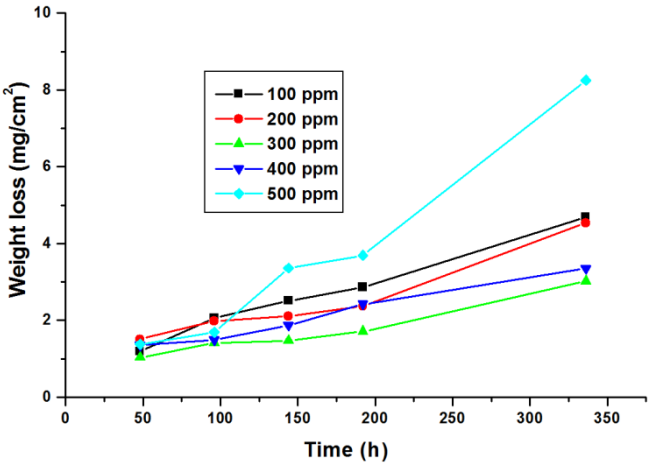

Fig. 7.9. Weight loss for mild steel in 1 M HCl when Hbpct was the inhibitor.

The compound Hanpt as an inhibitor gave minimum weight loss at about 500 ppm concentration in 1 M HCl for the mild steel. The minimum value for weight loss per unit was observed when 300 ppm solution of 1 M HCl. The variation in weight loss for mild steel in 1 M HCl is given in Fig. 7.10.

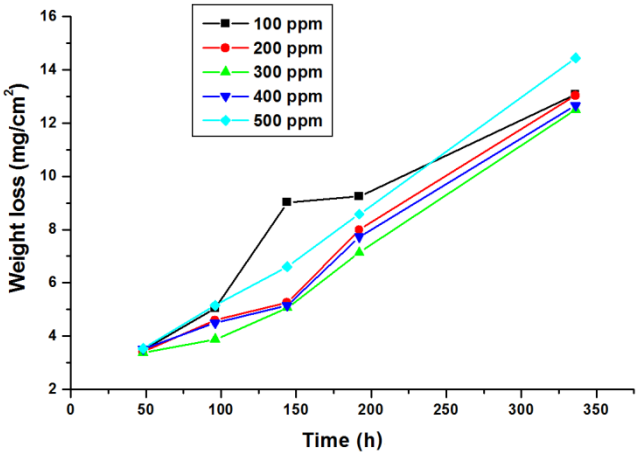

Fig. 7.10. Weight loss for mild steel in 1 M HCl when Hanpt was the inhibitor.

A comparison of weight loss per unit area for mild steel when different thiosemicarbazones were used as inhibitor is given in Fig .7.11. It is clear from the graph that as the time increases the weight loss per unit area of the mild steel was also increased. The minimum weight loss per unit was observed when Hbpct used as the inhibitor. Inhibitors Hbpct and H_2bsmt showed a very low weight loss per unit area as compared to other inhibitors. The action of H_2bsct was found to be different from all other inhibitors, as it showed a large increase in weight loss per unit area for the mild steel after 96 h. This could be explained on the basis of formation of a layer of thiosemicarbazone was formed within this time period. When time increases the action of H_2bsct will be the formation of a complex leading to corrosion instead of inhibition. Thus it could be suggested that H_2bsct could act as a good inhibitor only for a short period of time.

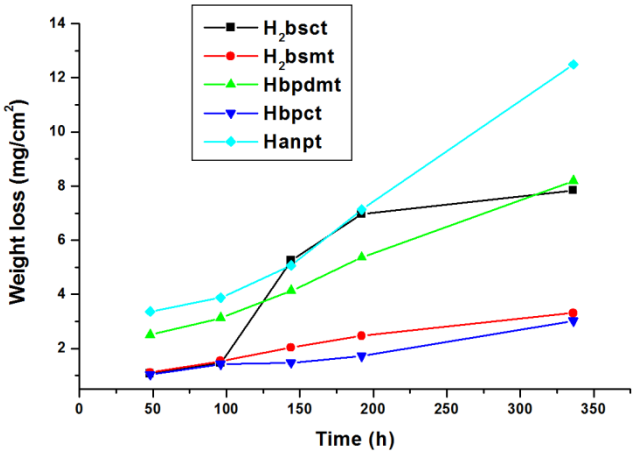

Fig. 7.11. Weight loss for mild steel in 1 M HCl at optimum concentration of thiosemicarbazones.

7.3.1.2. Corrosion rate

Corrosion rates for mild steel in 1 M HCl in the presence and absence of an inhibitor was calculated from Eq. 7.3. The results are tabulated in Table 7.2.

Table 7.2. Corrosion rate for mild steel

Sample	Con^{n} (ppm)	Time(h)				
		48	96	144	192	336
Blank		140	262	184	116	37
H_2bsct	100	20.3	11.7	21.2	20.0	15.9
	200	10.8	9.4	19.4	17.1	15.4
	300	9.8	6.9	15.9	15.9	10.2
	400	15.9	9.9	18.6	16.5	11.6
	500	18.1	25.1	19.2	17.9	13.4
H_2bsmt	100	15.9	11.1	9.1	9.6	9.3
	200	15.5	9.0	8.1	6.9	4.8
	300	10.1	6.6	6.2	5.7	4.4
	400	12.8	8.7	9.0	6.9	9.0
	500	15.9	9.2	9.4	10.5	10.1
Hbpdmt	100	29.1	16.8	16.5	13.4	11.1
	200	22.9	14.2	12.5	12.2	10.7
	300	24.7	16.1	14.3	14.1	11.8
	400	25.8	17.7	15.1	14.7	13.4
	500	27.8	20.5	16.4	15.7	15.7
Hbpct	100	13.9	9.4	7.7	6.5	6.1
	200	10.8	9.1	6.4	5.4	5.9
	300	9.4	6.5	4.5	3.9	4.0
	400	12.4	6.8	5.7	4.9	4.4
	500	12.6	7.8	10.2	8.4	10.7
Hanpt	100	31.7	23.1	27.5	21.5	17.1
	200	31.2	21.0	16.0	18.2	17.1
	300	30.8	17.7	15.5	16.3	16.3
	400	32.1	20.6	15.7	17.7	16.6
	500	32.3	23.5	20.2	19.6	18.9

Corrosion rate for mild steel in 1 M HCl without inhibitor is given in Fig. 7.12. The corrosion rate for mild steel increases with time and reaches a maximum upto 144 h with a value of 262 mpy after which the value

decrease. This is due to the formation of a protective layer of rust on the surface of the metal with time. Since our study is limited to a time period of two weeks, the protective layer remains on the surface and as time goes on this layer will be broken and will lead to drastic corrosion and hence destruction of the metal.

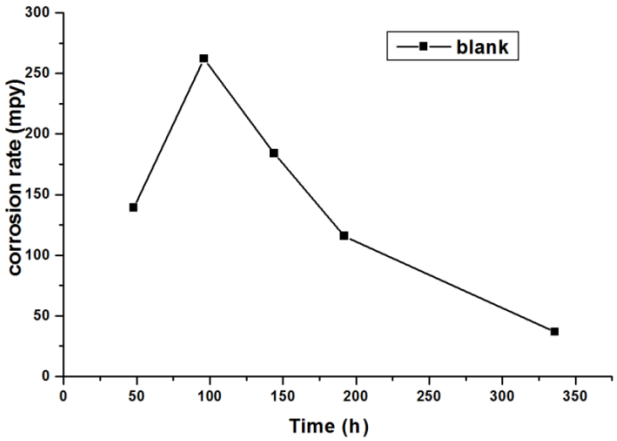

Fig. 7.12. Corrosion rate for mild steel in 1 M HCl in the absence of inhibitor.

The corrosion rate for mild steel in 1 M HCl with H_2bsct as the inhibitor is depicted in Fig. 7.13. It is clear from the figure that H_2bsct at a concentration of 300 ppm in 1 M HCl exhibited minimum corrosion rate for a time period of 336 h. The maximum corrosion rate is observed for a concentration of 100 ppm of H_2bsct in 1 M HCl for all time period except for 96 h. At 96 h H_2bsct with 500 ppm concentration exhibited maximum corrosion rate with a value of 25.1 mpy after that there is a decrease in corrosion rate as compared to other concentrations. This could be explained on the basis of formation of a strong complex on the surface of metal leading to destruction of the surface. With time this complex will adsorbed again on the surface leading to inhibition. The minimum corrosion rate for all other concentration was observed at 96 h.

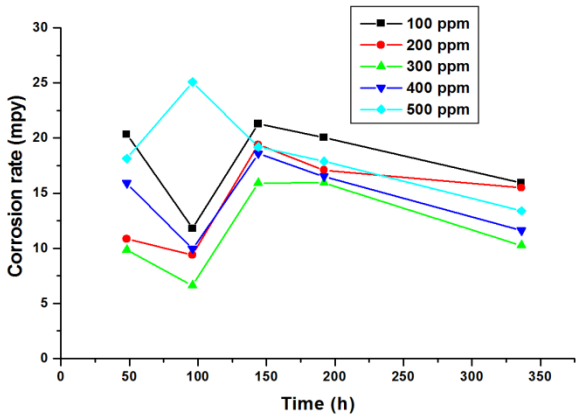

Fig. 7.13. Corrosion rate for mild steel in 1 M HCl with H_2bsct as the inhibitor.

Fig. 7.14 represents the corrosion rate of mild steel in 1 M HCl with H_2bsmt as the inhibitor. H_2bsmt at a concentration of 300 ppm in 1 M HCl showed a minimum corrosion rate for mild steel. It is observed that with time the corrosion rate decreases for this concentration of H_2bsmt in 1 M HCl. The corrosion rate did not show much change when concentration of inhibitor was 200 and 300 ppm. For all other concentrations the corrosion rate increases and reaches a maximum at 336 h (14 days). So 300 ppm is the optimum concentration for H_2bsmt with 1 M HCl for mild steel.

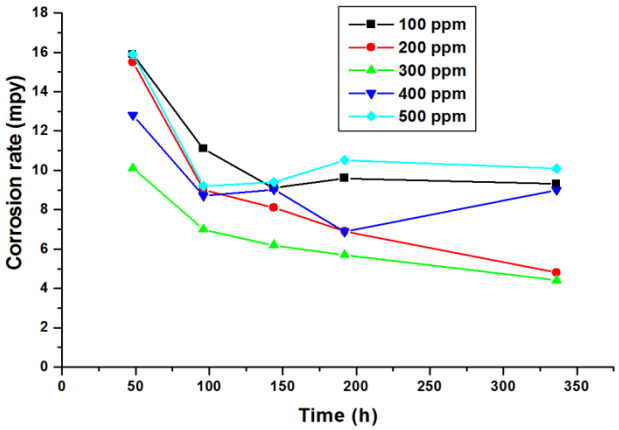

Fig. 7.14. Corrosion rate for mild steel in 1 M HCl with H_2bsmt as the inhibitor.

Corrosion rate for mild steel in 1 M HCl with various concentrations of Hbpdmt is given in Fig. 7.15. It is observed that a concentration of 200 ppm of Hbpdmt showed a minimum corrosion rate for mild steel in 1 M HCl as compared to other concentrations. From the figure it is evident that the corrosion rate of Hbpdmt does not vary much with change in concentration.

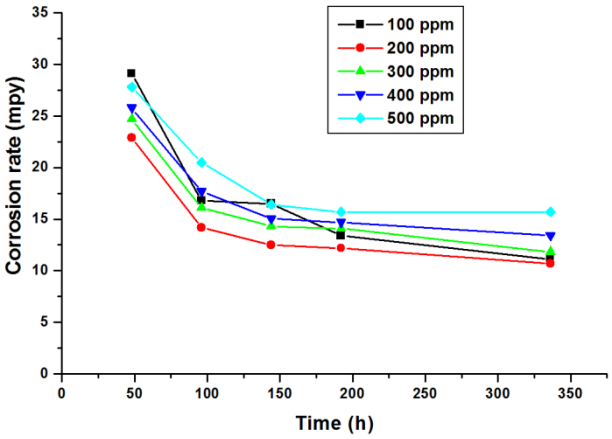

Fig. 7.15. Corrosion rate for mild steel in 1 M HCl with Hbpdmt as the inhibitor.

Fig. 7.16 represents the corrosion rate for mild steel in 1 M HCl when Hbpct was used as inhibitor. At an inhibitor concentration of 300 ppm in 1 M HCl, the corrosion rate was found to be minimum confirming it to be the optimum concentration for Hbpct. The corrosion rate for mild steel in the presence of inhibitor with concentrations of 100, 200, 300 and 400 ppm did not vary much with increase in time. But at a concentration of 500 ppm the corrosion rate showed an increase with time indicating increase in corrosion. The minimum value of 7.8 mpy for corrosion rate for mild steel with 500 ppm of Hbpct was observed at 96 h.

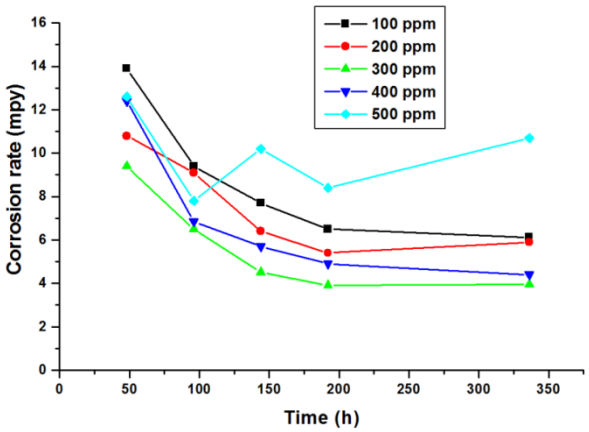

Fig. 7.16. Corrosion rate for mild steel in 1 M HCl with Hbpct as the inhibitor.

When Hanpt at variable concentration was used as the inhibitor for corrosion with 1 M HCl on mild steel corrosion rates decreased from a concentration of 100 to 300 and then increased from 400 to 500 ppm of Hanpt. The variation of corrosion rate with time when different concentrations of Hanpt was used as the inhibitor is given in Fig. 7.17.

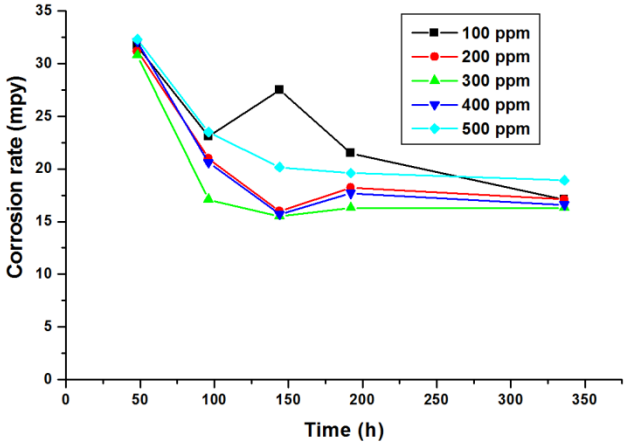

Fig. 7.17. Corrosion rate for mild steel in 1 M HCl with Hanpt as the inhibitor.

For Hanpt showed at a maximum corrosion rate with 100 ppm and a minimum with 300 ppm in 1 M HCl on mild steel. The minimum corrosion rate was observed for a concentration of 300 ppm of Hanpt in 1 M HCl with a value of 15.5 mpy for a time period of 144 h.

A comparison of all thiosemicarbazone with respect to corrosion rate at various time intervals at their respective optimum concentrations are given in Fig. 7.18. Hbpct showed a minimum corrosion rate of 3.9 mpy for a time period of 192 h as compared to all other thiosemicarbazones indicating it to be the best corrosion inhibitor for mild steel in 1 M HCl. The maximum corrosion rate was exhibited by Hanpt making it the least acceptable corrosion inhibitor as compared to other. The corrosion rate for Hbpct did not vary much with increase in time indicating the formation of a protective layer of the compound on the surface even at 336 h.

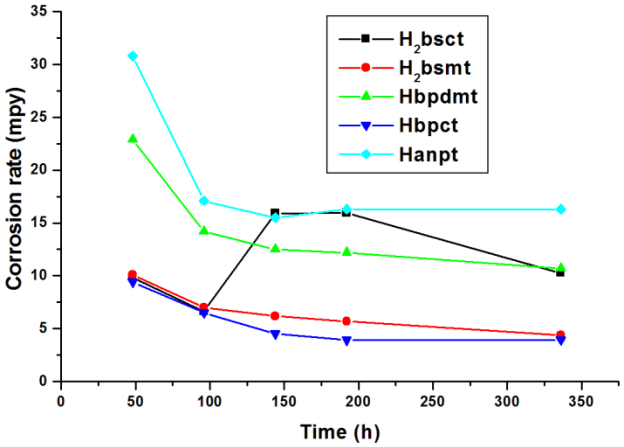

Fig. 7.18. Comparison of corrosion rate for mild steel in 1 M HCl with different thiosemicarbazones as inhibitors.

7.3.1.3 Corrosion inhibition efficiency

Corrosion inhibition efficiency of mild steel in different thiosemicarbazones were calculated using Eq. 7.2. Corrosion inhibition efficiency of mild steel containing thiosemicarbazones with different concentrations in 1 M HCl at a time interval of 48-336 h is tabulated in Table 7.3.

Table 7.3. Corrosion inhibition efficiency of thiosemicarbazones as inhibitors.

Sample	Concentration (ppm)	Time (h)				
		48	96	144	192	336
H_2bsct	100	85.4	95.5	88.4	82.6	56.5
	200	92.2	96.4	89.5	85.1	57.7
	300	93	97.3	91.4	86.1	72
	400	88.5	96.2	89.9	85.6	68.4
	500	86.9	90.3	89.6	84.5	63.5
H_2bsmt	100	88.5	95.7	95.1	91.7	77.5
	200	88.8	96.6	95.6	93.9	86.7
	300	92.6	97.4	96.6	95.0	88.0
	400	90.7	96.1	95.1	93.9	75.1
	500	88.4	96.4	94.9	90.8	72.2
Hbpdmt	100	78.8	93.5	91.1	88.3	69.7
	200	83.4	94.5	93.2	89.3	70.8
	300	82.2	93.8	92.2	87.6	67.7
	400	81.2	93.1	91.8	87.0	63.4
	500	79.9	92.0	91.2	86.3	56.7
Hbpct	100	89.9	96.4	95.8	94.3	83.3
	200	92.1	96.6	96.5	95.3	83.8
	300	93.2	97.6	97.5	96.6	89.2
	400	91.0	97.4	96.9	95.7	88.0
	500	90.8	97.0	94.4	92.7	70.3
Hanpt	100	77.1	91.1	85.1	81.7	53.3
	200	77.6	91.9	91.4	84.2	53.5
	300	77.8	93.2	91.7	85.7	55.4
	400	76.7	92.1	91.5	84.7	54.4
	500	76.5	91.0	89.2	82.8	48.0

Corrosion inhibition efficiency of mild steel with different concentrations of H_2bsct in 1 M HCl at various time intervals is given in Fig. 7.19. From the observations it is evident that 300 ppm concentration of H_2bsct with 1 M HCl exhibited maximum inhibition efficiency with a value of 97.3%. It is also evident that the maximum inhibition efficiency is exhibited at 96 h for all concentrations of the thiosemicarbazone. At this time the minimum inhibition efficiency was exhibited by 500 ppm of H_2bsct. So it is confirmed that 300 ppm is the optimum concentration for H_2bsct toward inhibition action.

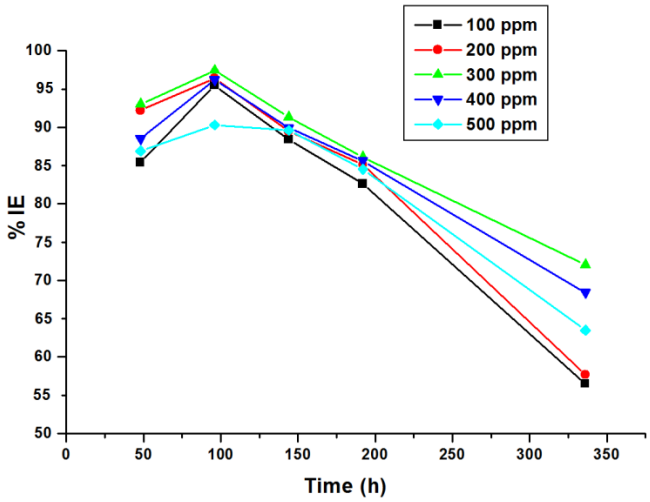

Fig. 7.19. Inhibition efficiency of mild steel in 1 M HCl with H_2bsct as the inhibitor.

Inhibition efficiency of mild steel in 1 M HCl with H_2bsmt was maximum at 96 h for a concentration of 300 ppm (Fig. 7.20) with a value of 97.4%. At 96 h it was observed that 100 ppm of H_2bsct with 1 M HCl is showing minimum inhibition efficiency for mild steel. Thus for H_2bsct 300 ppm is the optimum concentration to exhibit inhibition action.

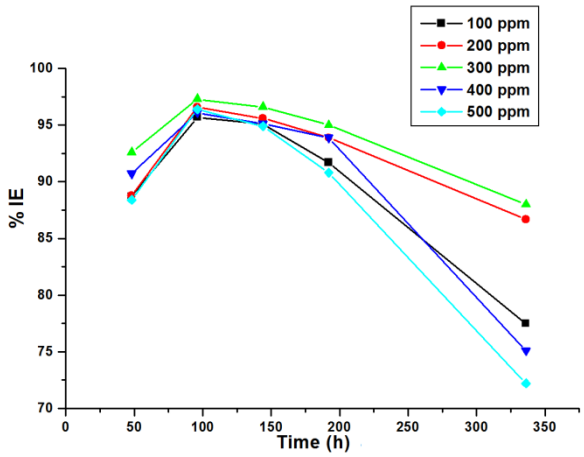

Fig. 7.20. Inhibition efficiency of mild steel in 1 M HCl with H_2bsmt as the inhibitor.

The variation of corrosion inhibition efficiency of mild steel in 1 M HCl with Hbpdmt as the inhibitor is given in Fig. 7.21. The maximum inhibition efficiency for the compound was observed for Hbpdmt at a concentration of 200 ppm with 1 M HCl at 96 h with a value 94.5%. The maximum inhibition efficiency for all concentrations of Hbpdmt was exhibited at 96 h. Thus 96 h was the optimum time and 200 ppm was the optimum concentration of Hbpdmt towards inhibition action for mild steel in 1 M HCl.

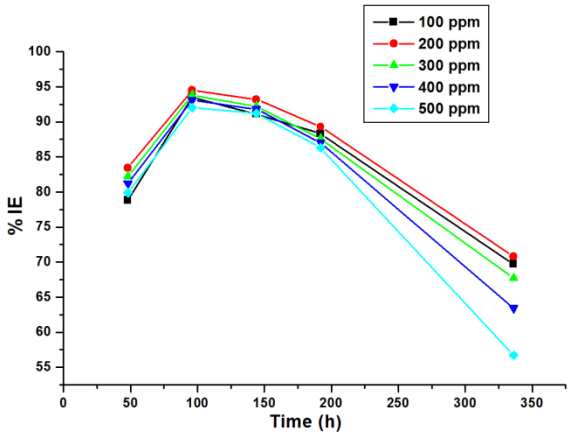

Fig. 7.21. Inhibition efficiency of mild steel in 1 M HCl with Hbpdmt as the inhibitor.

Fig. 7.22 gave the trend in corrosion inhibition efficiency of mild steel in 1 M HCl containing Hbpct with variable concentration for time interval of 48-336 h. It is evident that Hbpct with a concentration of 300 ppm at 96 h exhibit maximum corrosion inhibition efficiency with a value of 97.6%. The mild steel at this time showed good corrosion inhibition for all concentration of Hbpct. When mild steel is immersed in 1 M HCl containing Hbpct for longer time period the inhibition efficiency decreases.

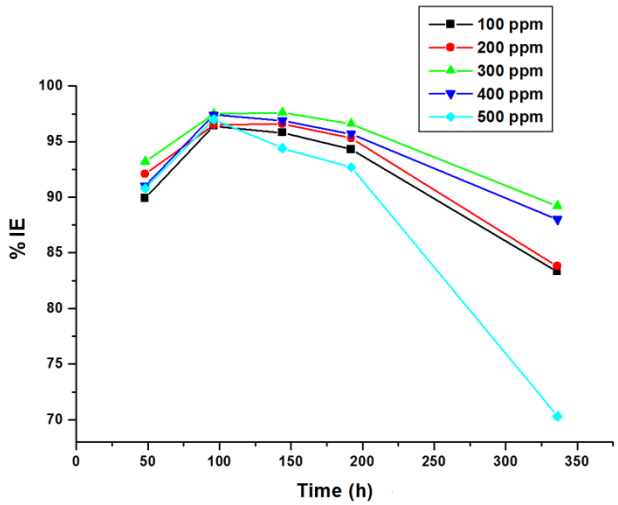

Fig. 7.22. Inhibition efficiency of mild steel in 1 M HCl with Hbpct as the inhibitor.

The mild steel in 1 M HCl containing Hanpt as the inhibitor exhibit corrosion inhibition efficiency as given in Fig. 7.23. The Hanpt at a concentration of 300 ppm with 1 M HCl exhibited maximum corrosion inhibition efficiency at 96 h with a value of 93.2%. When time increases, the corrosion inhibition efficiency of the mild steel decrease for all concentrations of Hanpt.

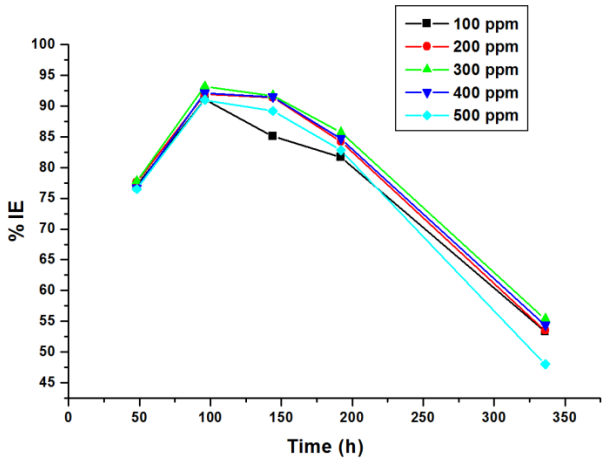

Fig. 7.23. Inhibition efficiency of mild steel in 1 M HCl with Hanpt as the inhibitor.

A comparison of corrosion inhibition efficiency of mild steel in 1 M HCl containing different thiosemicarbazones having optimum concentration at a time interval of 48-336 h is depicted in Fig. 7.24. From the figure it is clear that Hbpct gave maximum inhibition efficiency for mild steel in 1 M HCl. All thiosemicarbazones show maximum inhibition efficiency at 96 h. Thus 96 h is the optimum time for the thiosemicarbazones to exhibit corrosion inhibition action on mild steel in 1 M HCl.

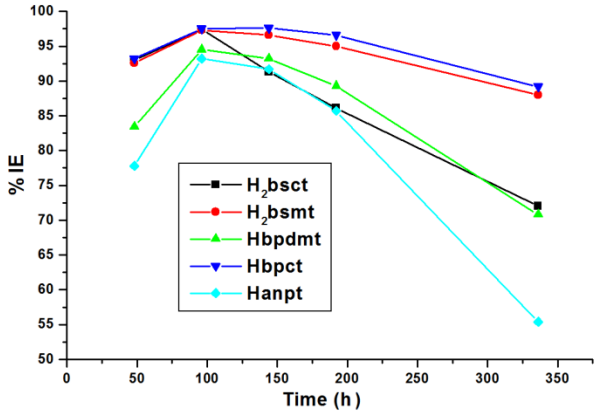

Fig. 7.24. Comparitive study of corrosion inhibition efficiency of mild steel in 1 M HCl containing different thiosemicarbazones.

From weight loss method it was observed that the corrosion inhibition decreases after 300 ppm concentration and may be attributed to the fact that at higher concentrations the tendency to form a stable complex may result and the metal may be peeled from the surface as a complex instead of forming a layer of the compound on the surface. It was found that Hbpct is the strongest corrosion inhibitor among the five thiosemicarbazones under study. The increase corrosion inhibition with concentration for the compounds in 1 M HCl suggest that the compounds have a great tendency to adsorb to the surface of mild steel *via* various intermolecular interactions. The corrosion inhibition efficiency of the thiosemicarbzones follow the order Hbpct > H_2bsmt > H_2bsct > Hbpdmt > Hanpt.

7.3.2. Adsorption isotherm behavior.

The adsorption isotherm behavior was studied using the surface coverage values obtained from Eq. 7.7 and plotting C/θ in mol L^{-1} against concentration C in mol L^{-1}. it is found that the adsorption of the sample at 96 hrs is fitted by Langmuir adsorption isotherm to Eq. 7.18 a modification of Eq. 7.4 [20]:

$$\frac{C}{\theta} = \frac{1}{K_{ads}} + C \quad \text{.....(7.18)}$$

The Langmuir adsorption isotherm for compounds H_2bsct, H_2bsmt, Hbpct and Hanpt are given in Figs. 7.25-7.28

On the basis of Langmuir isotherm, the standard free energy for adsorption can be calculated using the Eq. 7.9. The results are tabulated in Table 7.4. The negative value of the Gibbs free energy suggests that the adsorption is guided by a spontaneous process. It is found that the value of -20 kJ mol^{-1} or less indicates physisorption and a value around -40 kJ mol^{-1} indicates a threshold between chemisorption and physisorption [18,25]. In

the present study the $\Delta G°_{ads}$ values were found to be nearly -40 kJ mol^{-1}, which suggest that the adsorption may proceed *via* physisorption or chemisorption.

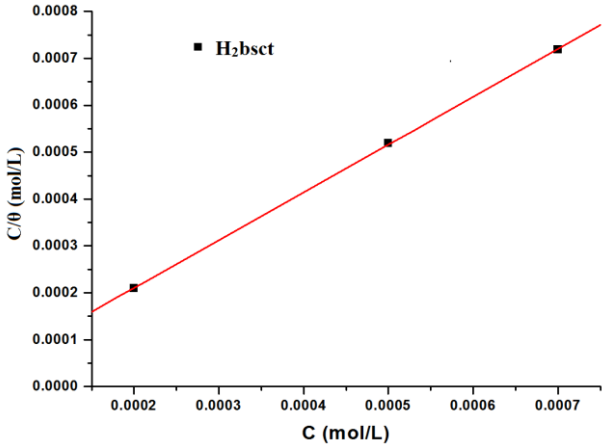

Fig. 7.25. Adsorption isotherm for H_2bsct.

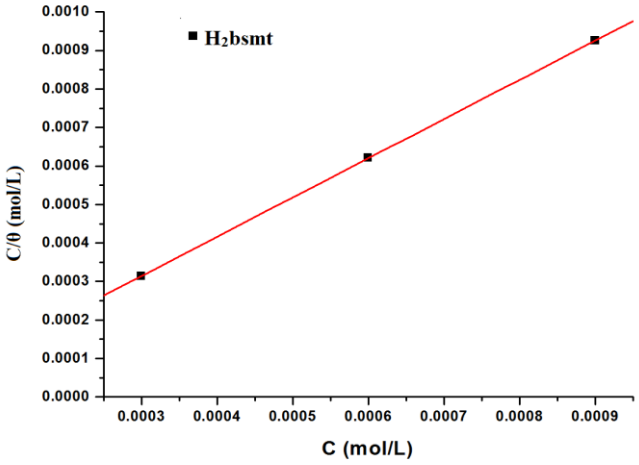

Fig. 7.26. Adsorption isotherm for H_2bsmt.

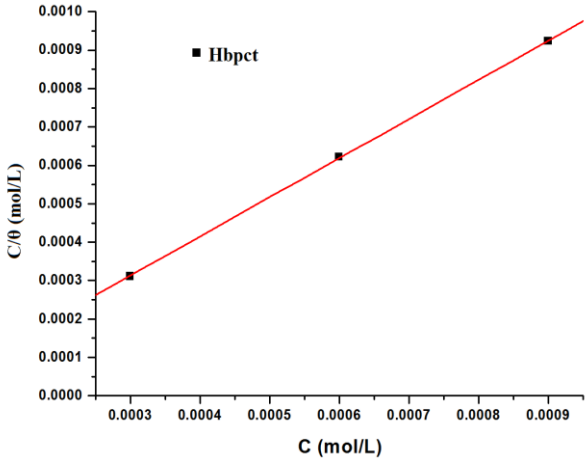

Fig. 7.27. Adsorption isotherm for Hbpct.

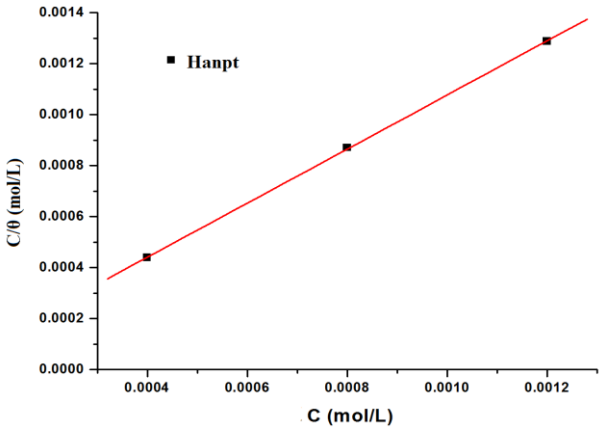

Fig. 7.28. Adsorption isotherm for Hanpt.

Table 7.4. The kinetic parameters of corrosion inhibition of various thiosemicarbazones at their optimum concentrations

Compound	K_{ads} (L/mol)×10^4	$-\Delta G^0_{ads}$ (kj/mol)
H_2bsct	7.1	31.81
H_2bsmt	5.8	30.57
Hbpct	5.0	30.60
Hanpt	20	29.60

7.3.3 Surface studies

The SEM images are taken to support the experimental findings by weight loss methods.

The SEM images of the metal surfaces before immersion in the corroding solution and in 1 M HCl solution were compared with that of the surfaces immersed in 1 M HCl containing different thiosemicarbazones as inhibitors at its optimum concentration. The SEM images of the surfaces after immersion for 96 h are given in Fig.7.29.

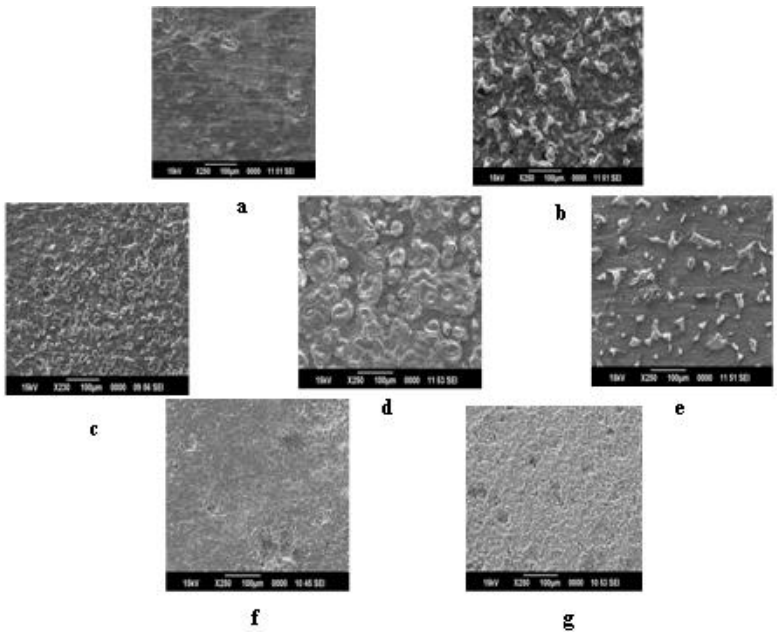

Fig. 7.29. a) Surface before immersion in 1 M HCl b) Surface after immersion in 1 M HCl c) Surface after immersion in mixture of 1 M HCl and Hbsct d) Surface after immersion in mixture of 1 M HCl and Hbsmt e) Surface after immersion in mixture of 1 M HCl and Hbpdmt f) Surface after immersion in mixture of 1 M HCl and Hbpct g) Surface after immersion in mixture of 1 M HCl and Hanpt.

It is found that the metal samples before immersion in 1 M HCl are displaying surface features similar to the surface after immersion in a mixture of 1 M HCl and Hbpct, which is further evidence for greater corrosion inhibition of the thiosemicarbazone Hbpct.

7.3.4. Electrochemical methods

7.3.4.1. Tafel polarization studies

The polarization studies of all the thiosemicarbazones were done for variable concentrations from 100 ppm to 500 ppm. It was observed that 1 M HCl under room temperature gave a corrosion current of about 446 mV cm^{-2}. E_{corr}, Tafel slopes βa and βc (for anodic polarization and cathodic polarization respectively), and i_{corr} values are given in Table 7.5. The inhibition efficiency was calculated using Eq. 7.17.

It is found that on adding inhibitor to 1 M HCl the corrosion current decreases. For H_2bsct on adding 100 ppm concentration of the compound to 1 M HCl decreases the corrosion current density to 41.4 mV cm^{-2}. On increasing the concentration of H_2bsct the corrosion current decreases further to 19.7 mV cm^{-2} for 300 ppm and on further increasing the concentration the corrosion current seems to increase indicating the optimum concentration of H_2bsct as an inhibitor was 300 ppm. The Fig. 7.30 represents Tafel polarization curves for mild steel in a mixture of H_2bsct and 1 M HCl and is compared with the Tafel plot obtained without inhibitor. The positive shift observed for corrosion potential suggests that H_2bsct acts as an anodic type inhibitor and act by decreasing the anodic current. The maximum corrosion inhibition efficiency was observed for 300 ppm concentration of H_2bsct with a value of 95.5%.

Table 7.5. Tafel polarization parameters

Sample	Con^{n} (ppm)	-E_{corr} (mV vs SCE)	β_a (mV dec^{-1})	β_c (mV $dec^{-1`}$)	i_{corr} (µA cm^{-2})	IE (%)
Blank		518	97.2	133.8	446	
	100	452	78	139	41.4	90.7
	200	437	56	247	21.5	95.1
H_2bsct	300	439	56	209	19.7	95.5
	400	453	82	100	76.0	82.9
	500	491	88	125	93.0	79.1
	100	501	87	132	130.0	70.8
	200	490	85	144	83.5	81.2
H_2bsmt	300	484	70	131	39.7	91.1
	400	500	90	130	140.0	68.6
	500	463	83	146	148.5	66.7
	100	479	112	155	235.0	47.3
	200	504	99	138	202.0	54.7
Hbpdmt	300	515	85	122	235.5	47.1
	400	503	85	139	243.0	45.5
	100	451	48	148	24.5	94.5
	200	457	51	152	23.3	94.7
Hbpct	300	430	43	183	19.2	95.7
	400	470	58	135	27.4	93.8
	500	514	70.	137	114.0	74.4
	100	520	125	143	392.0	12.1
Hanpt	200	513	100	133	304.5	31.7
	300	522	93	123	289.3	35.1
	400	523	113	137	327.5	26.5

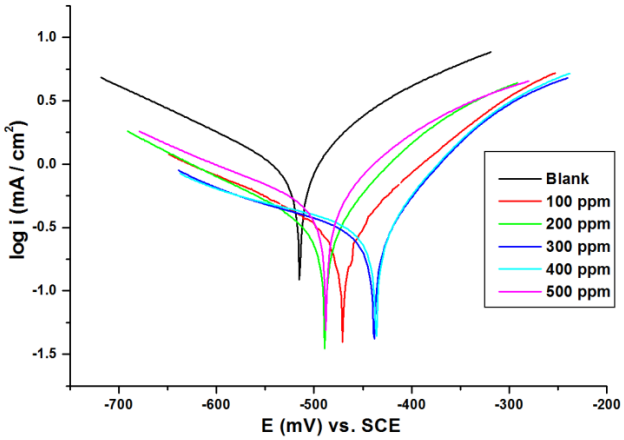

Fig. 7.30. Tafel polarization curves for mild steel in the presence and absence of H_2bsct at different concentrations.

On addition of 100 ppm solution of H_2bsmt to 1 M HCl the corrosion current decreases to a value of 130 mV cm^{-2} which decreases further upon increasing concentration of H_2bsmt and reach a value of 39.7 mV cm^{-2} when the concentration of compound becomes 300 ppm in 1 M HCl. Thus it is evident that 300 ppm concentration is the optimum concentration of the inhibitor H_2bsmt. The positive shift observed for E_{corr} value suggests that H_2bsmt acts as an anodic type inhibitor and inhibition was due to decrease in anodic current. There is no much difference in the anodic and cathodic slopes for different concentrations of H_2bsmt, suggest that H_2bsmt acts as a mixed type of inhibitor in which both anodic and cathodic reaction occur simultaneously [26]. The Fig. 7.31 represents Tafel plots for mild steel in 1 M HCl with and without inhibitor H_2bsmt with different concentrations. The calculated corrosion inhibition efficiency for mild steel in 1 M HCl in the presence of H_2bsmt at 300 ppm showed a maximum value of 91.1%.

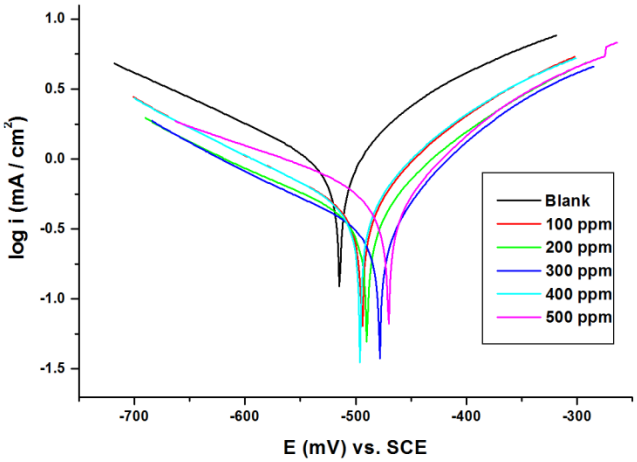

Fig. 7.31. Tafel polarization curves for mild steel in the presence and absence of H_2bsmt at different concentrations.

Tafel plots for mild steel in 1 M HCl with and without inhibitor Hbpdmt with different concentrations is given in Fig. 7.32. On addition of 100 ppm concentration of Hbpdmt the corrosion current decreases to 235 mV cm^{-2} and seemed to decrease up to a value of 202 mV cm^{-2} at a concentration of 200 ppm of Hbpdmt in 1 M HCl. So it is confirmed that 200 ppm was the optimum concentration of Hbpdmt. Further increase in concentration of Hbpdmt in 1 M HCl, the corrosion current increases. The shift in corrosion potential for mild steel in the presence of Hbpdmt with 1 M HCl was in the positive direction by a small value, gave the idea that this thiosemicarbazone is a weak inhibitor as compared to H_2bsct and H_2bsmt. The slopes for anodic and cathodic curves indicate that the inhibition is facilitated through both anodic and cathodic reactions and Hbpdmt acts as a mixed type of inhibitor. The study was limited to 500 ppm of Hbpdmt as the results were not good to interpret. The corrosion inhibition efficiency of mild steel was found to be maximum with a value of 54.7% for 200 ppm concentration of Hbpdmt in 1 M HCl.

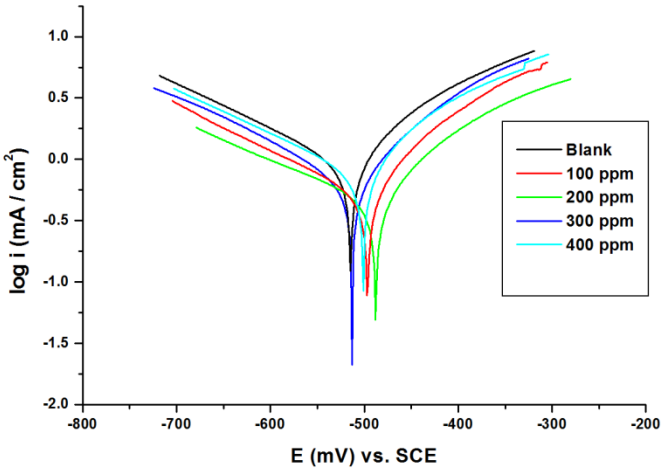

Fig. 7.32. Tafel polarization curves for mild steel in the presence and absence of Hbpdmt at different concentrations.

The compound Hbpct gives a decrease in corrosion current for mild steel to a value of 24.5 mV cm^{-2} on addition of 100 ppm of the compound in solution to 1 M HCl. This corrosion current decreased on further addition of Hbpct in 100 ppm amounts and showed a lowest value for corrosion current when 300 ppm of Hbpct in 1 M HCl is added. On further increase in concentration the corrosion current was found to increase, suggesting that 300 ppm concentration was optimum for Hbpct in 1 M HCl. The corrosion inhibition efficiency of mild steel in 1 M HCl is found to be maximum at 300 ppm concentration of Hbpct with a value of 95.7 mV cm^{-2}. The anodic and cathodic slopes did not vary much for different concentrations suggest that the corrosion inhibition was effected by both cathodic and anodic reactions and it act as a mixed type of inhibitor. The decrease in value of corrosion potential as compared to that of absence of inhibitor suggests that the inhibition aided through decrease in anodic current. Fig. 7.33 gave the Tafel polarization curves for mild steel in the presence and absence of Hbpct at different concentrations.

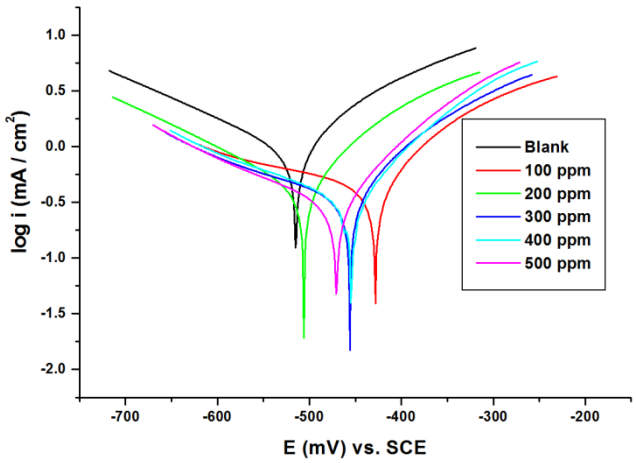

Fig. 7.33. Tafel polarization curves for mild steel in the presence and absence of Hbpct at different concentrations.

The Tafel polarization curves for mild steel in the presence and absence of Hanpt at different concentration was depicted in Fig. 7.34. On adding 100 ppm of Hanpt to 1 M HCl the corrosion current of mild steel found to decrease to a value of 392 mV cm^{-2}. The minimum corrosion current of 289.3 mV cm^{-2} was observed for a concentration of 300 ppm of Hanpt in the solution. The positive shift for corrosion potential of mild steel in the presence of Hanpt suggested that the inhibition was aided by decrease in anodic current. The variation in anodic and cathodic slopes suggested that the inhibition action was due to both anodic and cathodic reactions. The maximum corrosion inhibition efficiency of mild steel in Hanpt with 1 M HCl was found to be 35.3% at 300 ppm concentration. Thus 300 ppm is the optimum concentration of Hanpt to act as an inhibitor for corrosion on mild steel in 1 M HCl.

A comparative study of various thiosemicarbazones toward corrosion inhibition was represented in Fig. 7.35. It can be suggested that the thiosemicarbazone Hbpct with corrosion current of 19.2 mV cm^{-2} was the strongest inhibitor of all the thiosemicarbazones. The corrosion inhibition

efficiency was comparable with that found from weight loss method. The large difference found for Hbpdmt and Hanpt as that of weight loss method may be due to induced corrosion leading to strong reaction between the metal centers and thiosemicarbazones.

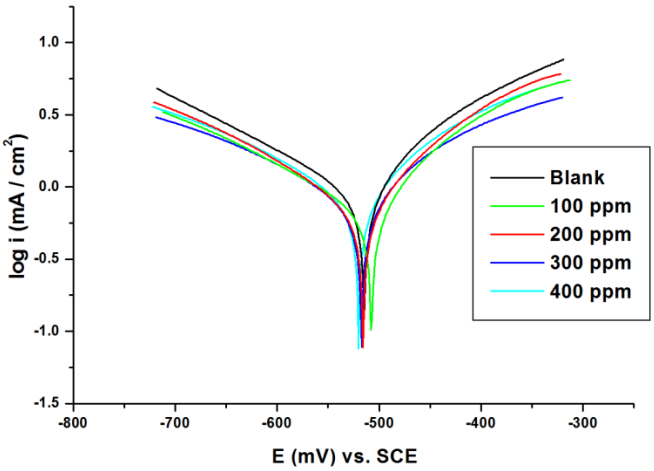

Fig. 7.34. Tafel polarization curves for mild steel in the presence and absence of Hbpct at different concentrations.

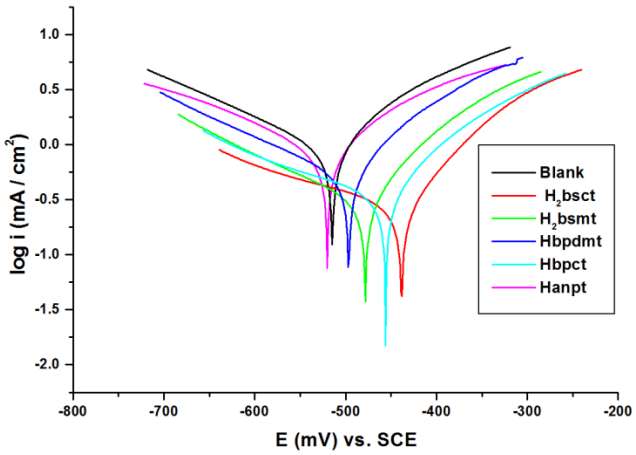

Fig. 7.35. A comparison of Tafel polarization curves for mild steel in the presence of different thiosemicarbazones.

7.3.4.2. Electrochemical impedance spectroscopy

7.3.4.2.1. Nyquist plots

The Nyquist plots for mild steel in 1 M HCl with different thiosemicarbazones were recorded for variable concentrations of thiosemicarbazones in 1 M HCl. The electrode resistance (R_e) of the mild steel is represented by a semicircle radius that appears in the low frequency region of the Nyquist plot. The smaller the diameter of the semicircle or the distance from the centre more would be the corrosion. It was found that the area under Nyquist curve increased from 100 ppm to 300 ppm concentrations of thiosemicarbazones and then decreased for all of the thiosemicarbazone except Hbpdmt, for which the increase in area was observed from 100 ppm to 200 ppm of thiosemicarbazones in 1 M HCl and then decreased. Figs.7.36 to 7.40 depicts Nyquist plots for all of the thiosemicarbazones.

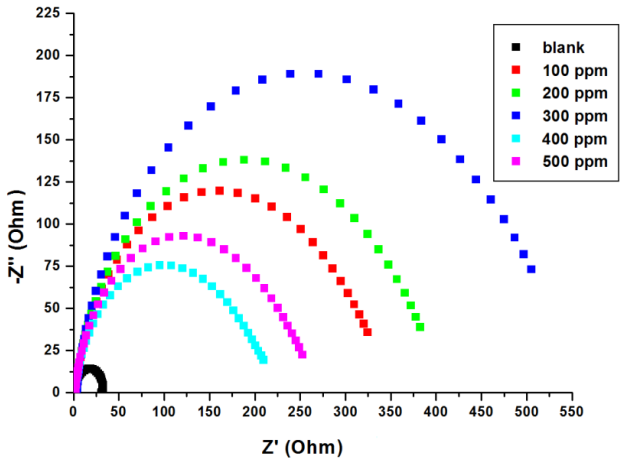

Fig. 7.36. Nyquist plots for mild steel in presence of various concentrations of H_2bsct with 1 M HCl.

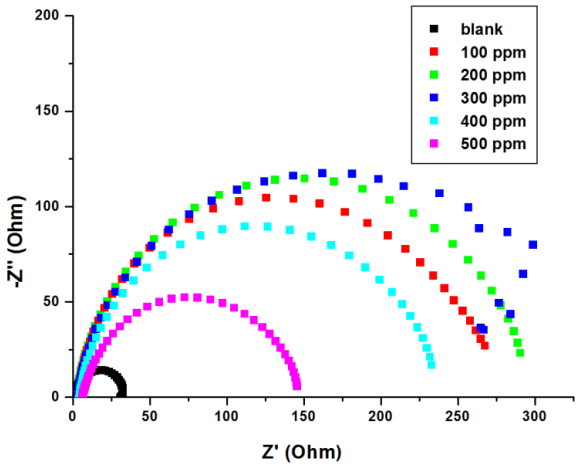

Fig. 7.37. Nyquist plots for mild steel in presence of various concentrations of H_2bsmt with 1 M HCl.

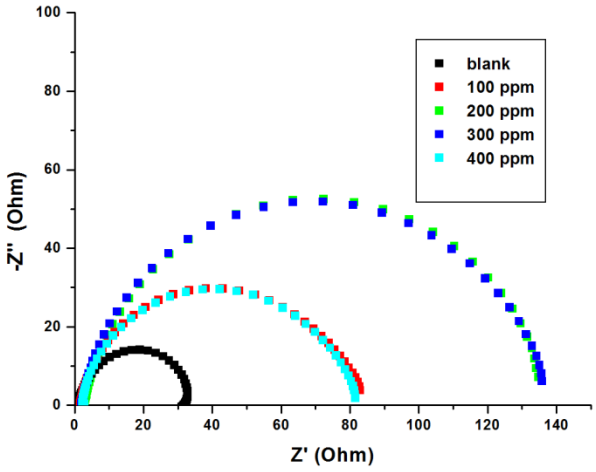

Fig. 7.38. Nyquist plots for mild steel in presence of various concentrations of Hbpdmt with 1 M HCl.

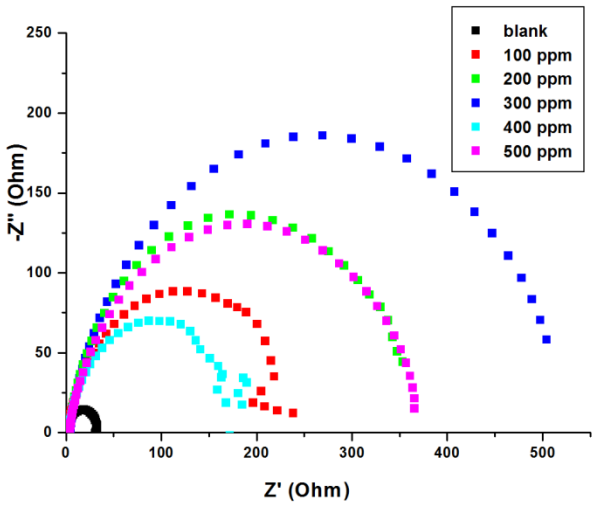

Fig. 7.39. Nyquist plots for mild steel in presence of various concentrations of Hbpct with 1 M HCl.

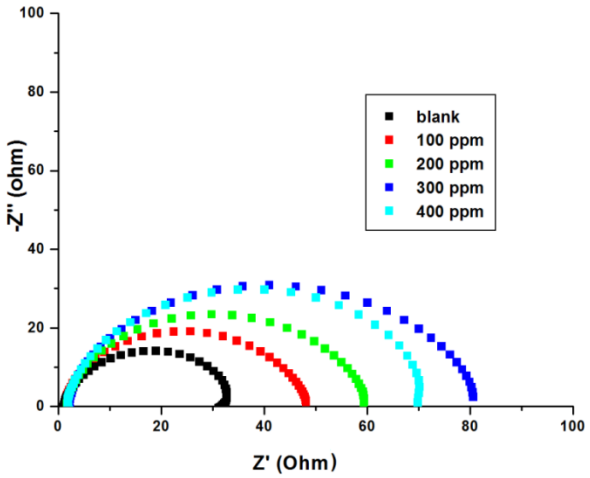

Fig. 7.40. Nyquist plots for mild steel in presence of various concentrations of Hanpt with 1 M HCl.

Fig.7.41 showed a comparative study of thiosemicarbazones at their optimum concentrations. It is found that the diameter of the curves for Hbpct and Hbsct are comparably high and the least is for Hanpt. This

confirms the grater inhibition action of Hbpct and Hbsct as compared to other thiosemicarbazones.

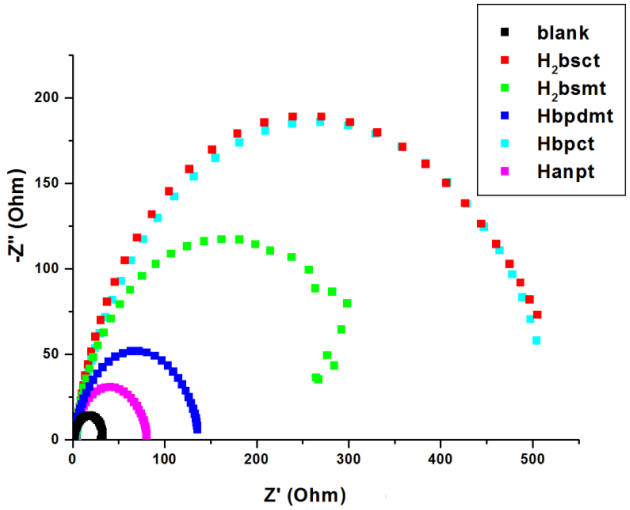

Fig. 7.41. Nyquist plots for mild steel in 1 M HCl containing different thiosemicarbazones at their optimum concentrations.

7.3.4.2.1 Bode plots

Bode plots were plotted with log (frequency) versus log (real component of resistance). The bode plots for mild steel in 1 M HCl in the absence and in the presence of various concentrations of thiosemicarbazones are given in Figs 7.42 to 7.46. In a Bode plot, the higher the magnitude of the curve, the greater is the corrosion resistance. It is found that the variation is similar to that of Tafel Plots and Nyquist plots. It was observed that 300 ppm concentration of the thiosemicarbazones except that for Hbpdmt is the optimum concentration with which the mild steel showed maximum inhibition efficiency. For Hbpdmt 200 ppm was observed to be the optimum concentration. The compounds Hbpct and Hbsct show comparatively high inhibition than for all of the other thiosemicarbazones and compound Hanpt shows least corrosion inhibition.

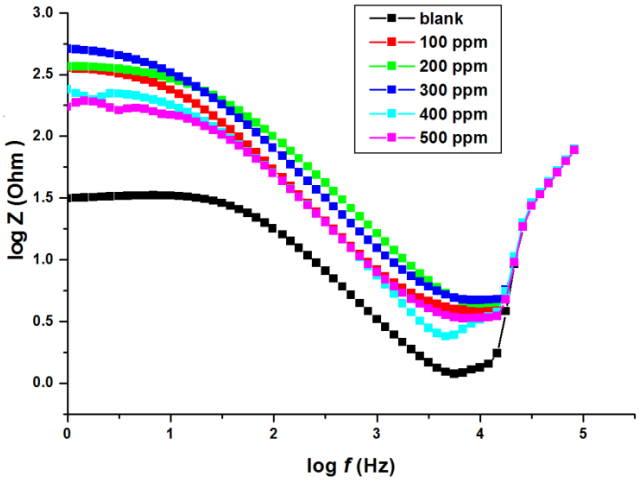

Fig. 7.42. Bode plot for mild steel in 1 M HCl in the presence and absence of various concentration of H_2bsct.

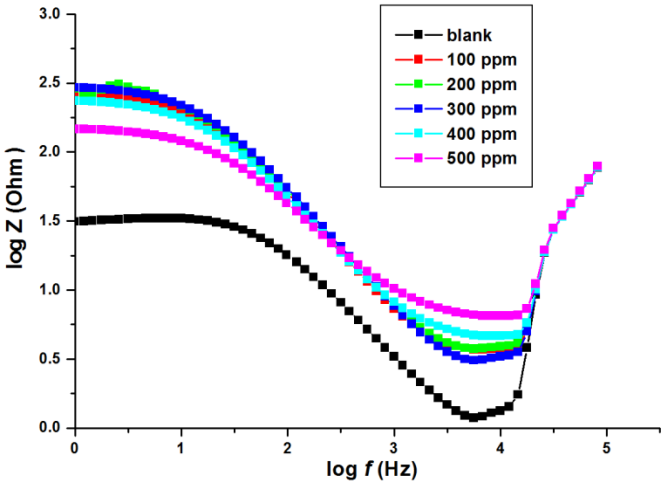

Fig. 7.43. Bode plot for mild steel in 1 M HCl in the presence and absence of various concentration of H_2bsmt.

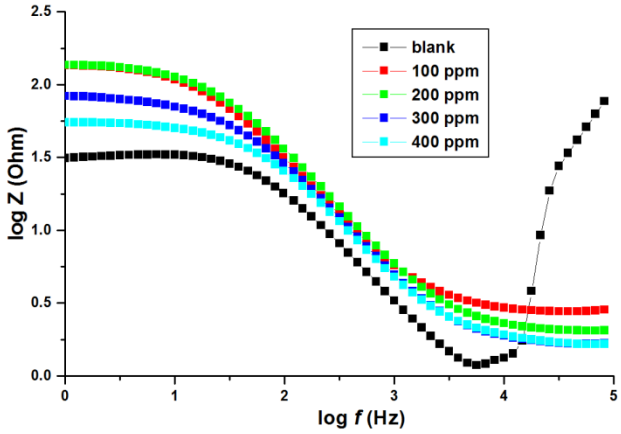

Fig. 7.44. Bode plot for mild steel in 1 M HCl in the presence and absence of various concentration of Hbpdmt.

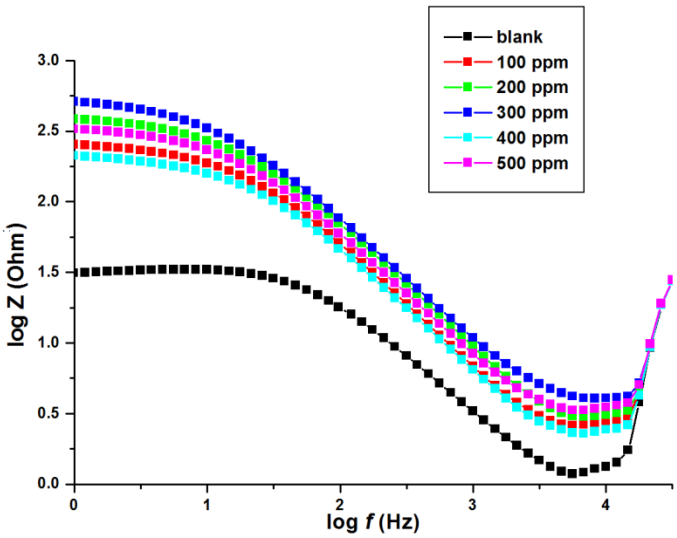

Fig. 7.45. Bode plot for mild steel in 1 M HCl in the presence and absence of various concentration of Hbpct.

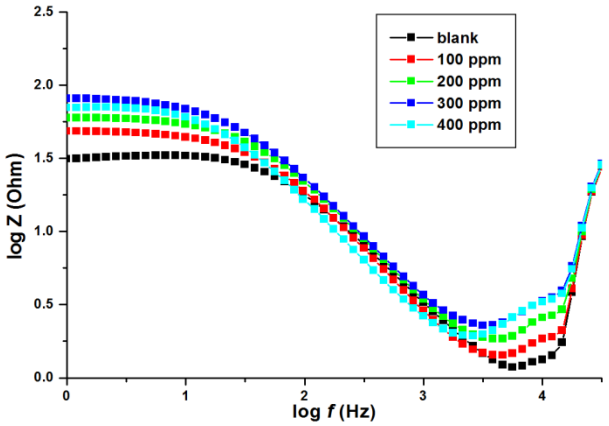

Fig. 7.46. Bode plot for mild steel in 1 M HCl in the presence and absence of various concentration of Hanpt.

A comparison of various inhibition of corrosion of mild steel in thiosemicarbazones at their optimum concentration with 1 M HCl was done. The compounds Hbpct and Hbsct show comparatively high inhibition than for all of the other thiosemicarbazones and compound Hanpt shows least corrosion inhibition. The graphical representation of comparison of different thiosemicarbazone at their optimum concentration towards corrosion inhibition on mild steel in 1 M HCl is given in Fig. 7.47.

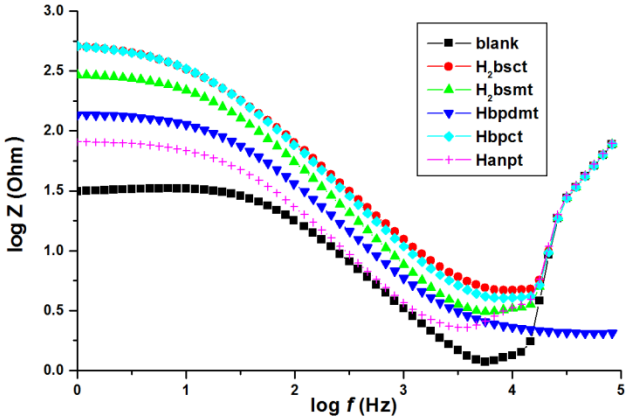

Fig. 7.47. Comparison of thiosemicarbazone when mild steel is immersed in a solution containing 1 M HCl and thiosemicarbazone.

Thus from electrochemical methods, it is found that the corrosion on mild steel is lowered in the presence of inhibitor like thiosemicarbazones. As per electrochemical methods it is confirmed that the order of corrosion inhibition offered by thiosemicarbazones to mid steel in presence of 1 M HCl, was Hbsct > H_2bsct > H_2bsmt > Hbpdmt > Hanpt.

7.3.5. Mechanism for inhibition action….

Form the studies it is evident that all the thiosemicarbazones act as good inhibitor to corrosion by 1 M HCl on mild steel. Many mechanisms have been suggested for corrosion inhibition of thiosemicarbazones. The thiosemicarbazones in the present study shows a good inhibition upto a concentration of 300 ppm and above this concentration corrosion predominates over inhibition. The surface study and adsorption studies suggest that physisorption or chemisorptions on the surface for its inhibitory action, which suggest that a chemical interaction is occurring on the surface and when the concentration increases the metal shows a tendency to form strong complexes *via* lone pair of electron on the nitrogen and deprotonated sulfur, and come to the solution which in turn increase corrosion. The compounds that show maximum inhibition efficiency in electrochemical studies contain N^4-cyclohexhylthiosemicarbazone in it, so it can be suggested that the structure of the compounds also have some effect on corrosion inhibition. The compounds which show minimum inhibition action is due to the formation of strong complex or are absorbed to a less extent on the surface. Studies revealed that the factors like structure, functional group of high electron density, planarity of the molecule *etc.* influence the corrosion inhibition to a greater extented.

Fig. 7.48 represents IR spectra for the powder separated from the surface of mild steel immersed in 1 M HCl for 96 h. It is already established from studies that the region 1000 to 400 cm^{-1} gives valuable information regarding the Fe–O lattice [27]. The band in the region 570

cm^{-1} corresponds to Fe–O stretching [27]. The characteristic band for Fe–O is observed at 687 cm^{-1} for the sample obtained in the absence of 1 M HCl. This band showed a shift to 697, 704 and 697 cm^{-1} for sample in 1 M HCl with inhibitors Hbpdmt, H_2bsct and Hanpt, respectively. The bands corresponding to the ligand C–H stretch is observed at 3100 cm^{-1}which. Unfortunately, we could not get good infrared spectra for other two samples. However, these results suggest that the ligands are present on the surface of the metal in adsorbed form.

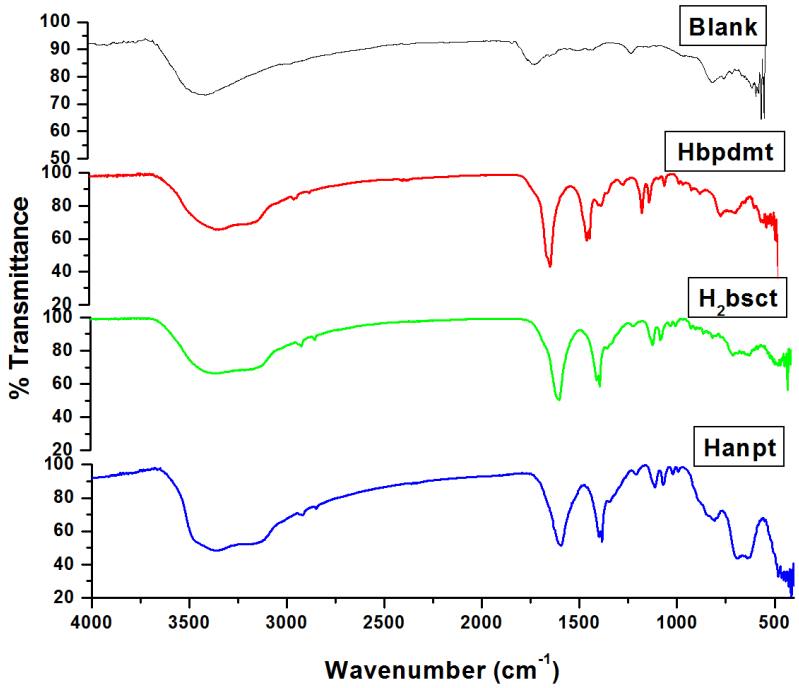

Fig. 7.48. Infrared spectra for the corroded powder obtained from the metal surface in the presence and absence of inhibitor.

From these investigations it is evident that the thiosemicarbazones H_2bsct, Hbpct and H_2bsmt act as good corrosion inhibitors, whereas Hbpdmt and Hanpt are not good corrosion inhibitors for mild steel in 1 M HCl. From the weight loss method and electrochemical methods it is

found that the thiosemicarbazones follow the order Hbpct > H_2bsmt > H_2bsct > Hbpdmt > Hanpt. There is a controversy between the position of H_2bsmt and H_2bsct and can be explained as follows. These two compounds show a large corrosion inhibition to same extent but it is found that for long term application, compound H_2bsmt is better as compared to H_2bsct as evident from the weight loss experiments.

7.5. Conclusion

In corrosion inhibition studies of mild steel in the presence and absence of five different thiosemicabazones namely 4-benzyloxy salicylaldehyde-N^4-cyclohexylthiosemicarbazone (H_2bsct), 4-benzyloxysalicy laldehyde-N^4-methyl thiosemicarbazone (H_2bsmt), 6-bromopyridine-N^4,N^4-dimethylthiosemicarbazone (Hbpdmt), 6-bromopyridine-N^4-cyclohexylthio semicarbazone (Hbpct), and acetone-N^4(4-nitrophenyl)thiosemicarbazone (Hanpt) were done. It is found that all thiosemicarbazones act as corrosion inhibitors for mild steel in 1 M HCl from both weight loss and electrochemical methods. The corrosion rate, corrosion inhibition efficiency was determined from a weight loss method. The studies proved that Hbpct acts as the best inhibitor of all. Tafel polarization studies reveal that the compounds act as inhibitors by decreasing anodic current. A comparison of inhibition action of all the compounds was done by impedance studies as well. From these studies it is found that Hbpct is the best corrosion inhibitor for mild steel in 1 M HCl with a corrosion inhibition efficiency of 97.6% for 300 ppm concentration by weight loss method. The compounds are active even after two weeks and confirm their ability to act as good corrosion inhibitors. The inhibition efficiency of mild steel in 1 M HCl in the presence of thiosemicarbazones synthesized in the present study were comparable with already reported results on thiosemicarbazones and other organic compounds [15,20].

References

[1] V.S. Sastri, Green Corrosion Inhibitors, John Wiley and Sons, Inc., Hoboken, New Jersey (2011)

[2] E. Kálmán, I. Felhosi H. Kármán, I. Lukovits, J. Telegdi, G. Palinkas, Material Science and Technology, Wiley-VCH Xerlag GmbH and Co. KGaA (2013).

[3] A. Singh, M.A. Quraishi, J. Mater. Environ. Sci. 6 (2015) 224.

[4] H. Frasch, U.S. Patent No: 556 (1985) 669.

[5] J.A. Aupperle, Proceedings of 18th Annual meeting of American Society for Testing and Materials, Philadelphia PA:ASTM (1915) 119.

[6] W.H. Hill, U.S. Patent No: 2384 (1945) 467.

[7] S.K. Shukla, M.A. Quraishi, R.A. Prakash, Corros. Sci. 50 (2008) 2867.

[8] X. Li, S. Deng, H. Fu, Corros. Sci. 53 (2011) 3241.

[9] L. Cavallaro, L. Felloni, G. Trabenelli, F. Pulidori, Electro Chim. Acta 8 (1963) 521.

[10] S.L. Granese, B.M. Rosales, C. Oviedo, J.O. Zerbino, Corros. Sci. 33 (1992) 1439.

[11] M.A. Quraishi, D. Jamal, Corros. 56 (2000) 156.

[12] M.A. Quraishi, D. Jamal, Mater. Chem. Phys.71 (2001) 202.

[13] S. John, R. Jeevana, K.K. Aravindakshan, A. Joseph, Egypt. J. Pet. 26 (2017) 405.

[14] M. Muralisankar, R. Sreedharan, S. Sujith, N.S.P. Bhuvanesh, A. Sreekanth, J. Alloys Compd. 695 (2017) 171.

[15] I. Lukovits, A. Shaban, E. Kalman, Electrochem. Acta 50 (2005) 4128.

[16] M.M. Solomon, S.A. Umoren, J. Colloid Interface Sci., 462 (2016) 29.

[17] M.A. Quraishi, S.K. Shukla, Mater. Chem. Phys. 113 (2009) 685.

[18] S.L.A. Kumar, M. Gopiraman, M.S. Kumar, A. Sreekanth, Ind. Eng. Chem. Res. 50 (2011) 7824.

[19] V.S. Sastri, Corrosion Inhibition, Principals and Application, John Wiley & Sons, New York (1998).

[20] D. Zahng, Y. Tang, S. Qi, D. Dong, H. Cang, G. Lu, Corros. Sci. 102 (2016) 517.

[21] Z. Ahmad, Principles of Corrosion Engineering and Corrosion Control, Elsevier Ltd. (2006).

[22] A.J. Bard, L.R. Faulkner, Electrochemical Methods, Fundamentals and Applications, Wiley Inter Science Publication, New York (2000).

[23] V.S. Sastri, E. Ghali, M. Elboujdani, Corrosion Prevention and Protection Practical Solutions, John Wiley & Sons (2007).

[24] S.W. Dean, R.A. Woodroof, J.S. Nicholas, Electrochemical methods for Evaluating Corrosion Inhibitors in Strong Acid Systems, in Laboratory tests and standards, ASTM STP 866, American Society for Testing and Materials, Philadelphia (1985) 228.

[25] N. Soltani, H. Salavati, N. Rasouli, M. Paziresh, A. Moghadasi, Iran J. Aanl. Chem. 2 (2015) 22.

[26] M.M. Solomon and S.A. Umoren, J. Colloid Interface Sci., 462 (2016) 29.

[27] M. Ishii, M. Naskahira, Infrared Adsorption Spectra and Cation Distribution in $(Mn,Fe)_3O_4$, Solid State Commun. 11 (1972) 209.

.....ൟ.....

Chapter 8

SUMMARY AND CONCLUSION

Thiosemicarbazones were found to be an important class of compounds from late 19th century owing to its biological, industrial and clinical applications. The presence of =N–NH–C(=S)– system enable these compounds to show thioamido-thioiminol tautomerism, which enable them to act as a neutral as well as anion in complexes. The presence of sulfur in the thiosemicarbazone moiety makes it suitable for many of its applications. Introduction of a hetro atom on the thiosemicarbzone moiety makes its coordination properties more interesting. These compounds can act as 'masked thiolate' ligands, which is a contributing factor to their ability to act as highly versatile donor to a large number of metals. A large verity of coordination geometries has been already reported.

Objectives of the present work

Upon suitable selection of aldehydes and thiosemicarbzides it is possible to synthesize NS, ONS and NNS donor thiosemicarbzones. The ability of these compounds to show large variety of coordination geometry contributes to many of its applications. Along with already established biological applications, thiosemicarbzones and its metal complexes were also found to show corrosion inhibition application in various solvents. One of such application is found in oil field, where con. HCl is used for easy extraction of oil from oil well.

The importance and fascinating properties of thiosemicarbazones observed in various field is the driving force to select them as the ligands for our present study. Five different thiosemicarbazones that can act as ONS, NNS and NS donor to metals such as vanadium, molybdenum, manganese, nickel, palladium, cobalt, copper and cadmium were selected. Introduction of heterocyclic bases such as 2,2'-bypyridine and 1,10-phnanthroline increased the number of coordination geometries.

The new thiosemicarbazones synthesized in the present study are

1) 4-Benzyloxysalicylaldehyde-N^4-cyclohexylthiosemicarbazone (H_2bsct)
2) 4-Benzyloxysalicylaldehyde-N^4-methylthiosemicarbazone (H_2bsmt)
3) 6-Bromopyridine-2-carbaldehyde-N^4,N^4-dimethylthiosemicarbazone (Hbpdmt)
4) 6-Bromopyridine-2-carbaldehyde-N^4-cyclohexylthiosemicarbazone (Hbpct)
5) Acetone-N^4-(4-nitrophenyl)thiosemicarbazone (Hanpt)

All the thiosemicarbazones were tested and compared for their corrosion inhibition action towards mild steel in 1 M HCl.

The thesis is divided into 8 chapters

Chapter 1

Chapter 1 deals with the literature review on synthesis and applications of various thiosemicarbazones and metals. The physicochemical techniques used for characterization of the synthesized compounds are also described.

Chapter 2

Chapter 2 include synthesis and characterization of ONS donor 4-benzyloxysalicylaldehyde-N^4-cyclohexylthiosemicarbazone. The compound is characterized using various physicochemical methods such as IR, UV and NMR. Single crystal X-ray diffractions studies on the crystals of the compound support its structure. VO(II), Ni(II), Cu(II), MoO_2(II), Pd(II) and Cd(II) complexes of the thiosemiarbazones were synthesized and characterized by IR, UV, NMR and EPR. Heterocyclic bases such as 1.10-phenanthroline and 2,2'-bypyridine are used as coligands. Single crystals MoO_2(II) complexes were obtained from slow evaporation of the compound from DMSO and DMF respectively, The single crystal X-ray crystallographic studies suggest that both the complexes have a distorted octahedral geometry. The vanadium complex exists in dimeric form which is confirmed from the magnetic moment values. All the complexes except that of cadmium is found form an octahedral geometry around the central metal. Presence of coordinated water is confirmed from TG-DTA analysis.

Chapter 3

In this chapter synthesis and characterization of ONS donor 4-benzyloxysalicylaldehyde-N^4-cyclohexylthiosemicarbazone and its VO(II), Co(II), Ni(II), Cu(II), MoO_2(II) and is given. Single crystal X-ray diffraction studies on the thiosemicarbazone and one of the metal complexes gives further evidence for their coordination geometry. Vanadium is found to form a dimer. The presence of lattice as well as coordinate water present in the complexes was confirmed from TG-DTA analysis. EPR spectra for the oxidovanadium complex suggest that the d^1 electron is residing in the d_{xy}^1 orbital. The copper complex gives well resolved axial spectra with hyperfine

splitting in the perpendicular region. The g values suggest that the unpaired electron in the Cu^{2+} molecule resides in the d_{x2-y2} orbital. The heterocyclic base pyridine was introduced to increase the number of coordination possibilities.

Chapter 4

Synthesis and characterization of an NNS donor 6-Bromopyridine-2-carbaldehyde-N^4,N^4-dimethylthiosemicarbazone is given in this chapter. The ligand is characterized by IR, UV and NMR techniques. Single crystals of the thiosemicarbzones were separated from the mother liquor and single crystal X-ray diffraction study was performed. Mn(II), Ni(II), Cu(II), MoO_2(II), Pd(II), and Cd(II) complexes of this thiosemicarbazone was synthesized and characterized by IR, UV, NMR techniques. TG-DTA analysis was also performed to identify the coordinated and lattice water along with the bases present in the complexes. The EPR studies of copper complexes give a hyperfine splitting in the parallel and perpendicular region indicated strong azomethane coordination to the metal centre. One of the nickel complexes was isolated as single crystals upon recrystallization from DMF. The X-ray crystallographic study reveals that the complex assumes a distorted octahedral geometry around the central metal atom.

Chapter 5

In this chapter synthesis and characterization of NNS donor 6-Bromopyridine-2-carbaldehyde-N^4-cyclohexhylthiosemicarbazone and its metal complexes were discussed. 6-Bromopyridine-2-carbaldehyde-N^4-cyclohexhylthiosemicarbazone was characterized by IR, UV and NMR techniques along with single crystal X-ray diffraction studies. Ni(II), Cu(II), Pd(II) and Cd(II) complexes of

this ligand was synthesized and characterized by IR, UV and NMR. The copper complexes give well resolved EPR spectra and the g values confirm that the unpaired electron is residing in the $d_{x^2-y^2}$ orbital. One of the nickel complexes was isolated as single crystal form mother liquor. The single crystal X-ray diffraction studies reveal that the ligand coordinate in the thio- iminol form and a distorted octahedral complex with two nitrate anions in the lattice, that balance the positive charge on the metal. The cadmium complex was also re-crystallized form DMF and the X-ray crystallographic studies reveal that the complex is having a distorted octahedral geometry.

Chapter 6

This chapter include synthesis and characterization of NS donor thiosemicarbazone acetone-N^4-(4-nitrophenyl)thiosemicarbzone and its metal complexes. The thisemicarbzone was characterized by IR, UV and NMR techniques. The single crystals of the compound were isolated from acetone solution and X-ray diffraction studies were performed. Co(III), Ni(II), Cu(II) Pd(II) and Cd(II) complexes of this ligand was synthesized and characterized by IR, UV and NMR. The copper complex gives axial EPR spectrum at 77 K. The nickel and copper complexes were separated as single crystals by re-crystallization from DMF solution. The X-ray diffraction studies reveal that both complexes give a distorted square planar complex with DMF in the lattice.

Chapter 7

This chapter deals with the corrosion inhibition studies of the thiosemicarbazones on mild steel in 1 M HCl solution. All the thiosemicarbzones were used for the study. The chapter gives a

brief literature review on corrosion inhibition studies using thiosemicarbazones as inhibitor and historical background of the study. The studies were done with 100, 200, 300, 400 and 500 ppm concentration solutions of compounds and done for 14 days with intervals of 2, 4, 6, 8 and 14 days. The inhibition studies were done using two different methods, weight loss method and electrochemical analysis method. All compounds were compared towards its inhibition activity and results are given in the graphical form. The weight loss per unit area, corrosion rate in mpy and corrosion inhibition efficiency was calculated using weight loss method. Form the electrochemical analysis Tafel plotes, Nyquist plots and Bode plotes were obtained and corrosion current and corrosion rates were obtained from Tafel plotes. The values are comparable as that of weight loss method. SEM images of the surfaces before and after study were also given. The adsorption on the metal surface found to follow Langmuir adsorption isotherm and from the negative ΔG values it is clear that the compounds follow physisorption. Form all the studies it is found that 300 ppm concentration is the optimum concentration for all the compounds except Hbpdmt, for which 200 ppm is the optimum concentration. The compound Hbpct is the strong corrosion inhibitor towards mild steel in 1 M HCl and Hanpt is the least corrosion inhibitor. The compounds show maximum inhibition efficiency for 4 days.

Chapter 7

Summary and Conclusion

.....ꕥ.....

List of Publications

Paper Published

[1] Crystal structure of N-[(E)-3,5-dichloro-2-hydroxybenzylidene]-4-nitrobenzohydrazide dimethylformamide monosolvate Bibitha Joseph, N. R. Sajitha, M. Sithambaresan, E. B. Seena and M. R.Prathapachandra Kurup, Acta Cryst. (2015). E71, o826–o827

[2] Crystal structure of aqua[(E)-N′-(5-bromo-2-oxidobenzylidene-κO) benzohydrazidato-κ^2O,N′]dioxidomolybdenum(VI)dimethylformamide monosolvate Radhika Sudheer, M. Sithambaresan, **N. R. Sajitha**, E. Manoj and M. R. Prathapachandra Kurup, Acta Cryst. (2015) E71, 702-705.

[3] Crystal structure of 2-[(E)-4-benzyloxy-2-hydroxybenzylidene]-N-cyclohexyl hydrazinecarbothioamide acetonitrile hemisolvate, **N. R. Sajitha**, M. Sithambaresan and M.R.P. Kurup, Acta Cryst. (2014) E70, o987-o988.

[4] (E)-2-(4-Benzyloxy-2-hydroxybenzylidene)-N-methylhydrazinecarbothioamide, **N. R. Sajitha**, M. Sithambaresan and M.R.P. Kurup, Acta Cryst. (2014) E70, o112-o113.

[5] 5,5'-Bis(benzyloxy)-2,2′-[hydrazinediylidenebis(methanylylidene)] diphenol, **N. R. Sajitha**, M. Sithambaresan and M.R.P. Kurup, Acta Cryst. (2013) E69, o1755.

Papers presented in symposia

[1] Participated and presented a poster entitled "**Synthesis, and characterization of 4-benzyloxysalicylaldehyde-N(4)-methylthiosemicarbazone**" in the International Conference on "Materials for the Millennium" (MatCon-2016) held at the Department of Applied Chemistry, Cochin University of Science and Technology, Kochi during 14-16th January 2016.

[2] Participated and presented a poster entitled "**Crystal structure of bis[N-(4-nitrophenyl)- 2-(propan-2- ylidene) hydrazinecarbothioamido] copper(II) N,N-dimethylformamide monosolvate** in the National Conference "Current Trends in Chemistry" (CTriC-2014) held at the Department of Applied Chemistry, Cochin University of Science and Technology, Kochi during 17-18 January 2014.

.....ഠോര.....